UNIVERSITY OF CALIFORNIA SAN DIEGO

Nanomedicines for Transient Ultrasound Imaging and Cancer Immunotherapy

A Dissertation submitted in partial satisfaction of the requirements
for the degree Doctor of Philosophy

in

Materials Science and Engineering

by

Tengyu He

Committee in charge:

Professor Jesse V. Jokerst, Chair
Professor Jinhye Bae
Professor Tariq Rana
Professor Nicole F. Steinmetz
Professor Liangfang Zhang

2023

The Dissertation of Tengyu He is approved, and it is acceptable in quality and form for publication on microfilm and electronically.

UNIVERSITY OF CALIFORNIA SAN DIEGO

2023

DEDICATION

To Mr. Keduan, Mrs. Yueyun Chen, and Miss. Wei He
For their endless love and support

致我的父亲何可端先生，母亲陈月云女士和妹妹何为小姐；
感谢他们无条件的爱和支持。

TABLE OF CONTENTS

LIST OF FIGURES

LIST OF TABLES

ACKNOWLEDGEMENTS

First, I would like to thank my advisor, Professor Jesse Jokerst, for his scientific and professional mentorship and endless support in my research in the past four years. I am always grateful for the many opportunities he has provided me with. I would also like to thank my committee members for their guidance and support: Professor Nicole F. Steinmetz, Professor Tariq Rana, Professor Liangfang Zhang, and Professor Jinhye Bae.

I would like to give thanks to my close collaborators. Thanks to Dr. Jing Wen for her great support in science. I am grateful for the diligent efforts of Zeliang Hu, Chuxuan Ling, and Yu-Ci Chang as Master Student Researchers. Thanks to Dr. Yong Cheng, Dr. Zhicheng Jin, Dr. Zhongchao Zhao, Dr. Jiajing Zhou, and Dr. Ming Xu for inspiring discussions in science.

I would like to express sincere gratitude to my family and friends. Thanks to my parents, Keduan He (何可端) and Yueyun Chen (陈月云), and sister Wei He (何为) for their endless love and unconditional support. Thanks to my uncle Biao He (何彪) and my brother Zhangfan Dong (董张帆) for their financial supports during the first year of my PhD study.

Chapter 1, in full, is unpublished material. The dissertation author was the author.

Chapter 2, in full, is a reprint of the material as it appears in "He, T.; Bradley, D. G.; Zhou, J.; Jorns, A.; Mantri, Y.; Hanna, J. V.; Jokerst, J. V., Hydro-Expandable Calcium Phosphate Micro/Nano-Particles with Controllable Size and Morphology for Mechanical Ablation. *ACS Applied Nano Materials* **2021,** *4* (4), 3877-3886." The dissertation author was the primary researcher and author of this paper.

Chapter 3, in full, is a reprint of the material as it appears in "He, T.; Bradley, D. G.; Xu, M.; Ko, S.-T.; Qi, B.; Li, Y.; Cheng, Y.; Jin, Z.; Zhou, J.; Sasi, L.; Fu, L.; Wu, Z.; Zhou, J.; Yim, W.; Chang, Y.-C.; Hanna, J. V.; Luo, J.; Jokerst, J. V., Bio-Inspired Degradable

Polyethylenimine/Calcium Phosphate Micro-/Nano-Composites for Transient Ultrasound and Photoluminescence Imaging. *Chemistry of Materials* **2022,** *34* (16), 7220-7231." The dissertation author was the primary researcher and author of this paper.

Chapter 4, in full, has been submitted for publication of the material as it may appear in "He, T.; Wen, J.; Wang, W.; Hu, Z.; Ling, C.; Zhao, Z.; Cheng, Y.; Chang, Y.-C.; Xu, M.; Jin, Z.; Amer, L.; Sasi, L.; Fu, L.; Steinmetz, N. F.; Rana, T. M.; Wu, P.; Jokerst, J. V., Peptide-Driven Proton Sponge Nano-Assembly for Imaging and Triggering Lysosome-Regulated Necrosis of Cancer Cells. *Advanced Materials* **2023**.". The dissertation author was the primary researcher and author of this paper.

VITA

2015 Bachelor of Engineering in Metallurgical Engineering, **Northeastern University**, Shenyang, China

2018 Master of Science in Materials Science and Engineering, **University of Chinese Academy of Sciences**, Beijing, China

2023 Doctor of Philosophy in Materials Science and Engineering, **University of California San Diego**, La Jolla, US

PUBLICATIONS

First-author

1. He, T.; Wen, J.; Wang, W.; Hu, Z.; Ling, C.; Zhao, Z.; Cheng, Y.; Chang, Y.-C.; Xu, M.; Jin, Z.; Amer, L.; Sasi, L.; Fu, L.; Steinmetz, N. F.; Rana, T. M.; Wu, P.; Jokerst, J. V., Peptide-Driven Proton Sponge Nano-Assembly for Imaging and Triggering Lysosome-Regulated Necrosis of Cancer Cells. *Advanced Materials* 2023 (Under review).
2. He, T.; Bradley, D. G.; Xu, M.; Ko, S.-T.; Qi, B.; Li, Y.; Cheng, Y.; Jin, Z.; Zhou, J.; Sasi, L.; Fu, L.; Wu, Z.; Zhou, J.; Yim, W.; Chang, Y.-C.; Hanna, J. V.; Luo, J.; Jokerst, J. V., Bio-Inspired Degradable Polyethylenimine/Calcium Phosphate Micro-/Nano-Composites for Transient Ultrasound and Photoluminescence Imaging. *Chemistry of Materials* 2022, *34* (16), 7220-7231.
3. He, T.; Bradley, D. G.; Zhou, J.; Jorns, A.; Mantri, Y.; Hanna, J. V.; Jokerst, J. V., Hydro-Expandable Calcium Phosphate Micro/Nano-Particles with Controllable Size and Morphology for Mechanical Ablation. *ACS Applied Nano Materials* 2021, *4* (4), 3877-3886.
4. Li*, Y.; He*, T.; Shi, L.; Wang, R.; Sun, J., Strain Sensor with Both a Wide Sensing Range and High Sensitivity Based on Braided Graphene Belts. *ACS Applied Materials & Interfaces* 2020, *12* (15), 17691-17698. (equal contribution)
5. He, T.; Jokerst, J. V., Structured Micro/Nano Materials Synthesized Via Electrospray: A Review. *Biomaterials Science* 2020, *8* (20), 5555-5573.
6. He, T.; Lin, C.; Shi, L.; Wang, R.; Sun, J., Through-Layer Buckle Wavelength-Gradient Design for the Coupling of High Sensitivity and Stretchability in a Single Strain Sensor. *ACS Applied Materials & Interfaces* 2018, *10* (11), 9653-9662.

Co-author

7. Qi, B.; Hariri, A.; Khazaeinezhad, R.; Fu, L.; Li, Y.; Jin, Z.; Yim, W.; He, T.; Cheng, Y.; Zhou, J.; Jokerst, J. V., A Miniaturized Ultrasound Transducer for Monitoring Full-Mouth Oral Health: A Preliminary Study. *Dentomaxillofac Radiol* 2023, *52* (1), 20220220.
8. Jin, Z.; Ling, C.; Yim, W.; Chang, Y. C.; He, T.; Li, K.; Zhou, J.; Cheng, Y.; Li, Y.; Yeung, J.; Wang, R.; Fajtova, P.; Amer, L.; Mattoussi, H.; O'Donoghue, A. J.; Jokerst, J. V., Endoproteolysis of Oligopeptide-Based Coacervates for Enzymatic Modeling. *ACS Nano* 2023, *17* (17), 16980-16992.
9. Jin, Z.; Li, Y.; Li, K.; Zhou, J.; Yeung, J.; Ling, C.; Yim, W.; He, T.; Cheng, Y.; Xu, M.; Creyer, M. N.; Chang, Y. C.; Fajtova, P.; Retout, M.; Qi, B.; Li, S.; O'Donoghue, A. J.; Jokerst, J. V., Peptide Amphiphile Mediated Co-Assembly for Nanoplasmonic Sensing. *Angewandte Chemie International Edition in English* 2023, *62* (4), e202214394.
10. Jin, Z.; Li, Y.; Li, K.; Zhou, J.; Yeung, J.; Ling, C.; Yim, W.; He, T.; Cheng, Y.; Xu, M.; Creyer, M. N.; Chang, Y. C.; Fajtova, P.; Retout, M.; Qi, B.; Li, S.; O'Donoghue, A. J.; Jokerst, J. V., Peptide Amphiphile Mediated Co-Assembly for Nanoplasmonic Sensing. *Angewandte Chemie International Edition in English* 2023, *62* (4), e202214394.
11. Cheng, Y.; Clark, A. E.; Yim, W.; Borum, R. M.; Chang, Y.-C.; Jin, Z.; He, T.; Carlin, A. F.; Jokerst, J. V., Protease-Responsive Potential-Tunable Aiegens for Cell Selective Imaging of Tmprss2 and Accurate Inhibitor Screening. *Analytical Chemistry* 2023, *95* (7), 3789-3798.
12. Chang, Y. C.; Jin, Z.; Li, K.; Zhou, J.; Yim, W.; Yeung, J.; Cheng, Y.; Retout, M.; Creyer, M. N.; Fajtova, P.; He, T.; Chen, X.; O'Donoghue, A. J.; Jokerst, J. V., Peptide Valence-Induced Breaks in Plasmonic Coupling. *Chemical Science* 2023, *14* (10), 2659-2668.
13. Zhou, J.; Yim, W.; Zhou, J.; Jin, Z.; Xu, M.; Mantri, Y.; He, T.; Cheng, Y.; Fu, L.; Wu, Z.; Hancock, T.; Penny, W.; Jokerst, J. V., A Fiber Optic Photoacoustic Sensor for Real-Time Heparin Monitoring. *Biosensors and Bioelectronics* 2022, *196*, 113692.
14. Yim, W.; Takemura, K.; Zhou, J.; Zhou, J.; Jin, Z.; Borum, R. M.; Xu, M.; Cheng, Y.; He, T.; Penny, W.; Miller, B. R., 3rd; Jokerst, J. V., Enhanced Photoacoustic Detection of Heparin in Whole Blood Via Melanin Nanocapsules Carrying Molecular Agents. *ACS Nano* 2022, *16* (1), 683-693.
15. Xu, M.; Zhou, J.; Cheng, Y.; Jin, Z.; Clark, A. E.; He, T.; Yim, W.; Li, Y.; Chang, Y. C.; Wu, Z.; Fajtova, P.; O'Donoghue, A. J.; Carlin, A. F.; Todd, M. D.; Jokerst, J. V., A Self-Immolative Fluorescent Probe for Selective Detection of Sars-Cov-2 Main Protease. *Analytical Chemistry* 2022, *94* (34), 11728-11733.
16. Wu, Z.; Zhou, J.; Nkanga, C. I.; Jin, Z.; He, T.; Borum, R. M.; Yim, W.; Zhou, J.; Cheng, Y.; Xu, M.; Steinmetz, N. F.; Jokerst, J. V., One-Step Supramolecular Multifunctional Coating on Plant Virus Nanoparticles for Bioimaging and Therapeutic Applications. *ACS Applied Materials & Interfaces* 2022, *14* (11), 13692-13702.

17. Retout, M.; Jin, Z.; Tsujimoto, J.; Mantri, Y.; Borum, R.; Creyer, M. N.; Yim, W.; He, T.; Chang, Y. C.; Jokerst, J. V., Di-Arginine Additives for Dissociation of Gold Nanoparticle Aggregates: A Matrix-Insensitive Approach with Applications in Protease Detection. *ACS Applied Materials & Interfaces* 2022, *14* (46), 52553-52565.

18. Jin, Z.; Yeung, J.; Zhou, J.; Cheng, Y.; Li, Y.; Mantri, Y.; He, T.; Yim, W.; Xu, M.; Wu, Z.; Fajtova, P.; Creyer, M. N.; Moore, C.; Fu, L.; Penny, W. F.; O'Donoghue, A. J.; Jokerst, J. V., Peptidic Sulfhydryl for Interfacing Nanocrystals and Subsequent Sensing of Sars-Cov-2 Protease. *Chemistry of Materials* 2022, *34* (3), 1259-1268.

19. Jin, Z.; Mantri, Y.; Retout, M.; Cheng, Y.; Zhou, J.; Jorns, A.; Fajtova, P.; Yim, W.; Moore, C.; Xu, M.; Creyer, M. N.; Borum, R. M.; Zhou, J.; Wu, Z.; He, T.; Penny, W. F.; O'Donoghue, A. J.; Jokerst, J. V., A Charge-Switchable Zwitterionic Peptide for Rapid Detection of Sars-Cov-2 Main Protease. *Angewandte Chemie International Edition in English* 2022, *61* (9), e202112995.

20. Jin, Z.; Ling, C.; Li, Y.; Zhou, J.; Li, K.; Yim, W.; Yeung, J.; Chang, Y. C.; He, T.; Cheng, Y.; Fajtova, P.; Retout, M.; O'Donoghue, A. J.; Jokerst, J. V., Spacer Matters: All-Peptide-Based Ligand for Promoting Interfacial Proteolysis and Plasmonic Coupling. *Nano Letters* 2022, *22* (22), 8932-8940.

21. Fu, L.; Ling, C.; Jin, Z.; Luo, J.; Palma-Chavez, J.; Wu, Z.; Zhou, J.; Zhou, J.; Donovan, B.; Qi, B.; Mishra, A.; He, T.; Jokerst, J. V., Photoacoustic Imaging of Posterior Periodontal Pocket Using a Commercial Hockey-Stick Transducer. *Journal of Biomedical Optics* 2022, *27* (5), 056005-056005.

22. Fu, L.; Jin, Z.; Qi, B.; Yim, W.; Wu, Z.; He, T.; Jokerst, J. V., Synchronization of Rf Data in Ultrasound Open Platforms (Uops) for High-Accuracy and High-Resolution Photoacoustic Tomography Using the "Scissors" Programming Method. *IEEE Transactions on Ultrasonics, Ferroelectrics, and Frequency Control* 2022, *69* (6), 1994-2000.

23. Cheng, Y.; Clark, A. E.; Zhou, J.; He, T.; Li, Y.; Borum, R. M.; Creyer, M. N.; Xu, M.; Jin, Z.; Zhou, J.; Yim, W.; Wu, Z.; Fajtova, P.; O'Donoghue, A. J.; Carlin, A. F.; Jokerst, J. V., Protease-Responsive Peptide-Conjugated Mitochondrial-Targeting Aiegens for Selective Imaging and Inhibition of Sars-Cov-2-Infected Cells. *ACS Nano* 2022, *16* (8), 12305-12317.

24. Zhou, J.; Xu, M.; Jin, Z.; Borum, R. M.; Avakyan, N.; Cheng, Y.; Yim, W.; He, T.; Zhou, J.; Wu, Z.; Mantri, Y.; Jokerst, J. V., Versatile Polymer Nanocapsules Via Redox Competition. *Angewandte Chemie International Edition in English* 2021, *60* (50), 26357-26362.

25. Zhou, J.; Creyer, M. N.; Chen, A.; Yim, W.; Lafleur, R. P. M.; He, T.; Lin, Z.; Xu, M.; Abbasi, P.; Wu, J.; Pascal, T. A.; Caruso, F.; Jokerst, J. V., Stereoselective Growth of Small Molecule Patches on Nanoparticles. *Journal of the American Chemical Society* 2021, *143* (31), 12138-12144.

26. Fu, L.; Ling, C.; Jin, Z.; Luo, J.; Palma-Chavez, J.; Wu, Z.; Zhou, J.; Zhou, J.; Donovan, B.; Qi, B.; Mishra, A.; He, T.; Jokerst, J. V., A More Compact Photoacoustic Imaging System to Detect Periodontitis. *medRxiv* 2021, 2021.11. 02.21265776.

27. Jiang, X.; Yu, J.; Wang, L.; He, T.; Zheng, H.; Gao, Q.; Shen, F., Fundamentals of the Reduction of Sfc in Co/Co2 Gas at 1000° C. *ISIJ International* 2020, *60* (10), 2191-2198.

28. Liu, J.; He, T.; Fang, G.; Wang, R.; Kamoun, E. A.; Yao, J.; Shao, Z.; Chen, X., Environmentally Responsive Composite Films Fabricated Using Silk Nanofibrils and Silver Nanowires. *Journal of Materials Chemistry C* 2018, *6* (47), 12940-12947.

29. Cao, Z.; Wang, R.; He, T.; Xu, F.; Sun, J., Interface-Controlled Conductive Fibers for Wearable Strain Sensors and Stretchable Conducting Wires. *ACS Applied Materials & Interfaces* 2018, *10* (16), 14087-14096.

Conference Presentation

30. He, T.; Jokerst, J. V., Biomimetic Synthesis of Versatile Biodegradable Polyethylenimine/Calcium Phosphate Micro-/Nanostructures for Transient Ultrasound Imaging. In *ACS* Spring, American Chemical Society: San Diego, California, US, 2022.

31. He, T.; Jokerst, J. V., Expandable Sol-Gel Nanomaterial as a Therapeutic Tool and Imaging Agent for Cancer Ablation. In International Chemical Congress of Pacific Basin Societies, Honolulu, Hawaii, US, 2021.

Patent

32. Sun, J.; He, T.; Wang, R.; Wang, Y., A kind of Graphene-Based Multifunctional Flexible Sensor Coupled with High Sensitivity and Stretchability. CN Patent CN107,655,397 B: 2018.

ABSTRACT OF THE DISSERTATION

Nanomedicines for Transient Ultrasound Imaging and Cancer Immunotherapy

by

Tengyu He

Doctor of Philosophy in Materials Science and Engineering

University of California San Diego, 2023

Professor Jesse V. Jokerst, Chair

Advancements in nanomedicines have enabled breakthroughs in both disease diagnosis and treatment, including ultrasound bioimaging and cancer immunotherapy. On the one hand, nanomedicines of various formulations have been used as ultrasound contrast and greatly improved the ultrasound imaging quality. However, an ideal ultrasound contrast agent— that has tunable, modifiable surface, biodegradability, biocompatibility, and sufficient stability (half-life) for transient ultrasound imaging— is yet to be explored. On the other hand, to overcome the limitations of immune checkpoint blockade therapy, — immune-related toxicity and inefficacy in immune-suppressive tumors— nanomedicines have been rationally designed to trigger immunogenic cell death (ICD) of tumor cells. However, further work is necessary to develop ICD-inducing nanomedicines that are biodegradable, biocompatible, and intrinsically

potent in inducing ICD. In this dissertation, I will discuss how creating novel nanomedicines can benefit both ultrasound imaging and cancer immunotherapy.

First chapter reviews applications of nanomedicines in both ultrasound imaging and ICD-based cancer immunotherapy, with a highlight of successes and limitations of existing nanomedicines.

Second chapter describes how sol-gel reaction combined with electrospray can generate biodegradable calcium phosphate micro/nano particles. Effects of synthetic parameters on the particle size and morphology are discussed in detail. The biodegradability of these particles was validated.

Third chapter illustrates a bio-inspired, facile, mild, and solution-based synthetic method for creating calcium phosphate micro/nano particles. Systematic investigations on synthetic parameters led to calcium phosphate particles with versatile sizes (396±128 nm to 63±8 μm) and morphologies (hexagonal micro-disc, micro-flower, micro-leaf, nano-butterfly, and nano-ribbon). A "phosphate sponge" mechanism was found to be the key for regulating the particle sizes and morphologies. These calcium phosphate micro/nano particles are proven to be biodegradable, non-toxic, and efficient in creating transient ultrasound contrast.

Fourth chapter studies the building of proton sponge nano-assembly (PSNA) optimized for imaging and triggering ICD of cancer cells. By carefully tuning the hydrophilic and hydrophobic components, the self-assembly tendency of PSNA was optimized. In turn, the PSNA with the highest fluorescence, positive surface charge density, intracellular fluorescence, and cancer cell cytotoxicity was achieved. The lysosome rupturing-regulated pyroptosis and necroptosis were triggered by PSNA, suggesting the great potential of the PSNA for anticancer immunity.

CHAPTER 1. NANOMEDICINES IN ULTRASOUND BIOIMAGING AND CANCER IMMUNOTHERAPY: AN INTRODUCTION

1.1. ABSTRACT

Advancements in nanomedicines have enabled breakthroughs in both disease diagnosis and treatment. Here, I provide a review of the literature discussing how nanomedicines have promoted ultrasound bioimaging and cancer immunotherapy.

Existing gas microbubbles and nanomedicine-based ultrasound contrast agents have greatly improved ultrasound imaging quality. However, an ideal ultrasound contrast agent— that has a tunable size (from nano to micro range), modifiable surface (for targeting and molecular imaging), biodegradability, biocompatibility, and sufficient stability (half-life) for transient ultrasound imaging— is yet to be explored. Phosphate glass micro/nanoparticles have been proven to be an ideal candidate for the next-generation transient ultrasound contrast because of their biodegradability and biocompatibility. However, a synthetic method for phosphate glass micro/nanoparticles that is simple, scalable, and versatile in size control is yet to be investigated.

Nanomedicines also found the potential to improve cancer immunotherapy. Immune checkpoint blockade therapy has reshaped cancer immunotherapy but still suffers from immune-related toxicity (due to the overexpansion of T cells by antibodies) and inefficacy in immune-suppressive (or immune-cold) tumors. Strategies for “normalizing” or “firing up” cold tumors are

urgently needed. A particularly appealing approach is applying nanomedicines to trigger immunogenic cell death (ICD) of tumor cells. During ICD of tumors, dying cells release not only tumor-associated antigens but also adjuvants including pro-inflammatory cytokines and damage-associated molecular patterns. Both antigenicity and adjuvanticity convert dying tumor cells into in-situ vaccines inducing tumor-specific immunity, thus overcoming the immune toxicity and "heating" the immune-cold tumors.

Nanomedicines have been rationally designed to trigger tumor-specific ICDs for anticancer immunity, such as targeted and stimulus-responsive nanomedicines. However, these nanomedicines still face some common limitations. First, most of these nanomedicines cannot degrade in physiological conditions or their degradation byproducts are toxic. Second, nanoformulations of sensitizing agents/drugs suffer from drug leakage. Third, nanomedicines relying on external stimuli face the limitations of penetration depth of stimuli (e.g. photon) and undesired damages on normal tissues by irradiation. Therefore, further work is necessary to develop ICD-inducing nanomedicines that are biodegradable, biocompatible, and intrinsically potent in inducing ICD (i.e., without the aid of sensitizing agents/drugs and external stimuli).

1.2. NANOMEDICINES FOR ULTRASOUND BIOIMAGING

1.2.1. Ultrasound Imaging

Ultrasound imaging has been consistently applied for the diagnosis of a wide range of diseases (e.g., heart diseases and cancers). This is because of several advantages: high spatial and temporal resolution, safety (no need for ionizing radiation), portability, wide availability, and relatively low cost.[1] According to a report,[2] the cost factor of ultrasound is five times lower than MRI and three times lower than CT; up to $736 million annually could be saved by replacing MRI with ultrasound for many standard studies.

Ultrasound is a sound wave with frequencies more than 20 kHz. The propagation of high-frequency sound waves in organs and tissues can be managed to produce images. A transducer both generates the sound pulses and detects returning echoes. The depth of a subject is determined by the time difference between firing pulses and returning echoes and the amplitude of the echo is displayed in a grayscale image. In addition, blood velocity can be measured by using the concept of Doppler shift. Both the velocity and direction of blood flow can be measured in this mode.[1, 3]

Although many tissues can be directly imaged by ultrasound, contrast agents can enhance the imaging quality. Gas microbubbles were contrasts most widely used clinically. These are microbubbles filled with air and stabilized by shells (e.g., proteins, lipids, or polymers).[4-5] Microbubbles enhance echoes because of the high acoustic impedance mismatch between the gas and blood/tissue.[6] In an acoustic field, bubbles oscillate due to positive and negative pressure changes; these oscillations are different from the surrounding medium because of differences in the compressibility and density between the gas and blood/tissue.[1, 7-8]

However, gas microbubbles suffer from low stability and short lifetime (less than 30 min) due to the fast diffusion of gas species.[9-11] Encapsulated gas bubbles have improved lifetime but

are unstable in circulation even when treated with polyethylene glycol.[12-14] Besides, microbubbles preclude the use of low frequencies because they can burst and result in local microvasculature rupture and hemolysis.[15] Moreover, the micron size (1–8 μm) has constrained many applications, such as tumor imaging where the pore size of tumor endothelium and trapping effects originated from the reticuloendothelial system limit the size to less than 380 nm.[16]

1.2.2. Nanomedicines as Ultrasound Contrasts

Nanomaterial-based ultrasound contrasts may overcome these limitations of gas microbubbles. The stability of nanomaterials can be chemically tunable. Also, nanomaterials of 50-400 nm can accumulate in tumor sites as a result of the leaky vasculature and imperfect lymphatic drainage associated with cancerous tissue and the slower circulation of the nanomaterials, known as the enhanced permeability and retention (EPR) effect.[17-18] Furthermore, nanomaterials are facilely surface-modifiable to enable active targeting of diseases. One challenge faced by nanomaterials is the relatively lower echogenicity at clinically relevant ultrasound frequencies (1–10 MHz). However, prolific research in the area has resulted in various nanomedicines that have circumvented this issue and enabled their application as ultrasound contrasts.

1.2.2.1. Nano-Contrast with Gas Core

Gas is thought to be the most echogenic phase considering the maximized acoustic impedance mismatch between gas and blood/tissue/bone. Gas nanobubbles, composed of a gas core and shells, have been investigated with formulations including lipid bilayer particles (liposomes),[19-22] polymeric-shelled particles,[23-26] and Pluronic incorporated lipid shells.[18, 27-28]

Yin and coworkers[29] proposed a phospholipid-shelled gas-core nanobubble and validated its in vivo echogenicity in tumors. The nanobubbles were made of octafluoropropane gas core and lipid shell. The enhanced contrast lasted for ~1 h with the nanobubbles (436.8±5.7 nm) but only

15 min with a micro-counterpart (1220±65 nm). This could be due to the better EPR effect-driven accumulation of nanobubbles in tumors.

Echogenic liposomes (ELIPs) are lipid bilayer nanoparticles that contain small amounts of inert gas in their lipid bilayer or micelles within their aqueous core.[19, 30] Surface modification with PEG greatly enhanced the stability, biocompatibility, and circulation time of ELIPs. Due to their gas core, as well as other advantages, these particles have been proposed as potential contrast agents for clinical ultrasound. However, due to their small size, low gas density, and rigid shell, ELIPs do not produce sufficient contrast at diagnostic ultrasound frequencies.[19, 21]

Nanobubbles with polymeric shells have also remarkably enhanced US contrast. Xu and coworkers[26] developed PLGA-shelled nanobubbles. Fluorescent Texas Red dye was encapsulated and a tumor-targeting ligand HuCC49ΔCH2 antibody was introduced for targeting TAG-72 overexpressed in epithelial-derived cancers. This nanobubble demonstrated enhanced ultrasound and fluorescent contrast in LS174T human colon cancer cells.

The surfactant is key to the stabilization and reduction of the size of bubbles. For example, Pluronic can change the packing of the lipids in the shell and reduce the size of the bubbles to 100 nm or below while maintaining their echogenicity at a level comparable to clinical agents.[27]

Certain bacteria genetically encode gas nanovesicles and use them to control their buoyancy. Shapiro and colleagues purified these gas vesicles from bacteria and studied these gas nanovesicles for ultrasonic imaging in mice. These gas vesicles have a protein shell with a thickness of 2 nm and sizes of 45−250 nm in width and 100−600 nm in length. The authors reported that these gas nanovesicles are imageable with ultrasound upon intravenous injection into mice in vivo and are more stable compared to many of the nanobubble alternatives.[31] Moreover, this work

suggests that a wholly new ability to image cells with ultrasound could thus result from transducing selected cells with the gene vectors encoding the gas nanovesicles.

1.2.2.2. Nano-Contrast with Liquid Core

Liquid nanodroplets made of perfluoropentane core and polymer shells such as PLGA and PLLA are alternatives to gas nanobubbles. Rapoport et al.[25] reported PEG-PLLA nanodroplets encapsulating perfluoropentane. These nanodroplets remain liquid at room temperature—due to perfluoropentane's boiling point under Laplacian pressure—and transform into gas particles at physiological temperatures. 4 h after intravenous injection, these nanodroplets were able to produce intense ultrasound signal in tumor and negligible signal in the kidneys or liver.

Recently, a chitosan cross-linked vitamin C lipid nanobubble was created for dual ultrasound and fluorescence imaging.[32] The chitosan-vitamin C shell was found to improve tumor accumulation due to its negative charge. This nanobubble enhanced ultrasound contrast in vivo.

1.2.2.3. Nano-Contrast with Solid Nanoparticles

Solid nanoparticles such as SiO_2 have been used for ultrasound contrast. Yang and colleagues produced a series of hollow silica nanospheres from 100 to 400 nm.[33] These hollow silica nanospheres were produced by a hard-template synthesis where a 25 nm silica shell was grown on top of polystyrene nanospheres (100−400 nm) by dropwise addition of tetraethyl orthosilicate (TEOS) under slight heat. The polystyrene was then removed by soaking in hot tetrahydrofuran (THF). While the 100 nm silica nanomaterials produced an ultrasonic signal at 6 MHz frequency, the authors found that the 400 nm spheres produced a higher signal.

One challenge faced by solid nanoparticles-based (<100 nm in at least one dimension) ultrasound contrasts such as SiO_2 is that they often produce poor contrast strength relative to their larger counterparts. This is because contrast interactions with acoustic waves require reflection, acoustic impedance mismatch, refraction, attenuation, or diffraction.[34] A trade-off must be reached

between the need for favorable in vivo biodistributions and kinetics and sufficient echogenicity to enhance contrast.[35-36] One creative way to improve the echogenicity of solid nanoparticles has been demonstrated by multiplying the number of interfaces in mesoporous SiO_2 ("rattle"-type mesoporous SiO_2).[37] This rattle structure provides double scattering/reflection interfaces in a single particle within the material to substantially increase contrast enhancement relative to the other two nanostructures (solid and hollow) containing only one scattering/reflection interface.

Multiwalled carbon nanotubes (MWNTs) of 20−30 nm in diameter and 400 nm in length were found to be surprisingly echogenic, which showed detectable ultrasonic contrast in living animals such as mice and pigs.[38-39] It was reported that the strength of the signal observed from MWNTs was at the same level as clinically used sulfur hexafluoride microbubbles, yet the signal does not degrade, as rapidly occurs with microbubbles.[39] However, it should be noted that a concentration as high as ~1 mg/mL of MWNTs was required to generate the high ultrasonic signal. Targeting MWNTs to PSCA (prostate stem cell antigen) via monoclonal antibodies has led to high ultrasonic contrast in the mouse prostate tumor grown in the abdominal wall.[38] However, the mechanism by which the high contrast is yet to be explored. One possibility is that the nanotubes may serve as the center of nucleation for air bubbles that generate the echogenic signal.[39]

1.2.2.4. Biodegradable Phosphate Glass: A Candidate for the Next-Generation Transient Ultrasound Contrast

An ideal ultrasound contrast agent should have a tunable size (from nano to micro range to allow for wide applications), modifiable surface (for targeting and molecular imaging), biodegradability, biocompatibility, and sufficient stability (half-life) for transient ultrasound imaging, which is yet to be explored. Gas microbubbles have significant limits from their size and short lifetime (less than 30 min) due to the fast diffusion of gas species.[9-11]. Nanobubbles of gas or liquid also suffer from a short lifetime (minutes to 1 hour).[22, 40] Encapsulated gas bubbles have an

improved lifetime but are unstable in circulation even when treated with polyethylene glycol.[12-14] Moreover, the biocompatibility of these shell materials is yet to be verified. Existing solid nanoparticles are hindered by their biodegradability; the long-term retention of non-degradable materials results in high toxicity.[41-42] Therefore, alternative materials must be investigated in search of candidates for the next-generation ultrasound contrast.

Phosphate-based bio-glasses are an attractive alternative because of their controllable biodegradability and good biocompatibility.[43-52] Phosphate glasses have better biodegradability than silicate because the terminal oxygen in the PO_4^{3-} tetrahedron makes the connectivity of the phosphate network more reduced.[46] Besides, when degraded, phosphate glasses release biocompatible ions routinely found in the human body (e.g. phosphorous, calcium, and sodium).[43-53] Finally, phosphate glasses can be facilely functionalized by loading imaging dyes[10] and drugs/biomolecules (e.g. trypsin inhibitor,[54] tetracyclines,[55] growth factors,[56] gentamicin sulfate[57], vancomycin[58]), opening up new opportunities for theranostic applications.

The potential of phosphate glass nanoparticles (PGNs) in transient ultrasound imaging has been demonstrated by Knowles and co-workers.[10] These PGNs are 200 nm – 500 nm synthesized via combining sol-gel with electrospray. The authors used PGNs as an ultrasound contrast to label mesenchymal stem cells and determined in vitro and in vivo detection limits of 5 and 9 μg/mL, respectively. Cell counts down to 4000 could be measured with ultrasound imaging. Moreover, the time stability of PGNs (~4 h) is significantly longer than existing gas micro/nanobubbles (minutes to 1 hour). Importantly, these PGNs biodegrade into aqueous media with degradation products that can be easily metabolized in the body.

However, this synthesis method puts a constraint on the wider applications of PGNs because of limited control over the particle size, low production rate, danger, and high energy

consumption. Therefore, a facile, mild, and scalable synthetic method for preparing micro-/nanoparticles of this material is yet to be explored.

1.3. NANOMEDICINES INDUCING IMMUNOGENIC CANCER CELL DEATH

1.3.1. Cancer Immunotherapies and Major Limitations

Cancer immunotherapies refer to therapies that utilize the patient's immune system to eradicate cancers. As early as 1893, William Coley had observed that live or inactivated bacteria could cause remission in sarcomas.[59] However, it was until the 1990s that the concept of cancer immunotherapy emerged based on the understanding of the interaction between immune cells and melanoma.[60-61] Following numerous research failures, it was until 2010 that the autologous cellular immunotherapy, sipuleucel-T, was approved for the treatment of prostate cancer[62], and in 2011 and 2014 that several significant antibodies were approved for treating melanoma (i.e., the anti-cytotoxic T lymphocyte-associated protein 4 (CTLA-4) antibody, ipilimumab, and anti-programmed cell death protein 1 (PD1) antibodies).[63] Now, cancer immunotherapy is a quickly evolving field creating a whole spectrum of immunotherapies including adoptive cellular therapy,[64-73] vaccines,[64] immune checkpoint blockade (ICB, e.g., anti-CTLA-4,[64, 74-76] Anti-PD1, and anti-PD-L1,[77-79]), cytokines (IL-2 and IFN-α),[80] combination immunotherapy,[73, 81] and beyond. Detailed discussions on the working principles and limitations of these immunotherapies can be found in review papers.[63-64, 66-69, 72-73, 76-77, 80-81]

For immune cells to recognize and kill tumors, it requires the completion of a whole cancer immunity cycle of seven steps: release of tumor-associated antigens (TAAs), TAAs' exposure to antigen-presenting cells (APCs, e.g., dendritic cells (DCs) and macrophages), priming and activation of T cells by APCs, trafficking of T cells to tumors, infiltration of T cells into tumors, recognition of tumors by T cells, and killing of tumors by T cells.[82] However, tumors have

developed mechanisms to suppress this cycle and achieve local immune evasion, induction of tolerance, and systemic disruption of T-cell signaling. Moreover, the immune editing process promotes the formation of less immunogenic tumors via selective pressure.[77, 83]

Deeper understandings of these immune-resistant mechanisms and cell-cell interactions between tumors and immune cells have led to breakthroughs in immunotherapies. Here we use the ICB therapies as examples for discussing how immunotherapies have benefited from such understandings. One strategy of tumors to suppress T cell functions is by expressing ligands that bind inhibitory receptors of T cells.[62, 64, 84] "Checkpoint blockade" refers to the blockade of some checkpoints, i.e., immune-inhibitory pathways. CTLA-4 is one such inhibitory receptor of T cells that down-regulates T cell activation. Ipilimumab, the first FDA-approved antibody, can target CTLA-4, recover CD28-mediated positive costimulatory signals (e.g., phosphoinositide 3-kinase (PI3K) and AKT pathways), and reverse the activity of T cells.[85] Ipilimumab is now a first-line therapy for melanoma patients with metastatic disease.[63, 74, 86] Other examples are anti-PD1 and anti-PD-L1 immunotherapies.[77-79] PD-1 receptors expressed on activated T cells also serve to suppress T cell responses and prevent damage to self-tissues[78, 87] Tumor cells upregulate the expression of programmed death ligand 1 (PD-L1) and PD-L2 on their surfaces, the two main ligands binding to PD-1. When bound by PD-L1 or PD-L2, PD-1 initiates a negative signal to dampen T cells' activation, proliferation, and cytotoxic potential.[88-90] Therefore, antibodies for PD-1, PD-L1, or PD-L2 can disrupt the PD1-PD-L1 or PD1-PD-L2 interactions and reverse the exhaustion of T cells.[91] For example, the anti-PD-1 antibody nivolumab has shown favorable and durable clinical responses in melanoma patients.[92] The anti-PD-L1 antibody atezolizumab has also shown efficacies in patients of the lung, colon, head and neck, and gastric cancers in addition to melanoma.[63]

Despite these encouraging therapeutic efficacies in cancer treatment, ICB therapies still suffer from two major limitations: immune toxicity and inefficacy in immune-cold tumors. First, because these antibodies target T cell receptors serving for minimizing autoimmune responses, ICB therapies can cause immune-related toxicity due to uncontrolled T cell activation.[74] For example, grades 3–5 (severe) immune-related side effects occurred in 10–35 % of patients treated via CTLA-4 blockade.[83] Second, ICB therapies only produced favorable responses in a limited portion of patients.[93] This is because ICB therapies rely on functioning T cells infiltrated into tumors but most cancers have developed an immune-suppressive (or immune-cold) tumor microenvironment (TME).[94-97] The immune suppression of TME can be understood in several aspects. First, tumor-infiltration of T cells is suppressed by the physical barrier from aberrant tumor vasculature; Second, functions of the cytotoxic T cells are hampered by immune suppressive cells such as regulatory T cell (Treg), myeloid-derived suppressive cells (MDSC) and M2 type tumor-associated macrophages (TAM);[98-101] Third, hypoxia and low pH (pH < 4) of TME further reduce the activity of cytotoxic T cells;[102] Moreover, T cell exhaustion is favored by glucose-reduced and cholesterol-enriched TME.[103-107]. Therefore, it is necessary to develop new strategies to reprogram (or normalize) the suppressive (or cold) TME.[108-110]

1.3.2. Immunogenic Cell Death

Triggering immunogenic cell death (ICD) of tumors is an emerging strategy that may resolve both issues of immune toxicity and immune-cold tumors. ICD refers to programmed cell death that can activate adaptive immune responses in an immunocompetent setting. According to recent studies, both antigenicity and adjuvanticity are indispensable for anticancer immunity.[111-112] During ICD of tumor cells, dying cells can release not only tumor-associated antigens but also adjuvants including pro-inflammatory cytokines (e.g., interleukin-1β (IL-1β) and IL-18) and damage-associated molecular patterns (DAMPs). Depending on the specific ICD types (discussed

later), DAMPs may include a combination of calreticulin, heat-shock proteins (e.g., HSP70 and HSP90), adenosine triphosphate (ATP), and/or high-mobility group box protein 1 (HMGB1). Specific roles and molecular mechanisms of each of these DAMPs are comprehensively discussed in review papers.[113-114] Briefly, DAMPs can stimulate the maturation of antigen-presenting cells (APC) such as dendritic cells, and facilitate the presentation of tumor antigens to the T cells; In turn, $CD8^+$ T cells' activation and infiltration into tumors are boosted, thus firing up the immune-cold TME and inducing anticancer immune responses.[115-122] Moreover, because the dying tumor cells themselves act like in situ vaccines, tumor-specific immunity is possible and the immune-related toxicity issue of other immunotherapies such as ICB could be overcome.[74, 83, 123-124]

Discovered ICD subtypes include immunogenic apoptosis, pyroptosis, necroptosis, and ferroptosis, which are discussed in detail as follows.

1.3.2.1. Immunogenic Apoptosis

Immunogenic apoptosis differs from typical apoptosis in its immunogenicity. Apoptosis has been thought to be immunogenically silent for a long time. This is because apoptosis is more often a regulated cell death allowing for the removal of dead cells by phagocytes without triggering the immune response.[113, 125] However, this view has been questioned by more recent studies—when caused by oxidative stress and endoplasmic reticulum stress, apoptotic cells also release DAMPs and become immunogenic.[125] For example, cancer cells have been treated ex vivo with anthracyclines, oxaliplatin, photodynamic therapy (PDT), or γ-irradiation to induce immunogenic apoptosis. When syngeneic immunocompetent mice were implanted with these apoptotic cells and subsequently rechallenged with live cancer cells, they rejected tumor growth.[113, 126-129]

Later, it has become clear that necrotic cell death pathways can also be regulated and immunogenic, such as pyroptosis, necroptosis, and ferroptosis.

1.3.2.2. Pyroptosis

Pyroptosis is a highly proinflammatory form of regulated necrosis. Due to its immunogenicity, pyroptosis is being studied as an emerging strategy for converting immune-cold tumors to hot.[130] Pyroptosis can be canonical (caspase 1 dependent) or non-canonical (caspase 3 and 11 dependent). Recent studies have well-defined these pathways.[116, 125] Take the caspase 1-dependent canonical pathway as an example, caspase 1 is activated from pro-caspase 1 in response to pathogenic infections or synthetic materials. Subsequently, caspase 1 cleaves proinflammatory cytokines (e.g., pro-IL-1β and pro-IL-18) and gasermin (GSDM) D. The N-terminal of GSDMD creates membrane pores and increases potassium efflux and water influx. Consequently, morphologically, pyroptosis is accompanied by membrane rupture, cellular swelling, and bubble formation. Meanwhile, matured proinflammatory cytokines are released out of cells, further causing inflammatory responses.[116, 125]

Pyroptosis can overcome the immune desert phenotype of TME and evoke anticancer immunity.[131-133] It has been shown that a high expression of GSDMs (e.g. GSDME) increases the tumor-infiltration of natural killer cells and $CD4^+$ and $CD8^+$ T cells in mice tumor model and, in turn, suppression of tumor growth; In contrast, GSDME-deficient tumors have lower level of immune cell infiltration.[131] Utilizing single-cell RNA sequencing, another study shows that pyroptosis of 4T1 tumor cells also induces macrophage M1 polarization and reduces suppressor cell populations in breast 4T1 tumors including monocytes, neutrophils, and myeloid-derived cells.[132] Pyroptotic tumor cells release a large amount of neoantigens, which can stimulate the systematic immune response and may provide a long-term tumor-suppressive effect.[133] Pyroptosis of tumor cells also induces effective antitumor immunity that synergizes with anti-PD1 ICB.[132]

1.3.2.3. Necroptosis

Necroptosis is another regulated necrosis with known immunogenicity. It initiates from the phosphorylation of receptor-interacting protein kinase (P-RIPK)-1. P-RIPK-1 upregulates P-RIPK-3. Together, these P-RIPKs activate phosphorylated mixed lineage kinase domain-like protein (P-MLKL). P-MLKL is the executor of necroptosis that forms membrane pores and causes cellular membrane rupture.[121, 134]

Just like pyroptosis, this feature of membrane rupture enables necroptotic cells to release cellular contents (tumor-associated antigens, DAMPs, chemokines, and pro-inflammatory cytokines) and become immunogenic.[115, 135]. It has been reported that necroptotic cancer cells act as effective vaccines to protect mice from the challenge of viable cancer cells.[135] The same study showed that necroptotic cancer cells induce the activation and maturation of bone marrow-derived dendritic cells (both in vitro and in vivo) and the cross-priming of T cells in vivo. Another study observed the production of pro-inflammatory cytokines/chemokines downstream of the RIPK1/RIPK3/NF-kB activation; These cytokines/chemokines are key for the cross-priming of CD8+ T cells.[115] The antigenicity of necroptotic cancer cells has been highlighted— when immune-dominant tumor antigen (AH1) was knocked out, necroptotic cancer cells were more immunogenic than apoptotic cells in a murine prophylactic tumor vaccination model.[136] Therefore, necroptosis may be a valuable tool for cancer immunotherapy.

1.3.2.4. Ferroptosis

Ferroptosis is another regulated necrosis featured in increased cell membrane permeability. It originates from the excessive generation of reactive oxygen species (ROS) and the depletion of polyunsaturated fatty acids (PUFAs). In turn, the membrane permeability is increased [125, 134]. In normal physiological conditions, excessive ROS accumulation is prevented by antioxidants such as glutathione peroxidase 4 (GPX4)), the transcription factor nuclear factor erythroid 2 (NFE2L2),

and some HSPs (e.g., HSP25, HSP beta 1(HSPB1) and HSP family A member 5 (HSPA5)).[137-138] These antioxidants can convert phospholipid hydroperoxides (PLOOH) into nontoxic lipid alcohols (L-OH).[137, 139] On the other hand, lysophosphatidylcholine acyltransferase 3 (LPCAT3), acyl-CoA synthetase long-chain family member 4 (ACSL4), and arachidonate lipoxygenases (ALOXs, e.g., ALOX12 and ALOX15) are all involved in the oxidation of PUFAs and consequent oxidative damages.[140-141] Iron can catalyze the peroxidation of PUFAs.

Although still under investigation, recent studies are in support of the immunogenicity of ferroptosis. Ferroptosis has been found to release cytokines and DAMPs (e.g., decorin, ATP, and HMGB-1); these biomarkers have been demonstrated to mediate the immunogenicity of ferroptosis.[142-145] For instance, decorin created by ferroptosis acts on macrophages to trigger producing proinflammatory cytokines.[143] Ferroptotic cells (e.g., murine fibrosarcoma MCA205 and pancreatic ductal adenocarcinoma KPC cells) elicited a vaccine-like effect in the murine tumor model and suppressed tumor growth.[146]

1.3.3. Smart Nanomedicines Inducing ICDs

Accumulating evidence supports that traditional nanomaterials can induce ICDs, such as nano-carbons,[147-148] silica nanoparticles (NPs),[149] quantum dots (QDs)[150], and metallic NPs[151]. These findings have inspired great efforts in the rational design of smart nanomedicines that can induce ICD for anticancer immunity in a more controlled manner. “Smart” means that such nanomedicines can either target tumors or be stimulus-responsive. Targeted nanomedicines can be further classified as passive and active targeting, while the stimulus responsive nanomedicines include those responsive to pH, enzyme, ATP, ROS, GSH, photon, ultrasound, and radio.

1.3.3.1. Targeted Nanomedicines

Passive Targeting

Nanomaterials of 50-200 nm have a higher tendency to accumulate in tumor sites, known as the enhanced permeability and retention (EPR) effect.[17] Tumor tissues, due to the abnormal metabolism, have more blood vessels present than normal tissues, causing better permeability of tumor sites.[152-153] Therefore, nanomaterials that have prolonged circulation time passively accumulate in tumor sites. Nanomaterials with EPR effect have been utilized to deliver ICD inducers to tumor sites. For example, liposomes, micelles, polymers, and proteins are applied to deliver platinum-based anticancer drugs to induce ICD of tumors.[154] Recently, Liu et al[155] developed a PEGylated liposome nanocarrier (met-oxa(IV)-liposome) loading water-soluble metformin for anticancer immunity. met-oxa(IV)-liposome is made of an amphiphilic OXA prodrug conjugated with 1,2-distearoyl-sn-glycero-3-phosphatidylethanolamine and other commercial lipid liposomes. The nanocarriers accumulated at the tumor site after intravenous injection. met-oxa(IV)-liposome gradually released metformin that inhibits oxygen consumption of tumor cells and relieves the hypoxic environment of the tumor. In addition, the gradually released OXA rejected CT26 tumors by inducing ICD-based antitumor immunity.

The overexpression of IDO induces the reduction of $CD8^+$ T cells and an increase in regulatory T cells (Tregs), which can cause immune evasion of tumors.[156-157] Zhai et al.[158] developed a heparin-functionalized graphene oxide (GH) applied for the transdermal delivery of docetaxel and 1-methyl-D-tryptophan, an indoleamine 2, 3-dioxygenase (IDO) inhibitor, termed as D-1/GH. The retention of this nanomedicine on tumor sites was enhanced due to EPR-like effects at the tumor-skin junction and the affinity of heparin for the protein. This enhanced accumulation allowed D-1/GH to infiltrate deeper into tumors. The ICD-induced release of "DMAPs" initiates antigen presentation and elicits subsequent antitumor immunity.

Active Targeting

Nanomaterials have also been surface-modified with ligands to achieve active targeting of tumors. Based on the specific subcellular organelle targets, these nanomaterials include those targeting endoplasmic reticulum, mitochondria, and cell membrane receptors.

CRT located in the endoplasmic reticulum (ER) is crucial for maintaining calcium homeostasis, intracellular signal transduction, and protein synthesis. ER stress can activate the signaling pathway that induces ICD.[159] PDT can induce ICD by ROS-based ER stress generation.[160-161] However, many PDTs fail to induce an effective ICD due to the short half-life of ROS. You et al.[161] created a nanomedicine termed FAL-ICG-HAuNS with the ER-targeting ability. Aided by the pardaxin (FAL) peptides, FAL-ICG-HAuNS localize in ER. Following the ER accumulation and NIR irradiation, this nanosystem can generate ER-localized ROS stress via the PTT and PDT of hollow gold nanospheres (HAuNS) and indocyanine green (ICG). CRT was exposed on the surface of dying cells as "eat me" signaling, which stimulated DC cell maturation and boosted the immune response to suppress tumor growth. You and coworkers[162-163] also demonstrated the efficacy of ER targeting in the induction of ICD. They created Par-ICG-Lipo, a liposome modified by ER-targeting pardaxin (Par) peptides and loaded with ICG. Par-ICG-Lipo was found to have a better accumulation in ER than those liposomes unmodified with Par. The ICG-enabled PDT induced ER stress, ICD, and release of DAMPs and tumor antigens, consequently enhancing the antitumor immune effect.

Mitochondria is also an important target. Intracellular oxidative stress in mitochondria can trigger ICD.[164] External stimuli can cause the collapse of mitochondrial membrane potential to release more ROS, thus forming positive feedback to damage the neighboring mitochondria.[165] Luan and colleagues[166] developed mitochondria-targeted NPs (BSA@T780/DOX NPs). BSA@T780/DOX NPs were made from bovine serum albumin (BSA) coating on the co-assembly

of DOX and T780. T780 is an IR780 derivative tailed with triphenylphosphonium, a mitochondria-targeted anchor. The BSA@T780/DOX NPs can damage mitochondria selectively via PDT and PTT. In turn, ICD was triggered and both the primary and bilateral tumors were eliminated due to anticancer immunity. Shen et al.[167] created a nanomaterial based on the self-assembly of OPDMA-Cela. OPDMA-Cela is a conjugation of poly(2-(N-oxide-N,N-diethylamino) ethyl methacrylate) (OPDEA) and celastrol (cela). OPDEA introduces the mitochondria targeting and Cela is an effective ICD inducer extracted from Chinese drugs. This strategy specifically delivered cela to mitochondria and triggered ICD.

Targeting receptors on the cell membrane is another example of active targeting. Folic acid (FA) receptors are overexpressed in many tumor cells. The research group of Cai prepared multifunctional sonosensitizers (FA-MnPs) to generate sonodynamic effects and simultaneously stimulate sonodynamic-induced immune responses by targeting FA receptors.[168] Yubin Huang et al.[169] designed a tumor-targeting liposome (FOIB@Lip) carrying FA, BMS-1 as PD-L1 inhibitors, and IR 780 and OXA as ICD inducers. FOIB@Lip was able to boost cancer immunotherapy through ICD. As a polysaccharide, not only has the advantages of good biocompatibility and non-immunogenicity but also can target tumors via specific binding to the $CD44^+$ receptor overexpressed on the tumor surface. Liu et al. utilized PEGylated HA to modify black phosphorus (BP) NPs (HA-BP).[170] HA-BP selectively accumulated in tumors due to the hyaluronic acid (HA) binding to $CD44^+$ receptors overexpressed on the tumor. Both in vitro and in vivo studies demonstrated that combined PDT and PTT of HA-BP can eliminate the primary tumors and induce ICD. ICD promoted DCs maturation and effector T cells and stimulated antitumor immune responses.

1.3.3.2. Stimulus-Responsive Nanomedicines

pH and Enzyme Responsive

Due to deregulated glycolysis, TME is known to be highly acidic. pH-responsive nanomedicines loaded with ICD-inducing drugs can specifically release drugs in TME to induce ICDs. Zhu et al.[171] have constructed polyethylene glycol coated poly(lactic-co-glycolic acid) (PLGA-PEG) nanoparticles coloaded with $CaCO_3$, DOX, and IDO1 inhibitor (aNLG919) named DNCaNPs for ICD of colorectal cancer (CT26). DNCaNPs are pH-responsive due to $CaCO_3$. Acid-triggered release of DOX killed tumors through ICD, during which DAMPs (CRT, HMGB1, and ATP) are released from dying cells. DAMPs facilitated the maturation of DCs and activation of cytotoxic T lymphocytes. Furthermore, the release of aNLG919 also depleted Tregs cells. Xia et al.[172] conjugated DOX to polyamidoamine dendrimer (PAMAM) via a pH-liable hydrazone bond. Immunoadjuvant (CpG ODNs) were loaded onto this nanoformulation, followed by modification with low molecular weight heparin (LMWH) to prevent uptake by the reticuloendothelial system. Acidic TME can cleave the hydrazone bonds of the nanoparticles (LMWH/PPD/CpG) and release CpG ODNs and DOX. The anticancer immunity of this nanomedicine was evaluated in a B16F10 tumor-bearing mice model. Analysis of tumor sections treated with this nanomedicine found LMWH/PPD/CpG caused the exposure of CRT and release of HMGB1. These DAMPs can facilitate the phagocytosis of tumor associated antigens. In turn, DCs and cytotoxic T lymphocytes were activated against the tumor cells.

pH and enzyme dual responsiveness may enable more tumor-specific immunomodulation. Su et al.[173] prepared MMP-2 and pH-responsive micellar nanoparticles (sAMcP) coloaded with PTX and anti-PD-1 antibody. Enzymatic (MMP-2) cleavage can release anti-PD-1 antibodies and low pH can release PTX. Anti-PD-1 reserved the activity of T cells for killing the tumor cells. PTX caused the ICD of tumor cells and the release of tumor-associated antigen and CRT, which further

boosted the anticancer immunity demonstrated in B16F10-bearing mice. Du et al.[174] developed cathepsin B/pH-responsive nanoconstructs (HRN) loaded with docetaxel (DTX). HRN was stable in blood circulation. However, the acidic TME and lysosomal cathepsin can disassemble the particle to release DTX. In the B16 expressing ovalbumin (B16OVA) tumor model, tumor tissue treated with HRN nanoparticles showed upregulation of CRT and HMGB1. The released DAMPs caused the maturation of DCs as evidenced by the upregulation of CD80 and CD86 markers. Moreover, the nanosystem was highly effective in activating cytotoxic T cells ($CD8^+$) and suppressing B16OVA tumors. Gao et al.[175] prepared HA-Psi-DOX, a DOX and hyaluronic acid nanoprodrug. In response to acidity and MMP-2, HA-Psi-DOX nanoparticles release DOX in TME. When evaluated in the B16F10 melanoma model, HA-Psi-DOX nanoparticles demonstrated the capability of triggering the ICD of tumor cells (as evidenced by the release of HMGB1) and anticancer immunity.

ATP Responsive

ATP concentration is higher in TME (100 ~ 500 μM) than in normal tissues (10 ~ 100 nM) due to hypoxia stress. Besides, intra and extracellular ATP levels are also different (1 ~ 10 mM and <0.4 mM, respectively).[176] Such differences have motivated the research on nanomedicines responsive to ATP for triggering ICDs. Yu et al.[177] developed a nano-complex, IR@ZIF-RGD, that can effectively deplete intracellular ATP and inhibit ATP synthesis by ATP-responsive ZIF90 and siRNA targeting thioredoxin reductase-2, respectively. In turn, tumor metabolism disorders and immunosuppression were reserved. IR@ZIF-RGD-induced oxidative stress and ICG-triggered photothermal therapy together provoked potent immunogenic cell death of tumor cells and antitumor immunogenicity. The vaccine effect of the nanocomplex has been demonstrated in vivo,

achieving suppressed growth of both primary and abscopal tumors, as well as inhibited tumor metastasis.

Jiang et al[178] created a nanocomposite made from silver nanoparticles (Ag NPs) and peptide-functionalized doxorubicin (PDOX) (Ag-TF@PDOX). ER stress was activated by the silver nanoparticle, which synergized with chemotherapy to enhance cytotoxicity and stimulate the ICD effect. It downregulated P-gp expression via the increased production of ATP-consuming chaperones. In addition, the peptide (CB5005) conjugated to DOX helped the cell membrane penetration and nuclear localization of the drug. The surface TA-Fe^{3+} enabled the nanocomposite with ATP-responsive disassembly and ATP depletion properties to improve biocompatibility and decrease ATP-dependent drug efflux. Ag-TF@PDOX also showed efficacy in improving dual-mode (PAI/MRI) imaging.

Sun et al[179] developed an ATP-responsive smart hydrogel that can release immune adjuvants in response to repeated chemo- or radiotherapy to reinforce antigen-specific immune response. Alginate was conjugated with an adenosine triphosphate (ATP)-specific aptamer, which was hybridized with immunoadjuvant CpG oligonucleotide. Alginate-based hydrogel can form after intratumoral injection. With low doses of oxaliplatin or X-rays, the hydrogel can trigger the release of ATP and ICD; ATP competitively bonds with ATP-specific aptamer to trigger CpG release. Therefore, the smart hydrogel can release the immune adjuvant synchronized with low-dose repeated chemo/radiotherapies, achieving synergistic responses in rejecting established tumors, as well as immune memory to reject re-challenged tumors.

ROS Responsive

Because of the abnormal upregulation of various inflammatory cytokines, ROS levels in tumors are higher than in normal tissues.[180]Chen et al. [181] developed a ROS-responsive hydrogel

loading chemotherapeutic SN38 and anti-PD-L1. Importantly, this was synthesized by crosslinking 7-ethyl- 10-hydroxycamptothecin modified by phenylboronic acid (PBA) (SN38-SA-BA) with polyvinyl alcohol; PBA is degradable by ROS. Exposed to ROS in tumors, SN38-SA-BA was oxidized and hydrolyzed to release chemotherapeutic SN38 and anti-PD-L1. SN38 stimulated ICD that releases a series of DAMPs, leading to antitumor immune responses. Also, the released anti-PD-L1 bound to PD-L1 to activate the T cell response, further restoring antitumor immunity. The therapeutic efficacy was confirmed by effective inhibition of the tumor growth.

Park et al.[182] developed a ROS-responsive self-immolative polymer (R–SIP) that can efficiently destroy redox homeostasis via self-immolation-mediated glutathione depletion in cancer cells. R–SIP is amphiphilic and self-assembles into nanoparticles in aqueous to encapsulate DOX. In 4T1 cancer cells, DOX-encapsulated R–SIP (DR-SIP) induces the phosphorylation of eukaryotic translation initiation factor 2α and overexpression of ecto-calreticulin, resulting in endoplasmic reticulum-associated ICD. As a result, DCs were matured by the released DAMPs. The potential of DR-SIP to elicit an immune response was further validated by inhibition of tumor growth in mice.

Zhang et al.[183] developed a self-augmented ROS-responsive nanocarrier loaded with immunogenic inducer paclitaxel (PTX) and indoleamine 2,3-dixoygenase 1 (IDO1) blocker 1-methyl-D, L-tryptophan (1-MT). The carrier was composed of PEG as hydrophilic segments, enzyme cleavable 1-MT ester, and ROS-sensitive peroxalate conjugation as hydrophobic blocks. The copolymer self-assembles into nanoparticles loaded with PTX. A positive feedback loop of ROS-accelerated PTX release and PTX-induced ROS generation was achieved. This nanoparticle evoked the ICD of tumor cells and antitumor immune responses with high effector T cell

infiltration. IDO inhibition also led to reprogrammed immunosuppressive TME with reduced regulatory T cells (Tregs) and M2-tumor-associated macrophages (M2-TAMs).

Du et al.[184] created nanoparticles named SPTP@UCNP-RB-DOX. It is made of upconversion nanoparticles (UCNPs) coated by ROS-responsive micelles. The synergistic effect of chemotherapy and NIR-triggered photodynamic therapy (PDT) led to activated antitumor immunity via inducing immunogenic cell death with $CD8^+$ and $CD4^+$ T cells infiltrating in tumors. Another example can be seen from a NIR-triggerable ROS-responsive cluster-bomb-like nanoplatform. This nano platform elicits ICD, normalizes the immunosuppressive tumor microenvironment, and induces systemic immune response.[185]

GSH Responsive

The amount of intracellular GSH is $100 \sim 1000$ times higher than in the extracellular microenvironment.[176] Moreover, tumor tissue is often hypoxic and the GSH level is at least four times higher than healthy tissue.[186] Therefore, tumor-specific induction of ICD can be achieved by enabling nanomedicines GSH responsive.

A nano platform based upon phosphorus dendrimer-copper (II) complexes- and toyocamycin-co-loaded polymeric nanoparticles coated with cancer cell membranes is stable under a physiological status but can be quickly dissociated within the reductive tumor microenvironment to exhaust GSH and release drugs.[187] The released phosphorus dendrimer-copper(II) complexes triggered mitochondrial dysfunction and toyocamycin-induced ER stress, both leading to cancer cell ICD and efficient inhibition of tumor growth. The anticancer immunity was reflected in improved DC maturation and tumor-infiltration of CTLs.

An efficient chemoimmunotherapy was demonstrated by an ICD nano-amplifier made of diselenide-bridged mesoporous organosilica nanoparticles and KP1339.[188] KP1339 is a ruthenium-

mediated antitumor agent that can evoke the cascade of ICD.[189-190] These KP1339-loaded nanoparticles showed controlled drug release through GSH-responsive degradation. ROS generation, GSH loss, and ER stress in tumor cells were demonstrated using these nanoparticles. Downstream activities included KP1339-induced ICD and robust antitumor immune response. These nanoparticles inhibited primary tumor growth with low systemic toxicity as well as alleviated distant spread and lung metastases.

A GSH-responsive nano assembly was developed to suppress MDSCs and induce ICD.[191-192] It can suppress lactate dehydrogenase A (LDHA) levels in tumors. MDSCs suppression was achieved by reducing LDHA levels. Meanwhile, this nano assembly enhanced tumor immunogenicity via doxorubicin-provoked ICD.[193]

A GSH-responsive nano prodrug made from F127-coated drug dimers was demonstrated to attenuate glycolysis of tumor cells and mediate immunosuppression.[194] The dimer connects lonidamine and NLG919 (IDO1 inhibitor) via a disulfide bond. Upon cleavage of the disulfide bond by excessive GSH, both drugs were released. Lonidamine can downregulate hexokinase II and damage mitochondria, leading to attenuation of glycolysis. NLG919 can prevent the accumulation of kynurenine and the infiltration of Tregs. The disulfide bond further depleted GSH and increased oxidative stress. Together, the ICDs of tumor cells were promoted.[195]

Photon Responsive

Recent advancements in nanomaterials enabled ICDs to be triggered in a photon-responsive manner. These include nanomedicines based on photodynamic therapy (PDT), photothermal therapy (PTT), and photon-controlled drug release.

PDT is a photon-activated ROS generation approach relying on the photosensitizer (PS). Nanomaterials with PDT capability may enable localized ROS generation at the subcellular level.

Zhou and coworkers[196] developed a TiO_2@Ru@siRNA nanocomposite made of TiO_2 nanoparticles coated with a Ru(II) PS and loaded with hypoxia-inducible factor-1α (HIF-1α) siRNA. TiO_2@Ru@siRNA can be localized in the lysosome. Irradiated by visible light, TiO_2@Ru@siRNA produced $O_2^{\bullet-}$ and $^1O_2$ and blocked the HIF-1α signal, resulting in the activation of pyroptosis and reduced tumor hypoxia. In vivo, TiO_2@Ru@siRNA inhibited tumor growth and evoked anticancer immunity. Chen and coworkers [197-198] reported a series of pH-sensitive nano-photosensitizers named ANPS for triggering pyroptosis. ANPS was made of a pH-sensitive copolymer, a PS (Ce6), and a quencher (QSY21). ANPS can selectively disassociate in more acidic lysosomes, leading to the separation of Ce6 and QSY21, an "on state". Released Ce6 produces a strong $^1O_2$ response. Activated ANPS can trigger phospholipase C signaling, activation of caspase-3 and GSDME, and photoinitiated pyroptosis. In mice, ANPS resulted in enhanced anti-tumor efficacy and minimized systemic side effects.

Photothermal therapies (PTT) use photothermal agents (PTA) to induce localized heat production and ablation of cancers. PTAs absorb energy from light exposure. The nonradiative decay process releases heat.[199] Instead of merely ablating tumors, recent studies show that nanomedicines based on PTT can also trigger pyroptosis. Zhang and coworkers[200] reported the first covalent organic frameworks (COF)-based pyroptosis inducer, COF-909-Cu. Mimicking key enzymes such as peroxidase (POD), superoxide dismutase (SOD), and glutathione peroxidase (GPx), COF-909-Cu showed good catalytic performances and a remarkable photothermal conversion. It also facilitated the Fenton-like ionization process. As a result, COF-909-Cu enhanced the intracellular H_2O_2 levels and the depletion of glutathione (GSH). Moreover, COF-909-Cu induced GSDME-dependent pyroptosis, which was accompanied by the release of DAMPs, boosted dendritic cell maturation, T cell clone development and potentially increased

sensitivity to immune checkpoint therapy. Zhao and coworkers[201] created biomimetic nanoparticles (BNP) loading indocyanine green (ICG) and decitabine (DCT). When exposed to NIR photoirradiation, the solution of BNPs had a temperature increased to 42 °C, demonstrating the good heat conversion capability of BNP. The temperature increase caused the disassociation of BNP and the release of ICG and DCT. DCT triggered the GSDME-dependent pyroptosis of cancer cells. Zhou and coworkers[202] developed a multifunctional and biodegradable oxidized bacterial cellulose (OBC)-based nanomaterial, TB/αPD-1@AuNCs/OBC. This material prevented tumor growth and induced pyroptosis via the photothermal effects of the gold nanocages. The pyroptosis process was accompanied by the release of HMGB1, LDH, and ATP and enhanced PD-1-mediated immunotherapy. Zhang and coworkers[203] reported a PTT carrier, DDP-silicene@mMSNs-RGD, a 2D core/shell nanosystem made from silicon-based biomaterials loaded with cisplatin (DDP). Irradiated by NIR, this material produced a local heat shock that can trigger DDP release. Meanwhile, Caspase-3 and GSDME-mediated pyroptosis were activated.

Activating the release of ICD-inducing drugs with photons is another emerging strategy. Ji and colleagues[204] reported a pyroptosis-inducing nanoagonist, OA@IR820. It was created via the assembly of oligomycin A (OA, an ATP synthase inhibitor) and IR820. NIA laser can trigger the disassociation of OA@IR820 release of OA. Due to the mitochondria-targeting capability, OA@IR820 resulted in efficient ATP inhibition and oxidative stress-mediated pyroptosis. Increased expression of pyroptosis-associated proteins (NLRP3, cleaved caspase-1, GSDMD-N, cleaved caspase-3, and IL-1β) was observed, suggesting the antitumor immunity of OA@IR820.

Sono Responsive

Sonodynamic therapy (SDT) also induces ICD by producing ROS as PDT. Instead of using photons, SDT relies on ultrasound, sonosensitizer, and oxygen.[205-206] Overall, SDT benefits from

a better penetration depth of ultrasound than photons in biological tissues and may overcome the limit faced by PDT.[207] Under the effect of ultrasound, tumor tissue absorbs more ultrasonic energy due to its dense arrangement and large volume causing temperature rise and structural destruction. Moreover, the small bubbles and respiratory vibration generated by ultrasound can activate sonosensitizer to generate ROS, leading to a tumor-killing effect.[208-209] SDT can be promoted by the rational design of nanomedicines. For example, Zhang et al.[210] developed a nano platform MON-PpIX-LA-CO_2. It was made from mesoporous organic silica (MON) loaded with sonosensitizer protoporphyrin (PpIX) and L-arginine (LA). PpIX can generate ROS and induce ICD under ultrasonic irradiation. LA can reversibly adsorb and release carbon dioxide and trigger the inertial cavitation effect. The generation of ROS and immunogenicity of SDT is promoted.

Mitochondria targeting can improve the efficacy of SDT for tumors. Cai and coworkers[168] reported a nano-sonosensitizer platform (FAMnP) that used folate liposomes (FA) loaded with manganoprotoporphyrin (MnPs) against triple-negative breast cancer (TNBC). With the help of folate, nanoparticles could effectively target TNBC cells overexpressing folate receptors and releasing MnP. The Mn^{2+} in MnP improved the ultrasonic effect of nano-sonosensitizer. FAMnPs showed significant inhibition of tumor growth, activation of the polarization of M2 macrophages to M1 macrophages, and release of DAMPs to induce ICD.

Huang and co-workers[211] synthesized nanodroplets (PMPS NDs) to target ER. Protoporphyrin was reacted with 4-methylbenzene sulfonylurea (MPS) and subsequently modified by cyclic-ArgGly-Asp (cRGD) peptide.[92] cRGD peptide promoted the accumulation of nanodroplets around tumor vascular endothelial cells; MPSU enabled it to target sulfonylurea receptors. Together, PMPS NDs selectively accumulated in the ER of tumor cells and generated toxic ROS in situ, which further induced DCs maturation and enhanced immunogenic effects.

The SDT effect is attenuated by tumor's inherent redox regulatory system that can counteract singlet oxygen. The nuclear factor (erythroid-derived 2)-like 2 (Nrf2)- mediated classical deoxidation signaling pathway maintains redox balance in tumor cells. Based on this, Zhang and coworkers[212] developed a nuclear-targeted nano-sonosensitizer TIR @ siRNA carrying transactivator of transcription peptide coupled to IR780 and Nrf2-siRNA. Nrf2-siRNA disrupted intracellular redox pathways. In turn, acoustically induced ICD was activated and the immunosuppressive TME was normalized.

Radio Responsive

Radiotherapy based on X-ray or γ high-energy ionizing radiation can directly damage DNA or interact with water molecules to form ROS. Radiotherapy is still limited by the low absorption of ionizing radiation by hypoxic tumors; an improved dose of radiation is impractical due to potential damage to the normal tissues. Nanomedicine can help here. For example, Kim and colleagues designed Au NPs (SAuNC) loaded with anti-PD-L1 to achieve combined radiotherapy and ICB therapy.[213] The SAuNC produces ROS after being sensitized by radio and induces ICD. Meanwhile, anti-PD-L1 is released upon radiation trigger, synergizing the ICD with ICB immunotherapy.

Emerging scintillators can transfer X-rays to luminescence, a key property that can benefit existing PDT due to the excellent tissue penetration of X-rays. This combined therapy is also termed radiodynamic therapy (RDT). Exposed to X-rays, MOFs[214] loaded with indoleamine-pyrrole 2, 3-dioxygenase (IDO) inhibitor (IDOi@nMOFs) caused the CRT exposure and induced ICD. Tumor infiltration of $CD8^+$ T cells was improved due to the released DAMPs and antigens. The anticancer immunity of this RDT is evidenced by the suppression of the distant tumor growth.

1.4. CONCLUSION

Nanomedicines have witnessed significant progress due to advancements in nanotechnology and can be powerful tools in both disease diagnosis and treatment. In this introduction, I focused on discussing how nanomedicines have facilitated ultrasound bioimaging and cancer immunotherapy.

Ultrasound contrast agents of both micro and nano sizes have greatly improved ultrasound imaging quality by creating an acoustic impedance mismatch between the agents and the background (tissue/blood/bone). Gas microbubbles suffer from short lifetime and sizes that are too big for molecular imaging of diseases such as tumors, which requires small sizes to achieve sufficient penetration. Emerging nanomedicines can overcome this issue due to their smaller sizes.

A wide range of nanomedicines have been evaluated for ultrasound imaging, including gas nanobubbles, liquid nanodroplets, and solid nanoparticles. Despite demonstrated promises of these nanomedicines, an ideal ultrasound contrast agent— that has tunable size (from nano to micro range), modifiable surface (for targeting and molecular imaging), biodegradability, biocompatibility, and sufficient stability (half-life) for transient ultrasound imaging— is yet to be explored. Here, phosphate glass is an ideal candidate due to its biodegradability and biocompatibility. However, a simple and scalable synthetic method that can create versatile sizes of phosphate glass micro/nanoparticles is yet to be investigated.

Immune checkpoint blockade therapy has reshaped cancer immunotherapy but still suffers from immune-related toxicity due to the overexpansion of T cells by antibodies. Moreover, they only produce favorable responses in a minority of patients. This is because many cancer types are “immune-cold”, i.e., they have developed immune-suppressive TME to suppress key steps in the anticancer immunity cycle (e.g., antigen presentation, dendritic cell maturation, T lymphocyte

activation, and infiltration). Therefore, there is an urgent need to advance strategies for "normalizing" or "firing up" cold TME.

A particularly appealing approach is applying nanomedicines to trigger immunogenic cell death (ICD) of tumor cells. Tumor cells undergoing ICD can release tumor-specific antigens and adjuvants including proinflammatory cytokines and DAMPs. These antigens and adjuvants, together, can boost the tumor-localized maturation of DCs and activation of $CD8^+$ T cells. In turn, the cold TME can be fired up due to reversed T cell populations, which may overcome the immune-related toxicity and inefficacy in immune-cold tumors faced by current CITs. Nanomedicines have been rationally designed to trigger tumor-specific ICDs for anticancer immunity. These include targeted nanomedicines and stimulus-responsive ones. The targeted types are enabled by the EPR effect or carefully modified surface ligands. Stimulus-responsive nanomedicines utilize tumor endogenous stimuli (e.g., pH, enzymes, ATP, ROS, and GSH) or external stimuli (e.g., photon, ultrasound, and radio).

Despite the demonstrated capability of inducing ICD and anticancer immunity, these nanomedicines still face some common limitations. First, most of these nanomedicines cannot degrade in physiological conditions or their degradation byproducts are toxic. Second, nanoformulations of sensitizing agents/drugs suffer from drug leakage. Third, nanomedicines relying on external stimuli face the limitations of penetration depth of stimuli (e.g. photon) and undesired damages on normal tissues by irradiation. Therefore, further work is necessary in search of ICD-inducing nanomedicines that are biodegradable, biocompatible, and intrinsically potent in inducing ICDs (i.e., without the aid of sensitizing agents/drugs and external stimuli).

1.5. ACKNOWLEDGEMENTS

Chapter 1, in full, is unpublished material. The dissertation author was the author.

CHAPTER 2. BIODEGRADABLE CALCIUM PHOSPHATE MICRO/NANO PARTICLES SYNTHESIZED VIA ELECTROSPRAY

2.1. ABSTRACT

Phosphate-based glasses are well-studied biodegradable materials in the bulk. However, less is known about the synthesis and properties of phosphate glass when prepared as microparticles or nanoparticles. These glasses have excellent biodegradability and biocompatibility. Therefore, phosphate glass micro/nano particles have significant potential for advances in drug delivery, bioimaging, degradable implants, and tissue engineering. In this study, calcium phosphate micro/nano particles (CPPs) with the composition $(P_2O_5)_{25}$-$(CaO)_{75}$ were prepared through a combination of the sol-gel and electrospray methods. This synthesis method shows great flexibility in controlling the size and morphology of CPPs. CPPs with an average diameter in the range of 345 to 952 nm and various morphologies including carnation flower-like, golf-ball-like, and apple-like were obtained. Optical microscopy was further used to demonstrate that the CPPs can have an average size increase of 95% in diameter and 720% in volume within the first 5-10 min of hydration in neutral aqueous media. The hydro-expansion process is accompanied by a two-stage ion release of phosphorous and calcium.

2.2. INTRODUCTION

Bulk phosphate-based glasses have been extensively studied for decades.[43-52, 215-218] This research interest is driven by three unique properties: biodegradability and biocompatibility,[43-52] tunable dissolution rate,[53, 58, 219] and ease of drug and biomolecule loading.[54-58, 220-221] Different from their silicate counterparts,[219, 222-224] phosphate glasses can completely dissolve in aqueous media and release ions such as Ca^{2+} and Na^{+} that are routinely found in the human body.[43-53] This bio-degradability is a direct result of the underlying chemical structure. Phosphate glass consists of an inorganic phosphate network along with modifiers such as metal oxides. The PO_4^{3-} tetrahedron unit contains at least one terminal oxygen and shares the other three with neighboring PO_4^{3-} units. This terminal oxygen reduces the connectivity of phosphate glasses compared to their silicate-based counterparts.[46]

The connectivity is further reduced by adding modifier metal oxides (e.g. CaO, Na_2O, MgO, K_2O, Al_2O_3, Fe_2O_3, and TiO_2), which depolymerize the glass structure by converting the bridging oxygens into non-bridging oxygens. Second, the capability of introducing versatile modifier oxides makes the dissolution rate tunable from hours to several weeks.[219] Third, phosphate glasses can have biomedical functions: Drugs and biomolecules (e.g. trypsin inhibitor,[54] tetracycline,[55] growth factors,[56] gentamicin sulfate[57], vancomycin[58]) can be easily loaded into the glass matrix and then released as the glass dissolves. These properties make phosphate glasses promising candidates for biological applications such as bioimaging,[10] drug delivery,[54-58, 220-221] tissue engineering,[53] bone regeneration,[218] bacterial control,[53] neural repair,[53, 225] oral healthcare,[226] bioresorbable optical fiber,[46] etc.

Bulk phosphate glasses are typically synthesized via the melt-quenching of precursors. This is a high-temperature process (~1000 ℃) and incompatible with most biomolecules and

drugs. More recently, sol-gel methods have been shown to create bulk phosphate glasses with a wide range of compositions below 200 °C.[52, 220, 227-231] In the sol-gel process, the phosphate precursors (e.g., n-butyl phosphate and triethyl phosphate) and desired metal oxide precursors (e.g., sodium methoxide and calcium methoxyethoxide) are mixed, hydrolyzed, and condensed to form the gel and carefully dried to form the glass.

Although bulk phosphate glasses are established, studies on the synthesis and properties of phosphate glass micro/nanoparticles are still limited. The reduction of the size to micro/nano range may benefit biomedical applications such as drug delivery, bioimaging, and degradable implants. One approach for the preparation of nano phosphate glasses is the combined sol-gel and electrospray method.[10] Electrospray is an electrohydrodynamic atomization process that generates fine charged droplets. Micro/nano- materials with controllable size and morphology can be formed once the as-generated droplets are further solidified.[232] This method has been used in previous research to generate biodegradable $(P_2O_5)_{55}$–$(CaO)_{30}$–$(Na_2O)_{15}$ glass nanoparticles in the range of 200-500 nm.[10] These phosphate glass nanoparticles demonstrate good biodegradability and were exploited as a transient contrast agent for ultrasound stem cell imaging. However, influences of synthetic parameters such as the solvent physical property and the electrospray voltage, flowrate, and working distance have not been explored in this work.

Here, we further refine this method to prepare $(P_2O_5)_{25}$-$(CaO)_{75}$ calcium phosphate particles (CPPs) via a combination of sol-gel and electrospray. CPPs of the size in the range of 345 to 952 nm and various morphologies including carnation flower-like, golf-ball-like, and apple-like were obtained by tuning the flowrate of the electrospray process and tri-butyl phosphate concentration. More importantly, we also report the discovery of the hydro-expansion property of CPPs associated with the degradation process in aqueous media at pH= 7. To the best of our

knowledge, this is the first detailed study of size and morphology control and the first report demonstrating the hydro-expansion property of phosphate-based glass micro/nano particles.

2.3. MATERIALS AND METHOD

2.3.1. Synthesis of CPPs

2.3.1.1. Synthesis of the Sol for Electrospray

The following chemicals were used without further purification: n-butyl phosphate (NBP, a mixture of mono-n-butyl and di-n-butyl, Alfa Aesar), calcium methoxyethoxide (CME, ABCR, 20% in methoxyethanol), 2-methoxyethanol (2-ME, Sigma Aldrich, 99.9%), tri-butyl phosphate (TBP, Sigma Aldrich, 99%). NBP was diluted by 2-ME in a molar ratio of 1: 3 (NBP:2-ME) and magnetically stirred at 800 rpm for 10 min. This mixture was cooled in an ice-bath. CME was added to the solution dropwise via a syringe pump (16 mL/h) with the solution being magnetically stirred. Upon the completion of CME addition, the solution was brought to room temperature and magnetically stirred overnight. See Table 2.4 for specific reactant addition.

2.3.1.2. Electrospray

The setup for electrospray is shown in Figure 2.1 (A). A 16 G metal needle was used as the emitter, which was charged by a high-voltage generator. A metal ring with a diameter of 2.5 cm was inserted 0.5 cm below the emitter, which was also charged by a secondary high-voltage generator. Both the emitter and ring electrode shared the same ground electrode. The ground electrode was inserted below the silicone oil bath. The ring electrode inserted between the emitter and the ground electrode serves for modifying the spatial distribution of the electric field and confine the spray inside the space that is collectible by the silicone oil bath.[233] A silicone oil bath maintained at 150 ℃ was used as the collection medium for particles. An appropriate amount of TBP was added to the sol from the previous step and vortexed for 10 seconds right before

electrospray. As-prepared sol solution was fed to the emitter at various flowrates and electrosprayed by the applied voltage. Various combinations of TBP addition, flowrate, emitter voltage (V_E), ring voltage (V_R), and working distance (ring-to-ground electrode distance, H_2) were studied to determine their influences on the particle size and morphology. See Table 2.4 for specific parameters. The resulting particles were centrifuged at 5000 rpm, washed with acetone three times, and then dried at 180 ℃ for 2 hours.

2.3.2. Characterizations

2.3.2.1. SEM, EDX, TEM, and DLS

SEM images were acquired with Zeiss Sigma 500 operated at 5 kV with a 30-μm aperture and 10 mm working distance. CPPs were drop-coated on a silicon substrate (Ted Pella Inc.) and sputter-coated with gold alloys before SEM. For EDX, CPPs without gold alloy coating were used and the voltage and aperture was 20 kV and 60 μm, respectively. TEM images were acquired with a JEOL 1200 EX II operating at 80 kV. DLS measurements were carried out using Zetasizer (ZS90, Malvern Panalytical) with CPPs in 2-methoxyethanol solution.

2.3.2.2. XRD, FTIR, and Solid State ^{31}P MAS NMR

Dried CPPs-4 powders were used for XRD, FTIR, and ^{31}P MAS NMR characterization. XRD and FTIR spectra were acquired using Panalytical XRD and Perkin Elmer FTIR. The solid state ^{31}P MAS NMR data were measured at ambient temperature using a Varian InfinityPlus-300 spectrometer (B_0 = 7.05 T) operating at a Larmor frequency of 121.5 MHz. The experiments were performed using a Varian HX 3.2 mm MAS probe spinning at a MAS frequency of 20 kHz. Quantitative data were acquired with direct detection (single pulse) methods using a $\pi/6$ flip angle and a recycle delay of 400 s. The NMR data processing was carried out using ssNake while spectral deconvolution was undertaken using Origin. All spectra were referenced against the IUPAC

recommended primary reference of 85% H_3PO_4 (δ_{iso}= 0.0 ppm) via a secondary reference of ammonia dihydrogen phosphate (ADP) (δ_{iso} = 0.99 ppm).

2.3.2.3. Hydro-Expansion Observation

The hydro-expansion of CPPs was observed using an inverted optical microscopy (Keyence). Here, 0.1 mL CPPs in ethanol solution (1mg/mL) was dropped to a 35 mm glass-bottom dish with a 14 mm micro-well #1.5 cover glass (Cellvis). 2 mL aqueous solutions with pH= 7 were added to the dish respectively to initiate the hydration of particles. The first image was taken after 2 minutes of waiting time, when particles naturally settled down on the bottom of the dish and self-stabilized. Images of the same area were taken at various time points and then analyzed by Image-Pro Plus 6 to determine the diameter of particles.

2.3.2.4. Biodegradation Monitoring

Biodegradation was monitored via ICP-MS (iCAP RQ, Thermo Scientific): 1.4 mg CPP-4 was deposited on a syringe filter with a pore size of 0.22 μm (Millex-GP). CPP-4 was used because the smallest particles found in this sample were larger than the pore size. ICP-MS samples were prepared as stated below. Millipore water was continuously pumped (1.2 mL/h) through the particle-deposited syringe filter using a syringe pump at room temperature. The liquid phase was collected at various time points (0 min, 5 min, 10 min, 20 min, 30 min, 1 h, 2 h, 4 h , 8 h, 24 h). 0.1 mL of each of these liquids was mixed with 0.571 mL 70% HNO_3 and left for overnight digestion. Subsequently, Millipore water was added to make a solution of 10 mL. The same process was repeated for a flow cell without particles to create negative controls. The release of P and Ca was measured with standard curves created in the range of 0-1000 ppb prepared from commercial phosphorus standard and calcium standard (TraceCERT). All samples and standards contain 4% HNO_3. Results were expressed as a cumulative ion release in mole versus time.

2.4. RESULTS AND DISCUSSION

2.4.1. Synthesis, Composition, and Structure of CPPs

CPPs were prepared with a combination of sol-gel and electrospray[10] (see **Materials and Method**). Briefly, a sol solution was prepared using n-butyl phosphate (NBP) and calcium methoxyethoxide (CME) as phosphate and calcium precursors, respectively. As-prepared sol solution was subsequently electrosprayed with the setup as shown in Figure 2.1 (A). In the electrospray, the sol solution was pumped through a metal needle and charged by the applied high voltage. As a result, fine droplets were formed and collected by the silicone oil bath maintained at 150 ℃. CPPs finally formed in the silicone oil bath after solvent evaporation. The size and morphology can be well controlled by adjusting the flowrate in the electrospray parameters and the solvent mixture of the sol (Figure 2.1 (B)), which will be discussed later. A summary of the sample ID and detailed synthetic parameters including the sol-gel recipe, flowrate, voltage, and working distance are provided in Table 2.4.

A comparison of the intended composition of CPPs and that determined by EDX and ICP-MS is shown in Table 2.1. The EDX and ICP-MS results are consistent with the intended CPPs composition, $(P_2O_5)_{25}$-$(CaO)_{75}$. Note that CPP-4 and CPP-9 were prepared without and with tri-butyl phosphate (TBP) addition, respectively. No significant compositional difference was found in these two samples indicating that TBP did not react with the sol. However, the addition of TBP was found to affect the morphology of particles, which will be discussed later.

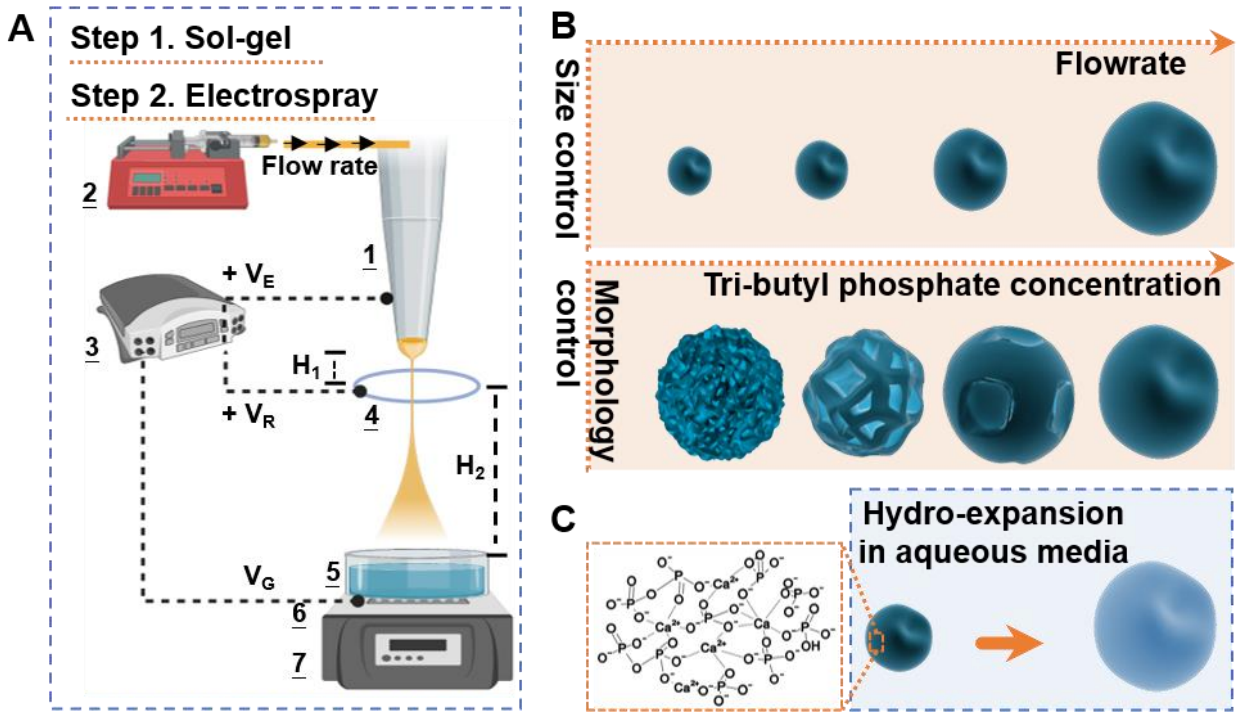

Figure 2.1 Scheme showing the electrospray process, control over the size and morphology, and hydro-expansion properties of CPP particles.

(A) Schematic illustration of the combined sol-gel and electrospray process. The sol solution prepared from the sol-gel chemistry (step 1) was pumped through the emitter charged with a high-voltage (step 2). This process generated fine droplets, which were collected by the heated silicone oil to form CPPs. 1, Emitter; 2, Syringe pump; 3, High voltage generator; 4, Ring electrode; 5, Silicone oil bath; 6, Ground electrode; 7, Hot plate. V_E, the voltage of the emitter; V_R, the voltage of the ring electrode; V_G, the voltage of the ground electrode; H_1, the distance between the emitter and ring; H_2, the distance between the ring and ground electrode (working distance). This figure was created with BioRender.com. Main findings of this study include (B) the size and morphology control achieved by tuning the flowrate and tri-butyl phosphate concentration, respectively and (C) the hydro-expansion behavior of CPPs in aqueous media. Inset: schematic illustration of the phosphate glass network modified by calcium oxide. Note that this scheme does not reflect the actual chemical structure and composition.

Table 2.1 Composition of CPPs

Sample ID	Intended[a]		EDX[b]		ICP-MS[b]	
	P_2O_5 (mol %)	CaO (mol %)	P_2O_5 (mol %)	CaO (mol %)	P_2O_5 (mol %)	CaO (mol %)
CPP-4[c]	25.0	75.0	24.6	75.4	25.1	74.9
CPP-9[c]	25.0	75.0	25.3	74.7	26.0	74.0

[a] The intended value was calculated based on the ratio of NBP and CME chemical input in the sol-gel process

[b] Both EDX and ICP-MS results were converted to mol% for comparison

[c] See Table 2.4 for specific synthetic parameters

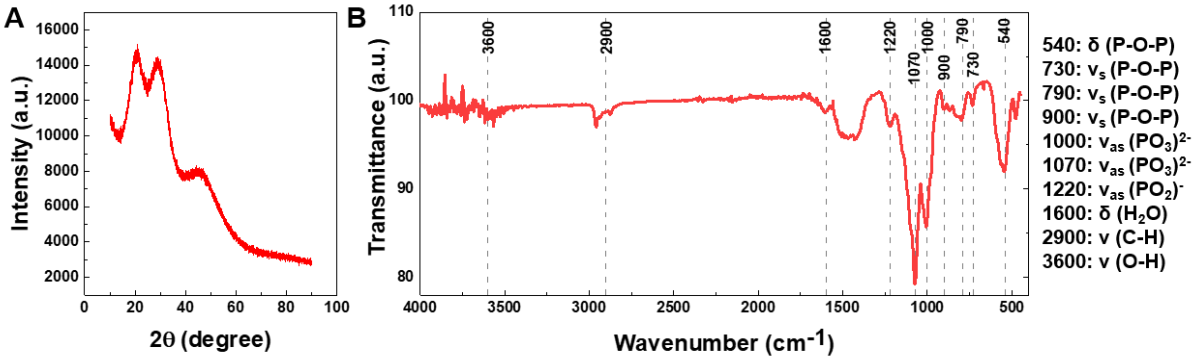

Figure 2.3 XRD and FTIR spectra of CPP-4.

(A) XRD pattern of CPP-4 indicating the amorphous nature and (B) FTIR spectrum and band assignments for CPP-4 indicating the presence of P-O-P bonding and Q^1 and Q^2 species. Abbreviations: ν, stretching; δ, deformation; s, symmetric; as, asymmetric. See Table 2.4 for detailed sample ID and synthetic parameters.

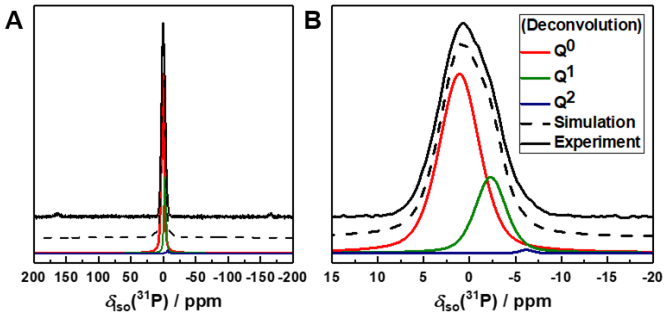

Figure 2.2 ^{31}P MAS NMR spectra of CPP-4.

(A) -200-200 ppm and (B) -15-15 ppm. Predominant Q^0 and Q^1 species indicate a low degree of polymerization.

Table 2.2 ^{31}P MAS NMR peak parameters of CPP-4

δ_{iso} (ppm)	Q^n	FWHM (ppm)	Relative Intensity (%)
1.1	Q^0	5.2	75.3
-2.3	Q^1	4.0	24.3
-6.2	Q^2	1.6	0.4

The structural characterization of the CPPs used a combination of XRD, FTIR, and ^{31}P MAS NMR techniques. The XRD pattern of the as-prepared CPPs (Figure 2.2 (A)) shows three

broad reflections observed between 20 and 60 degrees 2θ, which indicates the amorphous nature of these particles as reported in the literature.[234-236] Figure 2.2 (B) shows that the nature of bonding in the CPPs can be determined by FTI R. All bands are assigned according to previous literature reports.[52, 237-240] Specifically, the bands measured at 540, 730, 790, and 900 cm^{-1} are all assigned to vibrational and stretching modes of the P-O-P bonding. The Q^n terminology is widely applied for explaining the degree of polymerization of phosphate glasses.[52, 219, 228, 241] Here, n represents the number of bridging oxygens in the network. A higher n number represents a higher degree of polymerization of the glass network. The presence of Q^1 species is indicated by the symmetric and asymmetric PO_3^{2-} stretching modes at 1000 and 1100 cm^{-1}. The weak signals at 900 and 1220 cm^{-1} are assigned to the asymmetric P-O-P and PO_2^- vibrations, which indicates the presence of Q^2 units. However, the Q^2 signal is much weaker than Q^1 signal. The band around 3600 and 1600 cm^{-1} is assigned to the symmetric stretching and the deformation modes of O-H groups, respectively, which can originate from surface hydroxyl groups or physically adsorbed surface water. The band at 2900 cm^{-1} is assigned to C-H stretching modes associated with residual organics. Figure 2.3 shows the ^{31}P MAS NMR data measured under quantitative conditions from CPPs, where each deconvoluted resonance is assigned according to previous literature values.[10, 228, 242] From Table 2.2, 75.3% of Q^o, 24.3% of Q^1, and 0.4% of Q^2 species comprise the CPP structure, thus indicating a very low degree of polymerization throughout the phosphate network. Hence, the glass network is predominantly connected by P-O-Ca bonds rather than P-O-P bonds. The theoretical phosphate glass compositions sustaining pure Q^o, Q^1, and Q^2 speciation are $(P_2O_5)_{25}$-$(CaO)_{75}$, $(P_2O_5)_{33}$-$(CaO)_{67}$, and $(P_2O_5)_{50}$-$(CaO)_{50}$, respectively. Therefore, the theoretical composition of CPPs with 75.3% of Q^o, 24.3% of Q^1, and 0.4% of Q^2 species is close to $(P_2O_5)_{27.14}$-$(CaO)_{72.86}$ (calculated by

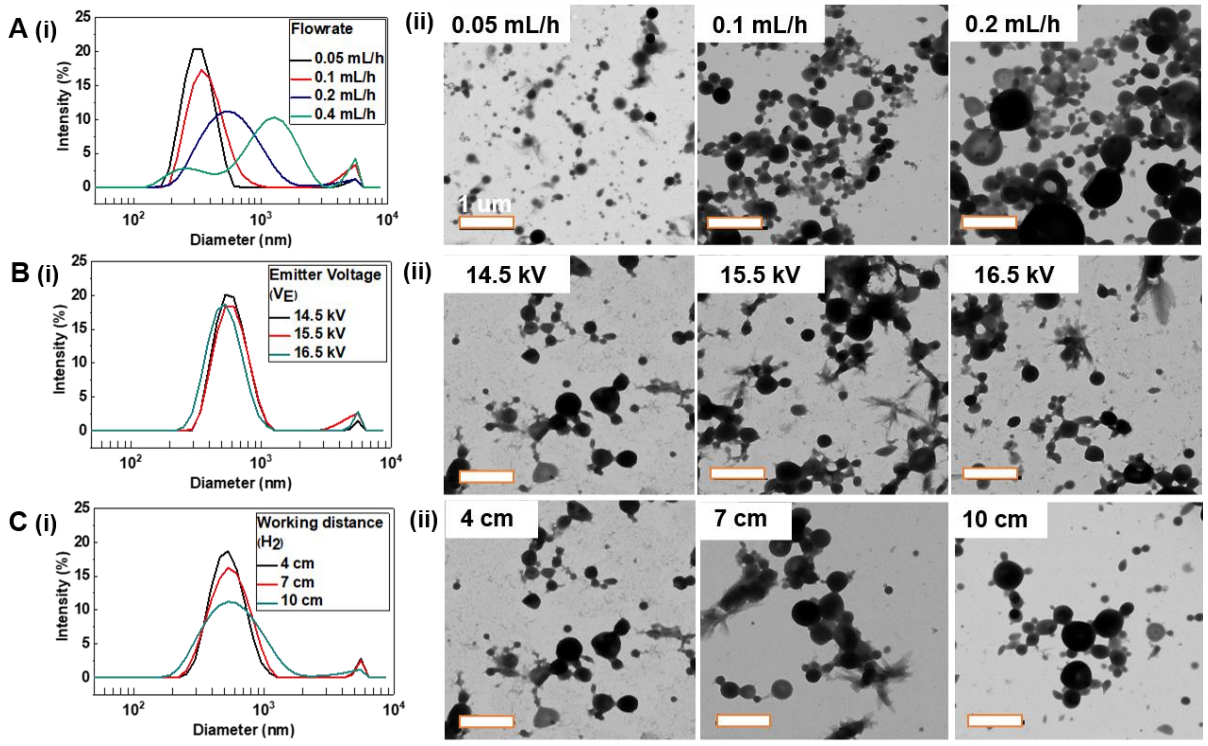

Figure 2.4 DLS Size Distribution and TEM images.

DLS and TEM images showing the effect of (A) flowrate, (B) emitter voltage, and (C) working distance on the size distribution of CPPs. The flowrate was adjusted from 0.05 (CPP-1) to 0.1 (CPP-2), 0.2 (CPP-4), and 0.4 (CPP-3) mL/h; the emitter voltage was adjusted from 14.5 (CPP-5) to 15.5 (CPP-6), and 16.5 (CPP-7) kV; the working distance was adjusted from 4 (CPP-5) to 7 (CPP-8), and 10 (CPP-4) cm. See Table 2.4 for details on synthetic parameters. See Figure 2.9 for the TEM image for CPP-3. The mean diameter of particles increases as the flowrate increases from 0.05 to 0.4 mL/h and does not vary significantly with the change of emitter voltage and working distance in the tested range. Scale bar, 1μm.

weighted average). This NMR-derived composition is consistent with EDX and ICP-MS results of Table 2.1.

2.4.2. Effects of Electrospray Parameters on the Size

The first electrospray parameter studied is the flowrate of the sol solution. In the electrospray process, as the applied voltage increases, the spraying mode changes from dripping mode to spindle mode, and Taylor cone-jet mode.[243-245] Throughout this study, the Taylor cone-jet mode was applied because it generates relatively more monodispersed particles with predictable

sizes. According to the scaling law,[232, 246-247] the jet diameter is proportional to the flowrate and governsthe size of as-generated droplets and particles. Our DLS and TEM results (Figure 2.4, Figure 2.12, and Table 2.4) are consistent with this prediction. As the flowrate increases from 0.05 (CPP-1) to 0.4 (CPP-3) mL/h, the mean diameter (Z-Ave.) of CPPs increases from 345.5 to 952.3 nm (Figure 2.4 (A)). The polydispersity index (PDI) maintains around 0.25 for CPPs prepared from the flowrate of 0.05-0.2 mL/h. The PDI, however, increases significantly to 0.564 when the flowrate is 0.4 mL/h. The increasing polydispersity is due to a less stable Taylor-cone jet when the flowrate is larger than 0.4 mL/h. The other two parameters, emitter voltage (14.5-16.5 kV) and working distance (4-10 cm), however, do not result in a significant change of the particle size (Figure 2.4 (B) and (C)). Note that a second peak ~ 5000 nm with 0.5-14% in intensity exists in all samples. This was attributed to larger particles formed due to the bursting spray caused by the occasional congestion of the nozzle. This bursting spray may also explain the relative polydisperse nature of as-prepared CPPs. More detailed size information (Z-Ave., PDI, peaks, peak percentage, and standard deviation for each peak) can be found in Table 2.4.

2.4.3. Effects of the Solvent Mixture on the Morphology

Both the size and morphology (or shape) have been known to greatly affect the cell internalization of synthetic particles.[248-252] It is therefore essential to be able to control the morphology of CPPs for potential biomedical applications. Electrospray not only shows flexibility in the control over the particle size but also the particle morphology. [10, 232, 253-264]

One factor that influences the morphology of particles during electrospray is the evaporation behavior of solvents. For example, the preparation of porous particles with tunable pore structures[253, 265-266] and non-spherical particles (e.g. red-blood cell-like)[267] have been demonstrated via controlling the evaporation of solvents. We hypothesized that the addition of a high-boiling point solvent to the sol solution can alter the solvent evaporation behavior and thus

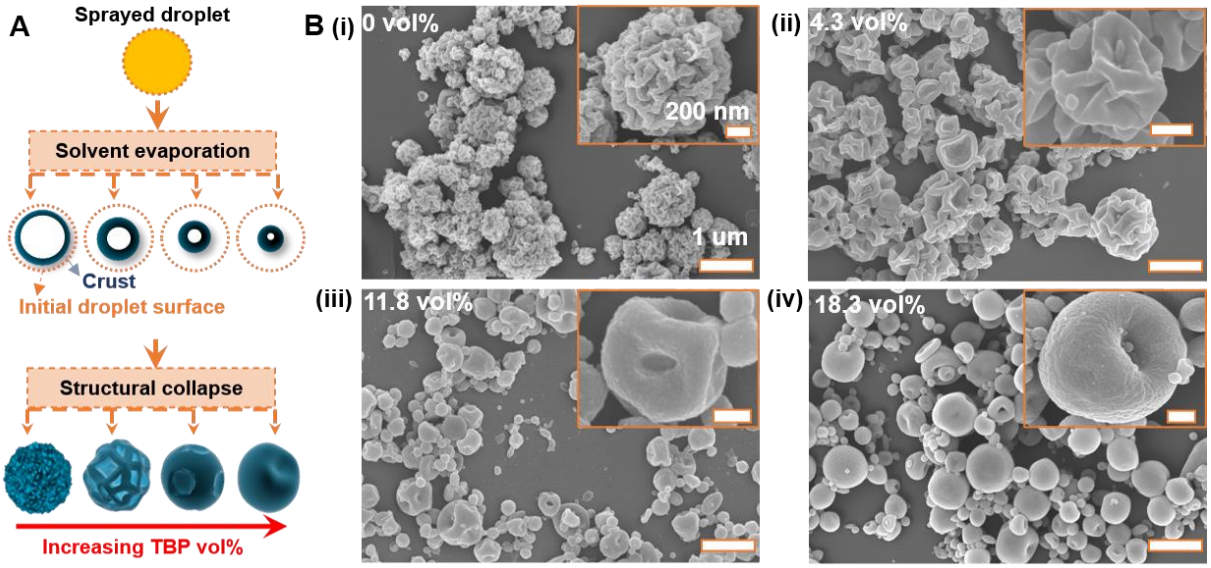

Figure 2.5 Effects of solvent boiling point on the morphology of CPPs.

(A) Schematic illustration of a hypothesized mechanism for the evolution of the morphology of CPPs. A higher amount of TBP increases the boiling point of the solvent mixture, which will slow down the evaporation of the solvent and allow for a more sufficient inward solute diffusion and a homogenous shrinkage of the droplet before the formation of a void crust. This more sufficient inward solute diffusion process can lead to a smaller void-to-crust volume ratio upon the complete solvent removal and a lower degree of structural collapse and, therefore, a smooth surface. (B) SEM images showing the evolution of the morphology of CPPs with the increase of tri-butyl phosphate (TBP) addition in the sol solution from (i) 0 vol% (carnation-like, CPP-9), (ii) 4.3 vol% (golf ball-like, CPP-10), (iii) 11.8 vol% (dented, CPP-11) to (iv) 18.3 vol% TBP (apple-like, CPP-4). The surface smoothness increases with the increase of TBP addition. Inset images: higher magnification images showing a representative particle for each case. Scale bar: 1um for all low-magnification images; 200 nm for all high-magnification images.

the morphology of CPPs. TBP was selected as a model additive because of its much higher boiling point relative to all other reactants in the sol solution (Table 2.3). Various amounts of TBP were added to the sol solution immediately before the electrospray. An interesting evolution of the morphology CPPs was observed with the increase of TBP addition (Figure 2.5 (B)). Without adding TBP, the CPPs surface is highly wrinkled and resembles a carnation flower (Figure 2.5 B(i)). As the added TBP increases from 4.3 to 18.3 vol%, the surface becomes increasingly smooth, and the morphology changes from golf ball-like (Figure 2.5 B(ii)) to mildly dented (Figure

2.5 B(iii)), and then apple-like (Figure 2.5 B(iv)). The increase of TBP concentration to 34.9 vol% can further reduce the surface dents and wrinkles (Figure 2.10).

The TBP does not participate in the chemical reactions because no significant compositional difference resulted from the TBP addition (Table 2.1). Therefore, the observed morphology evolution is more likely a result of changes in the physical properties of the sol caused by TBP addition. A possible mechanism is proposed and shown in Figure 2.5 (A). A higher amount of TBP addition will increase the overall boiling point of the solvent mixture meaning a slower evaporation rate. This reduced evaporation rate may allow for a more sufficient inward solute diffusion and homogenous shrinkage of the liquid droplet before the formation of a solid crust. As a result, a smaller void-to-crust volume ratio is possible upon the complete evaporation of solvents. Therefore, the particle is more robust to resist the tendency toward structural collapse and result in more smooth and spherical particles. On the contrary, with a less TBP addition, the solvent evaporation can be so fast that a crust forms in an early stage. After complete solvent evaporation, a larger void-to-crust volume ratio is possible. Such a relatively larger void volume will force the particle to have a higher degree of structural collapse and the formation of a more wrinkled surface. Of course, further studies are necessary to validate this hypothesis.

Table 2.3 Comparison of the boiling point of reactants

Chemical	Boiling point (°C) [a]
n-Butyl phosphate (Alfa Aesar)	~124
Calcium methoxyethoxide (ABCR, 20% in methoxyethanol)	118
2-Methoxyethanol (Sigma Aldrich, 99.9%)	124-125
Tri-butyl phosphate (Sigma Aldrich, 99%)	289

[a] Data provided by corresponding manufacturers

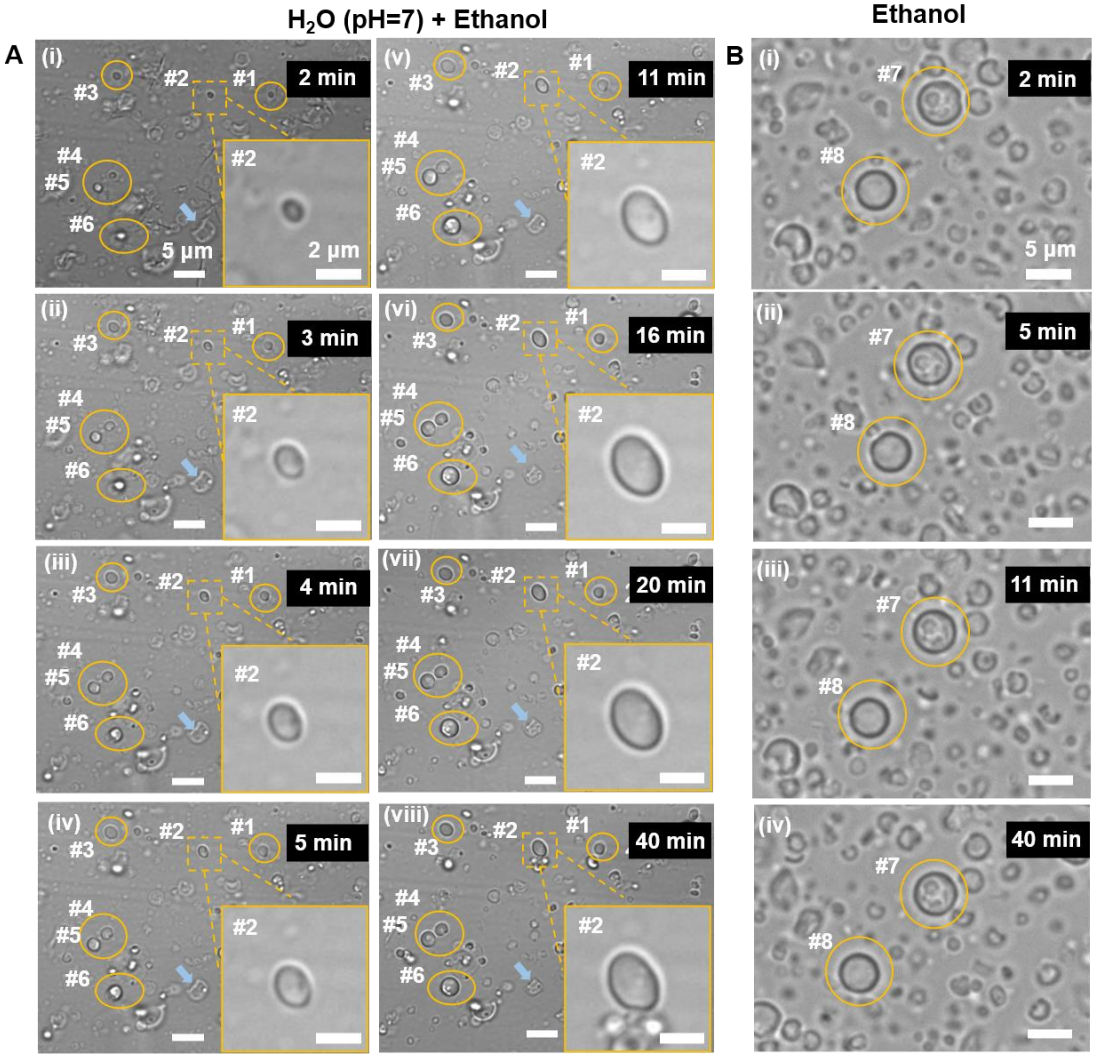

Figure 2.6 Optical microscopy images showing the size evolution of CPPs (CPPs-4).

(A) in H_2O (pH=7) + ethanol (Inset: high magnification images of particle #2) and (B) pure ethanol over time. CPPs expansion was observed in in the presence of H_2O but not in pure ethanol. The light blue arrow indicates a particle that shrinks over time, which may be attributed to the existence of internal voids. Scale bar: 5 μm for low magnification images and 2 μm for high magnification images.

2.4.4. Hydro-expansion and Degradation of CPPs

Bulk phosphate glasses have been known for their good bio-degradability. Here, the dissolution behavior of CPPs was investigated using an inverted optical microscope. Briefly, CPPs in ethanol solution was dropped to a 35 mm glass-bottom dish and then DI water (pH= 7) was

added to the dish to initiate the hydration. 2 minutes of waiting time was taken to allow particles to settle down and stabilize on the bottom of the dish. An interesting hydro-expansion behavior was observed for CPPs (Figure 2.6 (A)). Such dissolution/expansion behaviors were not observed in pure ethanol solution (Figure 2.6 (B)), indicating that the dissolution/expansion of CPPs is associated with the interaction between CPPs and water. Note that some particles only shrank even when pH=7 (highlighted by the blue arrow, Figure 2.6). This may be due to the void nature of some CPPs.

As an example of quantitative analysis, the average diameter of particles (CPPs-4) numbered in Figure 2.6 during the hydration process at pH=7 and pure ethanol was measured using Image-Pro Plus 6 software. The evolution of the diameter, relative diameter change ($(D-D_0)/D_0\%$), and relative volume change ($(V-V_0)/V_0\%$) over time is shown in Figure 2.7 (A) clearly shows that no size change occurred for CPPs in pure ethanol (#7 and #8). As for CPPs in the presence of neutral H_2O (#1-#7), an initial "burst" increase of diameter within the first 5 min was observed. After that, the diameter change reaches a plateau. The maximum relative diameter change varies from ~ 48% (particle #5, Figure 2.6 (B)) to ~173% (particle #2, Figure 2.6 (B)). Similarly, the relative volume change varies from ~ 230% (particle #5, Figure 2.6 (C)) to ~1950% (particle #2, Figure 2.6 (C)). The number-weighted average values for the maximum $(D-D_0)/D_0$ % and $(V-V_0)/V_0$ % are 95% and 720% respectively. The actual relative diameter change and volume change should be more than 95% and 720% because the diameter and volume at t=2 min were

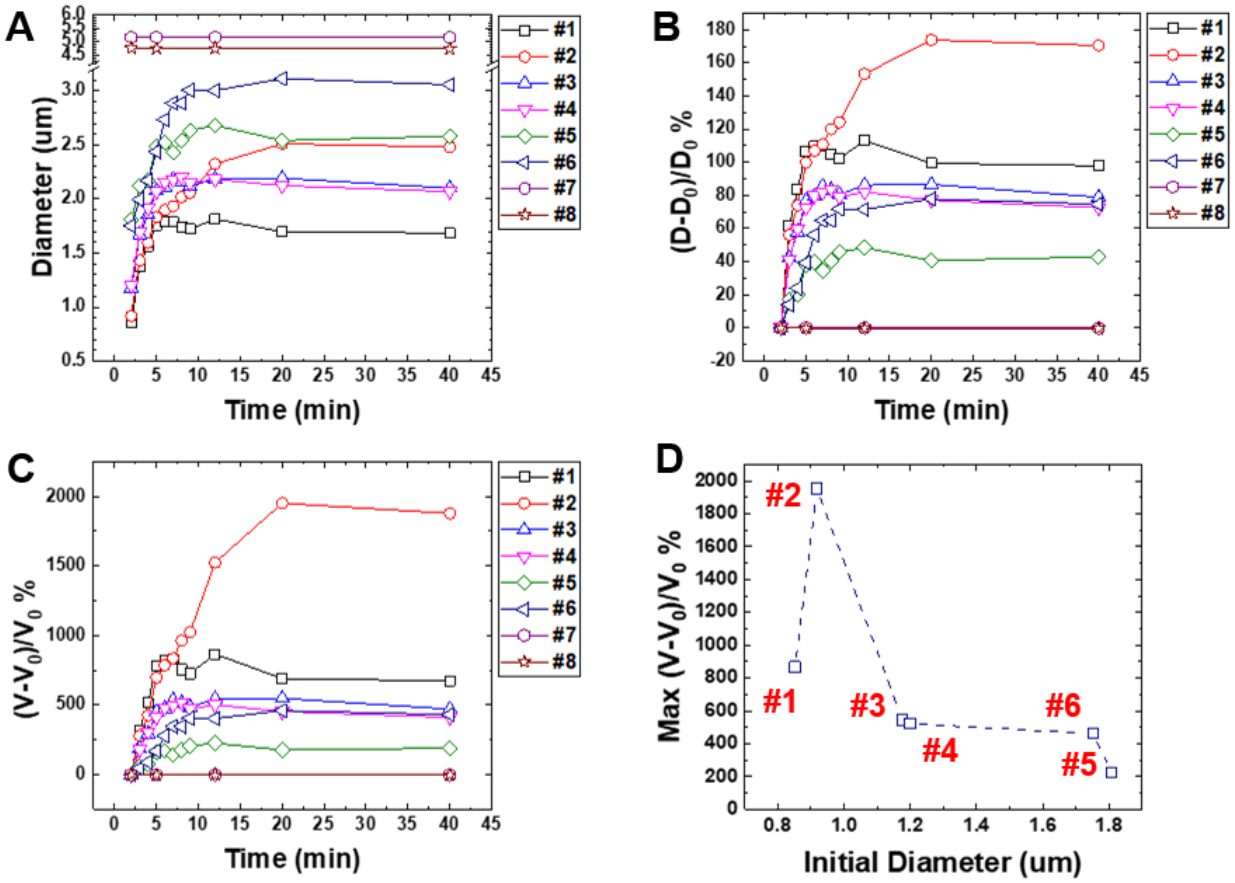

Figure 2.7 Quantification of the hydro-expansion of CPPs over time based on image analysis of optical microscopy images.

(A) Diameter versus time. (B) The change in relative diameter versus time. (C) Relative volume change versus time. (D) Maximum relative volume change versus initial diameter. For the calculation of relative diameter and volume changes, diameter and volume values at t=2 min were used as D_0 and V_0 and an ideal spherical shape was assumed. There was an initial burst increase of diameter within the first 5 min. The number average of the maximum $(D-D_0)/D_0$ % and $(V-V_0)/V_0$ % is 95% and 720% respectively. The maximum relative volume change decreases with increasing initial particle size.

used as the initial values in our calculation. Figure 2.7 (D) shows that the maximum relative volume change tends to decrease with the increase of the initial particle size. This could be a result of the difference in the surface-to-volume ratio of particles. The relative volume change of CPPs caused by the hydration is comparable with that of some polymer particles reported in the literature, e.g., 330% for chitosan microparticles,[268] 200% for P(St-co-DMAEMA) nanoparticles,[269] 230% for PLGA microparticles, [270] and 800% for gelatin nanoparticles.[271] SEM

images of CPPs hydrated at pH=7 and then dried at 100 ℃ (Figure 2.12) shows that the hydration process significantly altered the morphology of CPPs. For example, the wrinkled surface of CPP-9 became smooth. In some cases (CPP-10 and CPP-4), steps/facets typically observed in crystal materials appeared. We hypothesize that the observed hydro-expansion behavior may be attributed to chemical reactions between water and CPPs to form new calcium phosphate phase (s) that has (have) a larger volume. A more systematic study combining microscopy, FTIR, TGA, and XRD will be carried out in the future to verify the actual mechanism for the hydro-expansion.

The degradation of bulk phosphate-based glasses is known to release component ions. To monitor the ion release of CPPs, a dynamic dissolution experiment was carried out by using a home-made flow cell design. This flow cell is configured from a syringe and syringe filter. It allows for the deposition of CPPs on a syringe filter membrane and a continuous flow of Millipore water through the membrane. The liquid samples were collected at the desired time points for ICP-MS analysis. Figure 2.8 (A) shows the cumulative release of P and Ca ions expressed as molar. The ion release curve of both P and Ca can be divided into a non-linear region (t= 0-2h) and a linear region (t= 2- 8h). The non-linear region is featured with an initial burst release of ions, which is consistent with the observed initial burst increase of size (Figure 2.7). As a control experiment, Millipore water was running through a blank flow cell (without particles) and analyzed with ICP-MS (P-blank and Ca blank, Figure 2.8 (A)). As expected, no ion release was observed in the control experiment indicating no measurement error caused by the contamination from the flow cell. The calculated cumulative particle dissolution (Figure 2.8 (B)) shows that ~0.54 mg or 38% of the initial CPPs were dissolved after 8h. Interestingly, as shown in Figure 2.8 (C), the molar ratio of P/Ca released to water decreases in the first hour of dissolution. It then increases between 1 h and

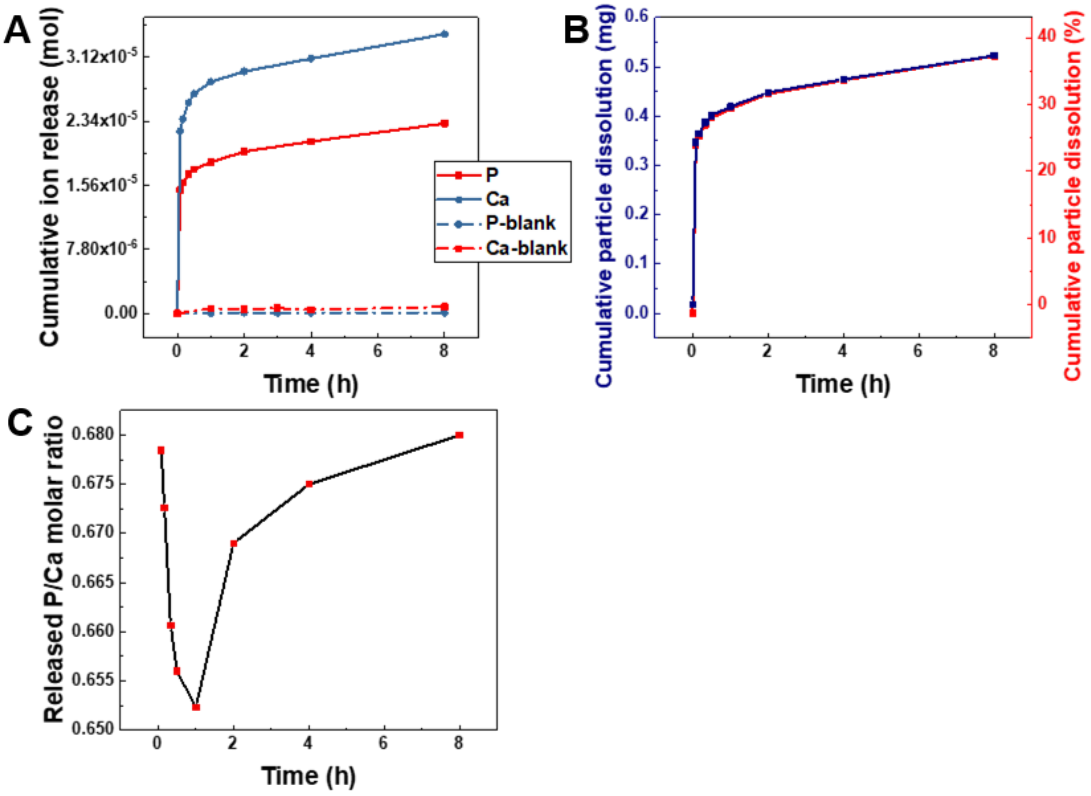

Figure 2.8 Dissolution of CPP-4 monitored with ICP-MS.

(A) Cumulative ion release of P and Ca ions versus time showing an initial burst release of P and Ca ions in the first hour and a linear release starting from the second hour. P-blank and Ca-blank curves were created from DI water running through a flow cell without particles. (B) Cumulative particle dissolution in weight (blue) and weight percentage relative to initial particles (red) over time calculated based on cumulative ion release. (C) Released P/Ca molar ratio versus time. The released P/Ca molar ratio decreases in the first hour and then increases.

8h. This subtle variance of P/Ca molar ratio over time may be attributed to the dissolution mechanism of CPPs. The dissolution of phosphate-based glasses can either be governed by the hydrolysis of the P-O bond of the P-O-P unit or the hydration of the Ca-O bond of the P-O-Ca unit. If the dissolution is governed by the hydrolysis of the P-O bond, each basic phosphate unit containing calcium will be released intactly. In other words, one will expect a constant P/Ca molar ratio detected from water over time. On the contrary, a changing P/Ca molar ratio was observed, indicating that the hydration of the Ca-O bond of the P-O-Ca unit is a more likely mechanism for the dissolution of CPPs. This is consistent with findings from previous research: the rate of

hydrolysis of P-O-P bonds is significantly slower than the rate of hydration of the entire phosphate anion[272] and, as a result, phosphate anions can be separated intactly from their accompanying metal cations.[273]

2.5. CONCLUSION

The preparation of calcium phosphate micro/nano- particles, $(P_2O_5)_{25}$-$(CaO)_{75}$, via the combined sol-gel and electrospray method was studied in detail. It was found that the flowrate has a significant effect on the size of CPPs, while the working distance and voltage of the emitter in the tested range do not. We also found that the surface smoothness of CPPs was improved with increasing tri-butyl phosphate concentration in the sol solution. This knowledge enabled us to prepare CPPs with an average diameter in the range of 345 to 952 nm and various shapes including carnation flower, golf-ball, and apple-like. Interestingly, a hydro-expansion behavior of CPPs in aqueous solutions of pH=7 was discovered with optical microscopy. Specifically, CPPs can have a more than 95% increase in diameter and a 720% increase in volume within the first 5-10 min of hydration in a neutral aqueous media. Such a hydro-expansion process is accompanied by a two-stage ion release of phosphorous and calcium.

2.6. ACKNOWLEDGEMENTS

Chapter 2, in full, is a reprint of the material as it appears in "He, T.; Bradley, D. G.; Zhou, J.; Jorns, A.; Mantri, Y.; Hanna, J. V.; Jokerst, J. V., Hydro-Expandable Calcium Phosphate Micro/Nano-Particles with Controllable Size and Morphology for Mechanical Ablation. *ACS Applied Nano Materials* **2021,** *4* (4), 3877-3886." The dissertation author was the primary investigator and author of this paper.

2.7. SUPPLEMENTARY INFORMATION

Table 2.4 Summary of synthetic parameters and size distribution measured by DLS

Sample ID	NBP (mL)	CME (mL)	2-ME (mL)	TBP		Flowrate (mL/h)	Emitter voltage (kV)	Ring voltage (kV)	H_1 (cm)	H_2 (cm)	Z-Ave (nm)	PDI	Peak 1			Peak 2		
				(mL)	(vol%)								Size (nm)	% Intensity	Std. Dev. (nm)	Size (nm)	% Intensity	Std. Dev. (nm)
CPP-1	1.3	11.6	1.88	3.3	18.3	0.05	32.5	30	0.5	10	345.5	0.23	329.7	97.9	82.49	5174	2.1	488.1
CPP-2	1.3	11.6	1.88	3.3	18.3	0.1	32.5	30	0.5	10	422.8	0.30	387.4	91.8	124.2	4807	8.2	764.4
CPP-3*	1.3	11.6	1.88	3.3	18.3	0.4	32.5	30	0.5	10	952.3	0.56	1271	75.4	509.3	5201	6.9	474.9
CPP-4	1.3	11.6	1.88	3.3	18.3	0.2	32.5	30	0.5	10	577.7	0.26	634.6	95.9	311.8	4360	4.1	1028
CPP-5	1.3	11.6	1.88	3.3	18.3	0.2	14.5	12	0.5	4	633.4	0.38	543.2	96.6	157.1	5524	3.4	290.6
CPP-6	1.3	11.6	1.88	3.3	18.3	0.2	15.5	12	0.5	4	641.7	0.24	599.6	98.4	158.9	5449	1.6	268.1
CPP-7	1.3	11.6	1.88	3.3	18.3	0.2	16.5	12	0.5	4	686.9	0.30	606.8	93.2	164.2	4787	6.8	731.3
CPP-8	1.3	11.6	1.88	3.3	18.3	0.2	23.5	21	0.5	7	643	0.42	567.7	97.0	182.1	5447	3.0	269.5
CPP-9	1.3	11.6	1.88	0	0	0.2	32.5	30	0.5	10	563.4	0.24	557.7	99.5	186.2	5208	0.5	469.6
CPP-10	1.3	11.6	1.88	0.7	4.3	0.2	32.5	30	0.5	10	558	0.18	600.2	98.6	212.6	5208	1.4	469.6
CPP-11	1.3	11.6	1.88	2	11.8	0.2	32.5	30	0.5	10	556.2	0.26	559.1	91.1	229.4	4022	8.9	1201
CPP-12	1.3	11.6	1.88	2	21.2	0.2	32.5	30	0.5	10	605.4	0.16	651.7	99.3	229.8	5221	0.7	461.8
CPP-13	1.3	11.6	1.88	2	28.7	0.2	32.5	30	0.5	10	570.1	0.28	574.8	85.9	269.6	3733	14.1	1159
CPP-14	1.3	11.6	1.88	2	34.9	0.2	32.5	30	0.5	10	633.9	0.20	652	97.9	209.9	5232	2.1	452.1

*** Peak 3 information for CPP-3:** Size: 288.5 nm; % Intensity: 17.8; Std. Dev.: 92.26 nm.

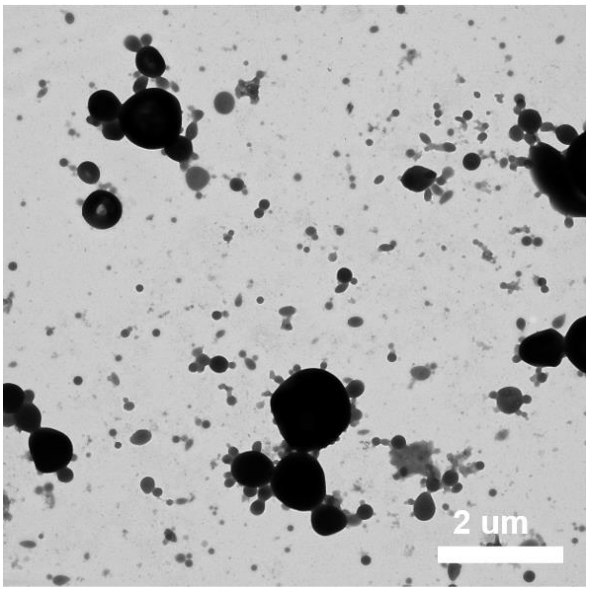

Figure 2.9 TEM image for CPP-3.

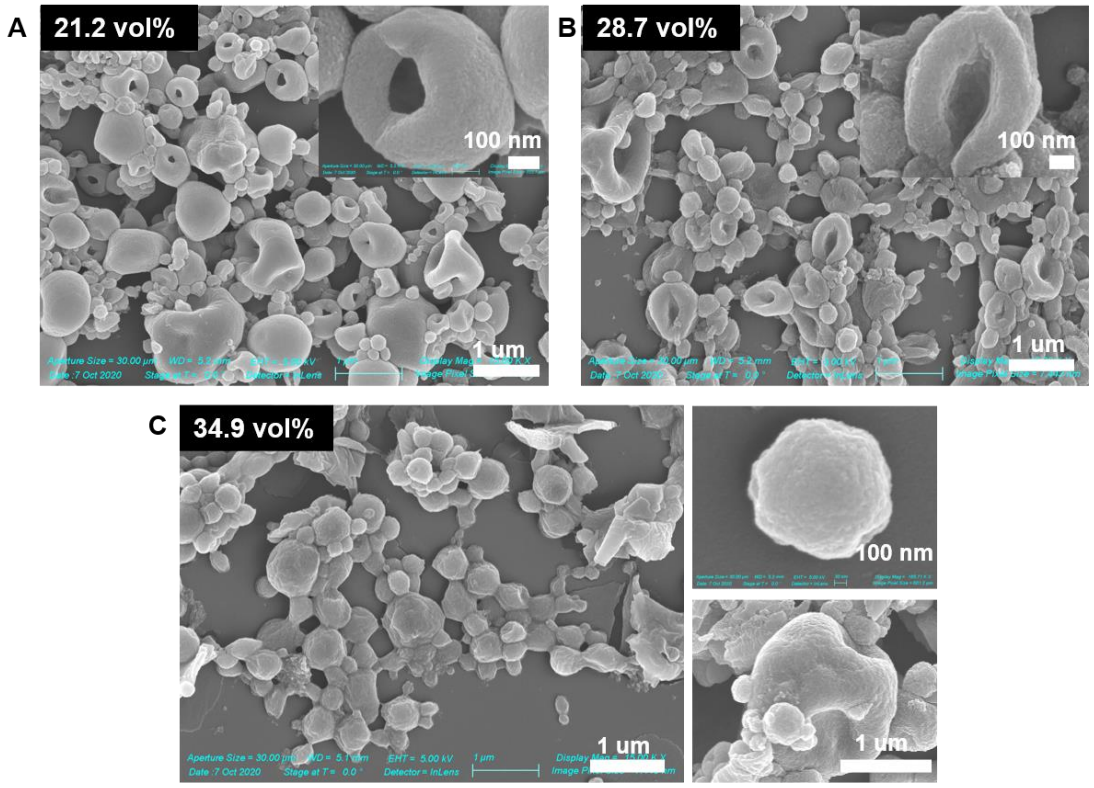

Figure 2.10 SEM images showing the evolution of the morphology of CPPs with the increase of tri-butyl phosphate (TBP) addition in the sol solution.

(A) 21.2 vol% (CPP-12), (B) 28.7 vol% (CPP-13), to (C) 34.9 vol% (CPP-14). Insets: higher magnification images of representative particles. Increase of TBP concentration to 34.9 vol% can further reduce the surface dents and wrinkles for nanoparticles. However, microparticles still maintain these wrinkles and dents in this condition.

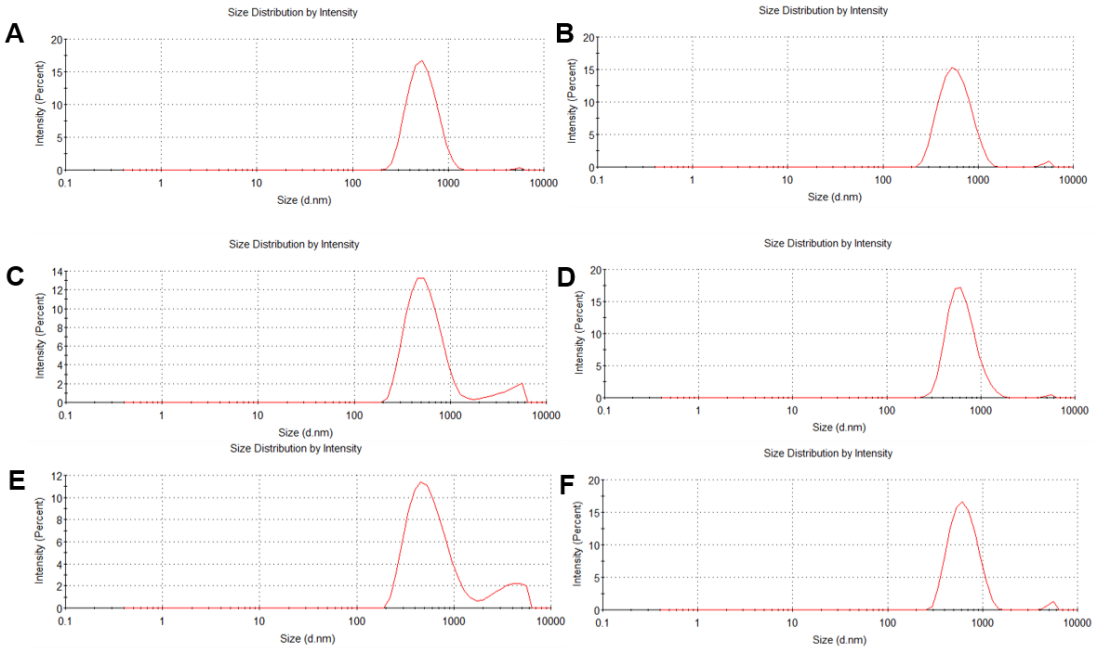

Figure 2.11 Intensity-based DLS size distribution.

(A) CPP-9, (B) CPP-10, (C) CPP-11, (D) CPP-12, (E) CPP-13, and (F) CPP-14.

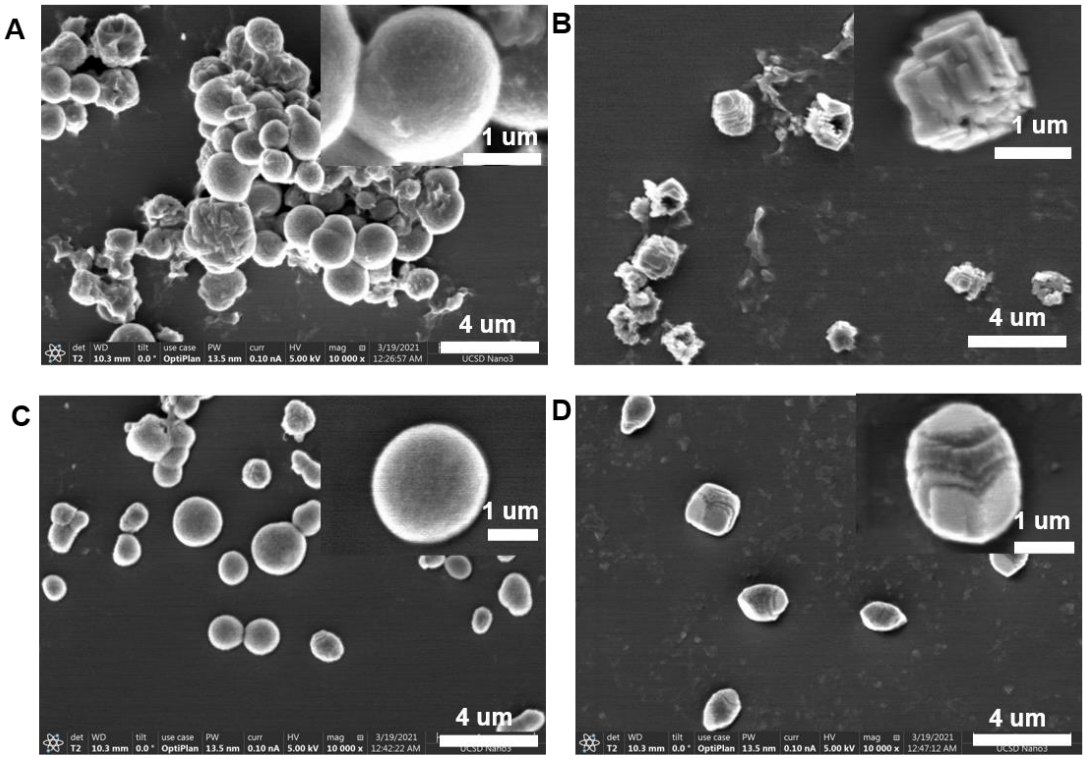

Figure 2.12 SEM images of particles hydrated at pH=7 and then dried at 100 ℃.

(A) CPP-9, (B) CPP-10, (C) CPP-11, and (D) CPP-4. The hydration process significantly altered the morphology of CPPs, e.g., the wrinkled surface of CPP-9 became smooth; steps typically observed in crystals appeared in CPP-10 and CPP-4.

CHAPTER 3. BIO-INSPIRED SYNTHESIS OF DEGRADABLE POLYETHYLENIMINE/CALCIUM PHOSPHATE MICRO-/NANO COMPOSITES FOR TRANSIENT ULTRASOUND IMAGING

3.1. ABSTRACT

Inorganic nanomaterials hold immense potential in theranostics but their translation is limited by the toxicity resulting from non-degradability. Bulk phosphate-based glasses offer great biodegradability, biocompatibility, and easiness in incorporating imaging dyes and drugs. However, the facile and mild solution-based synthesis of micro-/nano particles of this material is yet to be explored. Inspired by the biosilicification process in the diatom, we created PEI/phosphate aggregates via the hydrogen bonding between amine (PEI) and hydroxyl (phosphate) groups, which was proved by dynamic light scattering and ^{1}H nuclear magnetic resonance. The sol-gel reaction between the calcium precursor and PEI/phosphate aggregates yielded degradable polyethylenimine/calcium phosphate (PEI/CP) micro-/nano composites with versatile sizes (396±128 nm to 63±8 μm) and morphologies (hexagonal micro-disc, micro-flower, micro-leaf, nano-butterfly, and nano-ribbon). PEI/CPs composition and chemical structure were examined. PEI/CPs have negligible cell cytotoxicity and degrade within 24 h. In vitro studies showed the promise of PEI/CP in transient ultrasound and photoluminescence imaging.

3.2. INTRODUCTION

Inorganic nanomaterials hold immense potential in theranostics.[274-284] Specific for bioimaging, inorganic nanomaterials have the advantage of controllable size, chemically functionalizable surfaces, and unique physical properties creating imaging signals. For example, gold nanoparticles are a versatile imaging agent for photoacoustic imaging owing to surface plasmon resonance.[274] Semiconducting quantum dots have tunable emission spectra, photostability, and high efficiency ideal for fluorescent imaging.[285-287] Superparamagnetic iron oxide nanoparticles are good contrast agents for magnetic resonance imaging (MRI).[288-289] Silica nanoparticles have a high acoustic impedance mismatch and can improve ultrasound imaging.[11] Despite these successes, one major limitation of most inorganic nanomaterials is without/slow biodegradability and high toxicity resulted from the long-term retention.[290-294] Therefore, biodegradation into non-toxic and renal clearable components is an ideal property for theranostic nanomaterials.[295-300]

Metal oxide-doped phosphate (MODP) is an emerging class of biomaterial. MODP can be crystalline or non-crystalline. Crystalline MODP nanomaterials, e.g. calcium phosphate (CP) nanocrystals, can be easily prepared from the controlled precipitation of metal ions (e.g. Ca^{2+}) and $H(PO_4)^{2-}$ ions and show promising biomedical applications, e.g. gene delivery to breast cancer with fluorescent imaging.[301-303] However, these CP nanocrystals are not degradable at the physiological pH (~ 7.3), making them still suffer from the long-term retention problem when applied at the physiological pH. Even though they can degrade at more acidic conditions (pH <6), i.e. within the endosome/lysosome (pH 6-4.5), the resulted over-concentrated ions within the cell can trigger the cell necrosis.[303] On the other hand, amorphous MODP, or phosphate-based glasses, are known for excellent biodegradability and biocompatibility at both the physiological and acidic

pH values.[219] This degradability is a result of their amorphous structure: the terminal oxygen in the PO_4^{3-} tetrahedron reduces the connectivity of the phosphate network. After degradation, they release ions routinely found in the human body (e.g., PO_4^{3-}, Ca^{2+}, and Na^{+}).[53] Finally, phosphate glasses can be facilely functionalized by incorporating imaging dyes[10] and drugs[54, 57]. However, an obstacle to the wide theranostic application of phosphate glasses is the lack of facile, mild, and solution-based methods for preparing this material into monodispersed particles with controllable sizes. Ideally, the size should be tunable from nanometers to microns for customized theranostic tasks. Take ultrasound imaging as an example, the pore size of tumor endothelium constrains the size of contrast agents to less than 380 nm for tumor targeting;[16] Cell labelling requires the contrasts to be sufficiently small for efficient cell uptake.[11] While for the vascular imaging, contrasts of several microns (comparable to blood cells, e.g. microbubbles) are more suitable considering stronger echogenicity.[304-305] Phosphate glass particles (PGP) of 200 nm -3 μm have been prepared via sol-gel combined with electrospray.[10, 306-307] These PGPs show strong echogenicity effective in in-vivo ultrasound imaging and easiness in incorporating dyes for fluorescence imaging. Moreover, their biodegradability and biocompatibility circumvent the long-term toxicity issue.[10] However, this synthetic approach is limited by sophisticated instrumentation, risk of electric shock (20-30 kV), and high temperature (180 °C) incompatible with temperature-sensitive drugs, peptides, and proteins.[306-307]

One may learn from biosilicification in nature to design a solution-based method for preparing phosphate glass micro-/nano particles. Diatoms are unicellular photosynthetic organisms known for the sophisticated design of their silica-based cell walls via biosilicification process.[278, 308-310] In this process, silicic acids are attracted and templated by amine-rich polypeptides (silaffins) or long-chain polyamines via hydrogen bonding between the hydroxyl and amine groups. The

templated silicic acid further poly-condensates to form biosilica.[308, 310] We hypothesized that a similar interaction could happen between phosphate precursors and synthetic polyamines (e.g. polyethylenimine (PEI)), which may be exploited to produce phosphate micro-/nano particles.

Here, we report, for the first time, the synthesis of biodegradable PEI/calcium phosphate (PEI/CP) micro-/nano composites via the biomimetic route for transient ultrasound and photoluminescence imaging. Inspired by the bio-silicification process of diatoms, we applied PEI to template phosphate esters in solution and eventually produced PEI/CP particles with controllable size and morphology at a mild temperature range (25-90 °C). The interaction between phosphate precursors and PEI was systematically studied by dynamic light scattering (DLS) and ^{1}H nuclear magnetic resonance (NMR), confirming the formation of PEI/phosphate aggregates referred to as "phosphate sponges". These phosphate sponges act as nuclei and mediate the growth of PEI/CP particles. The size, morphology, composition, and chemical structure were characterized using DLS, scanning electron microscopy (SEM), transmission electron microscopy (TEM), optical microscopy, inductively coupled plasma mass spectroscopy (ICP-MS), energy-dispersive X-ray spectroscopy (EDX), Fourier transform infrared spectroscopy (FTIR), X-ray diffraction (XRD), and solid-state ^{31}P and ^{1}H magic angle spinning nuclear magnetic resonance (MAS NMR). Lastly, their biodegradability, cell cytotoxicity, and promise for transient ultrasound and photoluminescence imaging were validated.

3.3. MATERIALS AND METHOD

3.3.1. Materials

Ethanol (200 proof, Koptec) and phosphate buffered saline (PBS, x1, Corning) were purchased from VWR. Tri-n-butyl phosphate (TBP, 98%) and branched polyethylenimine (b-PEI, 1.8k MW) were purchased from Alfa Aesar. n-Butyl phosphate (NBP, a 1:1 mixture of mono-n-butyl and di-n-butyl) were purchased from Thermo Scientific. Dibutyl phosphate (DBP, 97.0%), branched polyethylenimine (b-PEI, 25k and 800 MW), chloroform-d ($CDCl_3$, 99.8 atom %D), and resazurin were purchased from Sigma-Aldrich. Calcium methoxyethoxide (CME, 20% in methoxyethanol) was purchased from ABCR Chemical. Ultrapure Agarose (Invitrogen) was purchased from Fisher Scientific.

3.3.2. Synthesis of PEI/CPs

Ethanol was used instead of water to avoid the uncontrollable hydrolysis of CME.[52, 219] Branched PEI (MW 1.8 k or 25k) was dissolved in ethanol to make a $1x10^{-5}$ mol/mL PEI stock solution. An appropriate amount of PEI stock solution was then diluted by extra ethanol to make a desired final PEI concentration. Under magnetic stirring at 500 rpm, NBP was added to the diluted PEI in ethanol. After stirring at room temperature for 1 h, CME was added, and the solution allowed for another 1 h stirring at room temperature. Then, the well mixed solution was incubated at a raised temperature with or without magnetic stirring for a certain reaction time. All detailed parameters including reagents addition, stir speed, temperature, and reaction time can be found in Table 3.1. As-prepared particles were purified by repeating centrifugation (5000 rpm, 20 min) and ethanol wash for 3 times.

3.3.3. ^{1}H NMR and DLS Study of the Interaction between PEI and Phosphate Esters

The interaction between PEI and phosphate esters was studied with the combination of liquid state ^{1}H NMR and DLS. PEI (25k MW) was first dissolved in either $CDCl_3$ (for liquid state

^{1}H NMR) or ethanol (DLS) to make 1mM PEI solutions. Then an appropriate amount of phosphate precursors (TBP, NBP, or DBP) were mixed with the PEI solution to make desired phosphate:b-PEI molar ratios. ^{1}H NMR spectra were recorded on a Bruker 300 MHz spectrometer and all chemical shifts are referenced to the reported literature[311] ($CDCl_3$: 7.26 ppm). DLS measurements were performed on a Malvern NANO-ZS90 Zetasizer to determine hydrodynamic sizes of PEI/phosphate ester aggregates.

3.3.4. Morphology and Size of PEI/CPs Particles

SEM images were obtained using Zeiss Sigma 500 operated at 5 kV with a 30-μm aperture and 10 mm working distance. Particles in ethanol were drop-coated on a silicon substrate (Ted Pella Inc.), dried at room temperature, and sputter-coated with gold alloys before SEM. TEM images and EDX mapping were acquired using an FEI Tecnai F20 instrument at an operation voltage of 200 kV. Particles in ethanol were drop-coated on a copper TEM grid and ethanol was evaporated naturally at room temperature before TEM imaging.

Keyence fluorescent microscope was used for observations of microparticles either in bright field mode or fluorescence mode (DAPI channel, excitation 358 nm). For characterizing the morphology, ethanol was used as the solvent. To monitor the particle degradation, particles were deposited in a flow cell[312] and PBS was flowed at 1.2 mL/min to simulate the human blood flow. See Figure 3.24 for details of the flow cell design. DLS measurements were performed on a Malvern NANO-ZS90 Zetasizer to determine hydrodynamic sizes of both PEI/phosphate ester aggregates and PEI/CP particles (<1.5 μm) dissolved in ethanol. The size distribution of PEI/CP particles larger than 1.5 μm was determined by image analysis over 500 particles using Image-Pro Plus software based on optical microscopy images.

3.3.5. Spectral Studies of the PEI/CPs Particles

PEI/CPs in ethanol were dried under vacuum at room temperature and used for spectral studies. **FTIR** spectroscopy was performed on a Perkin Elmer Spectrum Two FTIR Spectrometer. **XRD** was performed on Rigaku MiniFlex with Cu Kα radiation (λ = 1.5406 Å). **Solid state ^{31}P and ^{1}H MAS NMR.** All ^{31}P MAS NMR measurements were performed at 9.4 T using a Bruker 400 MHz Avance III HD spectrometer operating at Larmor frequency of 161.9 MHz (400 MHz for ^{1}H). Samples were loaded under a N_2 atmosphere into Bruker 3.2 mm rotors and spun at a magic angle spinning (MAS) frequency of 15 kHz. Each spectrum was acquired at room temperature by direct excitation (single pulse) methods employing π/4 pulses of length 2 μs and 80 kHz of ^{1}H decoupling which was applied during data (FID) acquisition. To ensure quantitative results a recycle delay of 300 s was used which were checked against tests of longer recycle delays. All data were referenced against the IUPAC recommended primary reference of 85% H_3PO_4 (δiso= 0.0 ppm), via a secondary solid reference of ammonia dihydrogen phosphate ($(NH_3)H_2PO_4$ or ADP) (δiso = 0.99 ppm). The corresponding ^{1}H MAS NMR room temperature measurements were undertaken at 16.4 T using a Bruker 700 MHz Avance III HD spectrometer operating at a Larmor frequency of 700.13 MHz. All samples were packed under a N_2 atmosphere into Bruker 1.3 mm rotors and spun at a MAS frequency of 60 kHz. To obtain quantitative spectra, direct excitation (single pulse) methods using π/4 pulses of length 1.25 μs were used in conjunction with a recycle delay of 10 s. All data were referenced against the IUPAC recommended primary reference of tetramethylsilane ($(CH_3)_4Si$ or TMS) (δiso= 0.0 ppm), via a secondary solid reference using the methyl (CH_3) group resonance from alanine (δiso = 1.1 ppm). The acquisition and processing of all SSNMR data was performed using the Bruker TopSpin software package, while deconvolution of spectra was performed using DMFit. Photoluminescence emission measurements were performed on an BioTek Synergy H1 microplate reader.

3.3.6. ICP-MS Measurements

ICP-MS measurements were carried out using iCAP RQ, Thermo Scientific. For ICP-MS analysis of particles' composition, overnight digestion of particles was carried out by adding 571 µL 70% Nitric acid to 0.01 mg dried particles in a glass vial. This solution was transferred to a 15mL plastic centrifugation tube and Millipore water was added to make a final solution of 10 mL. For ICP-MS analysis of particles' ion releases, 0.1 mL of 10 mg/mL particle in ethanol was deposited on a syringe filter (Millex-GP, 220 nm). Millipore water (pH 7.30) was continuously pumped (1.2 mL/h) through the particle-loaded syringe filter. The solution was collected at the time points of 0, 5, 10, 30, 60, 120, 240, 480, and 1440 min. Collected solutions were diluted 100 times with 4% HNO3 and measured by ICP-MS.

3.3.7. In vitro Ultrasound Imaging

Ultrasound images were captured with Verasonics, Vantage 256 system performed at 40 V with a L22-14vX transducer (18 MHz, 3k PRF, 6 pulse cycle, ~30% bandwidth, 128 elements, and 0.10 mm pitch). Ethanol solutions of PEI/CP-3 (34 ± 3 µm), PEI/CP-31 (7.8 ± 2.7 µm), PEI/CP-32 (4.8 ± 1.4 µm), and PEI/CP-18 (546 ± 131 nm) from 0 to 10 mg/mL were loaded into a 1.5 mL plastic centrifuge tube. The tube was immersed in a water bath and B-mode ultrasound images were acquired. To determine the ultrasound intensity decay during the particle dissolution, PEI/CP-3 (34 µm) and PEI/CP-31 (7.8 µm) were dispersed in 1:1 ethanol and PBS buffer solution with a final concentration of 2.5 mg/mL were used. The ultrasound intensity was then quantified by measuring the average RGB value of the same area of interest using Image J. For Doppler imaging, 10 mg/mL PEI/CP-31 (7.8 µm) in ethanol solution was pumped through a channel inside an agarose phantom (2 wt%) with a peristaltic pump. The average red value inside an area of interest was measured using Image J to quantify the power Doppler intensity.

3.3.8. Cell Cytotoxicity

The cytotoxicity of materials (pure PEI-1.8k, pure PEI-25k, fresh PEI/CP-5 and -15, and PEI/CP-5 and -15 degraded for 24 hours in PBS) were studied on both HEK 293T and HeLa cells using resazurin assay. 0.1 mL cell solution (200000 count/mL in DMEM with 10% FBS and 1% PS) were loaded to a 96-well plate and incubated for 24 hours (5% CO^2 at 37 °C). 0.01 mL materials in PBS buffer were added to wells containing cells in DMEM to make the final equivalent PEI concentration in the well in the range from 0 to 1 mg/mL. After materials addition, the cells were incubated for another 24 hours (5% CO^2 at 37 °C). 0.01 mL resazurin was then added to each well. After incubation for another 2 hours, the fluorescence was read. A well with only DMEM and resazurin dyes and another well with only cells, DMEM, and resazurin dyes were also prepared following the same volume and incubation condition. In the case of PEI/CP particles, the equivalent PEI concentration is defined as the resulting PEI concentration assuming a complete dissolution of PEI/CP particles. Therefore, to achieve the equivalent PEI concentration, higher PEI/CP mass concentration was used than pure PEI. The cell viability was calculated as follows:

$$\text{Cell viability} = \frac{\mathrm{FL}_{\mathrm{material}} - \mathrm{FL}_{\mathrm{empty}}}{\mathrm{FL}_{\mathrm{cell}} - \mathrm{FL}_{\mathrm{empty}}} \times 100\%$$

$FL_{material}$: fluorescence intensity read from the well with cells, DMEM, resazurin dyes, and materials (PEI-1.8k, PEI-25k, fresh PEI/CPs, or PEI/CPs degraded for 24 hours);

FL_{empty}: fluorescence intensity read from the well with only DMEM and resazurin dyes;

FL_{cell}: fluorescence intensity read from the well with only cells, DMEM, and resazurin dyes.

3.4. RESULTS AND DISCUSSION

3.4.1. Synthetic Strategy and Mechanism

We hypothesized that the hydroxyl-amine hydrogen bonding between silicic acid and polyamines found in diatom[308-309] could also form between the phosphate precursor and synthetic PEI. This interaction may result in templated phosphate precursor and be exploited to produce structured PEI/CP micro-/nano composites (Figure 3.1(A)). Besides, these PEI/CPs may be degradable in the aqueous environment and used as transient ultrasound and photoluminescence imaging agents.

The synthesis (Figure 3.1 (B)) simply added n-butyl phosphate (NBP) and calcium methoxyethoxide (CME) stepwise to branched PEI in ethanol. Ethanol was used instead of water to avoid the uncontrollable hydrolysis of CME.[52, 219] Then, the sol-gel reaction between NBP and CME was allowed at the controlled stirring rate (0-500 rpm), temperature (25-90 °C), and time (1-18.5 h) (see Materials and Method and Table 3.1 for detailed parameters). NBP was chosen as the phosphate precursor because of its well-known reactivity with CME.[219] Mixing PEI and NBP may form PEI/NBP aggregates with reactive NBP on the surface via the hydrogen bonding between the hydroxyl group (NBP) and amine group (PEI) (Figure 3.1 B(ii)). We term these aggregates as "phosphate sponge" in analogy to the well-known "proton sponge".[313] Upon the addition of CME (Figure 3.1 B(iii)), it may react with NBP on phosphate sponges' surface (via hydrolysis and polycondensation) to form PEI/CP micro-/nano composites (Figure 3.1 B(iv)).

To verify the as-proposed phosphate sponge mechanism, the interaction between phosphate esters and branched PEI of 25k MW was studied using dynamic light scattering (DLS) (Figure 3.2 (A) and S1) and ^{1}H nuclear magnetic resonance (NMR) (Figure 3.2 (B-D) and S2). Tri-butyl phosphate (TBP), di-butyl phosphate (DBP), and NBP are phosphate esters with 0, 1,

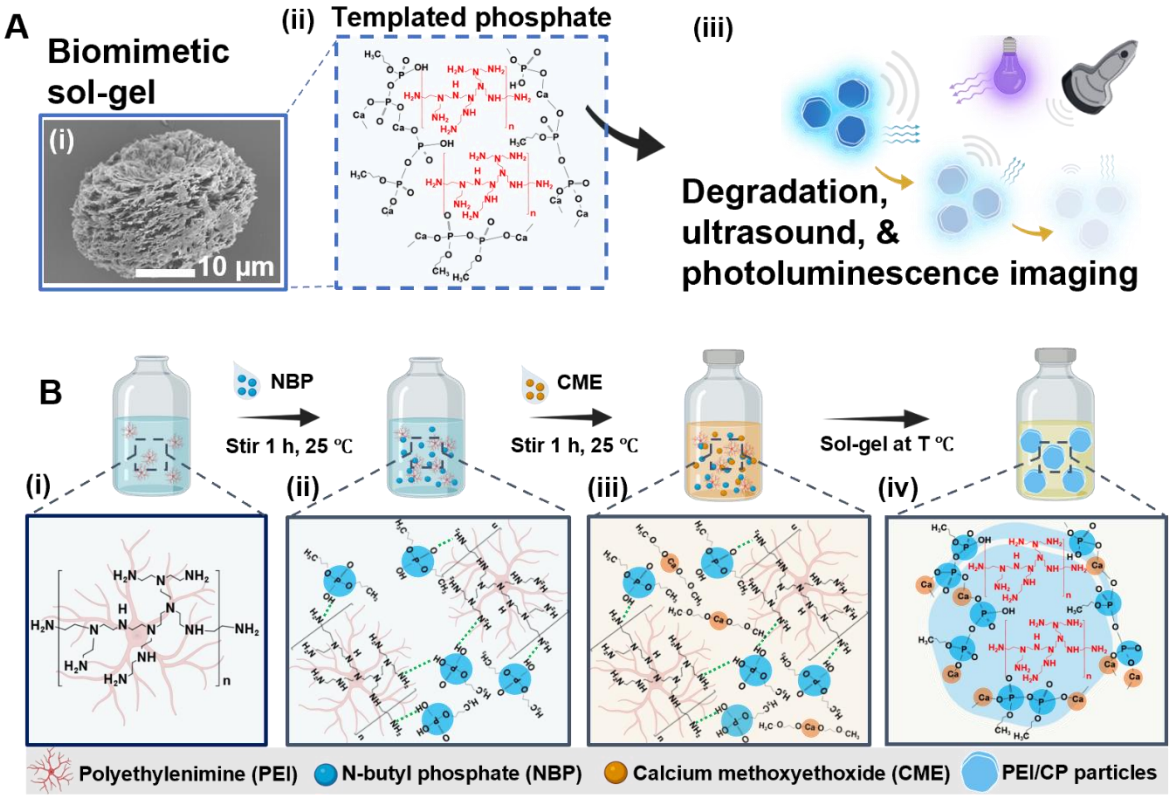

Figure 3.1 Diatom-inspired synthesis of PEI/CPs for transient ultrasound and photoluminescence imaging.

A(i) Scheme showing that mimicking the biosilicification, phosphate precursors can also be templated by PEI and further reaction between phosphate and calcium precursors produces PEI/CPs. A(ii) SEM image showing an example of as-prepared PEI/CP structure (PEI/CP-3). A(iii) Scheme showing the biodegradation and decay of the ultrasound and photoluminescence signal of PEI/CPs in water. (B) The synthesis simply adds NBP to B(i) PEI in ethanol to form B(ii) templated PEI/NBP aggregates. These aggregates serve as nuclei in B(iii) the sol-gel reaction between CME and NBP to form B(iv) PEI/CPs particles.

and 1.5 equivalent hydroxyl groups on average (Figure 3.14 (A)). In DLS measurements, ethanol was used to keep the same solvent condition as the synthesis process. DLS results showed a nearly invariant PEI hydrodynamic diameter (~10 nm) in the presence of increasing TBP (Figure 3.2 (A) and S1(B)). While a steady increment of the diameter was observed when increasing the DBP and NBP addition (Figure 3.2 (A) and S1 (C-D)), indicating the formation of PEI/phosphate aggregates is only possible when the phosphate precursor contains hydroxyl groups. To further prove that the

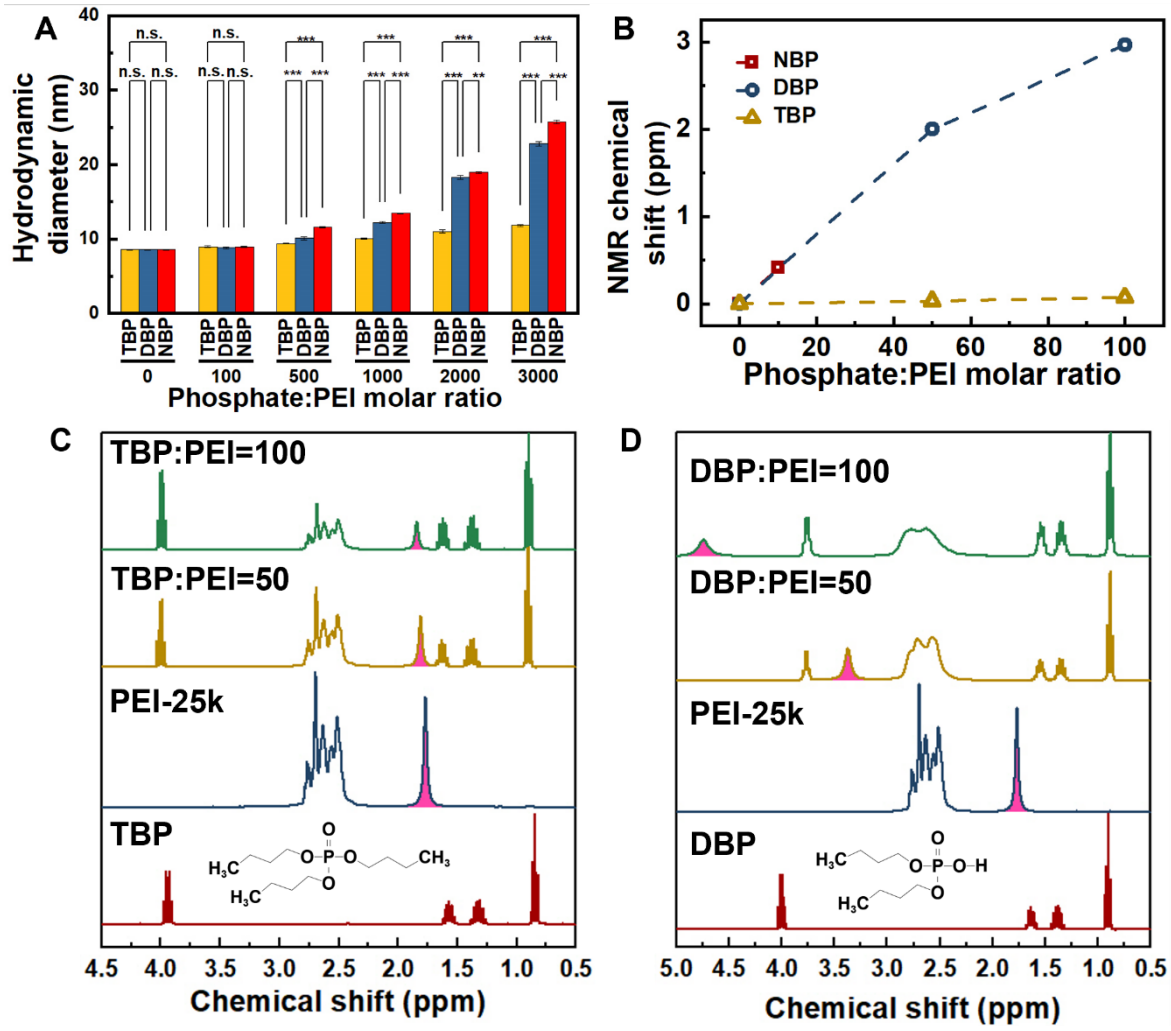

Figure 3.2 DLS and ^{1}H NMR proving the formation of "phosphate sponges".

(A) Hydrodynamic diameter of PEI/phosphate aggregates versus phosphate:PEI molar ratio as measured by DLS showing that the aggregate size increases only with phosphate esters containing hydroxyl groups (DBP and NBP). ns: not significant, * p<=0.05, ** p<=0.01, *** p<=0.001; n=3. (B) ^{1}H NMR chemical shift of amine versus phosphate:PEI molar ratio showing that the amine peak shifts only with phosphate esters containing hydroxyl groups (DBP and NBP). ^{1}H NMR spectra of PEI-25k (1 mM) and its mixture with (C) TBP and (D) DBP. 300 MHz, $CDCl_3$, 298 K. Amine peak of PEI (1.8 ppm) is filled in pink.

formation of PEI/phosphate aggregates is governed by the hydrogen bonding between hydroxyl and amine groups, the chemical shift of the amine groups (PEI) was tracked by ^{1}H NMR when PEI was titrated by these phosphate esters (Figure 3.2 (B-D) and S2). $CDCl_3$ was used as the solvent to exclude the hydroxyl groups from the solvent. The amine peak of PEI (1.8 ppm[314], highlighted

in pink, Figure 3.2 (C)) remained invariant despite increasing TBP addition. While in cases of both the DBP and NBP addition, the amine peak shifts steadily towards the downfield direction (Figure 3.2 (D) and S2). Therefore, both DLS and ^{1}H NMR results support the formation of the phosphate sponge via hydrogen bonding between hydroxyl and amine groups.

3.4.2. Exemplar Particles, Composition, and Chemical Structure

This PEI-mediated sol-gel approach is simple (stepwise additions of reactants and incubation) and mild (25 - 90 °C). Moreover, it is highly flexible in controlling PEI/CPs' morphology (Figure 3.3 (A)) and size (Figure 3.3 (B)) when parameters were tuned. These parameters include the PEI:NBP molar ratio, solution dynamic condition, PEI molecular weight, reaction temperature, and reaction time (See Table 3.1 for detailed parameters). The effects of these parameters will be discussed in detail later. Briefly, PEI/CP particles ranging from 63±8 μm to 396±128 nm and versatile morphologies were obtained, including hexagonal micro-disc (Figure 3.3 A(i-ii)), micro-flower (Figure 3.3 A(iii)), micro-leaf (Figure 3.3 A(iv)), nano-butterfly (Figure 3.3 A(v)), and nano-ribbon (Figure 3.3 A(vi)).

We expected as-prepared particles to be composites of PEI and calcium phosphate phases. The composite nature was proved using three tools. First, energy-dispersive X-ray (EDX) mapping shows three major elements: P, Ca, and N (Figure 3.3 A(vii-x)). Second, Fourier transform infrared (FTIR) spectra of seven representative PEI/CPs (Figure 3.16) show characteristic bands of PEI and phosphate species. Specifically, bands of PEI were seen at 2952-2862 and 1453 cm^{-1} (CH_2CH_2), 1620-1585 cm^{-1} (NH), and 1122 cm^{-1} (CN).[315-316] The phosphate phase was evidenced by bands at 1220 cm^{-1} (νas $(PO_2)^-$), 1000 and 1070 cm^{-1} (νas $(PO_3)^{2-}$), 900 cm^{-1} (νs (P-O-P)), and 790, 730, and 540 cm^{-1} (δ (P-O-P)).[52] Lastly, solid-state ^{31}P and ^{1}H magic angle spinning nuclear magnetic resonance (MAS NMR) shows the presence of phosphate species and amine groups (Figure 3.18).

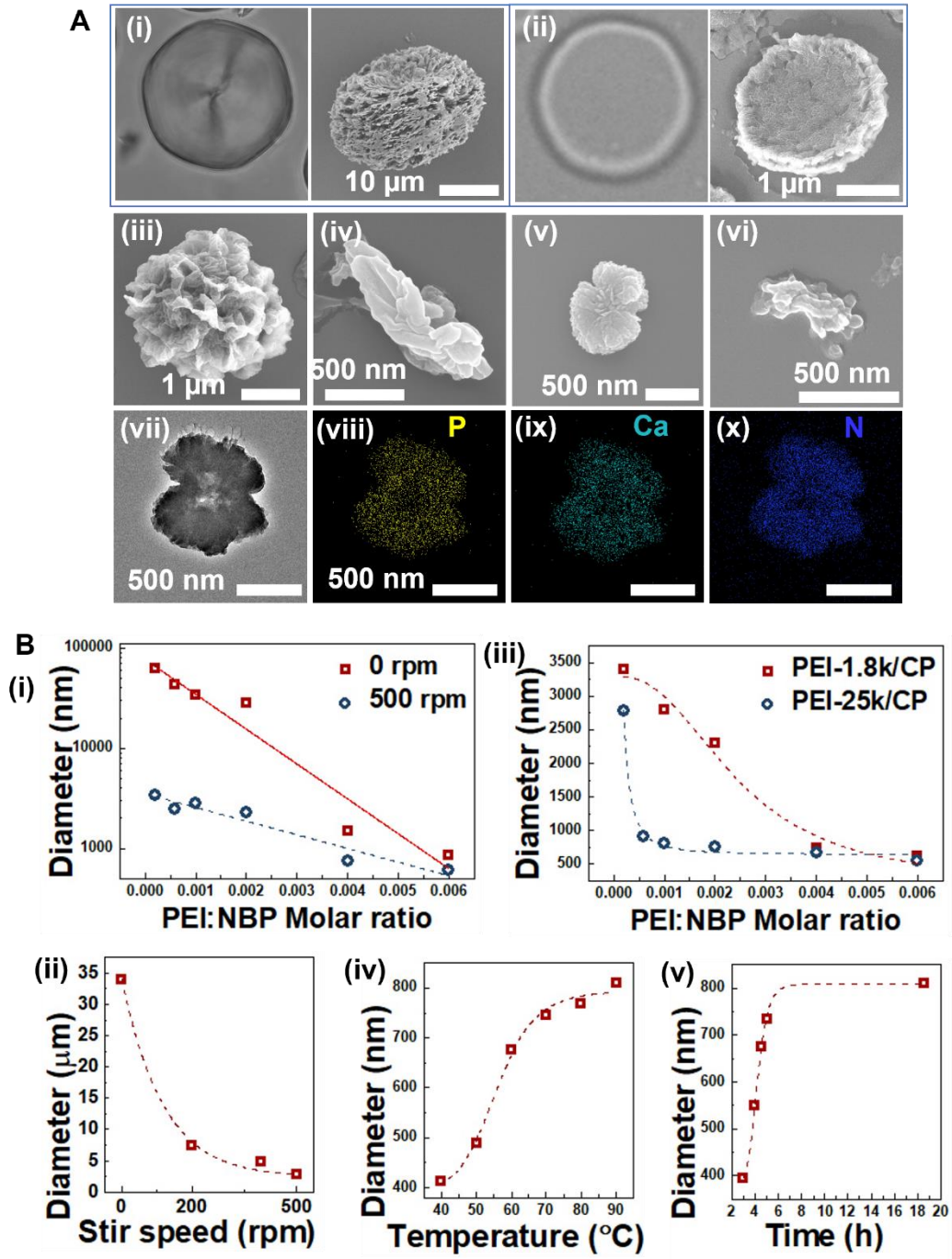

Figure 3.3 Exemplar particles and effects of synthetic parameters.

Optical microscopy and SEM images showing A(i-ii) hexagonal micro-discs (PEI/CP-3 and -10), A(iii) micro-flower (PEI/CP-5), A(iv) micro-leaf (PEI/CP-25), A(v) nano-butterfly (PEI/CP-17), and A(vi) nano-ribbon (PEI/CP-22). A(vii-x) TEM and EDX mapping of the nano-butterfly (PEI/CP-17) showing element P, Ca, and N. The diameter decreases with increasing B(i-ii) PEI:NBP molar ratio, stir speed, and B(iii) PEI molecular weight, while increasing with increasing B(iv) reaction temperature and B(v) time

The calculation of the composition based on inductively coupled plasma mass spectroscopy (ICP-MS) (Table 3.2) showed that the weight percentage of PEI (or calcium phosphate) varies from 67.34 (32.66%) to 50.26 (49.74%), depending on synthetic conditions. Besides, the calcium phosphate phase has a formula of $(P_2O_5)_x(CaO)_{1-x}$ with x varying from 0.31 to 0.40.

X-ray diffraction (XRD) spectra of PEI/CPs (Figure 3.17) were compared to those of nine typical calcium phosphate (CP) phases reported in the literature[306, 317-324]. The major XRD peaks of PEI/CPs created from PEI-25k match well with those of the HAp crystal[324] but are broader; PEI/CPs prepared from PEI-1.8k have an even broader XRDpattern like the amorphous electrospray CP,[306] indicating the glassy nature of PEI/CPs. Based on the broadness of XRD peaks, the degree of crystallization decreases in the order of HAp > PEI-25k/CP > PEI-1.8k/CP > electrospray CP.

There are three possible bonding types contributing to the PEI/CP network formation: P-O-P bonding, PO-Ca-OP bonding, and/or POH-NH_2 hydrogen bonding. We first investigated the nature of P-O-P bonding using solid-state ^{31}P MAS NMR. Q^n is widely applied to represent phosphate species, where n is the number of P-O-P bonding (i.e. bridging oxygens) in each PO_4^{3-} tetrahedron.[219] For PEI/CPs prepared from both PEI-1.8k and -25k, all ^{31}P resonances (Figure 3.18) were observed between -4 and 4 ppm, which can be assigned to the Q^1 speciation (i.e. pyrophosphates).[325] Therefore, pyrophosphate is the building block of PEI/CPs. Figure 3.18 shows the chemical structure of pyrophosphate with four isolated oxygens highlighted. Assuming the presence of calcium oxide and partially reacted NBP, each of the four isolated oxygens can form PO-Ca, PO-H, or PO-$CH_2CH_2CH_2CH_3$ groups. Pyrophosphate units containing different combinations of these chemical groups are different Q^1 species measurable by ^{31}P MAS NMR (Figure 3.18). We observed only one dominant Q^1 peak (~1ppm) in all PEI-25k/CPs (Figure 3.18

(D-H)) and those prepared from a high PEI-1.8k concentration (Figure 3.18 (C)). Pyrophosphate units in these PEI/CPs are mainly connected by PO-Ca-OP because their ICP-MS-measured composition (Table 3.2) is close to $(P_2O_5)_{0.33}(CaO)_{0.67}$, which is the theoretical composition of the Q^1 speciation saturated by Ca. In contrast, multiple Q^1 species were seen from PEI/CPs prepared from low PEI-1.8k concentrations (Figure 3.18 (A-B)). Besides, the ICP-MS-measured P_2O_5 ratio of these particles is larger than 0.33. Both results support the presence of PO-H and/or PO-$CH_2CH_2CH_2CH_3$ along with PO-Ca. PO-H may form hydrogen bonding with NH_2 (PEI) and therefore, further connects pyrophosphate units and extends the network. Indeed, ^{1}H MAS NMR results (Figure 3.18 (5A-B)) of PEI/CPs containing multiple Q^1 species also show multiple amine peaks including those highly shifted (>9 ppm), which supports the formation of POH-NH_2 hydrogen bonding.

3.4.3. Effects of PEI:NBP Molar Ratio

Sol-gel reactions were firstly performed using PEI-1.8k at 90 °C for 18.5 h without magnetic stirring. The PEI:NBP molar ratio was varied from 0.0002 to 0.006. The average diameter of PEI/CPs decreases as the molar ratio increases and can be tuned from 63±8 μm (ratio=0.0002) to 861 nm (ratio=0.006) (Figure 3.3 and Figure 3.4; See Figure 3.19 for size distributions.). PEI/CPs appeared to be porous hexagonal micro-discs with the size ranging from 28±6 to 63±8 μm when the molar ratio was between 0.0002 and 0.002 (Figure 3.4 (A-D)). High-magnification SEM images (Figure 3.4 (A-D)) indicate that these hexagonal micro-discs may be assembled from smaller micro-flakes, which is supported by particle growth studies shown later (Figure 3.8). This PEI:NBP molar ratio-dependent size change can be explained by the proposed phosphate sponge mechanism. Phosphate sponges can be considered as nuclei for particle growth. With a fixed NBP and CME addition, a higher PEI:NBP molar ratio results in a higher number-concentration of nuclei and, therefore, smaller particles.

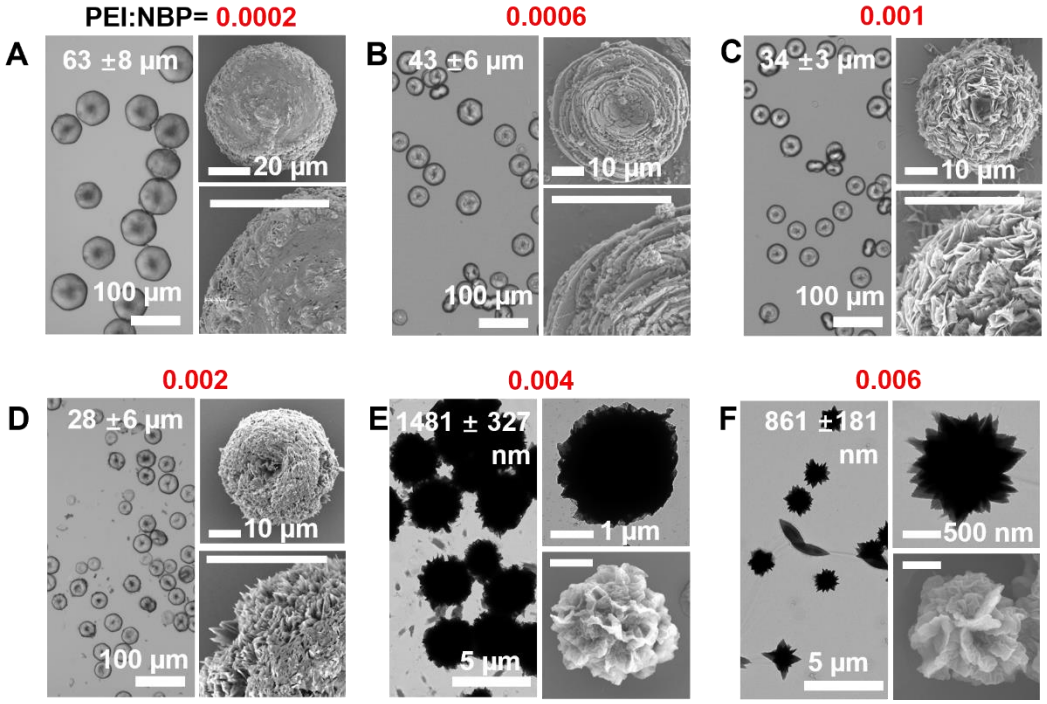

Figure 3.4 Effects of PEI:NBP molar ratio.

Optical microscopy (white, low-magnification), SEM (white, high-magnification), and TEM (black) images of PEI/CPs prepared from (A) PEI-1.8k, 90 °C, 18.5 h, no stirring, and various PEI:NBP molar ratio (PEI/CP-1 to -6).

3.4.4. Effects of Solution Dynamic Condition

We then repeated sol-gel reactions using PEI-1.8k at 90 °C for 18.5 h with magnetic stirring at 500 rpm. At the same PEI:NBP molar ratio, magnetic stirring at 500 rpm resulted in 18.5 to 1.4 times smaller particles than no stirring (Figure 3.3 (B)). These particles also appeared to be micro-discs with the molar ratio ranging from 0.0002 to 0.002 (Figure 3.5 (A-D)) and micro-/nano flowers when the ratio was above 0.002 (Figure 3.5 (E-F)). By carefully controlling the stirring speed from 0 to 200, 400, and 500 rpm, the average particle size can be finely tuned from 34±3 to 7.8±2.7, 4.8±1.4, and 2.8±1.3 µm (Figure 3.19 (C) and Figure 3.20).

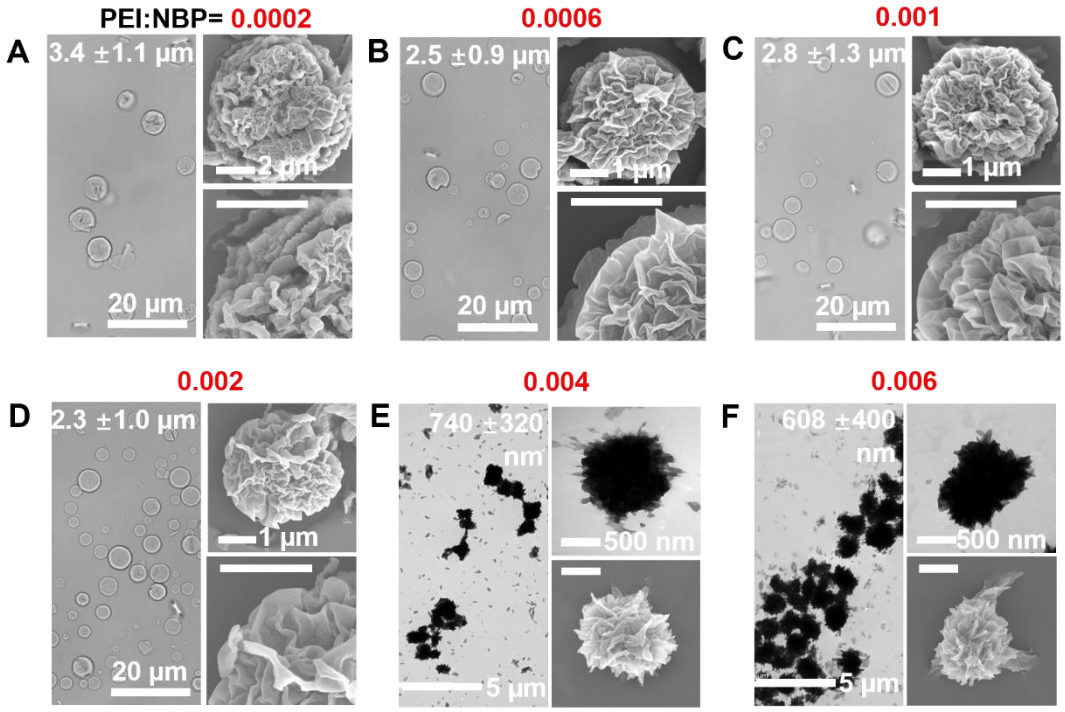

Figure 3.5 Effects of solution dynamic condition.

Optical microscopy (white, low-magnification), SEM (white, high-magnification), and TEM (black) images of PEI/CPs prepared from (B) PEI-1.8k, 90 °C, 18.5 h, 500 rpm stirring, and various PEI:NBP molar ratio (PEI/CP-7 to -12).

3.4.5. Effects of PEI Molecular Weight

To determine the influences of the PEI molecular weight, PEI-1.8k was replaced by either PEI-25k or PEI-800 while other conditions were kept the same (Figure 3.3 (B) and Figure 3.6). Comparing Figure 3.6 to Figure 3.4, at the same PEI:NBP molar ratio, PEI-25k resulted in smaller particles. This trend is clearer in Figure 3.3 (iii). The micro-disc shape (~2790 nm) appeared when the molar ratio was 0.0002 (Figure 3.6 (A)). When the molar ratio exceeded 0.0002, submicron-flowers (914±240 to 760±181 nm) and nano-butterflies (659±138 to 546±131 nm) were formed (Figure 3.6 (B-F)). The PEI molecular weight-dependent size change can be explained by the difference in chemical bonding. Based on the solid-state ^{31}P and ^{1}H MAS NMR results discussed before (Figure 3.18), PEI/CPs prepared from low-concentration PEI-1.8k can extend their network

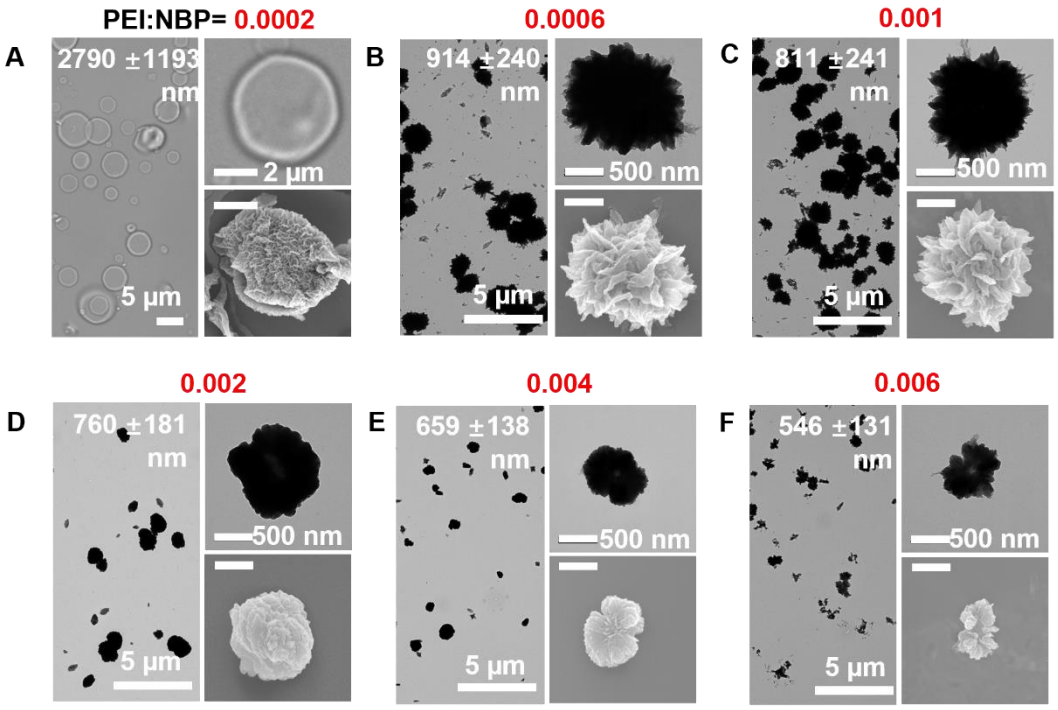

Figure 3.6 Effects of PEI molecular weight.

Optical microscopy (white, low-magnification), SEM (white, high-magnification), and TEM (black) images of PEI/CPs prepared from PEI-25k, 90 °C, 18.5 h, 500 rpm stirring, and various PEI:NBP molar ratio (PEI/CP-13 to -18).

via both PO-Ca-OP and POH-NH_2 hydrogen bonding, which explains for larger particles formed in these conditions. However, in the case of high- concentration PEI-1.8k and PEI-25k, the connection of pyrophosphate units via the POH-NH_2 hydrogen bonding is less likely, resulting in smaller particles. As shown in Figure 3.21, within the tested range of PEI:NBP molar ratio (0.0002 to 0.006), PEI-800 did not produce monodispersed particles with defined shapes as seen in the case of PEI-1.8 and PEI-25k. Instead, only amorphous gel-like products were observed. This difference indicates that PEI-800 may be too small to efficiently regulate the growth of monodispersed PEI/CP particles.

3.4.6. Effects of Reaction Temperature

Sol-gel reactions were also carried out at various temperatures (90, 80, 70, 60, 50, and 40 °C) with other parameters being kept constant (PEI-25k:NBP=0.001, magnetic stirring at 500 rpm, and 18.5 h). The average diameter of particles increased as the reaction temperature was raised (Figure 3.3 B(iv)). At 40 and 50 °C, particles have a nano-ribbon morphology (490 and 412 nm) (Figure 3.7 (A-B)). When the temperature was adjusted between 60 °C and 90 °C, particles possess the nano-flower morphology (from 811±241 to 768 ±148, 746±171, and 677±134 nm) (Figure 3.7 (C-F)). The temperature-dependent change of particle size can be explained by the reaction kinetics. A higher reaction temperature may result in faster reaction and particle growth and therefore, a larger size during a given period of reaction.

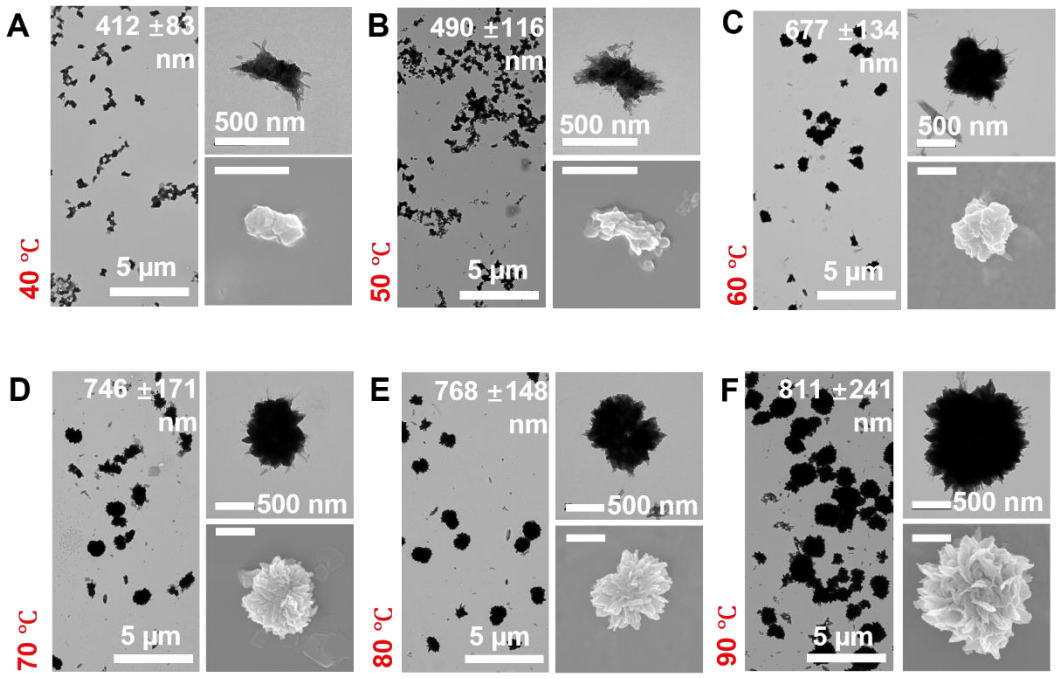

Figure 3.7 Effects of reaction temperature.

SEM (white) and TEM (black) images of PEI/CPs prepared from PEI-25k, PEI:NBP molar ratio 0.001, 90 °C, 18.5 h, 500 rpm stirring, and various temperature.

3.4.7. Effects of Reaction Time

Hexagonal micro-disc (PEI/CP-3) and nano-flower (PEI/CP-15) were chosen as models to understand the growth of PEI/CP particles. Particles were collected at different time points and examined. Figure 3.8 (A) shows the evolution of the hexagonal micro-disc (PEI/CP-3) over time. The first hour of reaction at room temperature resulted in an inhomogeneous mixture of nano-spheres (~80 nm) and nano-rods (LxW=400x150 nm, Figure 3.8 A(i)). After raising the temperature to 90 °C for another hour, these mixed structures transformed into homogenous micro-leaves (LxW=1200x400 nm, Figure 3.8 A(ii)). When extending the reaction time at 90 °C to 4 h (Figure 3.8 A(iii)), the size and shape of micro-leaves remained almost the same; Meanwhile, parts of these micro-leaves assembled to form a loose micro-disk structure (~7 μm in diameter), implying the transition from micro-leaves' growth to the assembly during this period. Finally, when the reaction time at 90 °C reached 18.5 h, micro-leaves disappeared, and larger and homogeneous hexagonal micro-discs (34±3 μm in diameter) were observed (Figure 3.8 A(iv))). In short, the formation of hexagonal micro-discs started with the growth of micro-leaves from a mixture of nano-spheres and nano-rods. As-formed micro-leaves then assembled to form the loose micro-disc structure. Finally, further deposition of materials on the micro-disc surface led to the formation of larger and denser hexagonal micro-discs.

A similar observation was performed for nano-flowers (PEI/CP-15, Figure 3.8 (B)). The growth of PEI/CP-15 also began with a mixture of nano-spheres and nano-rods with an average diameter of 396±128 nm (3 h at 90 °C, Figure 3.8 B(i)). After 4 h at 90 °C, these mixed particles transformed into homogenous nano-ribbons (549±104 nm, Figure 3.8 B(ii)). These nano-ribbons then evolved to nano-flowers with the size increasing from 676±120 nm (4.5 h at 90 °C, Figure 3.8 B(iii)) to 734±157 nm (5 h at 90 °C, Figure 3.8 B(iv)) and 811±241 nm (18.5 h at 90 °C, Figure 3.8 B(v)) (See Figure 3.3 B(v) for the diameter versus time relationship).

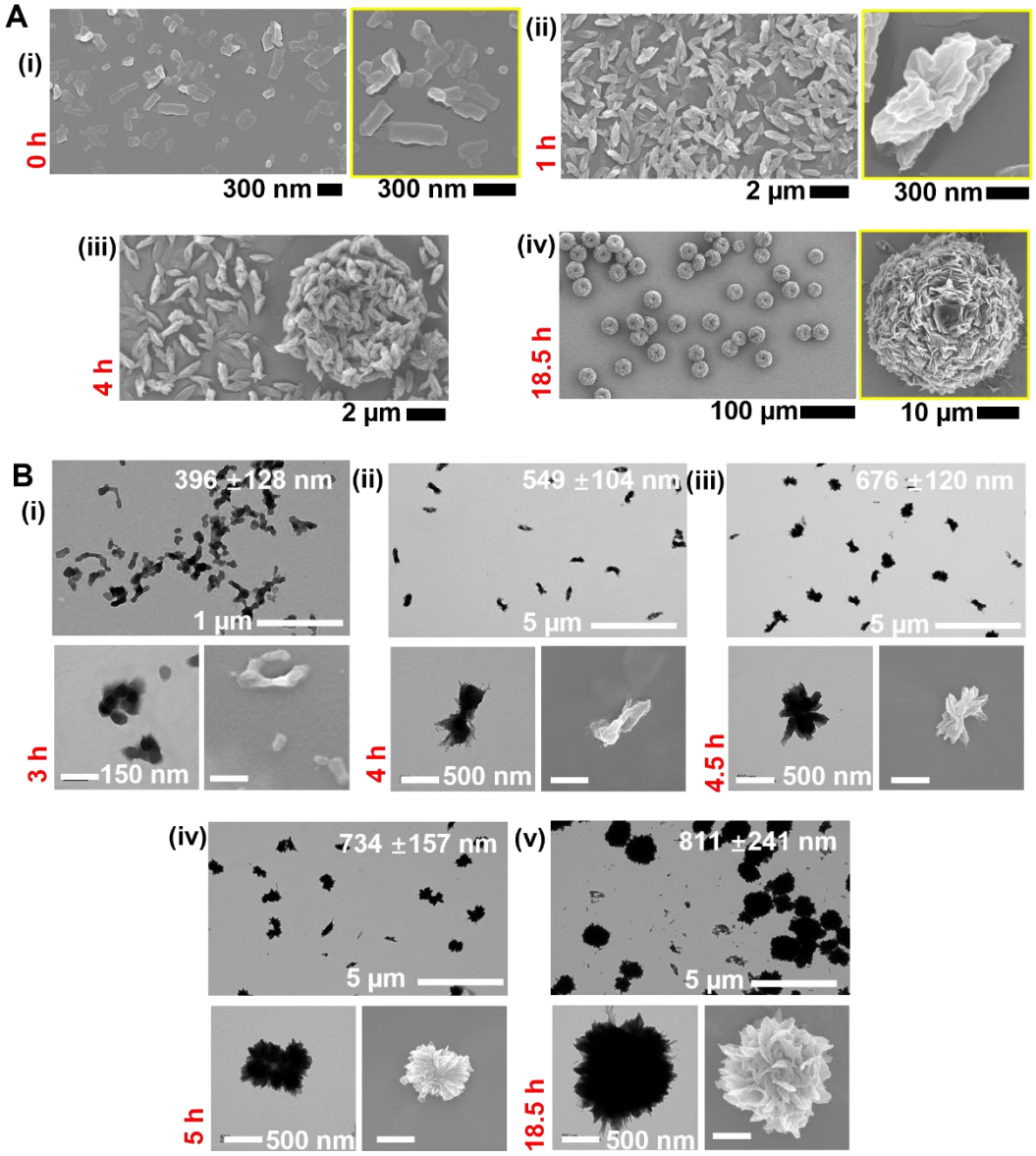

Figure 3.8 Effects of reaction time.

SEM (white) and TEM (black) images showing the growth process of (A) hexagonal micro-disc (PEI/CP-3) and (B) nano-flower (PEI/CP-15).

3.4.8. Degradability

The poor clearance of nanomaterials is a major impediment to clinical translation. By design, PEI/CPs should slowly degrade into small molecules and simple ions for renal clearance. We further tested the degradability of PEI/CPs. Optical microscopy images show that PEI/CPs gradually dissolved in PBS buffer (Figure 3.9 (A)). PEI/CPs were continuously hydrated by fresh

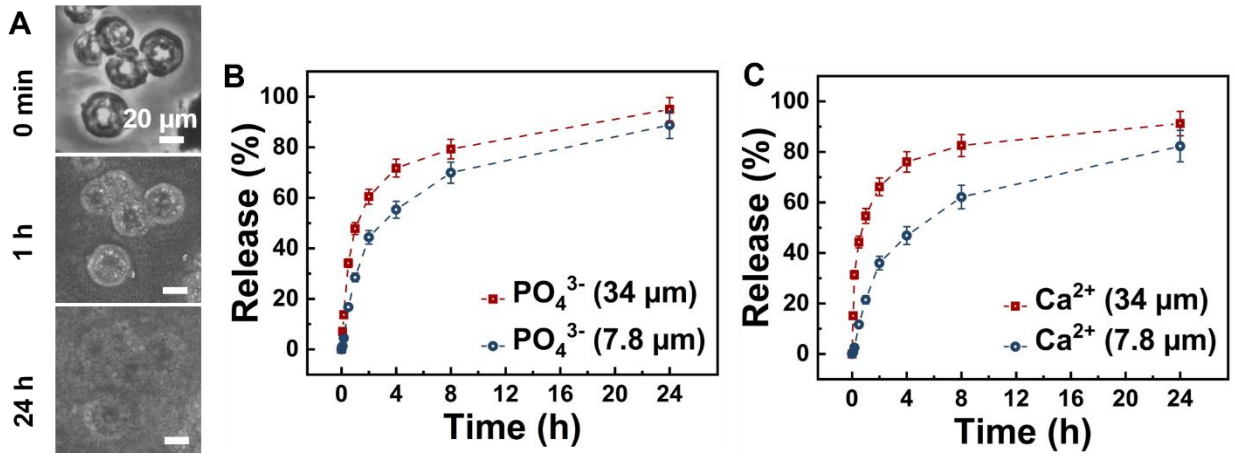

Figure 3.9 Biodegradability.

(A) Optical microscopy images showing the dissolution of PEI/CP-3 under a continuous flow of PBS. Ion release profile of (B) PO_4^{3-} and (C) Ca^{2+} from PEI/CP-3 under a continuous flow of fresh water (pH 7.30).

water (pH 7.30) and a release of about 80% - 90% major ions (i.e., PO_4^{3-} and Ca^{2+}) were detected within the first 24 h using ICP-MS (Figure 3.9 (B-C)).

3.4.9. Ultrasound and Photoluminescence Imaging

We hypothesized that PEI/CP particles can have a high acoustic impedance mismatch with the liquid phase and be used as ultrasound contrasts. To determine how the particle size and concentration affects the echogenicity, PEI/CPs in ethanol solution were added to tubes (Figure 3.10 (A)) and imaged in the B-mode at 18 MHz. Ethanol was used as the solvent at this step to prevent any uncertainties from the degradation caused by water. No ultrasound signal was detected from pure ethanol (Figure 3.10 A(ii)). At the same particle mass concentration (2.5 mg/mL), the ultrasound intensity increases with increasing particle size (546±131 nm to 34±3 μm, Figure 3.10 A(iii)), which is consistent with previous findings and can be attributed to the differences in the scattering cross-section.[16, 326] This size effect holds true for all concentrations tested (0-10 mg/mL, Figure 3.10 (B)). With a given size, the ultrasound signal increases as the mass concentration increases (Figure 3.10 (B)). A linear intensity-concentration relationship was seen at the lower

concentration range (Figure 3.22). Defining the limit of detection (LOD) as the concentration of particles creating the intensity at three standard deviations above the mean of the background and using the background value of 0.08±0.01 and the best-fit equations (Figure 3.22), we estimated the LOD of PEI/CPs of 34±3 µm, 7.8±2.7 µm, 4.8±1.4 µm, and 546±131 nm to be 0.17, 0.30, 1.47, and 11.10 µg/mL, respectively. The LOD of 546±131 nm PEI/CP is comparable with that reported for silica NPs. (18.5 µg/mL, 300 nm, at 16 MHz), which has been demonstrated feasible for in-vivo stem cell imaging.[11] Thanks to the degradability of PEI/CPs, the ultrasound intensity of PEI/CPs dissolving in a static PBS buffer dropped about 40% within the first 24 h, and only slightly in the next 24 h (Figure 3.10 (C)). Therefore, in practice, PEI/CPs can be dispersed in PBS buffer

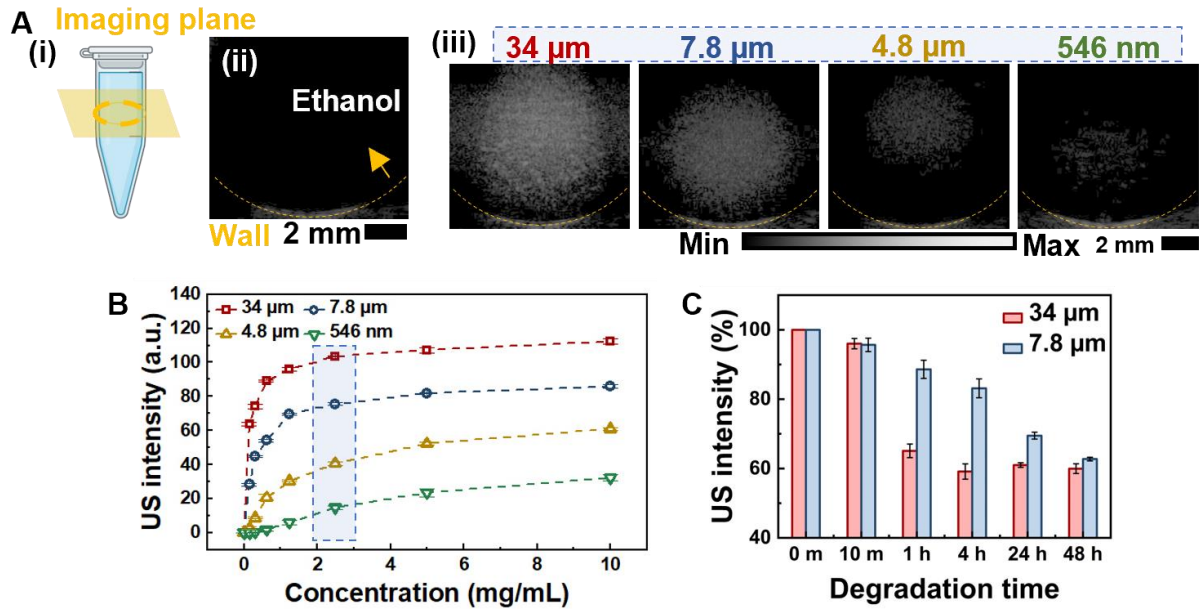

Figure 3.10 Transient B-mode ultrasound imaging.

A(i) Imaging slice in a tube. B-mode images of A(ii) ethanol and A(iii) 2.5 mg/mL ethanol solution of PEI/CP-3 (34 ± 3 µm), PEI/CP-31 (7.8 ± 2.7 µm), PEI/CP-32 (4.8 ± 1.4 µm), and PEI/CP-18 (546 ± 131 nm). Dashed lines and arrow show the tube wall. (B) Ultrasound intensity versus particle concentration. (C) Ultrasound intensity versus degradation time.

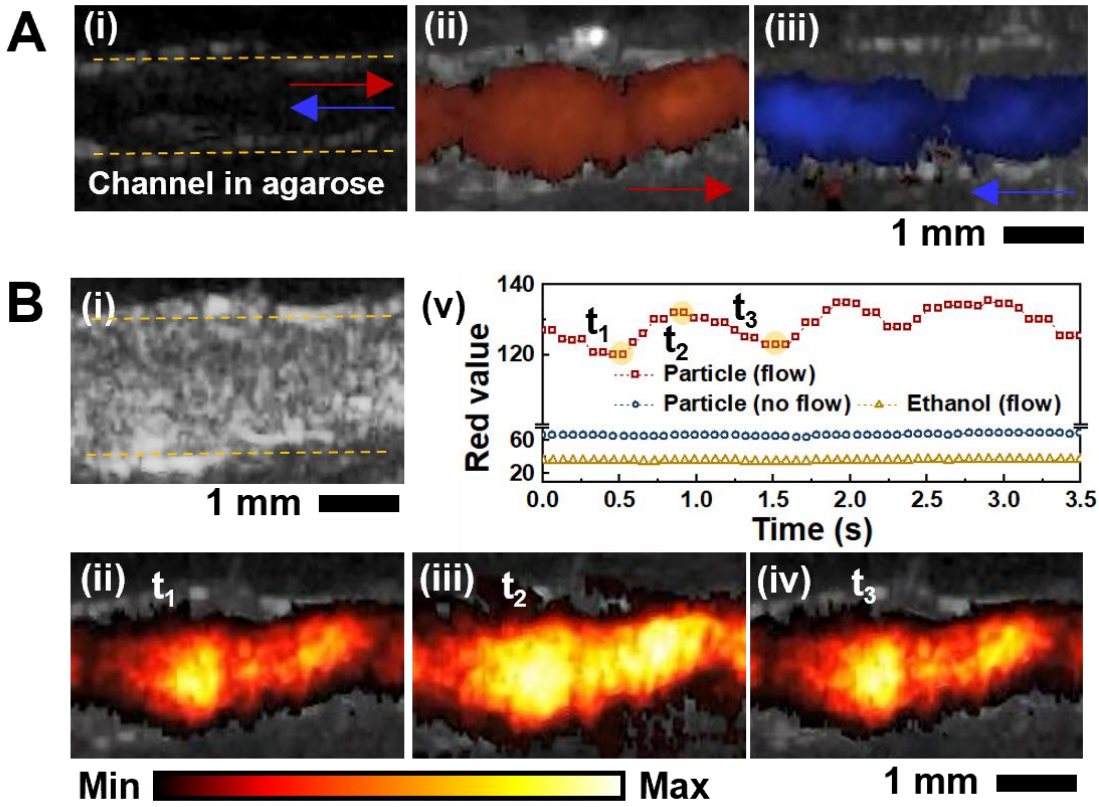

Figure 3.11 Doppler ultrasound imaging.

Overlay of color Doppler and B-mode images when flowing A(i) water and A(ii-iii) 10 mg/mL PEI/CP-31 (7.8 ± 2.7 μm) in ethanol. Overlay of power Doppler and B-mode images of 10 mg/mL PEI/CP-31 (7.8 ± 2.7 μm) in ethanol B(i) without and B(ii-iv) with flow at time points marked in B(v). B(v) Doppler intensity versus time.

and used as transient ultrasound contrast agents with a 24 h imaging window. They may bridge the gap between the unstable gas microbubbles (degrade within 30 min)[11] and slowly-degradable silica nanoparticles (degrade after 24 days)[327] considering the degradation speed.

Contrasts with size comparable to blood cells have been used for Doppler vascular imaging.[304-305] Here, we tested in vitro the potential of using PEI/CPs for Doppler imaging. As a negative control, pure ethanol was constantly pumped through a channel inside an agarose phantom using a peristaltic pump, which did not result in detectable color-Doppler signals (Figure 3.11 A(i)). In contrast, flowing 10 mg/mL PEI/CP-31 (7.8 μm) generated color-Doppler signals

with recognizable flow directions (red or blue, Figure 3.11 A(ii-iii). The power-Doppler mode is used clinically to monitor heartbeats and changes in blood flow rate. Taking advantage of the pulsive flow of the peristaltic pump, we were able to mimic the heartbeat. Heartbeat-like wavy power-Doppler signals were observed from the flow of PEI/CP-31 but not ethanol or stagnant particles (Figure 3.11 (B)).

PEI/CPs also emitted blue light when excited at 358 nm (Figure 3.12 (A)). This is due to the intrinsic photoluminescence of PEI reported previously, although the mechanism of this intrinsic photoluminescence is yet to be explored.[328] The emission peak of pure PEI-1.8k and PEI/CPs were found at 411 nm and 450 nm (excitation at 350 nm, Figure 3.23). The photoluminescence intensity increases linearly with PEI/CPs concentration (Figure 3.12 (B)). Although, considering the low quantum yield (1%) reported for PEI-1.8K and PEI-25k,[328] PEI/CPs may not be the best choice of fluorophores, this intrinsic photoluminescence can still be used for labelling and tracking these particles when necessary.

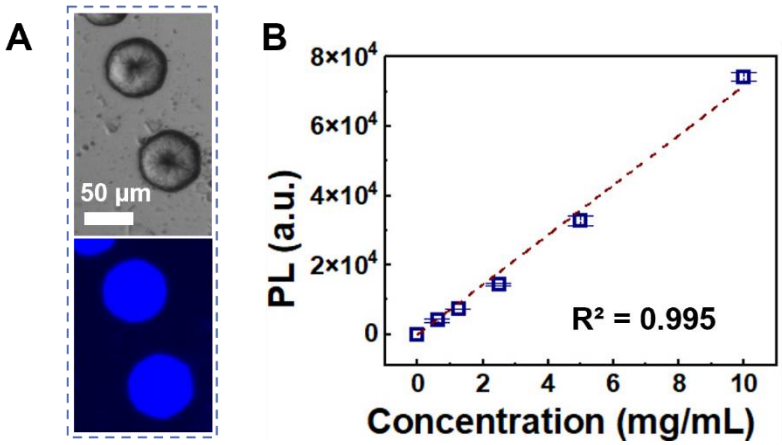

Figure 3.12 Photoluminescence imaging.

(A) Fluorescence microscopy images showing PEI/CP-3 emitting blue light (DAPI, excitation at 358 nm). (B) Photoluminescence intensity versus PEI/CP-3 concentration (excitation at 350 nm).

3.4.10. Cell Cytotoxicity

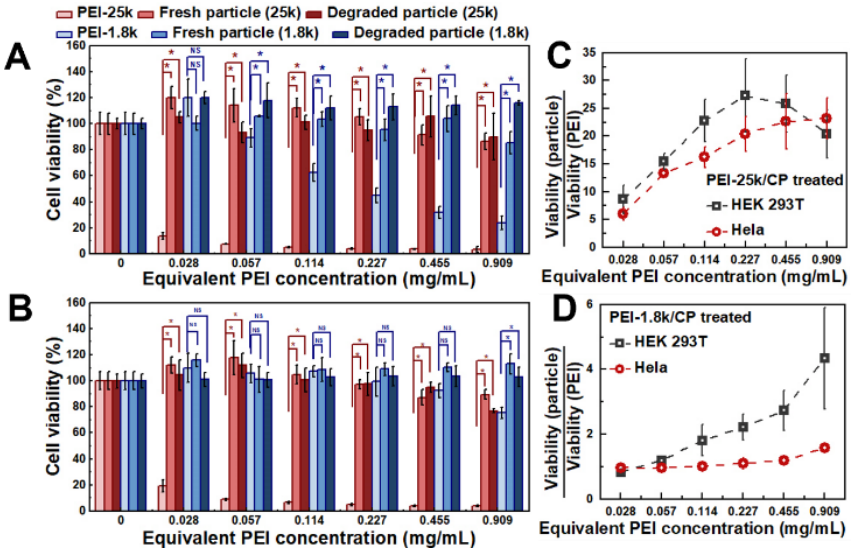

Figure 3.13 Cell cytotoxicity of pristine PEI and PEI/CPs.

Tests used resazurin assay on (A) HEK 293T and (B) HeLa cells. Ratio of cell viability treated with fresh particles to pristine PEI in the case of (C) PEI-25k and (D) PEI-1.8k. PEI/CP-5 was selected to represent particles made from PEI-1.8k and PEI/CP-15 for PEI-25k. PEI/CPs show negligible cytotoxicity compared to pristine PEI. *: $P \leq 0.05$; NS: not significant, i.e. $p > 0.05$; n=4.

The dose-dependent cytotoxicity of pure PEIs and PEI/CP composites was evaluated with HEK 293T and HeLa cells using the resazurin assay (Figure 3.13). Pure PEI-25k showed high cytotoxicity; a low dose of 0.028 mg/mL can dramatically reduce the cell viability to below 20%. PEI-1.8k is less toxic but still caused a steady drop in the viability of HEK 293T (Figure 3.13 (A)). Surprisingly, PEI/CPs have negligible cytotoxicity compared to PEIs. Both cell types treated with fresh and degraded PEI-25k/CP and PEI-1.8k/CP have viability above 85% in the concentration range tested except HeLa cells treated with 0.909 mg/mL degraded PEI-25k/CPs (77%). In the case of HEK 293T cells, fresh PEI-25k/CP and PEI-1.8k/CP, respectively, resulted in 9-26 and 1-4 times, respectively, higher viability than corresponding PEI; these values are 6-23 and 1-1.6 in the case of HeLa cells (Figure 3.13 (C-D)). The toxicity of pure PEI is originated from the damage of the cell membrane by abundant positive amine groups.[329] Therefore, the reduced cytotoxicity

of PEI/CPs compared to pure PEI can be explained by the charge neutralization by negative phosphate species in both intact and degraded phases.

3.5. CONCLUSION

We demonstrated a facile and mild (25-90 °C) synthesis mimicking the bio-silicification in diatoms for preparing PEI/CP composites. Using DLS and ^{1}H NMR, we proved the formation of proposed "phosphate sponges", which are aggregates composed of phosphate esters and PEI resulting from hydrogen bonding between hydroxyl (from phosphate ester) and amine groups (from PEI). These phosphate sponges served as nuclei in the reaction of CME and phosphate esters. By controlling parameters such as the PEI:NBP molar ratio, solution dynamic condition, PEI molecular weight, reaction temperature, and reaction time, PEI/CP composites were prepared with versatile sizes (396±128 nm to 63±8 μm) and morphologies (hexagonal micro-disc, micro-flower, micro-leaf, nano-butterfly, and nano-ribbon). PEI/CPs exhibited excellent biocompatibility and biodegradability, indicated by negligible cell cytotoxicity and degradation within 24 h. The echogenicity of PEI/CPs increases with the increment of size and concentration. PEI/CPs also generated Doppler signals containing the flow direction and speed information. Finally, PEI/CPs showed intrinsic blue photoluminescence. We envision that PEI/CPs are promising transient ultrasound and photoluminescence imaging agents.

3.6. ACKNOWLEDGEMENTS

Chapter 3, in full, is a reprint of the material as it appears in "He, T.; Bradley, D. G.; Xu, M.; Ko, S.-T.; Qi, B.; Li, Y.; Cheng, Y.; Jin, Z.; Zhou, J.; Sasi, L.; Fu, L.; Wu, Z.; Zhou, J.; Yim, W.; Chang, Y.-C.; Hanna, J. V.; Luo, J.; Jokerst, J. V., Bio-Inspired Degradable

Polyethylenimine/Calcium Phosphate Micro-/Nano-Composites for Transient Ultrasound and Photoluminescence Imaging. *Chemistry of Materials* **2022,** *34* (16), 7220-7231." The dissertation author was the primary investigator and author of this paper.

3.7. SUPPLEMENTARY INFORMATION

Table 3.1 Synthetic parameters and sample names

Sample name	Final vol (mL)	Extra ethanol (mL)	PEI MW	PEI (mol)	NBP (mol)	CME (mol)	Stir Speed (rpm)	Raised temperature (°C) [a]	Time at raised temperature (h) [b]
PEI/CP-1	11	10.32	1.8 k	2.00E-07	1.00E-03	5.00E-04	0	90	18.5
PEI/CP-2		10.28	1.8 k	6.00E-07	1.00E-03	5.00E-04	0	90	18.5
PEI/CP-3		10.24	1.8 k	1.00E-06	1.00E-03	5.00E-04	0	90	18.5
PEI/CP-4		10.14	1.8 k	2.00E-06	1.00E-03	5.00E-04	0	90	18.5
PEI/CP-5		9.94	1.8 k	4.00E-06	1.00E-03	5.00E-04	0	90	18.5
PEI/CP-6		9.74	1.8 k	6.00E-06	1.00E-03	5.00E-04	0	90	18.5
PEI/CP-7		10.32	1.8 k	2.00E-07	1.00E-03	5.00E-04	500	90	18.5
PEI/CP-8		10.28	1.8 k	6.00E-07	1.00E-03	5.00E-04	500	90	18.5
PEI/CP-9		10.24	1.8 k	1.00E-06	1.00E-03	5.00E-04	500	90	18.5
PEI/CP-10		10.14	1.8 k	2.00E-06	1.00E-03	5.00E-04	500	90	18.5
PEI/CP-11		9.94	1.8 k	4.00E-06	1.00E-03	5.00E-04	500	90	18.5
PEI/CP-12		9.74	1.8 k	6.00E-06	1.00E-03	5.00E-04	500	90	18.5
PEI/CP-13		10.32	25 k	2.00E-07	1.00E-03	5.00E-04	500	90	18.5
PEI/CP-14		10.28	25 k	6.00E-07	1.00E-03	5.00E-04	500	90	18.5
PEI/CP-15		10.24	25 k	1.00E-06	1.00E-03	5.00E-04	500	90	18.5
PEI/CP-16		10.14	25 k	2.00E-06	1.00E-03	5.00E-04	500	90	18.5
PEI/CP-17		9.94	25 k	4.00E-06	1.00E-03	5.00E-04	500	90	18.5
PEI/CP-18		9.74	25 k	6.00E-06	1.00E-03	5.00E-04	500	90	18.5
PEI/CP-19		10.24	25 k	1.00E-06	1.00E-03	5.00E-04	500	80	18.5
PEI/CP-20		10.24	25 k	1.00E-06	1.00E-03	5.00E-04	500	70	18.5
PEI/CP-21		10.24	25 k	1.00E-06	1.00E-03	5.00E-04	500	60	18.5
PEI/CP-22		10.24	25 k	1.00E-06	1.00E-03	5.00E-04	500	50	18.5
PEI/CP-23		10.24	25 k	1.00E-06	1.00E-03	5.00E-04	500	40	18.5
PEI/CP-24		10.24	1.8 k	1.00E-06	1.00E-03	5.00E-04	0	90	0
PEI/CP-25		10.24	1.8 k	1.00E-06	1.00E-03	5.00E-04	0	90	1
PEI/CP-26		10.24	1.8 k	1.00E-06	1.00E-03	5.00E-04	0	90	4
PEI/CP-27		10.24	25 k	1.00E-06	1.00E-03	5.00E-04	500	90	3
PEI/CP-28		10.24	25 k	1.00E-06	1.00E-03	5.00E-04	500	90	4
PEI/CP-29		10.24	25 k	1.00E-06	1.00E-03	5.00E-04	500	90	4.5
PEI/CP-30		10.24	25 k	1.00E-06	1.00E-03	5.00E-04	500	90	5
PEI/CP-31		10.24	1.8 k	1.00E-06	1.00E-03	5.00E-04	200	90	18.5
PEI/CP-32		10.24	1.8 k	1.00E-06	1.00E-03	5.00E-04	400	90	18.5
PEI/CP-33		10.32	800	2.00E-07	1.00E-03	5.00E-04	500	90	18.5
PEI/CP-34		10.28	800	6.00E-07	1.00E-03	5.00E-04	500	90	18.5
PEI/CP-35		10.24	800	1.00E-06	1.00E-03	5.00E-04	500	90	18.5
PEI/CP-36		10.14	800	2.00E-06	1.00E-03	5.00E-04	500	90	18.5
PEI/CP-37		9.94	800	4.00E-06	1.00E-03	5.00E-04	500	90	18.5
PEI/CP-38		9.74	800	6.00E-06	1.00E-03	5.00E-04	500	90	18.5

[a] All reactions were performed at room temperature for 1 hour then raised to a certain temperature as shown.
[b] The extra time at the raised temperature after 1 hour incubation at the room temperature.

Table 3.2 Composition determined by ICP-MS

Sample name	PEI wt%[a]	CP wt%[b]	CP composition, $(P_2O_5)_x(CaO)_{1-x}$[c]	
			x	1-x
PEI/CP-1	58.97	41.03	0.40	0.60
PEI/CP-3	50.26	49.74	0.38	0.62
PEI/CP-5	56.25	43.75	0.34	0.66
PEI/CP-15	61.73	38.27	0.35	0.65
PEI/CP-16	54.00	46.00	0.31	0.69
PEI/CP-18	67.34	32.66	0.33	0.67
PEI/CP-20	56.85	43.15	0.34	0.66
PEI/CP-22	57.16	42.84	0.33	0.67
PEI/CP-29	57.44	42.56	0.35	0.65

[a] Assuming the mass of PEI in particles equals to the mass of indissoluble material when PEI/CPs were dissolved by 70% nitric acid, the mass of PEI in particles were calculated by subtracting the mass of completely dissolved calcium phosphate from the mass of dried particles before dissolution.
[b] The mass of calcium phosphate is calculated from the $(P_2O_5)_x(CaO)_{1-x}$ formula and the mass of released PO_4^{3-} and Ca^{2+} ions determined by ICP-MS.
[c] The $(P_2O_5)_x(CaO)_{1-x}$ formula is calculated from released PO_4^{3-} and Ca^{2+} ions determined by ICP-MS.

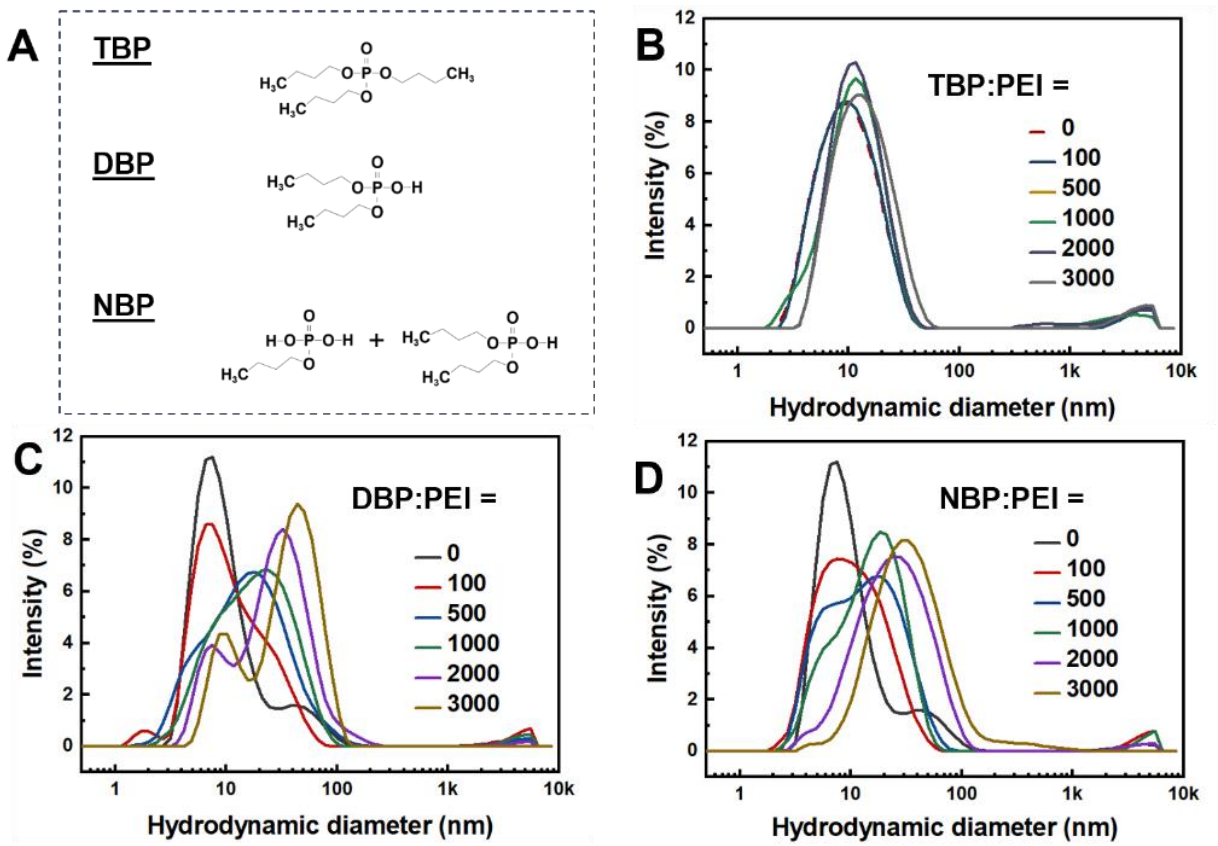

Figure 3.14 DLS results showing the formation of PEI/phosphate aggregates.

(A) Chemical structures of TBP, DBP, and NBP, which have 0, 1, and 1.5 hydroxyl groups, respectively. Size distribution of aggregates when PEI was mixed with (B) TBP, (C) DBP, and (D) NBP. The PEI in ethanol solution was 1 mM. In the case of NBP and DBP addition, the size of the aggregate increased with the increasing phosphate:PEI molar ratio. The size did not change when TBP was added indicating that the PEI/phosphate aggregate was formed in the presence of the hydroxyl group.

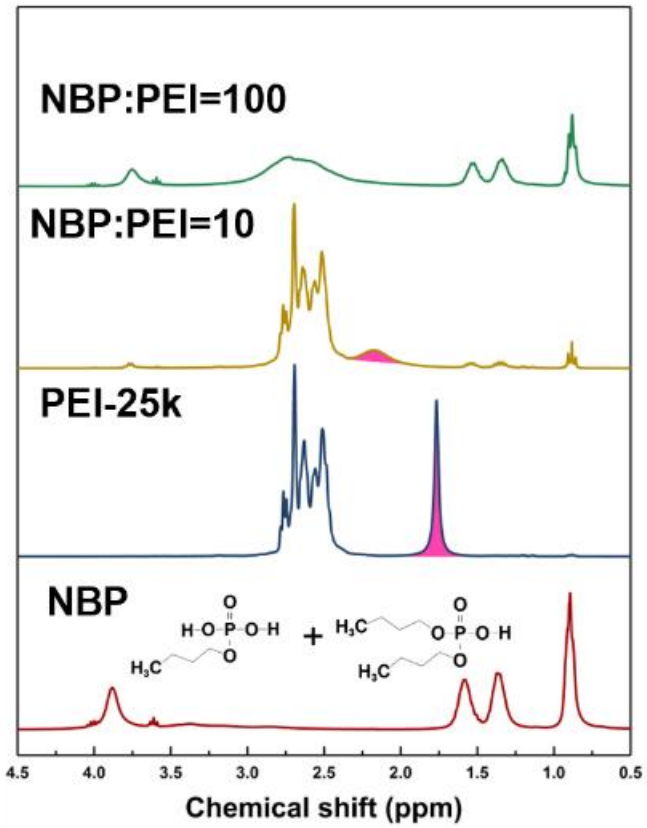

Figure 3.15 ^{1}H NMR titration (300 MHz, $CDCl_3$, 298 K) showing the formation of PEI/phosphate aggregates.

(A) Plots of ^{1}H NMR chemical shift of amine versus phosphate:PEI molar ratio. ^{1}H NMR spectra of PEI-25k (1 mM) and its mixture with (B) TBP, (C) DBP, and (D) NBP. The addition of TBP caused nearly no shift of the amine group of PEI (1.8 ppm[314], filled in pink), while the addition of DBP and NBP resulted in steady amine peak shifts to the lower field, indicating the hydrogen bonding between the hydroxyl group (phosphates) and amine group (PEI).

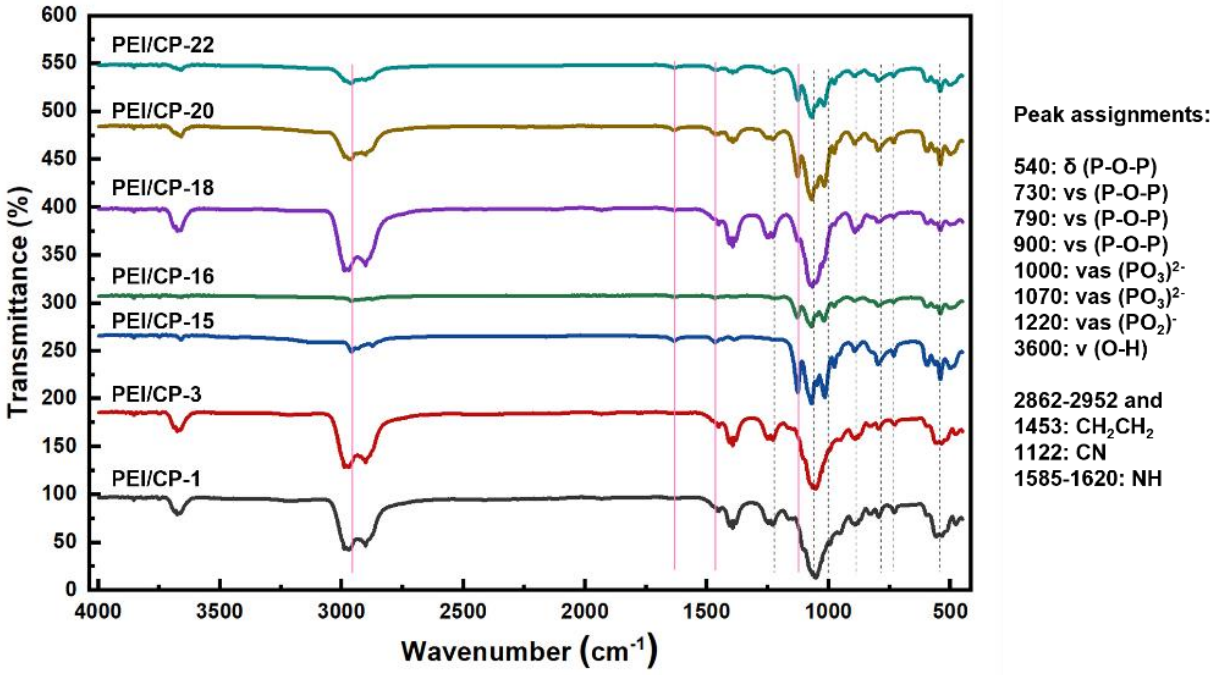

Figure 3.16. FTIR spectra of representative PEI/CPs.

Bands of PEI (pink solid lines)[315] and calcium phosphate (black dashed lines)[52] were seen.

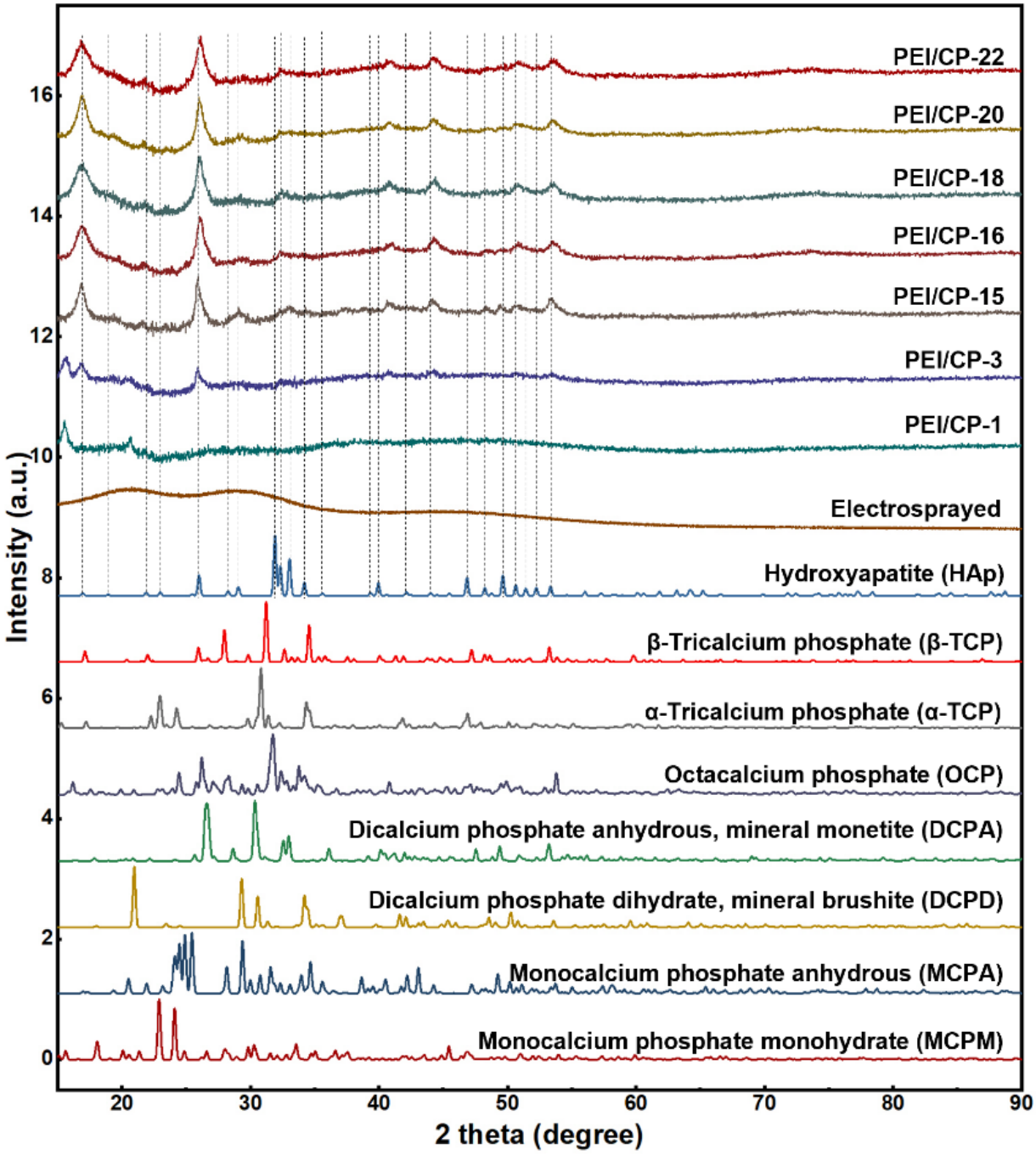

Figure 3.17 XRD spectra.

Comparison of PEI/CPs, electrosprayed calcium phosphate,[306] and commonly reported calcium phosphate crystals[317-318, 320, 322-324, 330-331]. PEI/CP-1 and -3 were made from PEI-1.8k, while PEI/CP-15, -16, -18, -20, and -22 were from PEI-25k. The degree of crystallization based on peak broadness: HAp > PEI-25k/CPs > PEI-1.8k/CPs > ES CP. Dashed lines indicate major peaks of HAp[324].

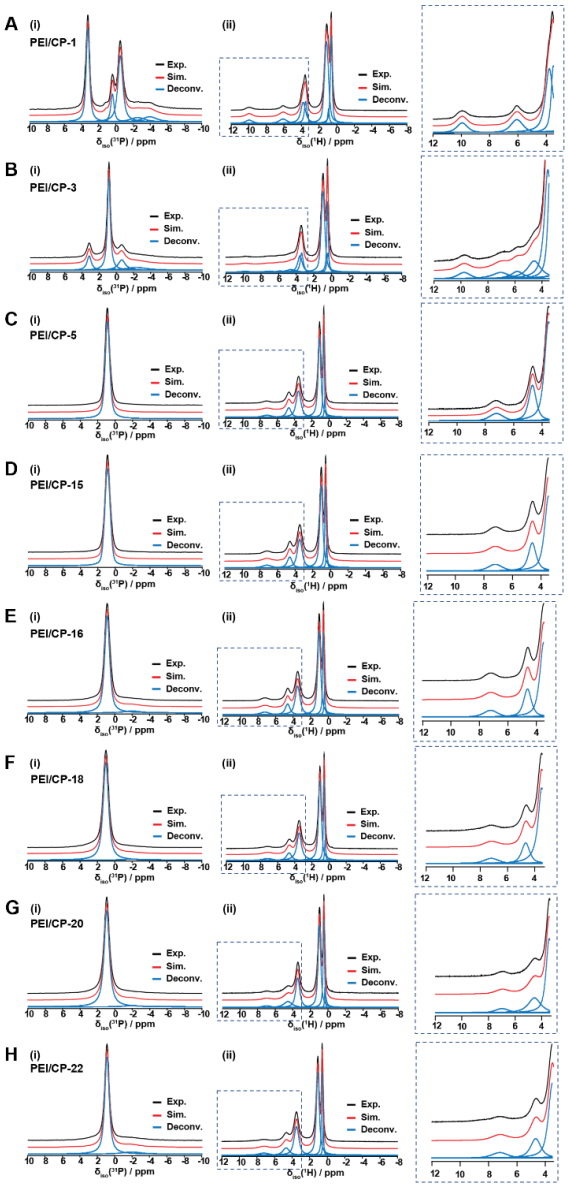

^{31}P and ^{1}H MAS NMR peaks

Sample	^{31}P δ_{iso} (ppm)	Speciation	Relative Intensity (%)	^{1}H δ_{iso} (ppm)	Speciation	Relative Intensity (%)
PEI/CP-1	3.3	Q^1	35	10.0	Amine	2.7
	1.1	Q^1	1	6.1	Amine	4.2
	0.4	Q^1	11	3.8	OH	15.2
	-0.5	Q^1	38	3.5	OH	8.6
	-2.6	Q^1	7	1.2	CH_2	43.6
	-4.0		8	0.9	CH_3	3.3
				0.6	CH_3	22.5
PEI/CP-3	3.2	Q^1	14	9.8	Amine	1.1
	0.9	Q^1	57	7.1	Amine	1.8
	0.3	Q^1	1	5.9	Amine	1.6
	-0.6	Q^1	16	4.6	OH	4.2
	-2.4	Q^1	12	3.6	OH	12.6
				3.4	OH	9.7
				1.0	CH_2	44.5
				0.5	CH_3	18.0
				0.4	CH_3	6.5
PEI/CP-5	0.9	Q^1	100	7.2	Amine	2.8
				4.7	OH	8.0
				3.5	OH	23.0
				1.1	CH_2	42.0
				0.6	CH_3	20.3
				0.5	CH_3	3.9
PEI/CP-15	0.9	Q^1	100	7.2	Amine	3.4
				4.6	OH	8.5
				3.5	OH	22.6
				1.0	CH_2	41.9
				0.6	CH_3	19.3
				0.4	CH_3	4.4
PEI/CP-16	0.9	Q^1	94	7.2	Amine	3.0
	-1.9	Q^1	6	4.7	OH	7.0
				3.5	OH	25.0
				1.1	CH_2	42.1
				0.6	CH_3	19.2
				0.5	CH_3	3.8
PEI/CP-18	1.0	Q^1	98	7.2	Amine	2.8
	-1.9	Q^1	2	4.7	OH	8.9
				3.5	OH	20.2
				2.4	CH_2	39.1
				1.1	CH_2	20.3
				0.6	CH_3	2.8
				0.5	CH_3	5.8
PEI/CP-20	0.9	Q^1	97	7.0	Amine	2.3
	-1.9	Q^1	3	4.6	OH	8.8
				3.4	OH	21.7
				1.0	CH_2	40.3
				0.5	CH_3	23.8
				0.1	CH_3	3.0
PEI/CP-22	0.9	Q^1	93	7.2	Amine	3.1
	-1.9	Q^1	7	4.7	OH	7.9
				3.5	OH	23.5
				1.1	CH_2	41.7
				0.6	CH_3	18.8
				0.5	CH_3	5.1

I

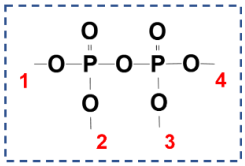

Figure 3.18 Solid state ^{31}P and ^{1}H MAS NMR spectra.

(A) PEI/CP-1 (B) PEI/CP-3, (C) PEI/CP-5, (D) PEI/CP-15, (E) PEI/CP-16, (F) PEI/CP-18, (G) PEI/CP-20, and (H) PEI/CP-22. (I) Scheme of the chemical structure of pyrophosphate. Red numbers show the four isolated oxygens. All ^{31}P resonances were observed between -4 and 4 ppm, which can be assigned to the Q^1 speciation.[325] PEI/CPs made from PEI-25k (PEI/CP-15, -16, -18, -20, and -22) have a dominant Q^1 peak at ~1 ppm, regardless of differences in PEI-25k concentration and reaction temperature. In contrast, there is a distribution of Q^1 species in PEI/CPs made from PEI-1.8k (PEI/CP-1 and -3). As the PEI-1.8k concentration increases (PEI/CP-1, -3, and -5), the number of Q^1 species decreases. ^{1}H MAS NMR results coincide with ^{31}P resonances; PEI-25k/CPs showed only a dominant ^{1}H MAS NMR amine peak at ~7.2 ppm, while PEI-1.8k/CPs contain multiple amine species between 5.9 ppm to 10 ppm. Again, as the PEI-1.8k concentration increases, the number of amine species decreases.

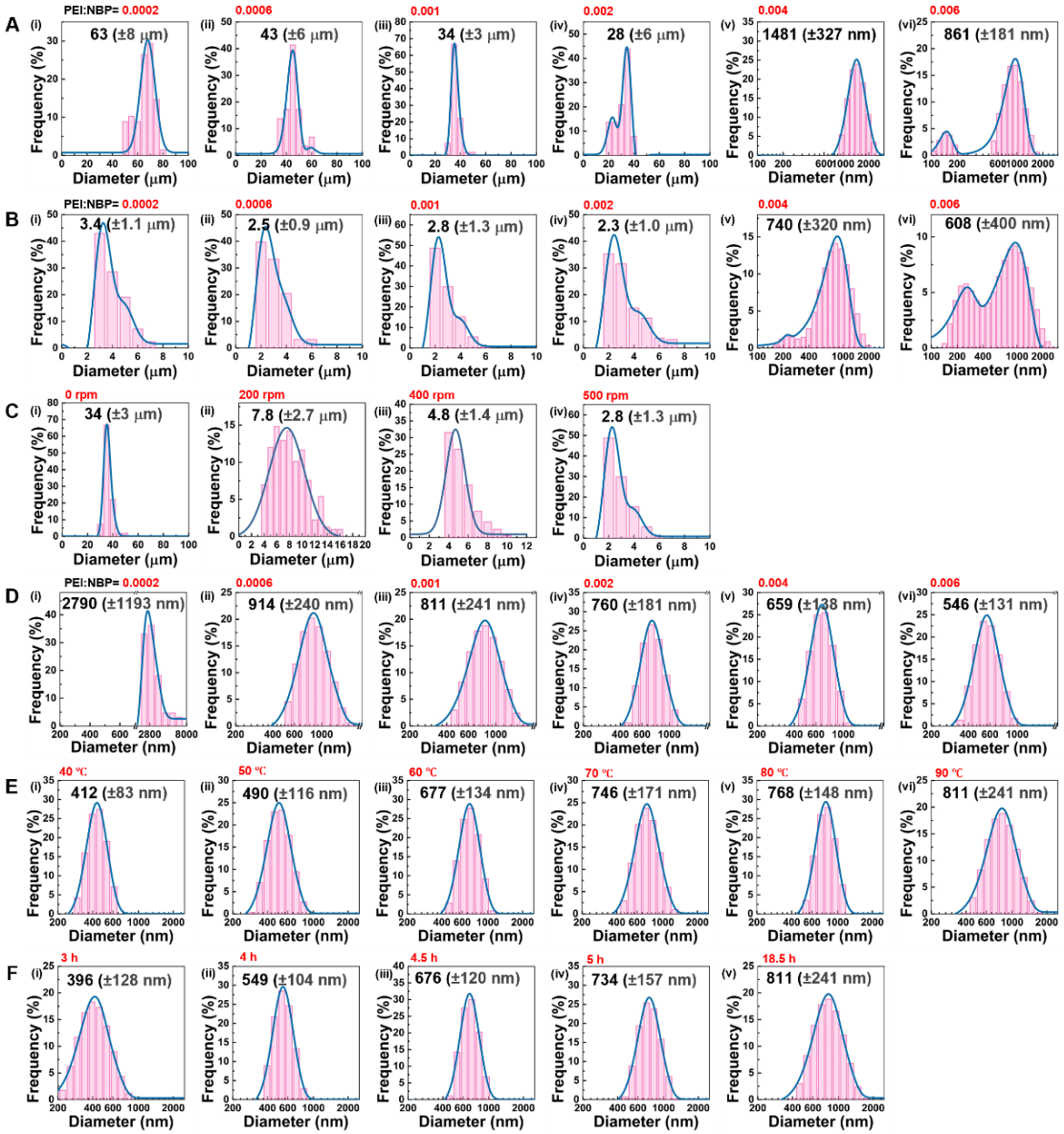

Figure 3.19 Size distribution of PEI/CPs.

Specific synthetic conditions: (A) PEI-1.8k at 90 ℃ for 18.5 hours without magnetic stirring and with varying PEI:NBP molar ratio (PEI/CP-1 to -6), (B) PEI-1.8k at 90 ℃ for 18.5 hours with magnetic stirring at 500 rpm and varying PEI:NBP molar ratio (PEI/CP-7 to -12), (C) PEI-1.8k at 90 ℃ for 18.5 hours with PEI:NBP molar ratio of 0.001 and varying stir speed (PEI/CP-3, -31, -32 and -9), (D) PEI-25k at 90 ℃ for 18.5 hours with magnetic stirring at 500 rpm and varying PEI:NBP molar ratio (PEI/CP-13 to -18), (E) PEI-25k for 18.5 hours with magnetic stirring at 500 rpm at varying temperature (PEI/CP-19 to -23 and -15), and (F) PEI-25k at 90 ℃ with magnetic stirring at 500 rpm for various reaction time (PEI/CP-27 to -30 and -15). The size of particles below 1.5 μm was measured by DLS, while those above were determined by optical microscopy image analysis of over 500 particles.

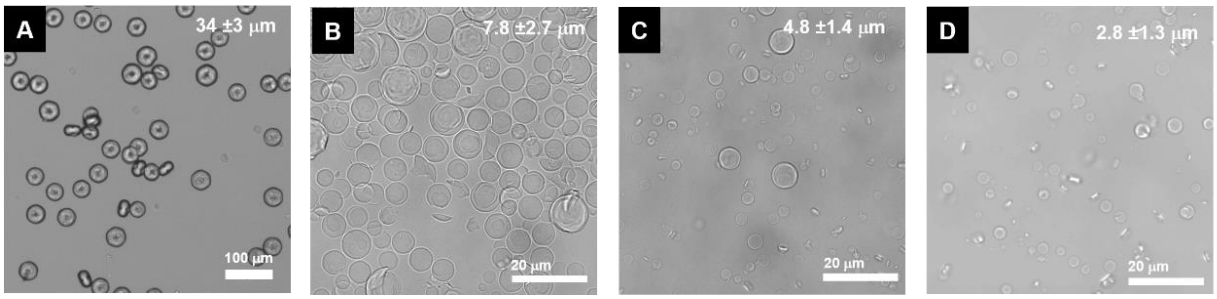

Figure 3.20 Optical microscopy images.

The particle diameter decreases with increasing stir speed. Specific conditions: PEI-1.8k, PEI:NBP molar ratio of 0.001, 90 °C, 18.5 hours and stir speed (A) 0 rpm (PEI/CP-3), (B) 200 rpm (PEI/CP-31), (C) 400 rpm (PEI/CP-32), and (D) 500 rpm (PEI/CP-9).

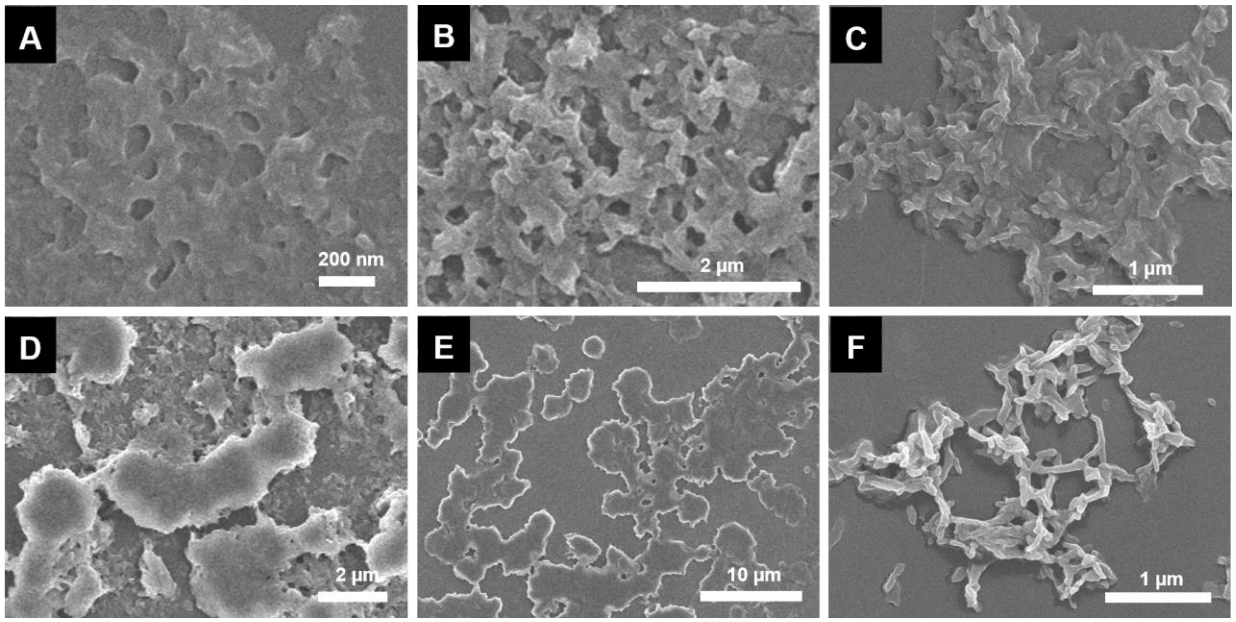

Figure 3.21 SEM images of PEI/CPs (PEI/CP-33 to -38).

Synthetic conditions: PEI-800, 90 ℃, 18.5 hours, stir speed 500 rpm, and PEI:NBP molar ratios of (A) 0.0002, (B) 0.0006, (C) 0.001, (D) 0.002, (E) 0.004, (F) 0.006.

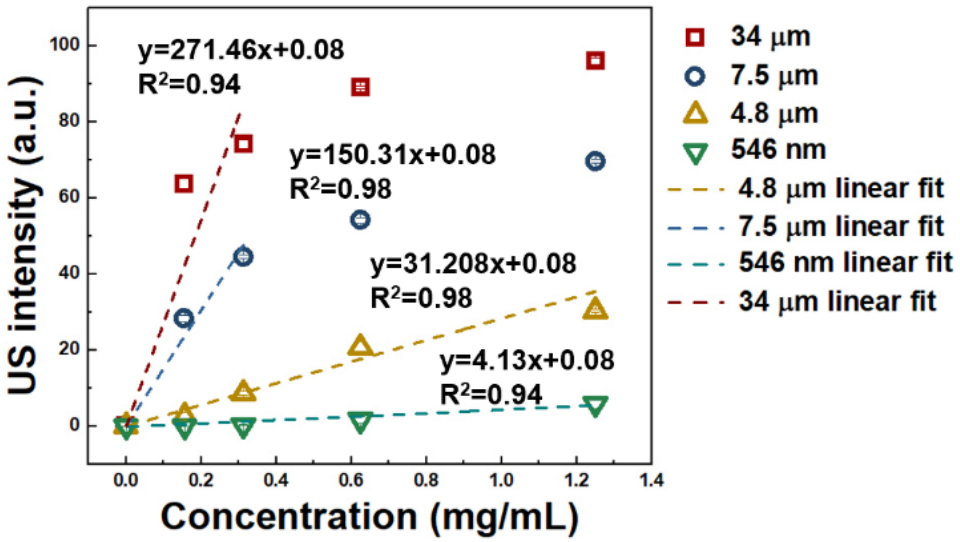

Figure 3.22 Plot of US intensity versus concentration.

From 0 – 1.4 mg/mL with linear fitting.

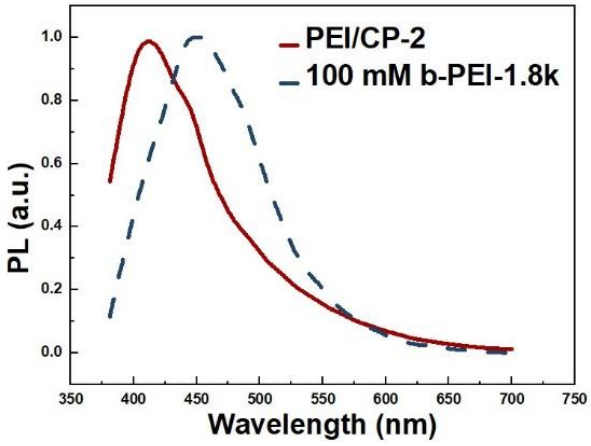

Figure 3.23 Photoluminescence emission spectra of PEI/CP-2 and PEI-1.8k.

Ethanol solution; excitation 350 nm.

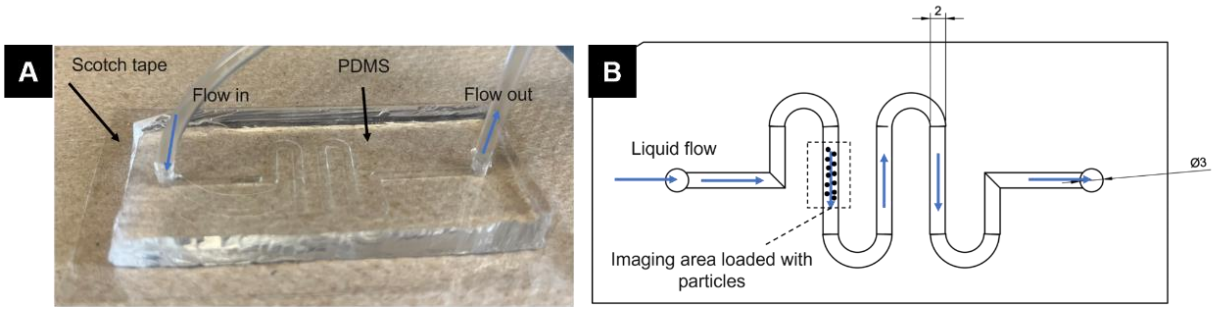

Figure 3.24 (A) Photo and (B) scheme of the flow cell setup for observing the PEI/CPs degradation under simulated human blood flow.

All measurements are in millimeters.

CHAPTER 4. PEPTIDE-DRIVEN PROTON SPONGE NANO-ASSEMBLY FOR IMAGING AND TRIGGERING IMMUNOGENIC CANCER CELL DEATH

4.1. ABSTRACT

Triggering immunogenic cell death (ICD, e.g., pyroptosis and necroptosis) of cancer cells with nanomedicines is an emerging approach for turning "immune-cold" tumors "hot"— a key challenge faced by cancer immunotherapies. Here, a proton sponge nano-assembly (PSNA) was created to image and trigger ICDs of cancer cells. The PSNA was constructed via conjugating low-molecular-weight branched PEI to a self-assembling peptide carrying tetraphenylethene pyridinium (PyTPE, an aggregation-induced emission-based luminogen). The self-assembly of PEI assisted by peptide-PyTPE led to the positive surface charge density and cell cytotoxicity of the PSNA. The self-assembly tendency of PSNA was optimized by tuning the hydrophilic and hydrophobic components. In turn, the PSNA with the highest fluorescence, positive surface charge density, intracellular fluorescence, and cancer cell cytotoxicity was achieved. Systematic mechanistic studies revealed that the lysosome rupturing-regulated pyroptosis and necroptosis are at least two causes of the cancer cell death. The known immunogenicity of pyroptosis and necroptosis implies the great potential of the PSNA to trigger anticancer immunity.

4.2. INTRODUCTION

Despite the potency of cancer immunotherapies (CIT) (e.g., immune checkpoint therapy), CIT only produces favorable responses in a minority of patients. This is because many cancer types are "immune-cold", i.e., they have mechanisms to suppress the immunity cycle involving antigen presentation, dendritic cells maturation, and T lymphocyte activation and infiltration.[332] Therefore, there is an urgent need to advance strategies for turning "cold" tumors "hot" (i.e., immune-active). A particularly appealing approach is applying nanomaterials to trigger immunogenic cell death (ICD) of cancer cells.[116-118]

Indeed, accumulating evidence supports that ICDs such as pyroptosis and necroptosis can convert immune-cold tumors into hot in-situ vaccines by releasing damage-associated molecular patterns (DAMPs) along with tumor-associated antigens from dying tumor cells; The released DAMPs including pro-inflammatory cytokines (e.g., Interleukin-1β (IL-1β) and IL-18), calreticulin, heat-shock proteins (e.g., HSP70 and HSP90), adenosine triphosphate (ATP), and/or high-mobility group box protein 1 (HMGB1) can stimulate the maturation of dendritic cells and the activation and infiltration of T cells, thus boosting anti-cancer immunity.[116-122] Furthermore, existing nanomaterials has been reported to trigger pyroptosis (e.g., nano-carbons,[147-148] silica nanoparticles (NPs),[149] quantum dots (QDs)[150], and metallic NPs[151]). These findings have inspired the emergence of nanomedicines with pyroptosis-induced anticancer immunity including inorganic NPs generating reactive oxygen species (ROS) (e.g., modified magnetic iron oxide NPs[333]), NPs disrupting ionic homeostasis[118, 303, 334] (e.g., NaCl NPs[334]), NPs generating photon-assisted ROS[117, 335] (e.g., acid-activatable nano-photosensitizer for PDT[335]), and nano-formulations encapsulating pyroptosis-drugs[116, 336] (e.g., liposome-based[336]).

While promising, these nanomedicines also have major limitations. For example, most non-degradable inorganic NPs can cause toxicity in vivo;[41-42, 290] NPs disrupting ionic homeostasis, such as NaCl NPs, are unstable in aqueous solution due to quick dissolution (half-life ~2.5 h);[334] NPs relying on photons to generate ROS are limited by the penetration depth of light and sophisticated instrumentation;[337] Nanoformulations of pyroptosis-drugs suffer from drug leakage[338] and cumbersome design for tumor targeting.[339] Ideally, future nanomedicines for inducing anticancer pyroptosis should be biodegradable, biocompatible, cancer-targeting, and intrinsically potent in triggering pyroptosis without the aid of external stimulus such as light.

Targeting lysosomes may provide an alternative solution. More than a membrane-enclosed and acidic organelle digesting and recycling intracellular macromolecules, the lysosome also plays a pivotal role in regulating cell death.[340] Damaged lysosomes not only interrupt intracellular macromolecule digestion but also cause the release of lysosome enzymes (e.g., hydrolytic cathepsins), both of which can trigger ICDs such as pyroptosis and necroptosis.[134, 341] Moreover, cancer cells have weaker lysosomal membranes than noncancerous cells.[342-343]

Polycations such as high-molecular-weight branched polyethylenimine (hwPEI, e.g., PEI-25kDa) are well-known for cell cytotoxicity originating from lysosome rupturing. This can be explained by the proton sponge effect[344-345], where hwPEI enhances the pH of lysosomes via the protonation of rich amine groups. Lysosomes actively concentrate protons (H^+ ions) via the proton pump to maintain acidic pH. This is accompanied by an increased influx of counterions (e.g., Cl^-), water, and, eventually, an increased osmotic pressure that ruptures lysosomes. However, the translation of hwPEI to a nanomedicine for anticancer immunity is hindered by uncontrollable toxicity due to fixed positive charge density.

Interestingly, low-molecular-weight branched PEI (lwPEI, e.g., 800 Da) does not possess cell cytotoxicity due to a lower buffering capacity.[345-346] We hypothesized that the positive surface charge density would be enhanced when lwPEI underwent self-assembly driven by a peptide, causing a dramatic enhancement in lysosome rupturing capability and cell cytotoxicity. A successful validation of this hypothesis could lead to an anticancer nanomedicine with numerous advantages. First, if the cell cytotoxicity were controllable by the self-assembly, then cancer-specific toxicity could be achievable by rendering the self-assembly activatable by tumors. Second, peptides can be easily functionalized with small molecules (e.g., drugs[347] and imaging molecules[348]). Third, the nanomedicine could be degraded into renal clearable amino acids, lwPEI, and/or other small molecules in vivo, considering the proven biodegradability of peptides[349] and the cut-off molecular weight ~30 - 50 kDa for glomerular filtration[350]. Finally, the formation of nano-assemblies introduces other advantages of nanomaterials, such as slower blood clearance and excellent tumor accumulation via the enhanced permeability and retention (EPR) effect.[116]

Here, we report the engineering of a proton sponge nano-assembly (PSNA) optimized for imaging and triggering potent pyroptosis and necroptosis of cancer cells via lysosome rupturing. A series of PSNA compounds were created by conjugating lwPEI with different self-assembling peptides carrying a tetraphenylethene pyridinium (PyTPE, an aggregation-induced emission (AIE)-based luminogen (AIEgen)). A systematic comparison of zeta potential and cell cytotoxicity was made between peptide-PyTPE-PEI and various combinations of its building blocks, thus revealing that peptide-PyTPE-PEI has the maximized positive surface charge density and cell cytotoxicity from the surface accumulation of PEI assisted by self-assembling peptide-PyTPE. PSNA was further optimized for cell imaging and cell cytotoxicity by tuning the number of hydrophilic and hydrophobic amino acids of the peptide and detailed characterizations of as-

formed nano-assemblies: morphology, size, self-assembly tendency (e.g., particle number concentration and AIE fluorescence), zeta potential, intracellular fluorescence, and cell cytotoxicity. The cell death mechanism triggered by the PSNA was studied in detail and indicates lysosome-regulated pyroptosis and necroptosis.

4.3. MATERIALS AND METHOD

4.3.1. Synthesis of Peptides (Acetylated)

The synthesis of peptides used the standard solid phase Fmoc synthesis method using 200 mg Fmoc-Gly-Wang resin. 2 × 4 mL 20% piperidine in DMF, 0.1 M amino acid in 3 mL DMF (5 equivalents), 0.1 M HBTU in 3 mL DMF (5 equivalents), and 0.2 M DIPEA in 3 mL DMF (10 equivalents) were used for each coupling cycle under the protection of nitrogen. After the completion of solid phase synthesis, the resin with peptides was washed by DMF three times and incubated with 0.5 mL pyridine and 0.5 mL acetic anhydride in 4 mL DMF at room temperature for 1 h for acetylation followed by three rounds of DCM washing and vacuum drying. When cleavage was necessary, acetylated peptides were cleaved off the resins by treating with cleavage cocktail containing trifluoroacetic acid (TFA, 88% v/v), phenol (5% w/v), water (5% v/v), and triisopropyl silane (TIPS, 2% v/v) for two hours followed by filtration to remove resin. Peptides were precipitated by addition of ice-cold diethyl ether to the filtrates (filtrates: diethyl ether = 1:9) and centrifuged. Peptides in the pellet were vacuum dried. Crude peptides were purified using semi-preparative HPLC. For peptides to be used for the synthesis of $(PAS)_1F_0$, $(PAS)_1F_1$, $(PAS)_1F_2$, $(PAS)_3F_2$, and $(PAS)_6F_2$, peptides are left intact on resin without cleavage.

4.3.2. Synthesis of Azide-Functionalized Tetraphenylethene Pyridinium (PyTPE)

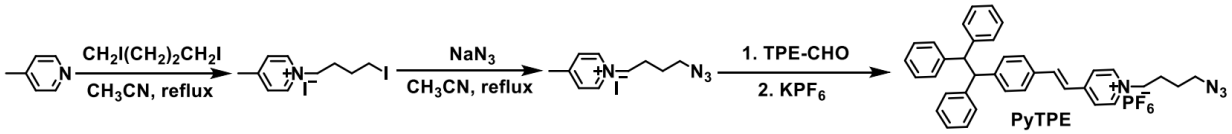

Scheme S1. The synthetic routes of PyTPE

PyTPE was synthesized according to the procedures in literatures.[351] Crude PyTPE was purified using semi-preparative HPLC. See Figure 4.12 for ^{1}H NMR and mass spectra.

4.3.3. Synthesis of Peptide-PyTPE

Coupling of PyTPE with peptides was via the copper-catalyzed azide-alkyne click reaction. Crude peptide on resin (before cleavage, 0.12 μmol), PyTPE (64 mg, 0.12 μmol), sodium ascorbate (47.5 mg, 0.24 μmol), and copper (I) iodide (45.7 mg, 0.24 μmol) were dissolved in DMSO/H_2O (v/v=9:1) solution and stirred at 60 °C for 24 h under the protection of nitrogen. The resin with peptide-PyTPE was washed by DMF three times, followed by three-time DMF and DCM wash, respectively, and vacuum dried. Peptide-PyTPE was cleaved of the resins by treating with cleavage cocktail containing TFA (88% v/v), phenol (5% w/v), water (5% v/v), and TIPS (2% v/v) for two hours followed by filtration to remove resin. Peptide-PyTPE was precipitated by addition of ice-cold diethyl ether to the filtrates (filtrates: diethyl ether = 1:9) and centrifuged. The pellet was vacuum dried. Crude peptide-PyTPE was purified using semi-preparative HPLC.

4.3.4. Synthesis of Peptide-PEI

Purified peptide (0.037 μmol), HBTU (0.149 μmol, 4 equivalents), and DIPEA (0.297 μmol, 8 equivalents) were dissolved in 5 mL DMF and vortexed for 20 seconds and then added to branched PEI (800 Da) (0.186 μmol, 5 equivalents) pre-dissolved in 1 mL DMF under nitrogen protection. The solution was stirred at 60 °C for 24 h under the protection of nitrogen. Peptide-PEI was precipitated by addition of ice-cold diethyl ether to the solution (solution: diethyl ether = 1:9) and centrifuged. The pellet was vacuum dried. Crude peptide-PEI was purified using semi-preparative HPLC.

4.3.5. Synthesis of Peptide-PyTPE-PEI

Peptide-PyTPE (0.037 μmol), HBTU (0.149 μmol, 4 equivalents), and DIPEA (0.297 μmol, 8 equivalents) were dissolved in 5 mL DMF and vortexed for 20 seconds and then added to branched PEI (800 Da) (0.186 μmol, 5 equivalents) pre-dissolved in 1 mL DMF under nitrogen

protection. The solution was stirred at 60 °C for 24 h under the protection of nitrogen. Peptide-PyTPE-PEI was precipitated by addition of ice-cold diethyl ether to the solution (solution: diethyl ether = 1:9) and centrifuged. The pellet was vacuum dried. Crude peptide-PyTPE-PEI was purified using semi-preparative HPLC.

4.3.6. Cell Culture

HeLa cells (Sigma Aldrich) were grown in DMEM (Dulbecco's Modified Eagle's Medium, Gibco, Lot No. 2263286). SKOV-3 cells (Sigma Aldrich) were grown in McCoy's 5A Medium (modified, Gibco, Lot No. 2193402). All the cell culture media were supplemented with 10% fetal bovine serum (FBS) and 100 units/mL of penicillin and 100 units/mL streptomycin (MediaTech, USA). All cells were maintained in a humidified, 5% carbon dioxide atmosphere at 37 °C.

4.3.7. CellTiter-Blue Cell Viability Assay to Study Cell Cytotoxicity

Cells were seeded into 96-well plates at the density of 1×10^4 cells in 100 µL medium per well and incubated overnight. Then the cells were treated with 10 µL various compounds dispersed in PBS (phosphate-buffered saline, 1×, Corning, Lot No.: 31222010) for 48 h. 20 µL CellTiter-Blue Cell Viability assay (Promega, G8080) was then added to each well. After incubation for another 2 h, the fluorescence was read with a plate-reader (Synergy H1, BioTek). Controls settings are as follows:

Blank well: cell culture medium + assay

Negative control: cells + cell culture medium + assay

Positive control: cells + cell culture medium + assay + 1 mg/mL PEI-25kDa

The cell viability was calculated as follows:

$$\text{Cell viability} = \frac{\text{FL}_{\text{exp}} - \text{FL}_{\text{blank}}}{\text{FL}_{\text{negative control}} - \text{FL}_{\text{blank}}} \times 100\%$$

Zeta potential and critical zeta potential change concentration

Zeta potential of compounds were measured using the diffusion barrier method.[352] Disposable folded capillary cells (Malvern, DTS1070) was pre-filled with PBS (phosphate-buffered saline, 1×, Corning, Lot No.: 31222010). 50 µL compounds in PBS was gently loaded into the bottom of the cell and zeta potential was immediately measured with a Malvern NANO-ZS90 Zetasizer. This whole process was triplicated for each measurement. Zeta potential versus concentration of compounds was plotted. The plot before reaching plateau was divided into two linear region and linearly fitted. The critical zeta potential change concentration was determined by the interception of the two linear fittings.

4.3.8. Transmission Electron Microscopy Imaging (TEM)

TEM images were acquired with a Jeol 1400 plus microscope (voltage 80 KeV). Compounds in PBS (125 µM) were drop-coated on copper TEM grids and dried at room temperature. Compound-coated TEM grids were further stained by drop coating uranyl acetate (2%, Electron Microscopy Sciences, Lot No.: 210205-01) for 20 s, followed by dropping DI water three times and drying at room temperature.

4.3.9. Particle Number Concentration, Size Distribution, and Light Scattering Imaging

Particle number concentration, size distribution, and light scattering images were acquired from 62.5 µM compounds in PBS using multi-laser nanoparticle tracking analysis (MANTA, Horiba).

4.3.10. Aggregation Induced Fluorescence Emission

100 µM compounds (OD = 0.1) in PBS were added to a 96-well plate and the emission spectra were read by a plate-reader (Synergy H1, BioTek) with an excitation at 405 nm and step resolution of 10 nm.

4.3.11. Confocal Imaging of Intracellular Fluorescence

SKOV-3 cells were seeded at a density of 2×10^4 in 200 µL medium in 35 mm dishes (Cellvis, Lot No.: D35-14-1.5-N) and cultured overnight followed by treatment of 250 µM compounds for 30 min. Cells were washed thrice with PBS. Cells were incubated with Hoechst 33342 (1 µg/mL, Immunochemistry) for 10 min. Cells were washed thrice with PBS and fixed by 4% paraformaldehyde in PBS (Thermo Scientific) at room temperature for 20 min. Cells were imaged by a confocal microscope (Leica SP8 with lighting deconvolution). Ex/Em for Hoechst 33342: 400 nm/410-430 nm; Ex/Em for tested compounds:400 nm/550-700 nm.

4.3.12. Optical Microscopy Imaging of Cell Bursting

Cells were seeded at a density of 2×10^4 in 100 µL in 96-well plates and cultured overnight. The medium was replaced by CO_2-independent medium (10% FBS, Gibco, 18-045-088) Cells were treated by 250 µM $(PAS)_1F_2$ compound followed by immediate time-lapse images acquisition at room temperature for 4 h. The same process was repeated for cells without $(PAS)_1F_2$ treatment as negative controls. Data was presented either as images or in video format.

4.3.13. Realtime-Glo Annexin V Apoptosis and Necrosis Assay to Study the Cell Death Mode

SKOV-3 cells were seeded at a density of 2500 cells in 12.5 µL CO_2-independent medium (Gibco, 18-045-088) in 384-well plates (Corning, white solid, CLS3570) and cultured overnight. The Realtime-Glo Annexin V Apoptosis and Necrosis assay (Promega, JA1011) was performed following the manufacturer's protocol. Cells were then immediately treated by 10 µg/mL digitonin (apoptosis positive control) or 250 µM $(PAS)_1F_2$. Luminescence and fluorescence were continuously read for 20 h at 37 ℃ with a plate-reader (Synergy H1, BioTek). The same process was repeated for cells without compound treatment for negative control.

4.3.14. Celltiter-Glo 2.0 Assay to Assess the ATP Level

SKOV-3 cells were seeded into 384-well plates (Corning, white solid, CLS3570) at a density of 2500 cells in 25 µL medium per well and incubated overnight. Then the cells were treated with 10 µL $(PAS)_1F_2$ (250 µM) for 24 h at 37 °C. After equilibrating the cells to room temperature, 25 µL CellTiter-Glo 2.0 Assay (Promega) was added and the luminescence was read after 15 min with a plate-reader (Synergy H1, BioTek). Controls settings are as follows:

Blank well: cell culture medium + assay

Negative control: cells + cell culture medium + assay

The relative ATP level was calculated as follows:

$$\text{Relative ATP level} = \frac{\text{Lumi.}_{\text{exp}} - \text{Lumi.}_{\text{blank}}}{\text{Lumi.}_{\text{negative control}} - \text{Lumi.}_{\text{blank}}} \times 100\%$$

4.3.15. Flow Cytometry to Study the Mechanism of Cell Internalization of $(PAS)_1F_2$

SKOV-3 cells were seeded at a density of 5×10^5 in 1 mL medium per well in a 12-well plate and cultured overnight. Cells inhibitions were achieved by 4 °C incubation or endocytic inhibitors treatment for 15 min. For endocytic inhibitors treatment, pitstop 2 (TargetMol, Lot No.: 148603), filipin from *S. filipinensis* (MedChemExpress, Lot No.:152222), 5-(N-ethyl-N-isopropyl)amiloride (EIPA, MedChemExpress, Lot No.:238298) were added to the cells to achieve final concentrations of 36, 15, and 45 µg/mL, respectively. After inhibition, cells were incubated with 250 µM $(PAS)_1F_2$ for 30 min at 4 °C or 37 °C (for endocytic inhibitors) after which the culture medium was removed, and cells were washed twice with PBS and detached with trypsin. The detached cells were suspended in PBS solution, centrifuged for 5 min at 400 x g and 4 °C. PBS was removed and replaced with 4% formaldehyde in PBS. The cells were incubated at room temperature for 20 min and centrifugation washed with a fresh portion of PBS. The cells were analyzed with BD FACSCelesta flow cytometer, registering 10000 events per sample. To verify

the efficacy of endocytic inhibitors, cells were inhibited by endocytic inhibitors as mentioned and FITC-labelled transferrin (5 μg/mL) (Jackson Immunoresearch Labs), dextran (100 ug/mL) (MedChemExpress, Lot No.:178439), and cholera toxin B subunit (10 μg/mL) (Sigma Aldrich) were added in replacement of $(PAS)_1F_2$ to pitstop 2 (36 μg/mL), EIPA (45 μg/mL), and filipin (15 μg/mL), inhibited cells, and incubated for 20 min, 1 h, and 1.5 h, respectively. Data were analyzed using FlowJo. Inhibition rate was calculated as follows:

$$\text{Inhibition} = \frac{\text{FL}_{\text{inhibition}} - \text{FL}_{\text{blank}}}{\text{FL}_{\text{staining}} - \text{FL}_{\text{blank}}} \times 100\%$$

$FL_{inhibition}$: fluorescence signals from inhibited cells with staining by either $(PAS)_1F_2$ or FTIC markers.

FL_{blank}: background fluorescence signals from cells without inhibition and staining.

$FL_{staining}$: fluorescence signals from stained cells (either $(PAS)_1F_2$ or FTIC markers) without inhibition.

4.3.16. Confocal Imaging to Study the Colocalization of $(PAS)_1F_2$ with Lysosomes and Mitochondria

SKOV-3 cells were seeded at a density of 2×10^4 in 200 μL medium in 35 mm dishes (Cellvis, Lot No.: D35-14-1.5-N) and cultured overnight. Cells were stained by Magic Red Cathepsin B assay (30 min, 25×, Immunochemistry, Catalog No.: 937, Lot No.: 23F15) or MitoView 633 (30 min, 100 nM, Biotium) to label lysosomes or mitochondria, followed by three rounds of PBS washing. The cells were then treated with $(PAS)_1F_2$ (250 μM) for 5, 15, or 30 min and washed by PBS three times. PBS was replaced by CO_2-independent medium (Gibco, 18-045-088) and immediately imaged by a confocal microscope (Leica SP8 with lighting deconvolution). Ex/Em for Magic Red Cathepsin B: 600 nm/630-700 nm; Ex/Em for MitoView 633: 630 nm/650-

700 nm; Ex/Em for $(PAS)_1F_2$:400 nm/550-700 nm. The Mander's colocalization coefficients were analyzed using ImageJ (JACoP plugin) for three confocal images.

4.3.17. Confocal Imaging to Assess Lysosome and Mitochondria Integrity

SKOV-3 cells were seeded at a density of 2×10^4 in 200 μL medium in 35 mm dishes (Cellvis, Lot No.: D35-14-1.5-N) and cultured overnight. Cells were stained by acridine orange for labeling lysosome (30min, 20 μM, Immunochemistry) or MitoView 633 (30 min, 100 nM, Biotium) for labeling mitochondria and washed by PBS three times, followed by staining with Hoechst 33342 (10 min, 1 μg/mL, Immunochemistry) and 3-time PBS wash. Subsequently, cells were treated with $(PAS)_1F_2$ (250 μM) for 1h and washed by PBS three times. PBS was replaced by CO_2-independent medium (Gibco, 18-045-088) and immediately imaged by a confocal microscope (Leica SP8 with lighting deconvolution). The same process was repeated for cells without $(PAS)_1F_2$ treatment as negative control. Ex/Em for acridine orange: 470 nm/630-700 nm; Ex/Em for MitoView 633: 630 nm/650-700 nm; Ex/Em for Hoechst 33342: 400 nm/410-430 nm; Ex/Em for $(PAS)_1F_2$:400 nm/550-700 nm. Organelles integrity was analyzed for 3 confocal images and calculated as follows:

$$\text{Integrity} = \frac{(\text{FL}_{\text{red}}/\text{FL}_{\text{blue}})_{\text{exp}}}{(\text{FL}_{\text{red}}/\text{FL}_{\text{blue}})_{\text{negative control}}} \times 100\%$$

$(FL_{red}/FL_{blue})_{exp}$: red fluorescence (organelles) normalized by blue fluorescence (nuclei) from the experiment group.

$(FL_{red}/FL_{blue})_{negative\ control}$: red fluorescence (organelles) normalized by blue fluorescence (nuclei) from the negative control group.

4.3.18. Magic Red Cathepsin B Assay for Assessment of Cathepsin B Release

SKOV-3 cells were seeded at a density of 2×10^4 in 200 μL medium in 35-mm dishes (Cellvis, Lot No.: D35-14-1.5-N) and cultured overnight. Cells were stained by Magic Red

Cathepsin B assay (30 min, 25×, Immunochemistry, Catalog No.: 937, Lot No.: 23F15) for labeling cathepsin B and washed by PBS three times followed by staining with Hoechst 33342 (10 min, 1 μg/mL, Immunochemistry) and PBS washing thrice. Subsequently, cells were treated with $(PAS)_1F_2$ (250 μM) for 10, 20, and 25 min, respectively and washed by PBS three times. Cells were fixed by 4% paraformaldehyde in PBS (Thermo Scientific) at room temperature for 20 min and immediately imaged by a confocal microscope (Leica SP8 with lighting deconvolution). The same process was repeated for cells without $(PAS)_1F_2$ treatment as negative control. Ex/Em for Magic Red Cathepsin B: 600 nm/630-700 nm; Ex/Em for Hoechst 33342: 400 nm/410-430 nm; Ex/Em for $(PAS)_1F_2$:400 nm/550-700 nm.

4.3.19. FLICA 660 Caspase-1 Assay for Assessment of Cleaved Caspase-1

SKOV-3 cells were seeded at a density of 2×10^4 in 200 μL medium in 35 mm dishes (Cellvis, Lot No.: D35-14-1.5-N) and cultured overnight. Cells were co-incubated with FLICA 660 Caspase-1 assay (30×, Immunochemistry, Catalog No.: 9122, Lot No.: 22B28) and compounds ($(PAS)_1F_2$ (250 μM, 1 h) or Nigericin (20 μM, 24 h, Immunochemistry) and washed by PBS three times. Cells were stained with Hoechst 33342 (1 μg/mL, 10 min, Immunochemistry) and washed thrice with PBS. Cells were then fixed with 4% paraformaldehyde in PBS (Thermo Scientific) at room temperature for 20 min and immediately imaged by a confocal microscope (Leica SP8 with lighting deconvolution). Ex/Em for FLICA 660: 630 nm/650-700 nm; Ex/Em for Hoechst 33342: 400 nm/410-430 nm; Ex/Em for $(PAS)_1F_2$:400 nm/550-700 nm.

4.3.20. Western Blot Analysis

SKOV-3 cells were seeded at a density of 4×10^5 per well in a 6-well plate and cultured overnight. The medium was replaced/washed by FBS-free medium three times. Depending on targeted proteins, cells were challenged by 250 μM $(PAS)_1F_2$ for 30 min (for cleaved caspase-3 and -8), 1 h (for cleaved caspase-1, GSDMD-NT, P-MLKL, and cleaved caspase-3 and -8), or 4 h

(for IL-1β). The conditioned medium was removed for later use. Cells were washed by PBS three times and lysed for 30 min at 4°C in RIPA buffer containing protease and phosphatase inhibitor cocktail (Thermo Scientific, 78441) and centrifuged at 12,000 × g for 10 min. The conditioned medium (serum free) was centrifuged at 500 g for 5 min to remove cell debris and then concentrated by Centrifugal Filters (Amicon® Ultra, 10 kDa NMWCO). Protein concentrations were measured and held consistent via a bicinchoninic acid assay (BCA) protein assay kit (Bio-Rad, 5000002). All samples were boiled in loading buffer for 10 min before gel electrophoresis. Proteins were separated by 4-12% NuPAGE Bis-Tris gels and transferred to PVDF membranes. Membranes were blocked with 5% nonfat dry milk and incubated with primary antibodies at 4 °C overnight. Then, membranes were incubated with horseradish peroxidase-conjugated goat anti-mouse IgG (Cell Signaling Technology, 7076) or goat anti-rabbit IgG (Cell Signaling Technology, 7074) for 1 h at RT. Blots were visualized using ECL substrate (Thermo Scientific, 35050). The following primary antibodies were used: anti-GAPDH (Proteintech, HRP-60004), Apoptosis/Necroptosis Antibody Sampler Kit (Cell Signaling Technology, 92570), and Pyroptosis Antibody Sampler Kit (Cell Signaling Technology, 43811).

4.3.21. Lumit Human IL-1β Immunoassay for Detection of Cleaved IL-1β In Medium

SKOV-3 cells were seeded into 384-well plate (Corning, white solid, CLS3570) at a density of 2000 cells in 18 µL medium per well and cultured overnight. Cells were challenged by $(PAS)_1F_2$ (250 µM) or Nigericin (20 µM) for 1h. Lumit Human IL-1β Immunoassay (Promega) was performed following the manufacturer's protocol. The luminescence signal was read with a plate-reader (Synergy H1, BioTek) and the concentration of cleaved IL-1β in the conditioned medium was calculated from a standard curve of luminescence versus concentration.

4.3.22. Inhibition of Cell Death

Cells were seeded into 384-well plates at the density of 2500 cells in 25 µL medium per well and incubated overnight. Cells were incubated with either NaCl in water or inhibitors in PBS (CA-074, Pepstatin A, E-64d, zVAD-fmk, and necrosulfonamide (NSF), all from Apexbio Technology) for 1 h followed by $(PAS)_1F_2$ (125 or 250 µM) for 24 h. Here, 5 µL CellTiter-Blue Cell Viability assay (Promega, G8080) was then added to each well. After incubation for another 2 h, the fluorescence was read and the cell viability was calculated as mentioned before.

4.4. RESULTS AND DISCUSSION

4.4.1. Proof of Concept: Self-Assembly Controllable Surface Charge Density and Cell Cytotoxicity

We envisioned that lwPEI conjugated to a self-assembling peptide carrying PyTPE could form the proton sponge nano-assembly (PSNA) in aqueous environment. The PSNA would have both enhanced fluorescence (from AIEgen aggregation) and positive surface charge density (from PEI aggregation) compared to its building blocks (Figure 4.1 (A)). The enhanced fluorescence could be useful for cell imaging, while the increased positive surface charge density could boost cell cytotoxicity and trigger immunogenic cancer cell death (Figure 4.1 (B)).

We synthesized a series of PSNA compounds with the formula (ACE)LAGGGG$(F)_y$Pra(PyTPE)$(PAS)_x$G(PEI) (reads from the N-terminal to C-terminal) (Figure 4.1 (A); see Materials and Method and Figure 4.12-Figure 4.18 for method and mass and NMR spectra). Single-letter codes[353] were used for amino acids unless otherwise specified. ACE represents acetylation. LAG is a fragment of PLG*LAG (i.e., a matrix metalloproteinases-2 (MMP-2)-cleavable substrate), which is to make the current design compatible with future functionalization with MMP-2 cleavable cargos (e.g., imaging agents and drugs). For example, cargo-PLG*LAGGGG$(F)_y$Pra(PyTPE)$(PAS)_x$G(PEI) can be cleaved by MMP-2 to release cargo-PLG and PSNA. G is a common spacer. Pra represents L-propargylglycine containing an alkyne group for conjugating azide-PyTPE via click chemistry. PEI-800 Da is to offer positive charges and PyTPE to introduce AIE fluorescence and hydrophobicity. F (hydrophobic) and PAS (combination of P, A, and S, hydrophilic[354]) are the amino acids whose repetition number can be

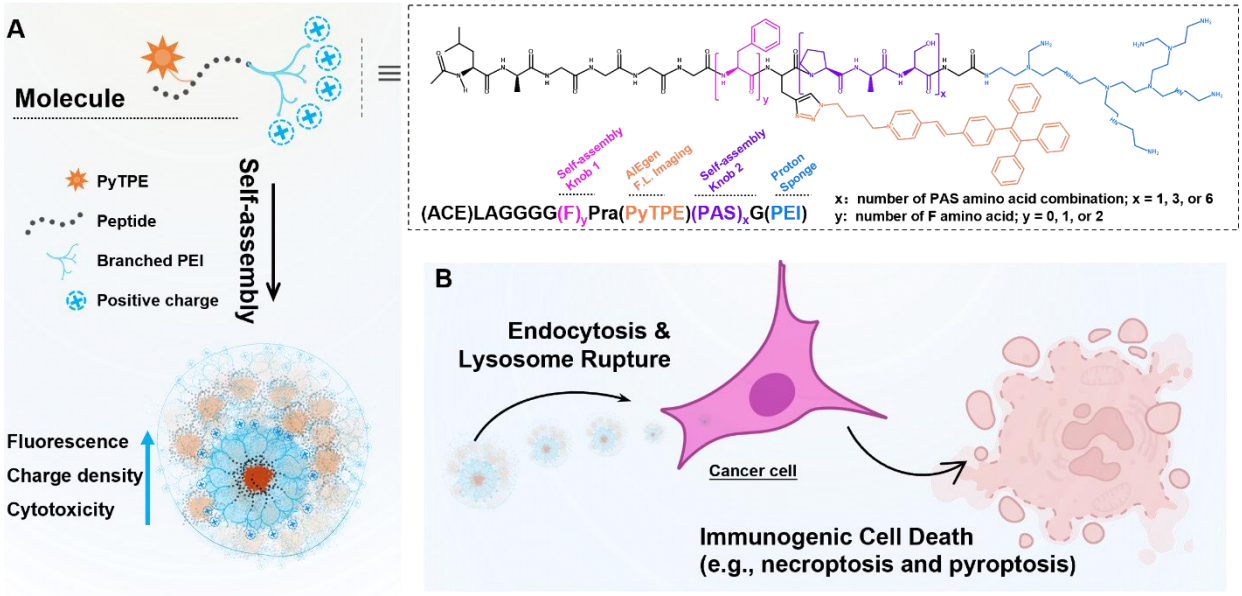

Figure 4.1 Design of the proton sponge nano-assembly (PSNA).

(A) Scheme showing the chemical structure of the PSNA monomer and the formation of the proton sponge nano-assembly from PSNA monomer. The assembly enhances the aggregation-induced fluorescence, charge density, and cell cytotoxicity. (B) Scheme showing that PSNAs can be internalized by cancer cells via endocytosis to trigger immunogenic cell death pathways such as necroptosis and pyroptosis.

varied to further control the self-assembly tendency of PSNAs. These compounds were named $(PAS)_xF_y$. For example, $(PAS)_1F_2$ is (ACE)LAGGGGFFPra(PyTPE)PASG(PEI).

As a proof of concept, $(PAS)_1F_2$ and its building blocks were compared to understand whether the self-assembly can control the surface charge density and cell cytotoxicity (i.e., PEI, peptide-PEI, peptide-PyTPE-PEI, peptide, and peptide-PyTPE. Figure 4.2. See Figure 4.12, Figure 4.13, and Figure 4.16 for mass and NMR spectra). These compounds can be divided into two groups: positively charged (PEI, peptide-PEI, and peptide-PyTPE-PEI) and negatively charged (peptide and peptide-PyTPE). In both groups, only the compound containing PyTPE self-assembled (i.e., peptide-PyTPE-PEI and peptide-PyTPE) as evidenced by TEM images (Figure 4.2 (B)) and a significantly higher particle number concentration (n=3, $P<0.001$, Figure 4.2 (C)).

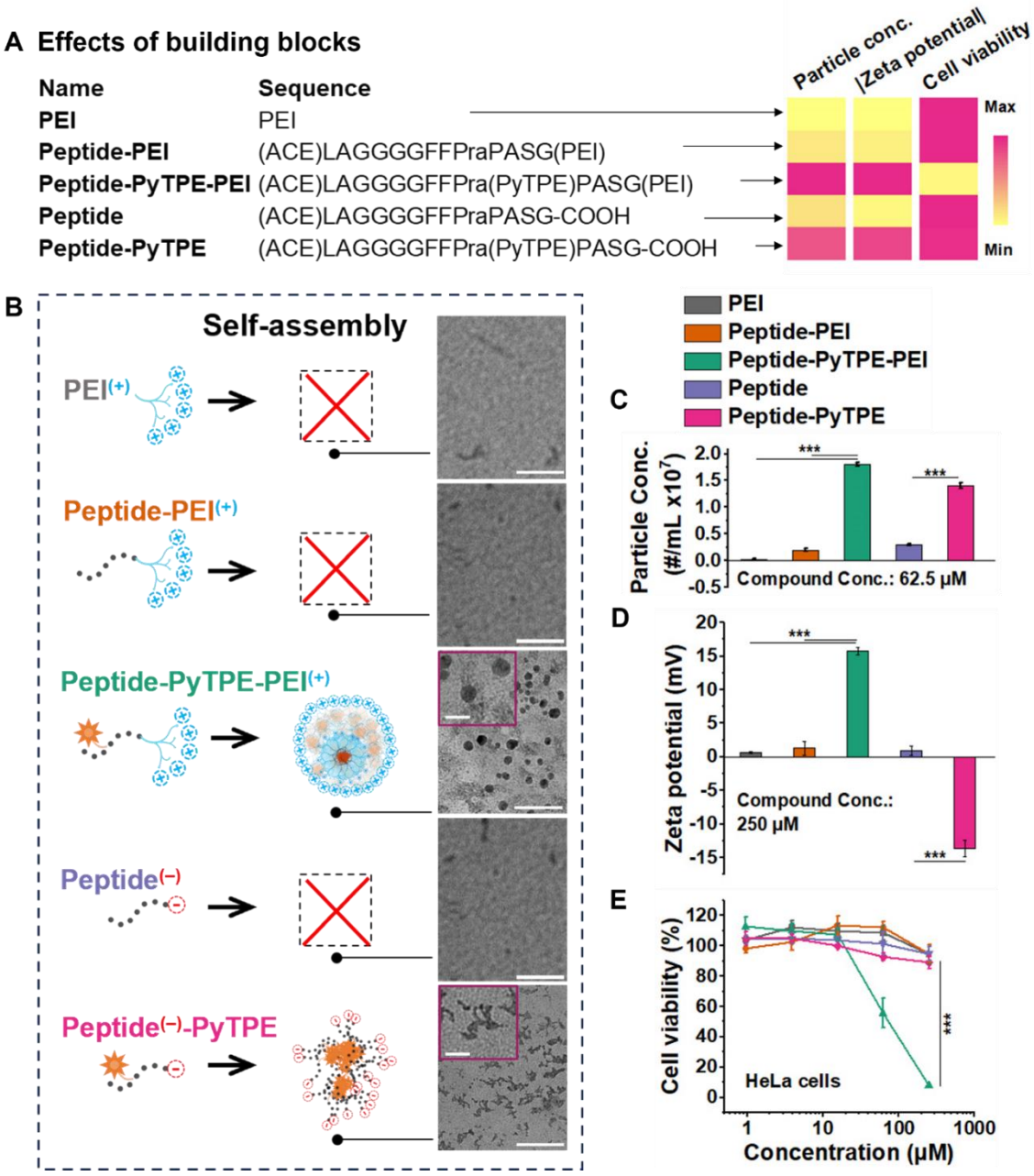

Figure 4.2 Self-assembly controls surface charge density and cell cytotoxicity.

(A) Heat map showing effects of building blocks on particle number concentration, |zeta potential|, and cell cytotoxicity. Data from (C-E) was normalized to 0-100 scale. (B) Schemes and TEM images and (C) plot of particle number concentration showing peptide-PyTPE-PEI and peptide-PyTPE formed nano-assemblies. n=3, ***:P<0.001. Scale bar, 100 nm. Inset: higher-magnification images, scale bar, 25 nm. Schemes were created with BioRender.com. Plots of (D) zeta potential (n=3, P<0.001) and (E) cell cytotoxicity (n=4, ***:P<0.001) showing compounds forming nano-assemblies (i.e., peptide-PyTPE-PEI and peptide-PyTPE) have a higher surface charge density and only peptide-PyTPE-PEI with a higher positive surface charge density exhibited strong cell cytotoxicity.

Therefore, the stronger hydrophobicity introduced by PyTPE favors a higher tendency to self-assemble. Meanwhile, although PEI, peptide-PEI, and peptide can be charged at the molecular level, they showed neutral zeta potential, thus indicating a low surface charge density (Figure 4.2 (D)). However, self-assembled peptide-PyTPE-PEI and peptide-PyTPE showed significantly stronger positive (+15.8 mV) or negative zeta potential (–13.6 mV) (n=3, P<0.001, Figure 4.2 (D)), indicating that the self-assembly of charged molecules increases the surface charge density. Cell cytotoxicity tests further indicate that only self-assembled peptide-PyTPE-PEI with a higher positive surface charge density exhibited a stronger cytotoxicity (n=4, ***:P<0.001, Figure 4.2 (E)), consistent with the reported correlation between charge and cytotoxicity.[355] These results clearly show that the self-assembly of charged molecules (e.g., PEI) can enhance the surface charge density and thus increase the cell cytotoxicity of the assembled products.

4.4.2. Optimization of the Self-Assembly Tendency, Intracellular Fluorescence, and Cell Cytotoxicity

We next created a PSNA with optimized AIE fluorescence, positive surface charge density, intracellular fluorescence, and cell cytotoxicity. Inspired by the known hydrophobicity of PyTPE, we further tuned the number of hydrophilic components, PAS, and the hydrophobic F in the peptide backbone of PSNAs: $(PAS)_1F_0$, $(PAS)_1F_1$, $(PAS)_1F_2$, $(PAS)_3F_2$, and $(PAS)_6F_2$ (Figure 4.14-Figure 4.18). These PSNAs were compared for morphology, size, particle number concentration, AIE fluorescence, zeta potential, and cell cytotoxicity (Figure 4.3, Figure 4.4, and Figure 4.19). These characterizations showed that $(PAS)_1F_2$ had the highest tendency to self-assemble as evidenced by the highest particle number concentration, AIE fluorescence, and zeta potential (Figure 4.3 (A)). In turn, $(PAS)_1F_2$ has the strongest intracellular fluorescence and cancer cell cytotoxicity (Figure 4.3 (A) and Figure 4.4).

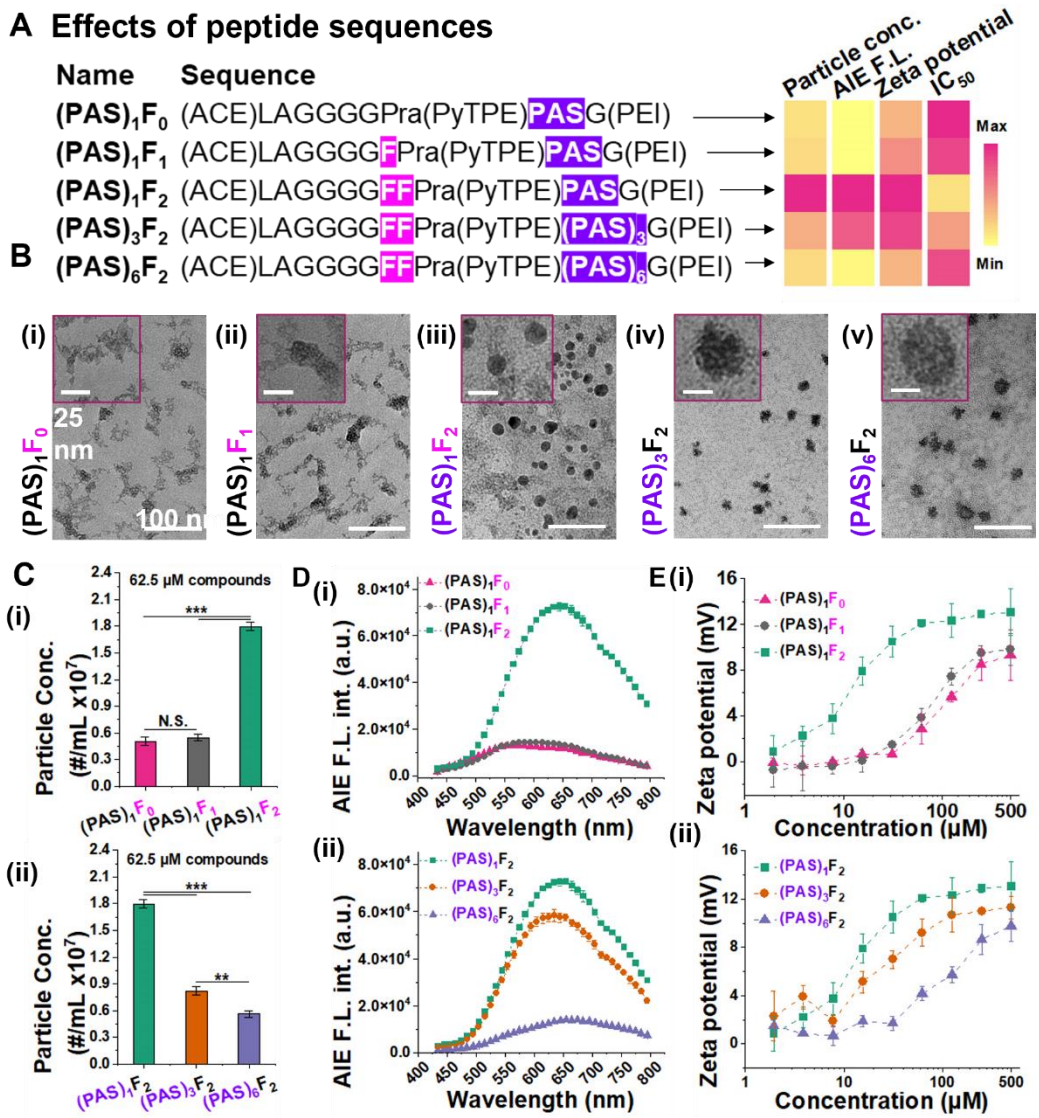

Figure 4.3 Physical properties as a function of F and PAS numbers.

(A) PSNA sequences and heat map showing $(PAS)_1F_2$ is optimized in particle number concentration, AIE F.L., zeta potential, and cell cytotoxicity. The heat map was created by normalizing data from Figure 3 and Figure 4B to 0-100 scale. (B) TEM images of dried PSNAs. Inset: higher-magnification images. (C-E) Plots showing (C) particle number concentration, (D) AIE F.L., and (E) zeta potential increases with increasing F number and decreasing PAS number. n=3, N.S.: P>0.05, **: 0.001<P<0.01, ***:P<0.001.

The detailed comparison of PSNAs' properties is discussed as follows. When fixing the PAS number at 1 and increasing the F number from 0 to 1 and 2, as-formed nano-assemblies changed from 80 nm branched nanoribbons ($(PAS)_1F_0$) to 94 nm branched nanoribbons ($(PAS)_1F_1$) and 22 nm nanospheres ($(PAS)_1F_2$) (Figure 4.3 B(i-iii) and Figure 4.19 (A-C)). Meanwhile, the

particle number concentration (Figure 4.3 C(i)), AIE fluorescence intensity (Figure 4.3 D(i-ii)), and zeta potential (Figure 4.3 E(i)) increase with increasing F number. This suggests that increasing F number favors self-assembly and increases the positive surface charge density of PSNA because of the stronger hydrophobic interactions due to more F residues.

The products remain spherical when fixing the F number at 2 and increasing the PAS number from 1 to 3 and 6; the size changed slightly from 22 nm ($(PAS)_1F_2$) to 28 nm ($(PAS)_3F_2$) and 44 nm ($(PAS)_6F_2$) (Figure 4.3 B(iii-v) and Figure 4.19(C-E)). The particle number concentration (Figure 4.3 C(ii)), PyTPE fluorescence intensity (Figure 4.3 D(iii-iv)), and zeta potential (Figure 4.3 E(iii)) decrease with increasing PAS number, thus indicating that more PAS hinders the self-assembly and decreases the positive surface charge density of PSNAs. This can be explained by more hydrophilicity and steric repulsion introduced by more PAS.[354] In theory, an F number >2 (e.g., $(PAS)_1F_3$) or PAS number <1 (e.g., $(PAS)_0F_2$) may offer an even higher self-assembly tendency, but this was practically impossible: both $(PAS)_1F_3$ and $(PAS)_0F_2$ were not soluble in water/PBS (data not shown).

The AIE fluorescence of PSNAs can be useful for cell labelling and understanding PSNAs' intracellular activities. To validate and compare PSNAs' cell labelling capability, SKOV-3 cells were incubated with PSNAs and imaged by a confocal microscope (Figure 4.4 (A)). PSNAs were successfully internalized by cells and emitted yellow fluorescence (Figure 4.4 A(i-iii)). Moreover, $(PAS)_1F_2$ shows a 2.5-fold higher intracellular fluorescence than that of $(PAS)_1F_0$ and $(PAS)_6F_2$ ($n=3$, $0.001<P<0.01$, Figure 4.4 A(iv)) due to a stronger AIE intensity (Figure 4.3 (D)) and better cell uptake due to more positively charged surface (Figure 4.3 (E)) of $(PAS)_1F_2$.

In addition to intracellular fluorescence, we studied if PSNAs also differed in cancer therapy. The goal was to turn "immune cold" cancers "hot", and thus cells of two "immune cold"

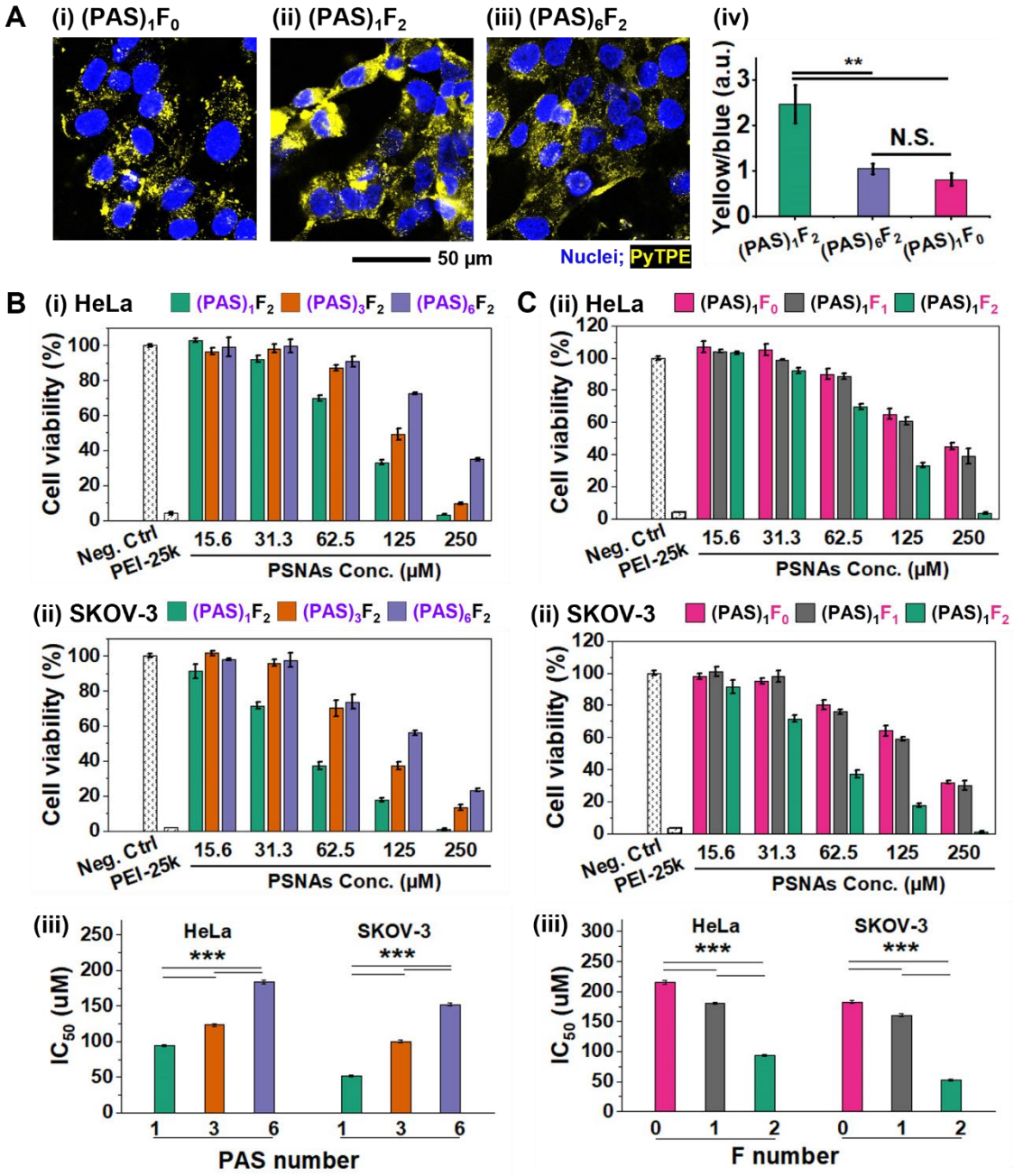

Figure 4.4 Intracellular fluorescence and cell cytotoxicity as a function of F and PAS numbers.

(A, i-iii) Confocal images and (A, iv) plot of yellow F.L./blue F.L. versus PSNA sequences showing $(PAS)_1F_2$ has the highest intracellular fluorescence. n=3, N.S.: P>0.05, **: 0.001<P<0.01. Effects of (B) PAS and (C) F amino acids on the cell cytotoxicity of PSNAs tested from HeLa and SKOV-3 cell lines. Cell cytotoxicity increases with increasing F number and decreasing PAS number. n=4, ***:P<0.001.

cancer types, cervical and ovarian cancer, were used (i.e., HeLa and SKOV-3 cells).[356-357] Figure

4.4 (B) shows that cell cytotoxicity of PSNAs on both HeLa and SKOV-3 cell lines increase with increasing F number and decreasing PAS number. Remarkably, the IC_{50} value of $(PAS)_1F_2$ is only half (tested from HeLa) and one-third (tested from SKOV-3) of the IC_{50} value of $(PAS)_0F_2$ and $(PAS)_6F_2$, thus indicating that $(PAS)_1F_2$ has the strongest cancer cell killing efficacy ($n=4$, $P<0.001$). The effect of F and PAS numbers on cell cytotoxicity can be explained by their role in determining the self-assembly tendency and, therefore, positive surface charge density (Figure 4.3). Analysis of cell viability versus the zeta potential of PSNAs with varying F and PAS numbers indicates that cell viability is inversely proportional to zeta potential (Pearson's coefficient <-0.94, $p<0.05$, Figure 4.20).

4.4.3. Induction of Cell Necrosis

As a first step to understanding the cell killing mechanism of $(PAS)_1F_2$, we monitored the change of cell morphology of $(PAS)_1F_2$-treated HeLa and SKOV-3 using an optical microscope (Figure 4.5 (A)). Versus the control group (without $(PAS)_1F_2$), $(PAS)_1F_2$-treated cells swelled and ruptured over time, thus indicating cell necrosis instead of apoptosis. To further confirm the mode of cell death, we performed the Realtime-Glo Annexin V Apoptosis and Necrosis Assay (RGAVAN) on SKOV-3 cells. The RGAVAN assay can report phosphatidylserine (PS) components exposed to the outer leaflet of the cell membrane in luminescence and cell membrane rupture in fluorescence.[358] A combination of luminescence(+)/delayed fluorescence(+) signal or luminescence(+)/fluorescence(-) signal corresponds to apoptosis, while concurrent luminescence(+)/fluorescence(+) or luminescence(-)/fluorescence(+) signal represents necrosis.[358] The efficacy of the RGAVAN assay was verified by the luminescence(-)/fluorescence(-) signal from the negative control (without compound treatment) and luminescence(+)/delayed fluorescence(+) signal from the apoptosis-positive control (10 ug/mL digitonin) (Figure 4.5 B(i)). $(PAS)_1F_2$-treated SKOV-3 cells (Figure 4.5 B(ii)) showed luminescence(-)/fluorescence(+) signal,

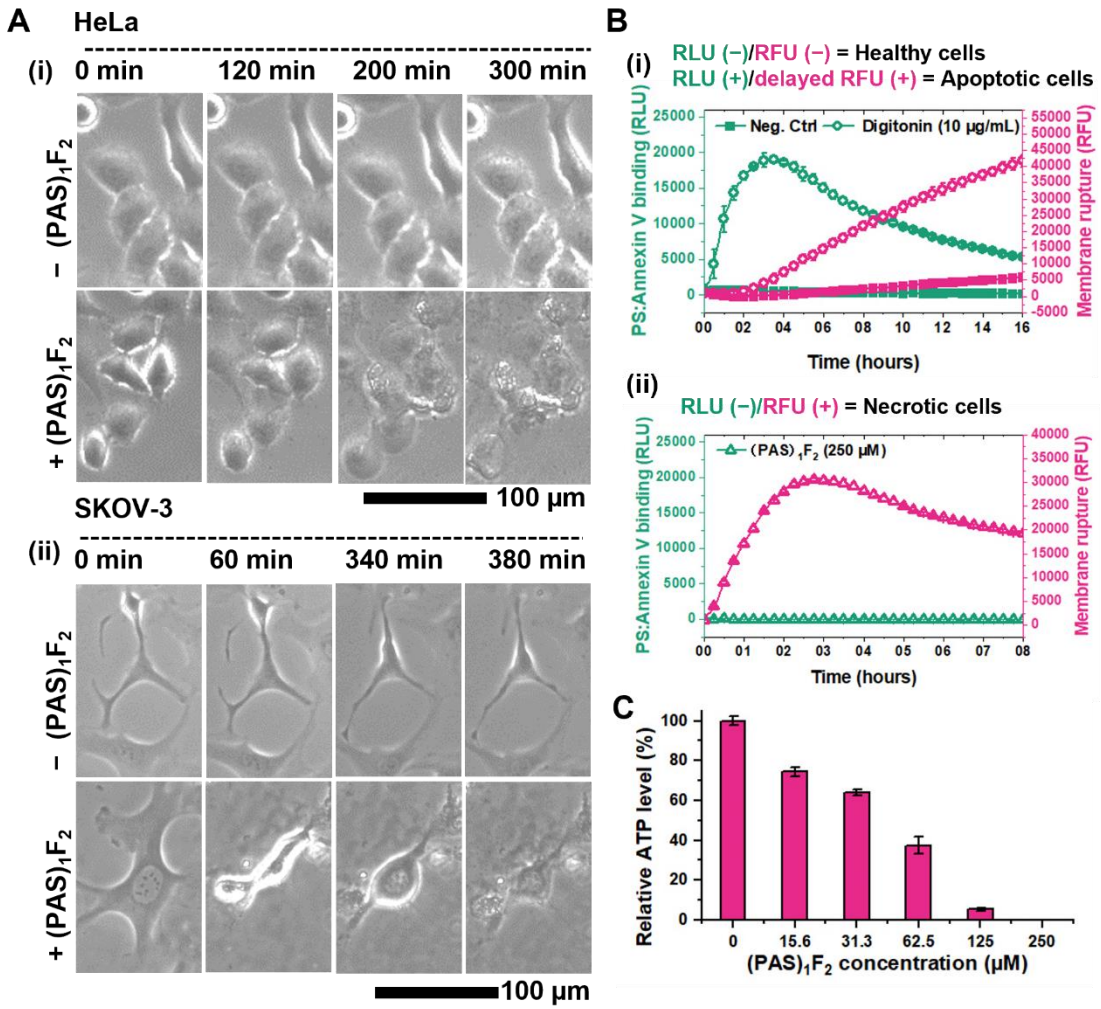

Figure 4.5 Observation of cell necrosis.

(A) Optical microscopy images showing the swelling and rupturing of HeLa and SKOV-3 cells challenged by PAS_1F_2. (B) Realtime-Glo Annexin V Apoptosis and Necrosis Assay results reporting (B,i) healthy SKOV-3 cells without compound treatment (negative control) and apoptotic SKOV-3 cells challenged by digitonin and (B, ii) necrotic SKOV-3 cells challenged by PAS_1F_2. (C) Plot of relative ATP level showing ATP level of SKOV-3 cells decreases as the PAS_1F_2 concentration increases.

thus clearly indicating necrosis. The possibility of apoptosis was further ruled out by negative western blot bands of known apoptosis initiators: cleaved caspase-8 and caspase-3 (Figure 4.21). The necrosis of SKOV-3 cells was accompanied by a depletion of ATP level (Figure 4.5 (C)) in addition to the observed cell swelling and rupturing.

4.4.4. Subcellular Activities of PSNAs and Cell Death Mechanism

Questions thus arise about how $(PAS)_1F_2$ causes necrosis and what sub-type(s) of necrosis occur(s). One possibility is that $(PAS)_1F_2$ ruptured lysosomes via the proton sponge effect of PEI followed by the release of lysosome enzymes that trigger regulated necrosis such pyroptosis and necroptosis. To prove this hypothesis, we carefully tracked the subcellular activities of $(PAS)_1F_2$ and detected the expression of pyroptosis- and necroptosis-related proteins with immunoassays.

4.4.4.1. PSNAs entered cells via endocytosis

We first determined whether $(PAS)_1F_2$ was internalized by cells via endocytosis because this is a prerequisite for nanomaterials to eventually accumulate in lysosomes. Thanks to the optimized AIE fluorescence of $(PAS)_1F_2$, we could study how the blockade of well-known endocytic pathways affect the cell internalization of $(PAS)_1F_2$ using flow cytometry. These pathways include caveolae-mediated endocytosis, clathrin-mediated endocytosis, and macropinocytosis—these are known to be blocked by metabolic inhibitors filipin from *Streptomyces filipinensis*, pitstop 2, and 5-(N-ethyl-N-isopropyl)amiloride (EIPA), respectively.[344] We first proved the efficacy of these metabolic inhibitors with controls using FTIC-labelled markers specific to each endocytic pathway, i.e., 10 kDa dextran for macropinocytosis, transferrin for clathrin-mediated endocytosis, and cholera toxin B subunit for caveolae-mediated endocytosis (Figure 4.22).[344] Next, the cell uptake of $(PAS)_1F_2$ by inhibited SKOV-3 cells was quantified by flow cytometry (Figure 4.6 (A)). Figure 4.6 (B) shows that a 4 °C treatment resulted in 60% inhibition of $(PAS)_1F_2$ internalization, thus indicating that endocytic pathways collectively contributed to 60% of $(PAS)_1F_2$ internalization, while the rest was via nonendocytic pathways (e.g., membrane insertion and membrane fusion).[344] More specifically, caveolae-mediated and clathrin-mediated endocytosis contributed to 37% and 24% internalization as seen in the filipin

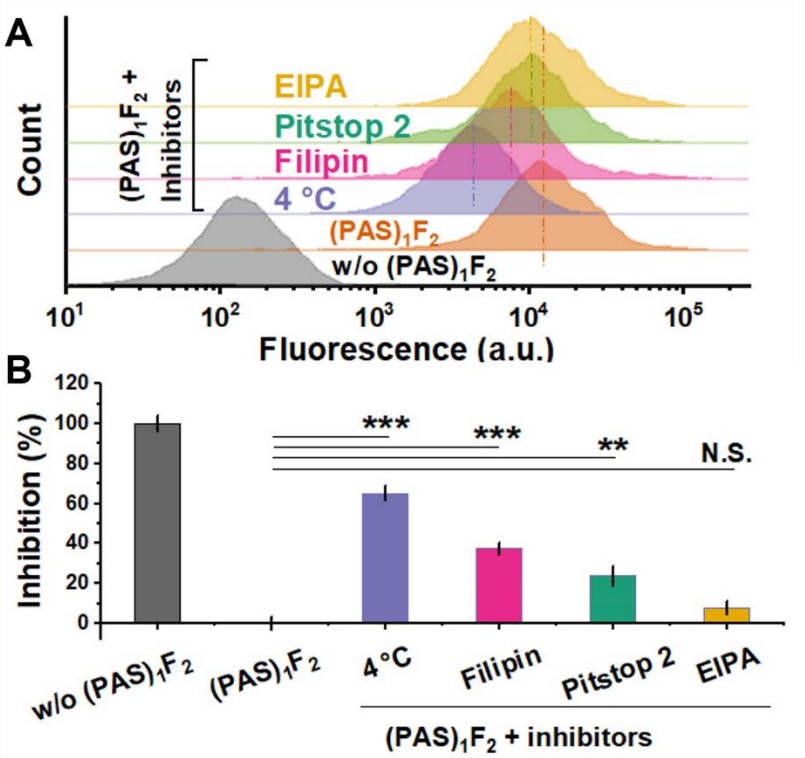

Figure 4.6 PSNAs entered cells via endocytosis.

(A) Flow cytometry histograms and (B) plot of the inhibition rate showing significant inhibition of cell uptake of PAS_1F_2 by endocytic inhibitors. n=3, N.S.: P>0.05, *: 0.01<P<0.05, **: 0.001<P<0.01, ***:P<0.001.

and pitstop 2 inhibition rate. Note that EIPA did not result in significant inhibition compared to the non-inhibited control (N=3, P>0.05).

4.4.4.2. PSNAs accumulated in and ruptured lysosomes and mitochondria

Of particular interest is whether $(PAS)_1F_2$ can accumulate in and rupture lysosomes and mitochondria after cell internalization. It is interesting for two reasons. First, lysosomes and mitochondria dysfunction are tightly related to cell death.[340] Second, these two organelles can be targets of $(PAS)_1F_2$ considering the observed endocytosis of $(PAS)_1F_2$ (Figure 4.6) and potential interactions with organelle membranes via charges and hydrophobic forces.[348, 355] To determine the $(PAS)_1F_2$ accumulation in organelles, SKOV-3 cells' lysosomes and mitochondria were labelled by Magic Red and MitoView 633, respectively, followed by $(PAS)_1F_2$ treatment for 5, 15,

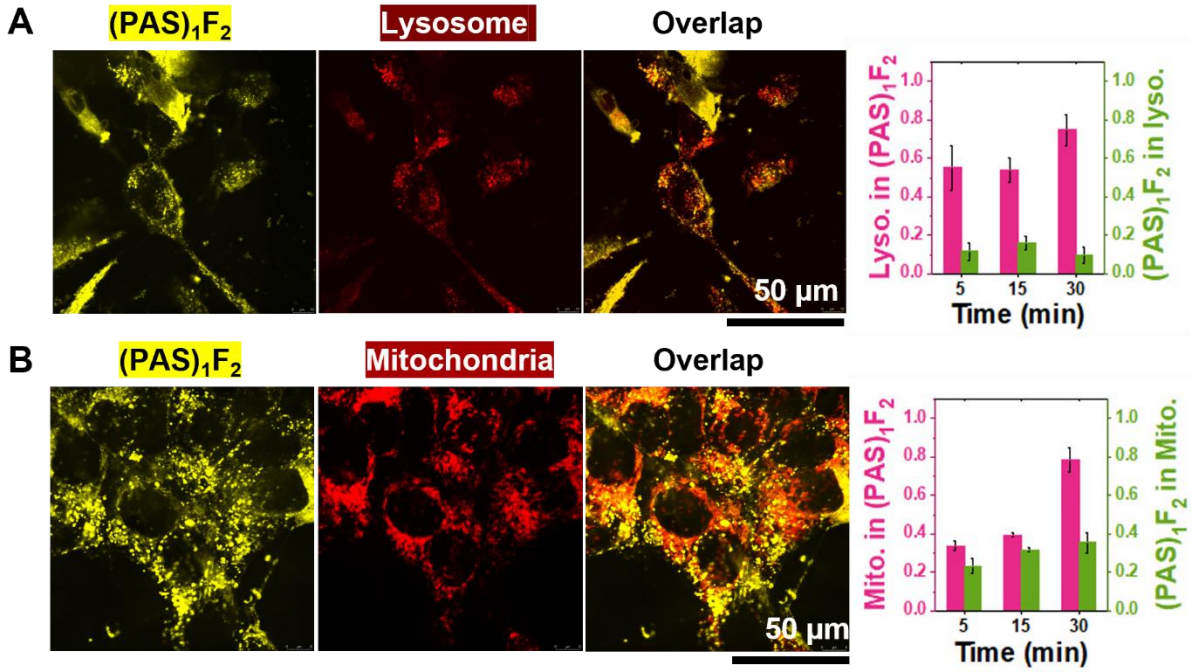

Figure 4.7 PSNAs accumulated in lysosomes and mitochondria.

Confocal images and analysis of Mander's colocalization coefficients showing the colocalization of PAS_1F_2 with (A) lysosomes and (B) mitochondria.

or 30 min. The colocalization of $(PAS)_1F_2$ with these organelles was quantified using Mander's colocalization coefficients[359] determined from confocal images, i.e., the ratio of subject A in subject B and B in A (Figure 4.7). With an incubation of 30 min, 75% lysosomes and 79% mitochondria signals colocalized with $(PAS)_1F_2$ signals, confirming the accumulation of $(PAS)_1F_2$ in lysosomes and mitochondria.

We further evaluated whether this accumulation could damage these organelles. SKOV-3 cells were stained by acridine orange, MitoView 633, and Hoechst 33342 to label lysosomes, mitochondria, and nuclei, respectively. These cells were then incubated with $(PAS)_1F_2$ for 1 h. Organelle integrity was quantified based on the normalized acridine orange and MitoView 633 fluorescence signals from confocal images (see details in Materials and Method). Figure 4.8 shows

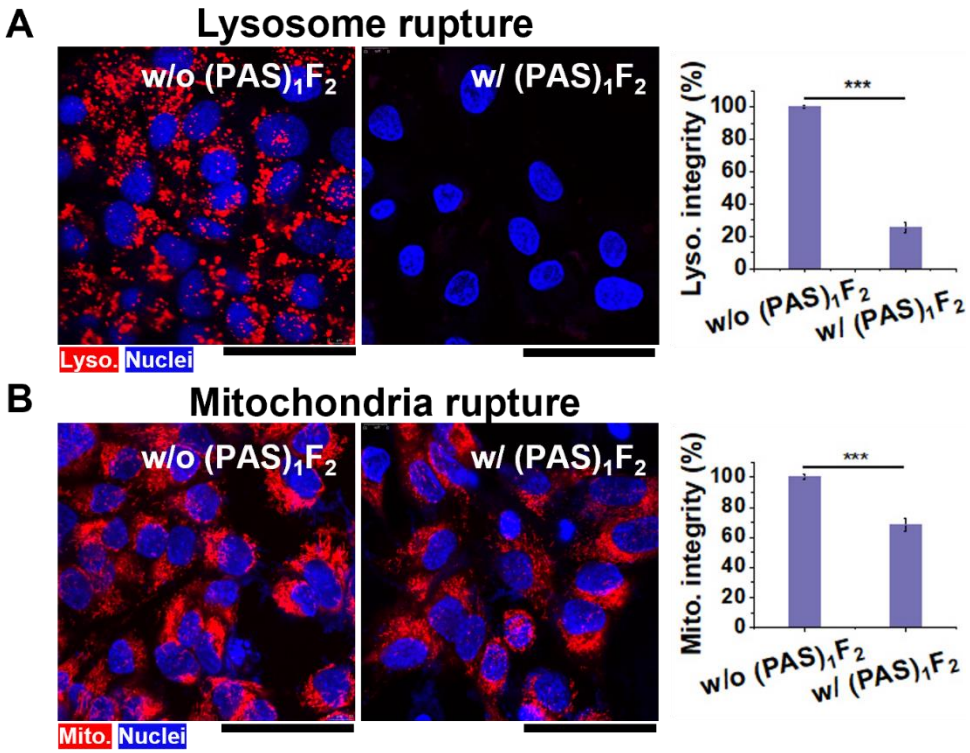

Figure 4.8 PSNAs ruptured lysosomes and mitochondria.

Confocal images and plots of organelles' integrity showing PAS_1F_2 ruptured (A) lysosomes and (B) mitochondria. n=3, N.S.: P>0.05, *: 0.01<P<0.05, **: 0.001<P<0.01, ***:P<0.001.

that $(PAS)_1F_2$ ruptured 75% and 32% lysosomes and mitochondria, respectively (P<0.001, compared to control).

4.4.4.3. Rupture of lysosomes triggered pyroptosis and necroptosis

We focused here on the downstream cell activities of lysosome rupture considering the tight relationship between lysosome dysfunction and regulated necrosis and the observed necrosis (Figure 4.5 and S10).[134, 341] The rupture of lysosomes may trigger at least two sub-types of regulated necrosis: pyroptosis and necroptosis. Damaged lysosomes release hydrolytic enzymes such as cathepsin B, which may activate pyroptosis.[116] Besides, lysosome dysfunction would upregulate receptor-interacting protein kinases (RIPKs), which can activate the necroptosis pathway.[134]

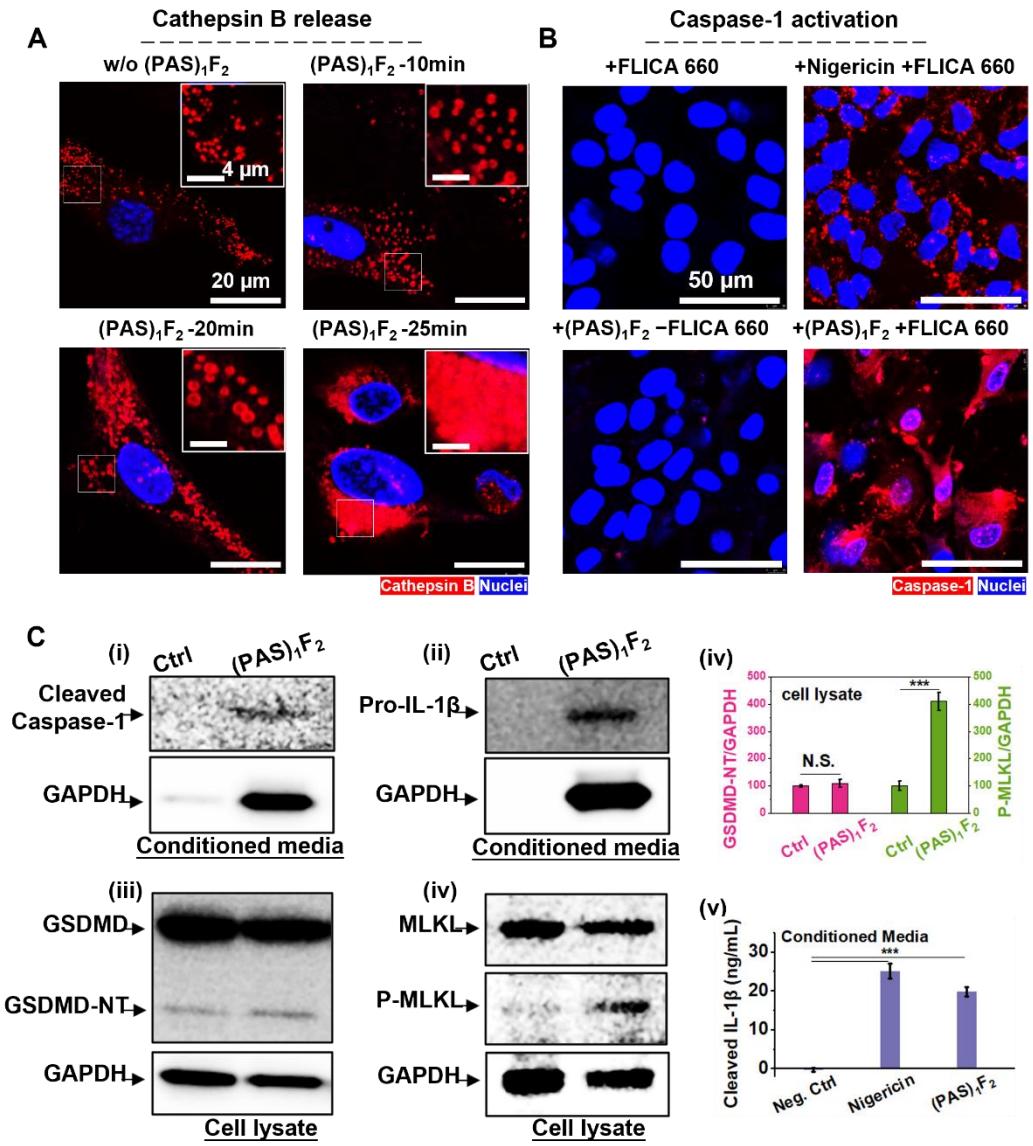

Figure 4.9 Rupture of lysosomes triggered pyroptosis and necroptosis.

(A) Confocal images showing the enlargement of lysosomes and release of cathepsin B (diffusive red F.L.) in PAS_1F_2-treated SKOV-3 cells. Inset, enlarged images of the area of interest (white box). (B) Confocal images showing the activation of caspase-1 in PAS_1F_2-treated SKOV-3 cells. (C) Detection of pyroptosis and necroptosis related proteins in PAS_1F_2-treated SKOV-3 cells. Western blotting showing (C, i) upregulated cleaved caspase-1 (conditioned media), (C, ii) upregulated Pro-IL-1β (conditioned media), (C, iii) unchanged GSDMD and GSDMD-NT (cell lysate), and (C, iv) upregulated P-MLKL (cell lysate). (C, v) Quantification of relative GSDMD-NT and P-MLKL levels showing significant increase in P-MLKL but non-significant increase in GSDMD-NT compared to the control (w/o PAS_1F_2). n=3, N.S.: P>0.05, *: 0.01<P<0.05, **: 0.001<P<0.01, ***:P<0.001. (C, vi) Cleaved IL-1β concentration measured by Lumit Human IL-1β Immunoassay from conditioned media. n=3, N.S.: P>0.05, *: 0.01<P<0.05, **: 0.001<P<0.01, ***:P<0.001.

We first investigated whether lysosome rupturing activated the pyroptosis pathway. SKOV-3 cells were stained by Magic Red to report cathepsin B activities followed by treatment with $(PAS)_1F_2$. The release of cathepsin B from lysosomes to cytoplasm was confirmed by confocal images showing the enlargement of lysosome size (indicator of permeabilization) and more and more diffusive cathepsin B signal over time (Figure 4.9 (A)). Cathepsin B cleaves pro-caspase-1 to form capase-1, the initiator of pyroptosis.[116] In a separate confocal observation, both $(PAS)_1F_2$ and nigericin (positive control) treated SKOV-3 cells showed positive FLICA 660 signal (reporter of cleaved caspase-1); this FLICA 660 activation was not seen in negative controls (FLICA 660-only and $(PAS)_1F_2$-only) (Figure 4.9 (B)). The activation of caspase-1 was further confirmed by western blotting (Figure 4.9 C(i)).

In pyroptosis, caspase-1 will cleave pro-IL-1β to IL-1β and gasdermin D (GSDMD) to N-terminal of GSDMD (GSDMD-NT); GSDMD-NT is known to form membrane pores and trigger membrane rupture, while mature IL-1β can be subsequently released into the extracellular environment, thus contributing to immune responses.[116] Both pro-IL-1β (Figure 4.9 C(ii)) and cleaved IL-1β (Figure 4.9 C(vi)) were detected in conditioned media of $(PAS)_1F_2$-treated SKOV-3 cells, thus confirming the maturation and release of IL-1β through ruptured membrane. However, the western blotting (Figure 4.9 C(iii) and (v)) shows insignificant upregulation of GSDMD-NT versus the negative control ($n=3$, $P>0.05$). Although the reason for absent GSDMD-NT requires further study, all other evidence converged on the activation of pyroptosis by $(PAS)_1F_2$.

The absence of GSDMD-NT, the membrane-pore former, inspired us to investigate whether an alternative mechanism can explain the cell rupture. Indeed, lysosomes are known to digest RIPKs. The fact that lysosomes were ruptured by $(PAS)_1F_2$ (Figure 4.8) suggested that RIPKs could be upregulated, which can further upregulate phosphorylated RIPKs (P-RIPKs) and

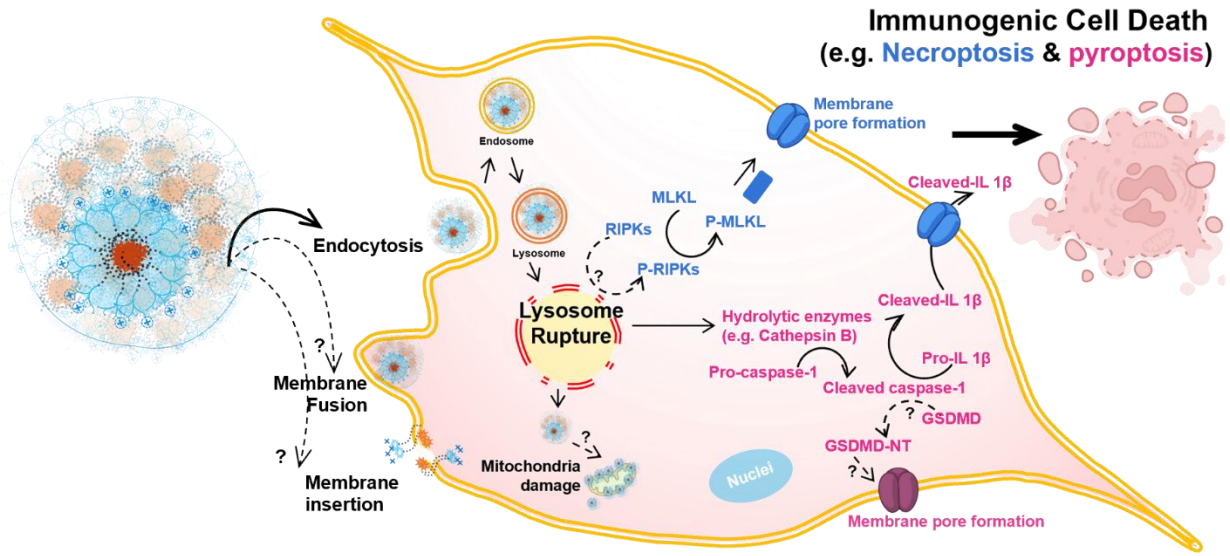

Figure 4.10 Mechanism of PSNAs-induced cancer cell death.

PSNAs can be internalized by cancer cells via endocytosis. Internalized PSNAs accumulated in and ruptured lysosomes and mitochondria. Rupture of lysosomes resulted in the activation of the pyroptosis and necroptosis pathways and the release of pro-inflammatory cytokines (e.g., IL-1β) known to induce anticancer immunity. Solid arrows: pathways supported by experimental data; dashed arrows: presumed pathways to be verified.

phosphorylated mixed lineage kinase domain-like protein (P-MLKL). P-MLKL is the executor of necroptosis that also forms membrane pores.[121, 134] The upregulation of P-MLKL was detected from the $(PAS)_1F_2$-treated SKOV-3 cells by western blotting (Figure 4.9 C(iv) and (v)), which showed four-fold higher P-MLKL intensity compared to the negative control (n=3, $P<0.001$).

Together, we concluded that $(PAS)_1F_2$ triggered immunogenic cancer cell death (pyroptosis and necroptosis) via steps of cell endocytosis, accumulation in and rupture of lysosomes, cathepsin B release, caspase-1 activation, maturation and extracellular release of IL-1β, and formation of phosphorylated MLKL (Figure 4.10).

4.4.4.4. Contribution of lysosome rupturing, pyroptosis, and necroptosis to cell death

To further understand the contribution of lysosome rupturing, pyroptosis, and necroptosis to cell death, the cell viability was measured in various inhibition conditions. First, we hypothesized that lysosome rupture was the cause of cell death and that it originated from the

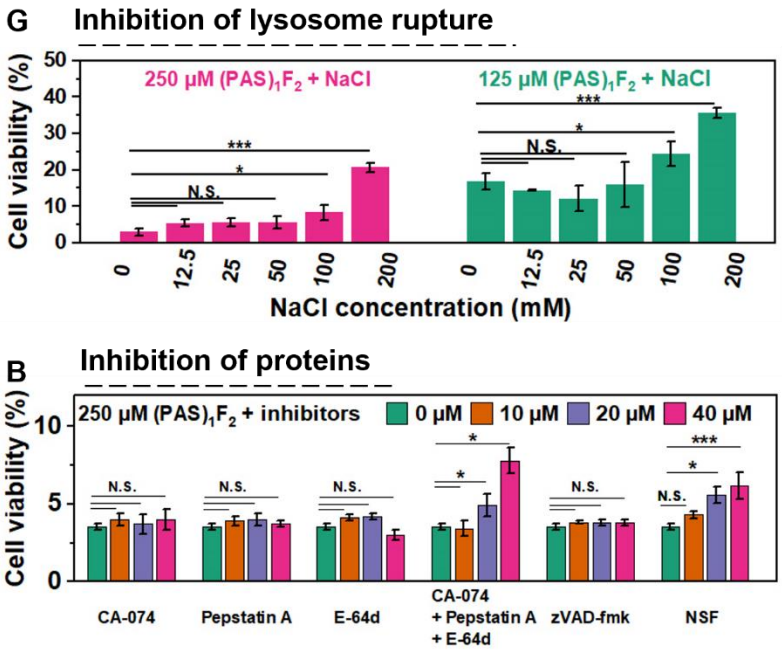

Figure 4.11 Contribution of lysosome rupturing, pyroptosis, and necroptosis to cell death. Inhibition of PAS_1F_2-treated SKOV-3 cells' death by pre-incubation with (A) NaCl and (B) inhibitors of downstream proteins of lysosome rupturing, i.e., cathepsins (inhibitor: CA-074, Pepstatin A, and E-64d), caspase-1 (inhibitor: Z-VAD-FMK), and GSDMD-NT and P-MLKL (inhibitor: NSF). NaCl resulted in fold-increase of cell viability, while protein inhibitors had less effects. n=4, N.S.: P>0.05, *: 0.01<P<0.05, **: 0.001<P<0.01, ***:P<0.001.

osmotic pressure increase caused by the proton sponge effect. If this holds, then the inhibition of lysosomes' osmotic pressure increase would improve the viability of $(PAS)_1F_2$–challenged cells. SKOV-3 cells were preincubated with NaCl prior to $(PAS)_1F_2$ to buffer the osmotic pressure change in lysosomes.[303] As shown in Figure 4.11 (A), the cell viability increases with increasing NaCl concentration. When challenged by 250 μM $(PAS)_1F_2$, cells pre-incubated with 200 mM NaCl showed 7-fold higher viability versus no NaCl addition (n=4, P<0.001). This increase was 2-fold in the case of 125 μM $(PAS)_1F_2$ and 200 mM NaCl co-incubation (n=4, P<0.001). However, NaCl treatment did not rescue cells to 100% viability. These results suggest that lysosome rupture is associated with an osmotic pressure change and is vital in controlling cell death; however, this lysosome rupture is not the only cause of cell death. Finally, we studied how the inhibition of

downstream proteins of lysosome rupture affects cell death. Figure 4.11 (B) shows that the inhibition of cathepsins (by CA-074, pepstatin A, and E-64d), caspase-1 (by zVAD-fmk), and P-MLKL (by necrosulfonamide (NSF)) has negligible or very subtle effects on reversing the cell death versus inhibiting lysosome rupturing by NaCl. This is not surprising considering that $(PAS)_1F_2$ may cause other organelles to dysfunction besides the lysosome. Moreover, ruptured lysosomes would lead to other pathways beyond activating pyroptosis and necroptosis.[29] Future work will study other cell death mechanisms such as those associated with potential mitochondria dysfunctions. Direct cell membrane insertion and permeabilization by $(PAS)_1F_2$ is also worth studying because $(PAS)_1F_2$ contains positive and hydrophobic components.[360-361]

4.5. CONCLUSIONS

We successfully synthesized a series of proton sponge nano-assemblies (PSNAs) by conjugating branched PEI (800 Da) with self-assembling peptide-PyTPE. Using peptide-PyTPE-PEI (PAS_1F_2) and its building blocks as models, we proved that higher hydrophobicity favors the self-assembly of PSNA. Moreover, the self-assembly of charged molecules enhanced the surface charge density, thus leading to dramatically increased cell cytotoxicity observed from peptide-PyTPE-PEI with the highest positive surface charge density. Considering the pivotal role of self-assembly, the self-assembly tendency of PSNAs was further optimized by varying the number of hydrophobic (F) and hydrophilic components (PAS). Specifically, increasing F and decreasing PAS numbers favored a higher self-assembly tendency (measured by particle number concentration and AIE fluorescence), thus yielding $(PAS)_1F_2$ with the maximized AIE fluorescence, positive surface charge density, intracellular fluorescence intensity, and cancer cell cytotoxicity. Necrotic cells with increasing size, ruptured membrane, and depletion of ATP were

observed when challenged by $(PAS)_1F_2$. Here, 60% of $(PAS)_1F_2$ entered cells via endocytosis, followed by its accumulation in and rupturing of lysosomes and mitochondria. The release of cathepsin B, activation of caspase-1, phosphorylation of MLKL, and maturation and extracellular release of IL-1β were all detected, thus converging on the activation of pyroptosis and necroptosis. Cell death inhibition studies using NaCl (osmotic pressure inhibitor) and other pyroptosis and necroptosis-related inhibitors suggested that other cell death mechanisms may exist in addition to as-determined lysosome-regulated pyroptosis and necroptosis. The successful induction of these highly immunogenic death pathways implies the great promise of $(PAS)_1F_2$ in anticancer immunity. Moreover, the dynamic self-assembly-dependent cytotoxicity of $(PAS)_1F_2$ suggests that cancer-specific toxicity is highly possible by further linking $(PAS)_1F_2$ with an inhibitor of self-assembly via a cancer-cleavable linker (e.g., PLGLAG).

4.6. ACKNOWLEDGEMENTS

Chapter 4, in full, has been submitted for publication of the material as it may appear in "He, T.; Wen, J.; Wang, W.; Hu, Z.; Ling, C.; Zhao, Z.; Cheng, Y.; Chang, Y.-C.; Xu, M.; Jin, Z.; Amer, L.; Sasi, L.; Fu, L.; Steinmetz, N. F.; Rana, T. M.; Wu, P.; Jokerst, J. V., Peptide-Driven Proton Sponge Nano-Assembly for Imaging and Triggering Lysosome-Regulated Necrosis of Cancer Cells. Advanced Materials 2023.". The dissertation author was the primary researcher and author of this paper.

4.7. SUPPLEMENTARY INFORMATION

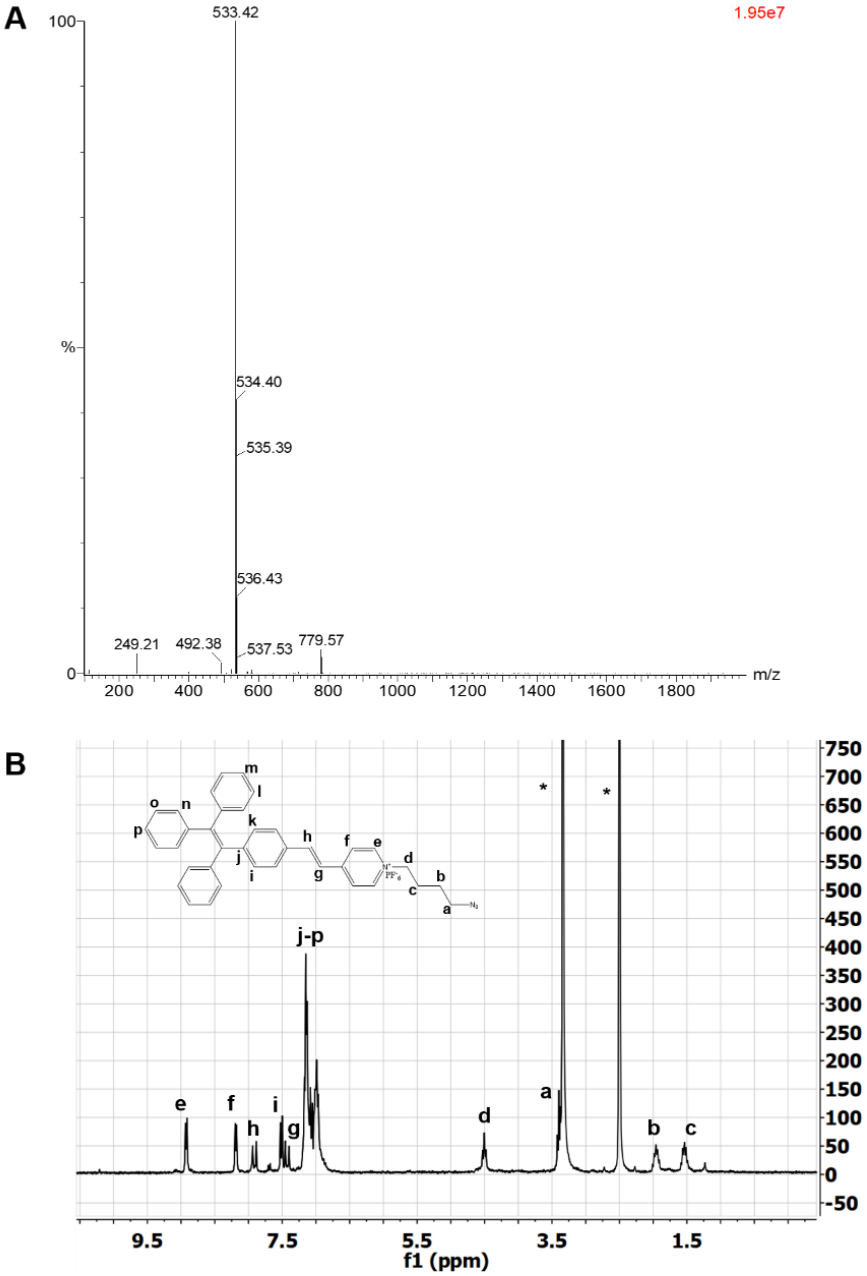

Figure 4.12 Chemical characterizations of PyTPE.

(A) ESI-MS spectrum. $[M]^+$ calcd., 533.27; found, 533.42. (B) ^1H NMR spectrum. 300 MHz, DMSO-d6, *: solvent peaks.

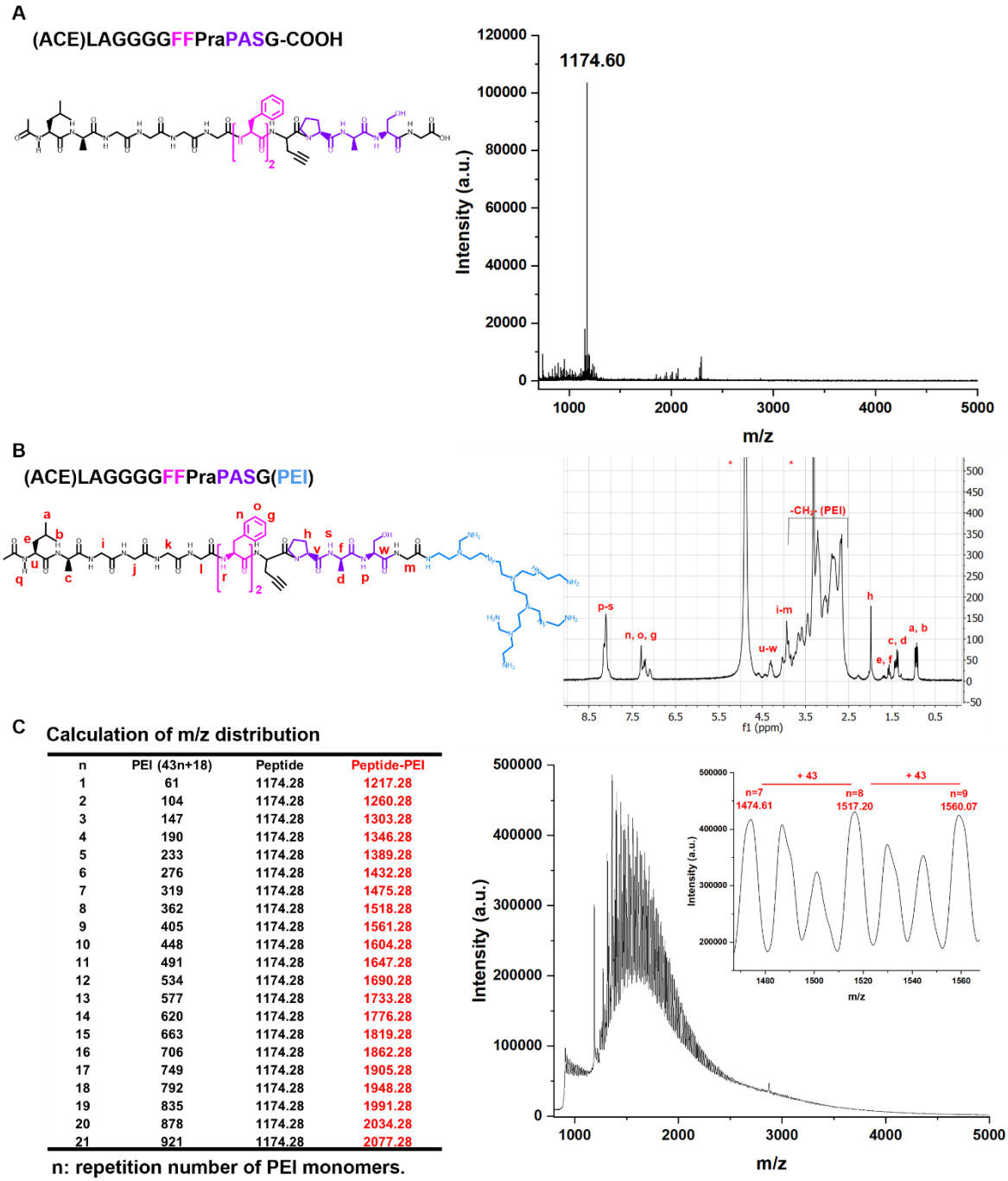

n	PEI (43n+18)	Peptide	Peptide-PEI
1	61	1174.28	1217.28
2	104	1174.28	1260.28
3	147	1174.28	1303.28
4	190	1174.28	1346.28
5	233	1174.28	1389.28
6	276	1174.28	1432.28
7	319	1174.28	1475.28
8	362	1174.28	1518.28
9	405	1174.28	1561.28
10	448	1174.28	1604.28
11	491	1174.28	1647.28
12	534	1174.28	1690.28
13	577	1174.28	1733.28
14	620	1174.28	1776.28
15	663	1174.28	1819.28
16	706	1174.28	1862.28
17	749	1174.28	1905.28
18	792	1174.28	1948.28
19	835	1174.28	1991.28
20	878	1174.28	2034.28
21	921	1174.28	2077.28

Figure 4.13 Chemical characterizations of peptide-PEI and its intermediate.

(A) Chemical structure and high-resolution mass spectrum (MALDI-TOF) of (ACE)LAGGGGFFPraPASG-COOH. [M]+ calcd. 1174.28, found 1174.60. (B) Chemical structure and 1H NMR spectrum of (ACE)LAGGGGFFPraPASG(PEI). 300 MHz, methanol-d4.*: solvent peaks. (C) Calculation of m/z distribution and MALDI spectrum of (ACE)LAGGGGFFPraPASG(PEI) showing the mass distribution due to PEI polymeric characteristics. Insert= m/z range between 1450-1600. A peak gap of 43 was found matching the mass differences of PEI monomers.

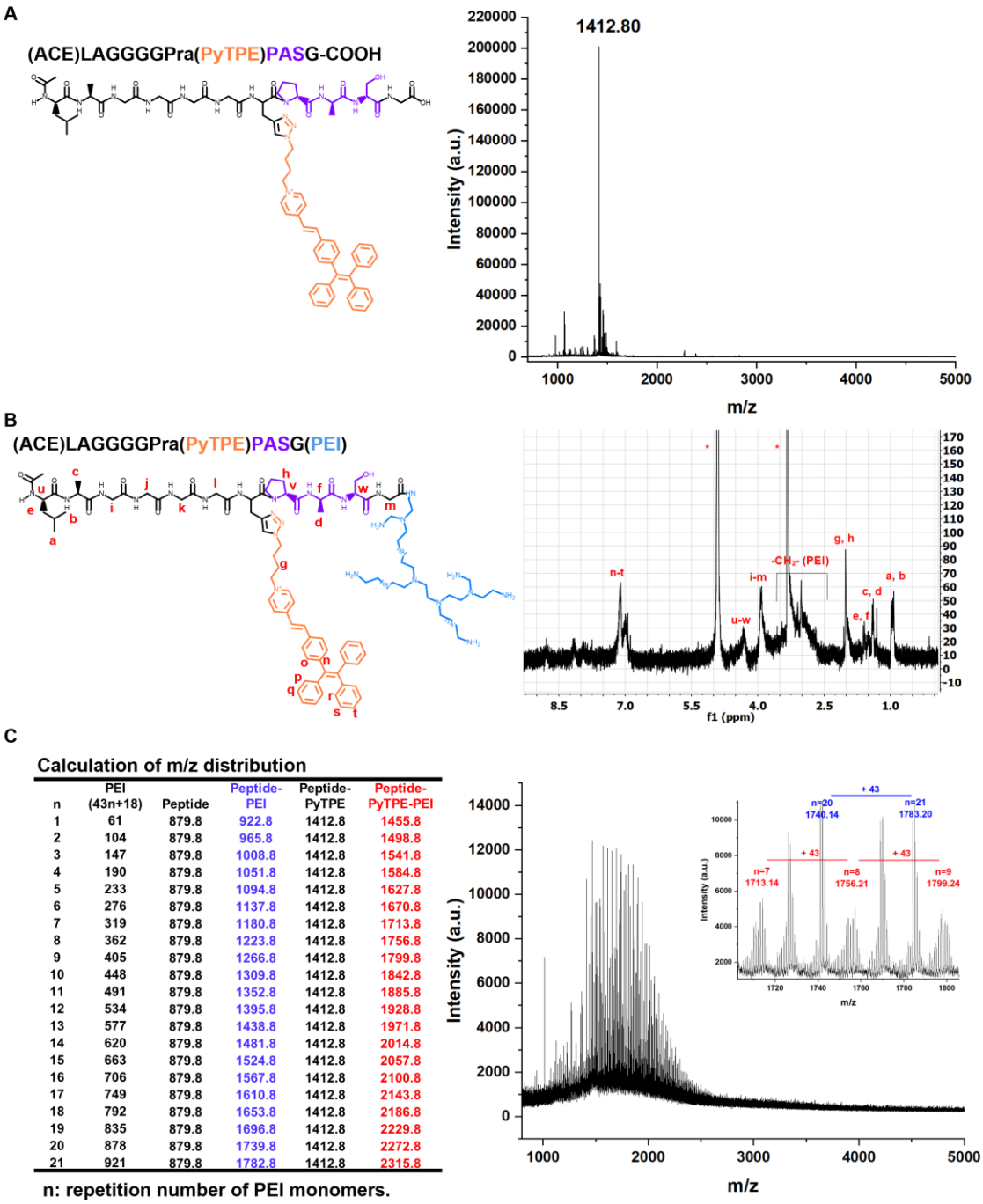

n	PEI (43n+18)	Peptide	Peptide-PEI	Peptide-PyTPE	Peptide-PyTPE-PEI
1	61	879.8	922.8	1412.8	1455.8
2	104	879.8	965.8	1412.8	1498.8
3	147	879.8	1008.8	1412.8	1541.8
4	190	879.8	1051.8	1412.8	1584.8
5	233	879.8	1094.8	1412.8	1627.8
6	276	879.8	1137.8	1412.8	1670.8
7	319	879.8	1180.8	1412.8	1713.8
8	362	879.8	1223.8	1412.8	1756.8
9	405	879.8	1266.8	1412.8	1799.8
10	448	879.8	1309.8	1412.8	1842.8
11	491	879.8	1352.8	1412.8	1885.8
12	534	879.8	1395.8	1412.8	1928.8
13	577	879.8	1438.8	1412.8	1971.8
14	620	879.8	1481.8	1412.8	2014.8
15	663	879.8	1524.8	1412.8	2057.8
16	706	879.8	1567.8	1412.8	2100.8
17	749	879.8	1610.8	1412.8	2143.8
18	792	879.8	1653.8	1412.8	2186.8
19	835	879.8	1696.8	1412.8	2229.8
20	878	879.8	1739.8	1412.8	2272.8
21	921	879.8	1782.8	1412.8	2315.8

Figure 4.14 Chemical characterizations of $(PAS)_1F_0$ and its intermediate.

(A) Chemical structure and high resolution mass spectrum (MALDI-TOF) of (ACE)LAGGGGPra(PyTPE)PASG-COOH. $[M]^+$ calcd. 1413.20, found 1412.80. (B) Chemical structure and ^1H NMR spectrum of (ACE)LAGGGGPra(PyTPE)PASG(PEI). 300 MHz, methanol-d4.*: solvent peaks. (C) Calculation of m/z distribution and MALDI spectrum of (ACE)LAGGGGPra(PyTPE)PASG(PEI) showing the mass distribution due to PEI polymeric characteristics. Insert= m/z range between 1700-1800. Blue= peptide-PEI; Red=peptide-PyTPE-PEI. A peak gap of 43 was found matching the mass differences of PEI monomers.

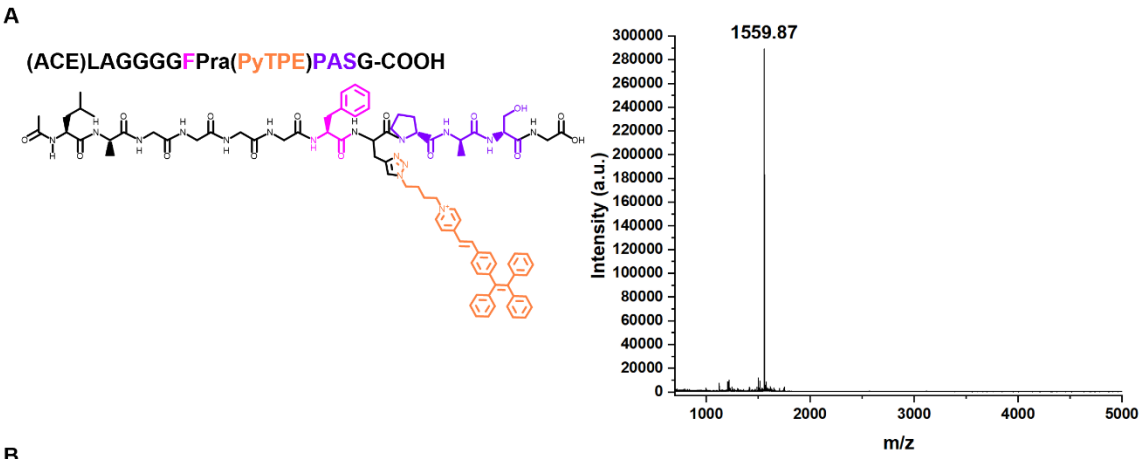

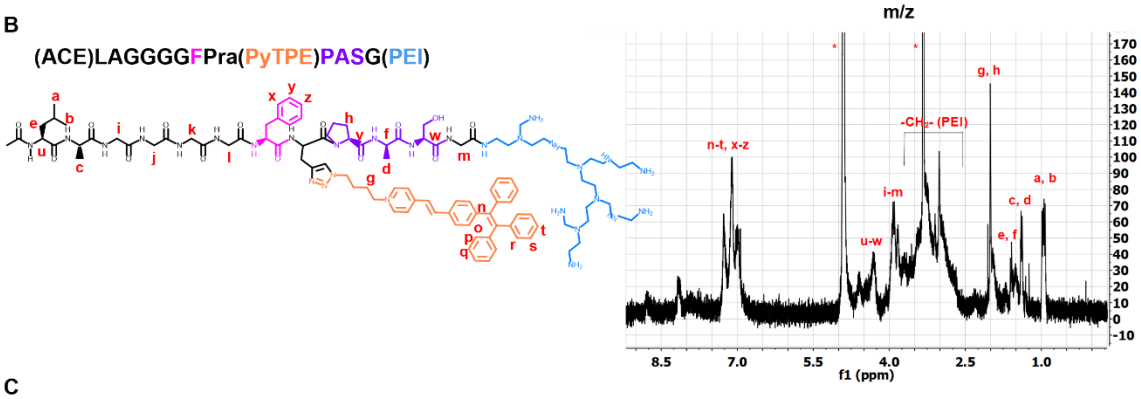

C

Calculation of m/z distribution

n	PEI (43n+18)	Peptide	Peptide-PEI	Peptide-PyTPE	Peptide-PyTPE-PEI
1	61	1027	1070	1560	1603
2	104	1027	1113	1560	1646
3	147	1027	1156	1560	1689
4	190	1027	1199	1560	1732
5	233	1027	1242	1560	1775
6	276	1027	1285	1560	1818
7	319	1027	1328	1560	1861
8	362	1027	1371	1560	1904
9	405	1027	1414	1560	1947
10	448	1027	1457	1560	1990
11	491	1027	1500	1560	2033
12	534	1027	1543	1560	2076
13	577	1027	1586	1560	2119
14	620	1027	1629	1560	2162
15	663	1027	1672	1560	2205
16	706	1027	1715	1560	2248
17	749	1027	1758	1560	2291
18	792	1027	1801	1560	2334
19	835	1027	1844	1560	2377
20	878	1027	1887	1560	2420
21	921	1027	1930	1560	2463

n: repetition number of PEI monomers.

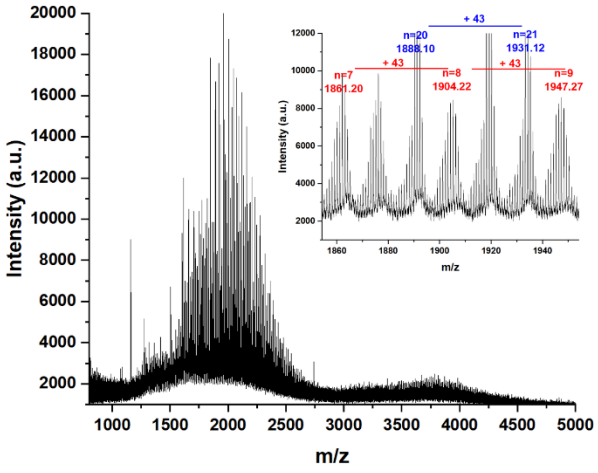

Figure 4.15 Chemical characterizations of (PAS)$_1$F$_1$ and its intermediate.

(A) Chemical structure and high resolution mass spectrum (MALDI-TOF) of (ACE)LAGGGGFPra(PyTPE)PASG-COOH. $[M]^+$ calcd. 1560.80, found 1559.87. (B) Chemical structure and ^{1}H NMR spectrum of (ACE)LAGGGGFPra(PyTPE)PASG(PEI). 300 MHz, methanol-d4.*: solvent peaks. (C) Calculation of m/z distribution and MALDI spectrum of (ACE)LAGGGGFPra(PyTPE)PASG(PEI) showing the mass distribution due to PEI polymeric characteristics. Insert= m/z range between 1850-1950. Blue= peptide-PEI; Red=peptide-PyTPE-PEI. A peak gap of 43 was found matching the mass differences of PEI monomers.

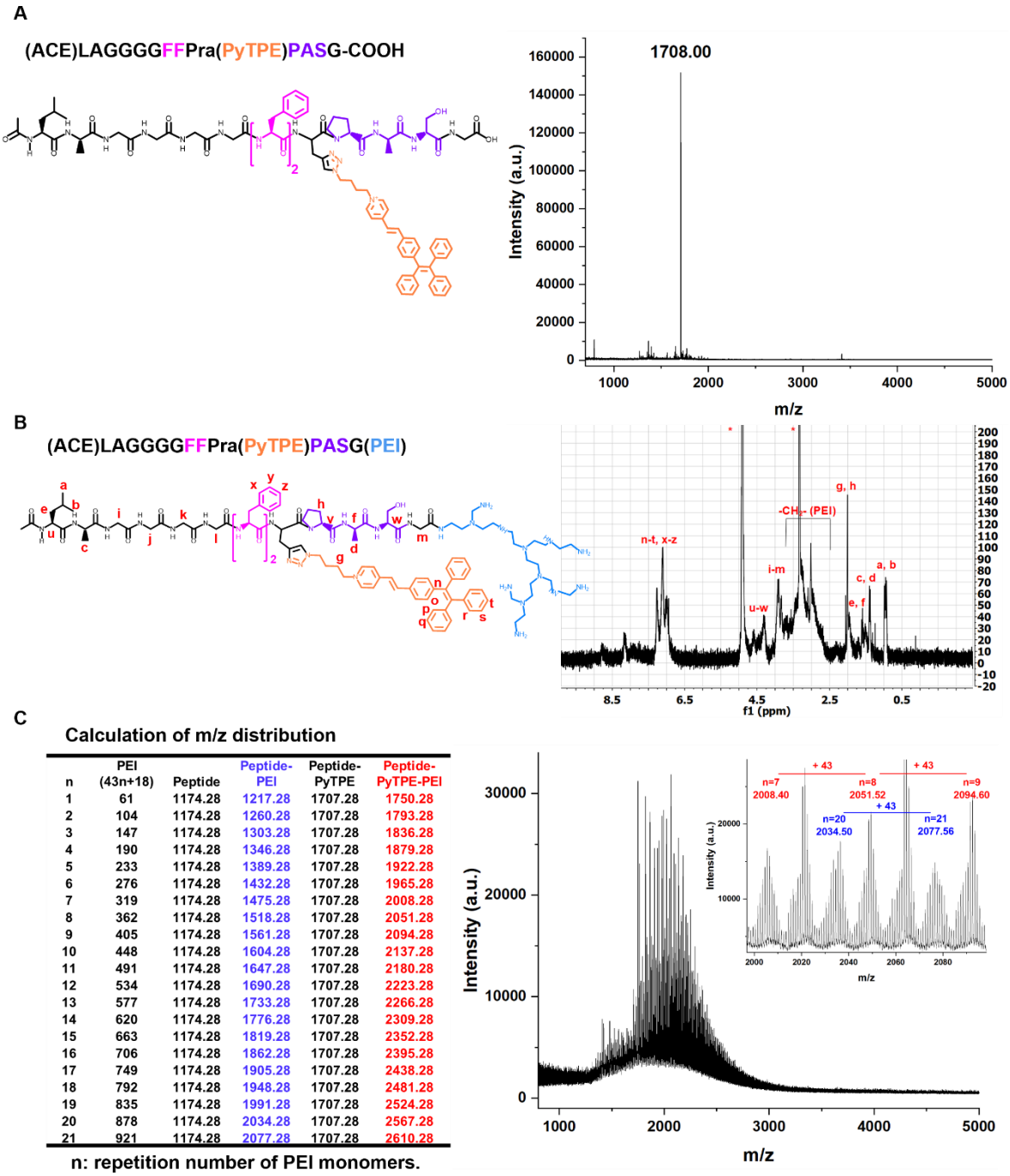

n	PEI (43n+18)	Peptide	Peptide-PEI	Peptide-PyTPE	Peptide-PyTPE-PEI
1	61	1174.28	1217.28	1707.28	1750.28
2	104	1174.28	1260.28	1707.28	1793.28
3	147	1174.28	1303.28	1707.28	1836.28
4	190	1174.28	1346.28	1707.28	1879.28
5	233	1174.28	1389.28	1707.28	1922.28
6	276	1174.28	1432.28	1707.28	1965.28
7	319	1174.28	1475.28	1707.28	2008.28
8	362	1174.28	1518.28	1707.28	2051.28
9	405	1174.28	1561.28	1707.28	2094.28
10	448	1174.28	1604.28	1707.28	2137.28
11	491	1174.28	1647.28	1707.28	2180.28
12	534	1174.28	1690.28	1707.28	2223.28
13	577	1174.28	1733.28	1707.28	2266.28
14	620	1174.28	1776.28	1707.28	2309.28
15	663	1174.28	1819.28	1707.28	2352.28
16	706	1174.28	1862.28	1707.28	2395.28
17	749	1174.28	1905.28	1707.28	2438.28
18	792	1174.28	1948.28	1707.28	2481.28
19	835	1174.28	1991.28	1707.28	2524.28
20	878	1174.28	2034.28	1707.28	2567.28
21	921	1174.28	2077.28	1707.28	2610.28

Figure 4.16 Chemical characterizations of $(PAS)_1F_2$ and its intermediate.

(A) Chemical structure and high resolution mass spectrum (MALDI-TOF) of (ACE)LAGGGGFFPra(PyTPE)PASG-COOH. $[M]^+$ calcd. 1707.28, found 1708.00. (B) Chemical structure and ^1H NMR spectrum of (ACE)LAGGGGFFPra(PyTPE)PASG(PEI). 300 MHz, methanol-d4.*: solvent peaks. (C) Calculation of m/z distribution and MALDI spectrum of (ACE)LAGGGGFFPra(PyTPE)PASG(PEI) showing the mass distribution due to PEI polymeric characteristics. Insert= m/z range between 2000-3000. Blue= peptide-PEI; Red=peptide-PyTPE-PEI. A peak gap of 43 was found matching the mass differences of PEI monomers.

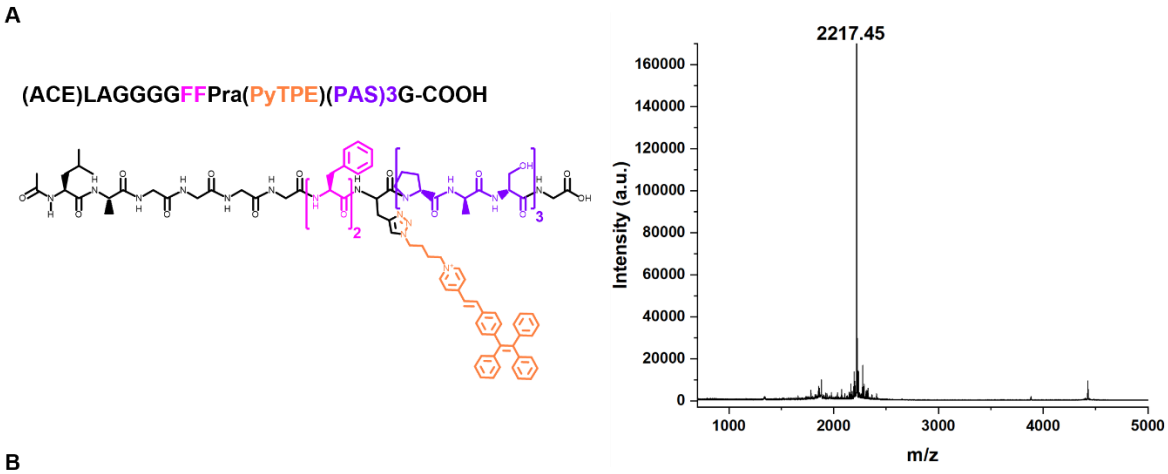

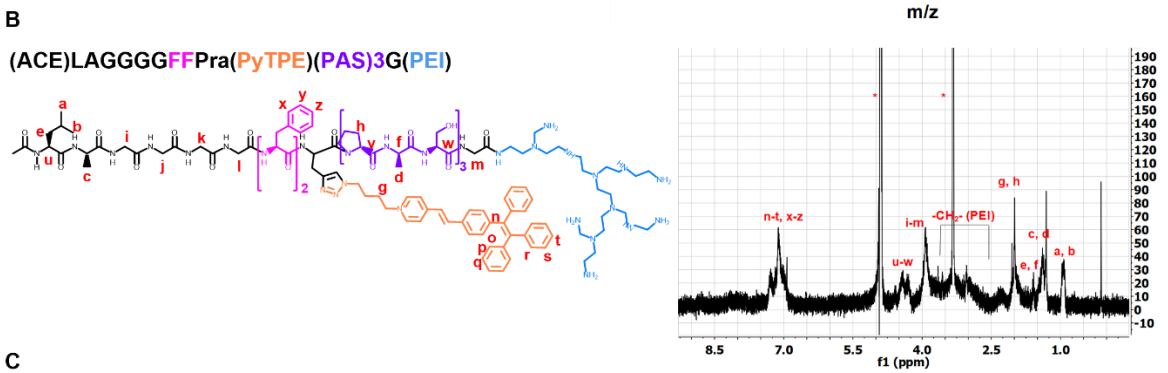

C

Calculation of m/z distribution

n	PEI (43n+18)	Peptide	Peptide-PEI	Peptide-PyTPE	Peptide-PyTPE-PEI
1	61	1684.83	1727.83	2217.83	2260.83
2	104	1684.83	1770.83	2217.83	2303.83
3	147	1684.83	1813.83	2217.83	2346.83
4	190	1684.83	1856.83	2217.83	2389.83
5	233	1684.83	1899.83	2217.83	2432.83
6	276	1684.83	1942.83	2217.83	2475.83
7	319	1684.83	1985.83	2217.83	2518.83
8	362	1684.83	2028.83	2217.83	2561.83
9	405	1684.83	2071.83	2217.83	2604.83
10	448	1684.83	2114.83	2217.83	2647.83
11	491	1684.83	2157.83	2217.83	2690.83
12	534	1684.83	2200.83	2217.83	2733.83
13	577	1684.83	2243.83	2217.83	2776.83
14	620	1684.83	2286.83	2217.83	2819.83
15	663	1684.83	2329.83	2217.83	2862.83
16	706	1684.83	2372.83	2217.83	2905.83
17	749	1684.83	2415.83	2217.83	2948.83
18	792	1684.83	2458.83	2217.83	2991.83
19	835	1684.83	2501.83	2217.83	3034.83
20	878	1684.83	2544.83	2217.83	3077.83
21	921	1684.83	2587.83	2217.83	3120.83

n: repetition number of PEI monomers.

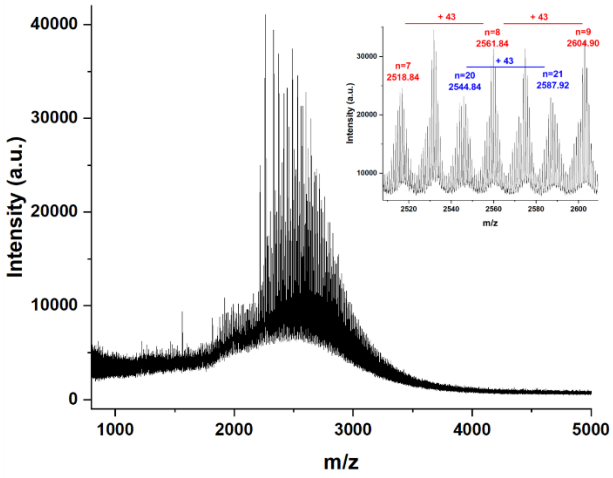

Figure 4.17 Chemical characterizations of $(PAS)_3F_2$ and its intermediate.

(A) Chemical structure and high resolution mass spectrum (MALDI-TOF) of (ACE)LAGGGGFFPra(PyTPE)(PAS)3G-COOH. $[M]^+$ calcd. 2217.83, found 2217.45. (B) Chemical structure and ^1H NMR spectrum of (ACE)LAGGGGFFPra(PyTPE)(PAS)3G(PEI). 300 MHz, methanol-d4.*: solvent peaks. (C) Calculation of m/z distribution and MALDI spectrum of (ACE)LAGGGGFFPra(PyTPE)(PAS)3G(PEI) showing the mass distribution due to PEI polymeric characteristics. Insert= m/z range between 2500-2650. Blue= peptide-PEI; Red=peptide-PyTPE-PEI. A peak gap of 43 was found matching the mass differences of PEI monomers.

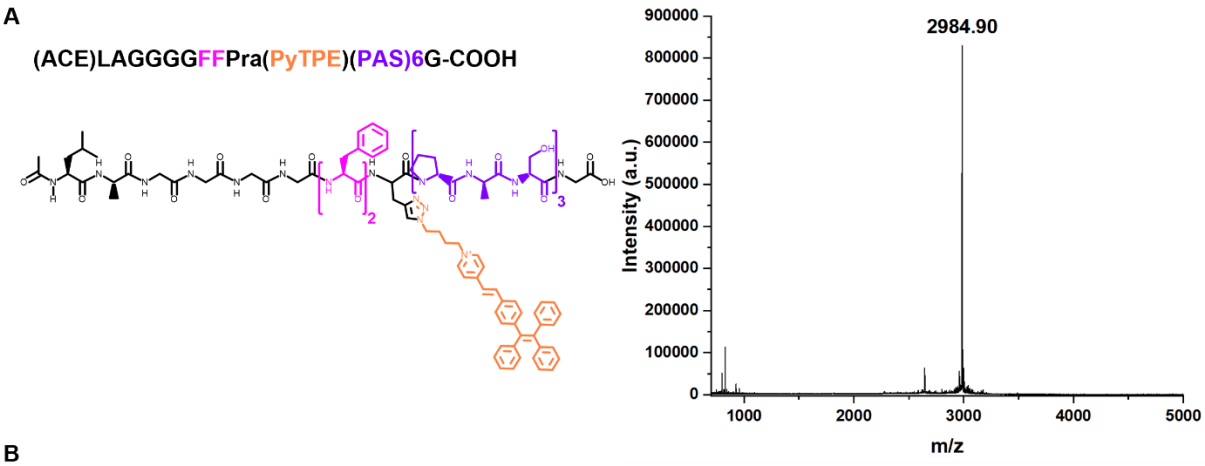

C

Calculation of m/z distribution

n	PEI (43n+18)	Peptide	Peptide-PEI	Peptide-PyTPE	Peptide-PyTPE-PEI
1	61	2450.65	2493.65	2983.65	3026.65
2	104	2450.65	2536.65	2983.65	3069.65
3	147	2450.65	2579.65	2983.65	3112.65
4	190	2450.65	2622.65	2983.65	3155.65
5	233	2450.65	2665.65	2983.65	3198.65
6	276	2450.65	2708.65	2983.65	3241.65
7	319	2450.65	2751.65	2983.65	3284.65
8	362	2450.65	2794.65	2983.65	3327.65
9	405	2450.65	2837.65	2983.65	3370.65
10	448	2450.65	2880.65	2983.65	3413.65
11	491	2450.65	2923.65	2983.65	3456.65
12	534	2450.65	2966.65	2983.65	3499.65
13	577	2450.65	3009.65	2983.65	3542.65
14	620	2450.65	3052.65	2983.65	3585.65
15	663	2450.65	3095.65	2983.65	3628.65
16	706	2450.65	3138.65	2983.65	3671.65
17	749	2450.65	3181.65	2983.65	3714.65
18	792	2450.65	3224.65	2983.65	3757.65
19	835	2450.65	3267.65	2983.65	3800.65
20	878	2450.65	3310.65	2983.65	3843.65
21	921	2450.65	3353.65	2983.65	3886.65

n: repetition number of PEI monomers.

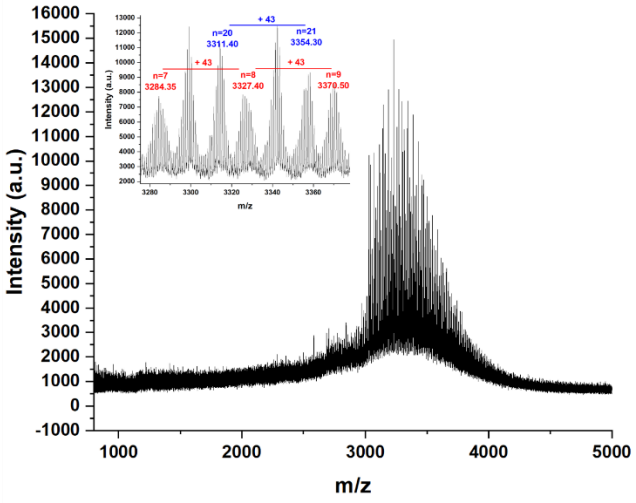

Figure 4.18 Chemical characterizations of $(PAS)_6F_2$ and its intermediate.

(A) Chemical structure and high resolution mass spectrum (MALDI-TOF) of (ACE)LAGGGGFFPra(PyTPE)(PAS)6G-COOH. $[M]^+$ calcd. 2983.65, found 2984.9. (B) Chemical structure and ^1H NMR spectrum of (ACE)LAGGGGFFPra(PyTPE)(PAS)6G(PEI). 300 MHz, methanol-d4.*: solvent peaks. (C) Calculation of m/z distribution and MALDI spectrum of (ACE)LAGGGGFFPra(PyTPE)(PAS)6G(PEI) showing the mass distribution due to PEI polymeric characteristics. Insert= m/z range between 3200-3400. Blue= peptide-PEI; Red=peptide-PyTPE-PEI. A peak gap of 43 was found matching the mass differences of PEI monomers.

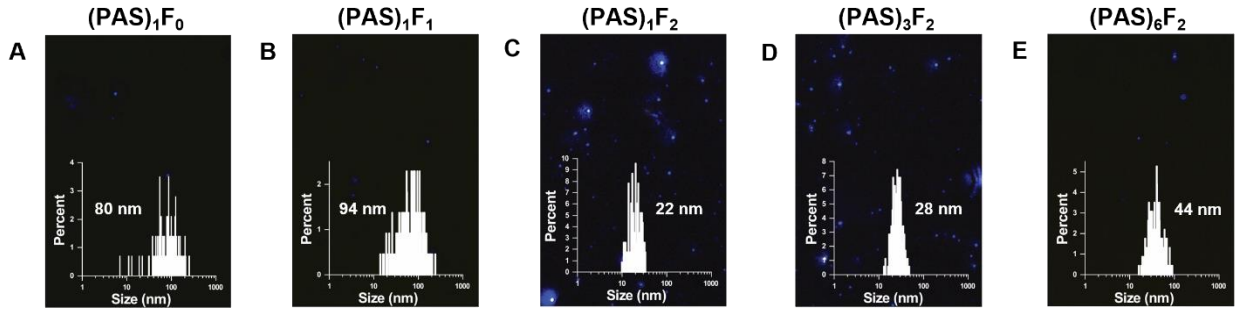

Figure 4.19 Light scattering microscopy images and size distributions.

(A) $(PAS)_1F_0$, (B) $(PAS)_1F_1$, (C) $(PAS)_1F_2$, (D) $(PAS)_3F_2$, (E) $(PAS)_6F_2$ measured by multi-laser nanoparticle tracking analysis (MANTA). 62.5 μM in PBS. Background: one frame of light scattering microscopy images showing particles in blue. Inset: size distribution histograms processed from 3000 frames of light scattering microscopy images.

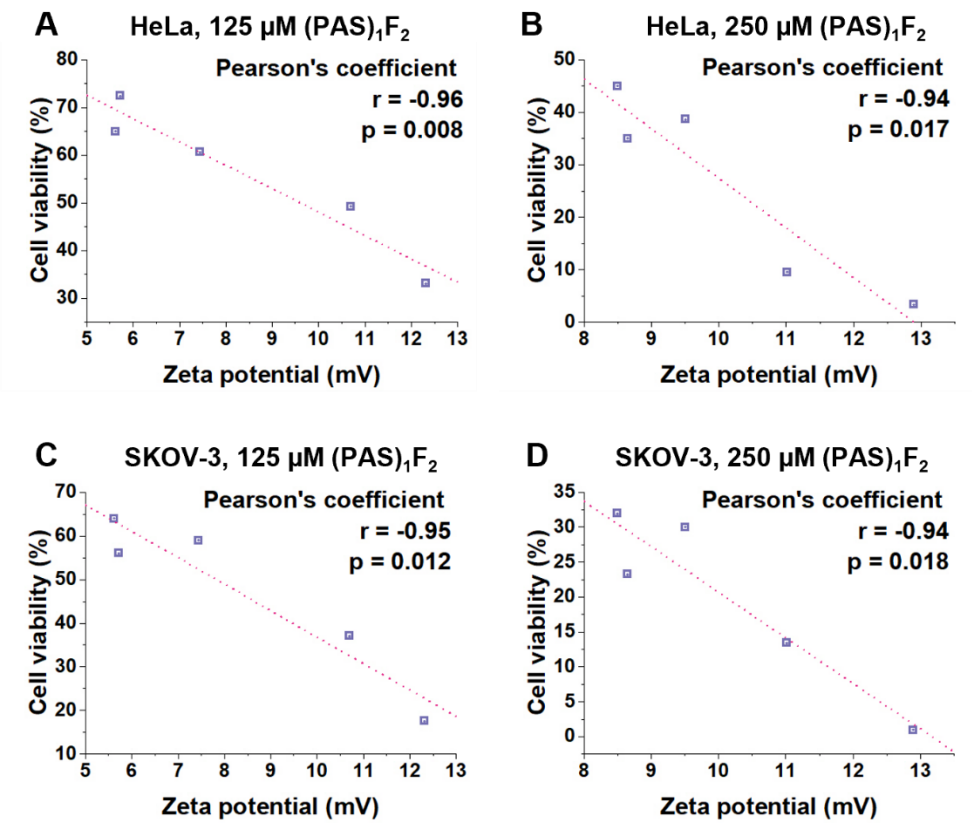

Figure 4.20 Analysis of Pearson's coefficient between cell viability and zeta potential.

(A) HeLa cells treated by 125 μM $(PAS)_1F_2$, (B) HeLa cells treated by 250 μM $(PAS)_1F_2$, (C) SKOV-3 cells treated by 125 μM $(PAS)_1F_2$, (D) SKOV-3 cells treated by 250 μm $(PAS)_1F_2$. Cell cytotoxicity is inversely proportional to zeta potential (Pearson's coefficient <-0.94, $p<0.05$)

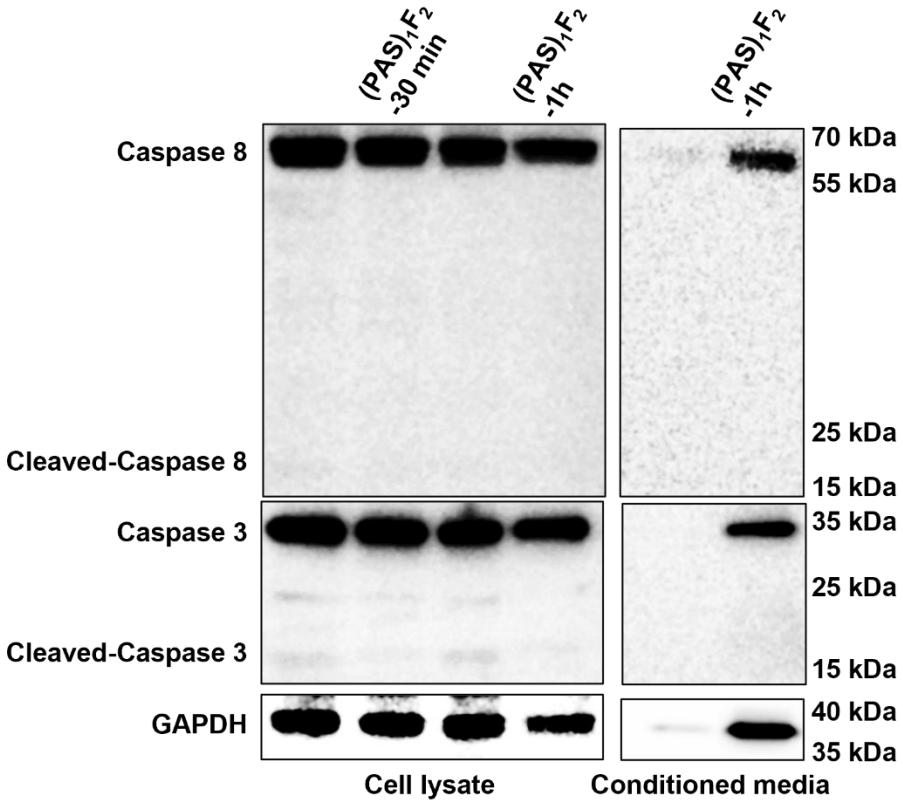

Figure 4.21 Western blot showing no expression of apoptosis related proteins (cleaved caspase 3 and cleaved caspase 8).

SKOV-3 cells were treated by $(PAS)_1F_2$ for 30 min or 1 h. Both the cell lysate and conditioned media were sampled and detected.

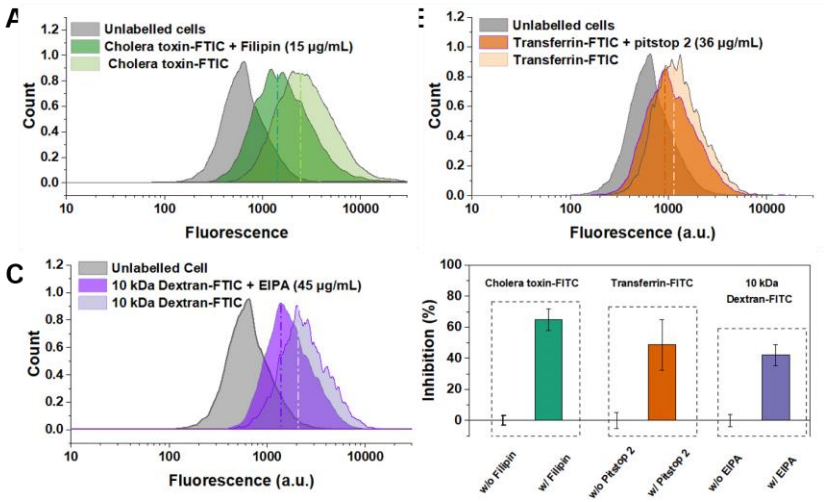

Figure 4.22 Efficacy of endocytic inhibitors.

Flow cytometry histograms of SKOV-3 cells' internalization of (A) cholera toxin-FITC, (B) transferrin-FITC, and (C) 10 kDa dextran-FITC. (D) Quantification of the inhibition rate showing filipin, pitstop 2, and EIPA inhibitors were effective in blocking caveolae-mediated endocytosis, clathrin-mediated endocytosis, and macropinocytosis, respectively.[344]

REFERENCES

(1) Perera, R. H.; Hernandez, C.; Zhou, H.; Kota, P.; Burke, A.; Exner, A. A., Ultrasound Imaging Beyond the Vasculature with New Generation Contrast Agents. *Wiley Interdisciplinary Reviews: Nanomedicine and Nanobiotechnology* **2015,** *7* (4), 593-608.

(2) Parker, L.; Nazarian, L. N.; Carrino, J. A.; Morrison, W. B.; Grimaldi, G.; Frangos, A. J.; Levin, D. C.; Rao, V. M., Musculoskeletal Imaging: Medicare Use, Costs, and Potential for Cost Substitution. *Journal of the American College of Radiology* **2008,** *5* (3), 182-188.

(3) Bushberg, J. T.; Boone, J. M., *The Essential Physics of Medical Imaging*. Lippincott Williams & Wilkins: 2011.

(4) Feinstein, S.; Voci, P.; Segil, L.; Harper, P., Contrast Echocardiography. Philadelphia, PA: Harcourt Brace Jovanovich: 1991.

(5) Quaia, E., Microbubble Ultrasound Contrast Agents: An Update. *European Radiology* **2007,** *17*, 1995-2008.

(6) Stride, E.; Saffari, N., Microbubble Ultrasound Contrast Agents: A Review. *Proceedings of the Institution of Mechanical Engineers, Part H: Journal of Engineering in Medicine* **2003,** *217* (6), 429-447.

(7) Kooiman, K.; Vos, H. J.; Versluis, M.; De Jong, N., Acoustic Behavior of Microbubbles and Implications for Drug Delivery. *Advanced Drug Delivery Reviews* **2014,** *72*, 28-48.

(8) van Rooij, T.; Daeichin, V.; Skachkov, I.; de Jong, N.; Kooiman, K., Targeted Ultrasound Contrast Agents for Ultrasound Molecular Imaging and Therapy. *International Journal of Hyperthermia* **2015,** *31* (2), 90-106.

(9) Min, K. H.; Min, H. S.; Lee, H. J.; Park, D. J.; Yhee, J. Y.; Kim, K.; Kwon, I. C.; Jeong, S. Y.; Silvestre, O. F.; Chen, X., Ph-Controlled Gas-Generating Mineralized Nanoparticles: A Theranostic Agent for Ultrasound Imaging and Therapy of Cancers. *Acs Nano* **2015,** *9* (1), 134-145.

(10) Foroutan, F.; Jokerst, J. V.; Gambhir, S. S.; Vermesh, O.; Kim, H.-W.; Knowles, J. C., Sol–Gel Synthesis and Electrospraying of Biodegradable (P2o5)55–(Cao)30–(Na2o)15 Glass Nanospheres as a Transient Contrast Agent for Ultrasound Stem Cell Imaging. *Acs Nano* **2015,** *9* (2), 1868-1877.

(11) Jokerst, J. V.; Khademi, C.; Gambhir, S. S., Intracellular Aggregation of Multimodal Silica Nanoparticles for Ultrasound-Guided Stem Cell Implantation. *Science Translational Medicine* **2013,** *5* (177), 177ra35-177ra35.

(12) Klibanov, A. L., Targeted Delivery of Gas-Filled Microspheres, Contrast Agents for Ultrasound Imaging. *Advanced Drug Delivery Reviews* **1999,** *37* (1-3), 139-157.

(13) Schutt, E. G.; Klein, D. H.; Mattrey, R. M.; Riess, J. G., Injectable Microbubbles as Contrast Agents for Diagnostic Ultrasound Imaging: The Key Role of Perfluorochemicals. *Angewandte Chemie International Edition* **2003,** *42* (28), 3218-3235.

(14) Kono, Y.; Hölscher, T.; Mattrey, R. F., Use of Ultrasound Microbubbles for Vascular Imaging. In *Nanoparticles in Biomedical Imaging*, Springer: 2008, pp 311-325.

(15) Klibanov, A. L., Ligand-Carrying Gas-Filled Microbubbles: Ultrasound Contrast Agents for Targeted Molecular Imaging. *Bioconjugate Chemistry* **2005,** *16* (1), 9-17.

(16) Casciaro, S.; Conversano, F.; Ragusa, A.; Ada Malvindi, M.; Franchini, R.; Greco, A.; Pellegrino, T.; Gigli, G., Optimal Enhancement Configuration of Silica Nanoparticles for

Ultrasound Imaging and Automatic Detection at Conventional Diagnostic Frequencies. *Investigative Radiology* **2010,** *45* (11), 715-724.

(17) Fang, J.; Nakamura, H.; Maeda, H., The Epr Effect: Unique Features of Tumor Blood Vessels for Drug Delivery, Factors Involved, and Limitations and Augmentation of the Effect. *Advanced Drug Delivery Reviews* **2011,** *63* (3), 136-151.

(18) Perera, R. H.; Solorio, L.; Wu, H.; Gangolli, M.; Silverman, E.; Hernandez, C.; Peiris, P. M.; Broome, A.-M.; Exner, A. A., Nanobubble Ultrasound Contrast Agents for Enhanced Delivery of Thermal Sensitizer to Tumors Undergoing Radiofrequency Ablation. *Pharmaceutical Research* **2014,** *31*, 1407-1417.

(19) Huang, S.-L.; Hamilton, A. J.; Pozharski, E.; Nagaraj, A.; Klegerman, M. E.; McPherson, D. D.; MacDonald, R. C., Physical Correlates of the Ultrasonic Reflectivity of Lipid Dispersions Suitable as Diagnostic Contrast Agents. *Ultrasound in medicine & biology* **2002,** *28* (3), 339-348.

(20) Negishi, Y.; Hamano, N.; Tsunoda, Y.; Oda, Y.; Choijamts, B.; Endo-Takahashi, Y.; Omata, D.; Suzuki, R.; Maruyama, K.; Nomizu, M., Ag73-Modified Bubble Liposomes for Targeted Ultrasound Imaging of Tumor Neovasculature. *Biomaterials* **2013,** *34* (2), 501-507.

(21) Alkan-Onyuksel, H.; Demos, S. M.; Lanza, G. M.; Vonesh, M. J.; Klegerman, M. E.; Kane, B. J.; Kuszak, J.; McPherson, D. D., Development of Inherently Echogenic Liposomes as an Ultrasonic Contrast Agent. *Journal of Pharmaceutical Sciences* **1996,** *85* (5), 486-490.

(22) Yin, T.; Wang, P.; Zheng, R.; Zheng, B.; Cheng, D.; Zhang, X.; Shuai, X., Nanobubbles for Enhanced Ultrasound Imaging of Tumors. *International Journal of Nanomedicine* **2012**, 895-904.

(23) Díaz-López, R.; Tsapis, N.; Santin, M.; Bridal, S. L.; Nicolas, V.; Jaillard, D.; Libong, D.; Chaminade, P.; Marsaud, V.; Vauthier, C., The Performance of Pegylated Nanocapsules of Perfluorooctyl Bromide as an Ultrasound Contrast Agent. *Biomaterials* **2010,** *31* (7), 1723-1731.

(24) Wheatley, M. A.; Forsberg, F.; Oum, K.; Ro, R.; El-Sherif, D., Comparison of in Vitro and in Vivo Acoustic Response of a Novel 50: 50 Plga Contrast Agent. *Ultrasonics* **2006,** *44* (4), 360-367.

(25) Rapoport, N.; Gao, Z.; Kennedy, A., Multifunctional Nanoparticles for Combining Ultrasonic Tumor Imaging and Targeted Chemotherapy. *Journal of the National Cancer Institute* **2007,** *99* (14), 1095-1106.

(26) Xu, J. S.; Huang, J.; Qin, R.; Hinkle, G. H.; Povoski, S. P.; Martin, E. W.; Xu, R. X., Synthesizing and Binding Dual-Mode Poly (Lactic-Co-Glycolic Acid)(Plga) Nanobubbles for Cancer Targeting and Imaging. *Biomaterials* **2010,** *31* (7), 1716-1722.

(27) Wu, H.; Rognin, N. G.; Krupka, T. M.; Solorio, L.; Yoshiara, H.; Guenette, G.; Sanders, C.; Kamiyama, N.; Exner, A. A., Acoustic Characterization and Pharmacokinetic Analyses of New Nanobubble Ultrasound Contrast Agents. *Ultrasound in medicine & biology* **2013,** *39* (11), 2137-2146.

(28) Krupka, T. M.; Solorio, L.; Wilson, R. E.; Wu, H.; Azar, N.; Exner, A. A., Formulation and Characterization of Echogenic Lipid− Pluronic Nanobubbles. *Molecular Pharmaceutics* **2010,** *7* (1), 49-59.

(29) Yin, T.; Wang, P.; Zheng, R.; Zheng, B.; Cheng, D.; Zhang, X.; Shuai, X., Nanobubbles for Enhanced Ultrasound Imaging of Tumors. *International Journal of Nanomedicine* **2012,** *7* (null), 895-904.

(30) Huang, S.-L.; McPherson, D. D.; MacDonald, R. C., A Method to Co-Encapsulate Gas and Drugs in Liposomes for Ultrasound-Controlled Drug Delivery. *Ultrasound in medicine & biology* **2008,** *34* (8), 1272-1280.

(31) Shapiro, M. G.; Goodwill, P. W.; Neogy, A.; Yin, M.; Foster, F. S.; Schaffer, D. V.; Conolly, S. M., Biogenic Gas Nanostructures as Ultrasonic Molecular Reporters. *Nature Nanotechnology* **2014,** *9* (4), 311-316.

(32) Mai, L.; Yao, A.; Li, J.; Wei, Q.; Yuchi, M.; He, X.; Ding, M.; Zhou, Q., Cyanine 5.5 Conjugated Nanobubbles as a Tumor Selective Contrast Agent for Dual Ultrasound-Fluorescence Imaging in a Mouse Model. *Plos One* **2013,** *8* (4), e61224.

(33) An, L.; Hu, H.; Du, J.; Wei, J.; Wang, L.; Yang, H.; Wu, D.; Shi, H.; Li, F.; Yang, S., Paramagnetic Hollow Silica Nanospheres for in Vivo Targeted Ultrasound and Magnetic Resonance Imaging. *Biomaterials* **2014,** *35* (20), 5381-5392.

(34) Smith, B. R.; Gambhir, S. S., Nanomaterials for in Vivo Imaging. *Chemical Reviews* **2017,** *117* (3), 901-986.

(35) Prabhakar, U.; Maeda, H.; Jain, R. K.; Sevick-Muraca, E. M.; Zamboni, W.; Farokhzad, O. C.; Barry, S. T.; Gabizon, A.; Grodzinski, P.; Blakey, D. C., Challenges and Key Considerations of the Enhanced Permeability and Retention Effect for Nanomedicine Drug Delivery in Oncology. AACR: 2013.

(36) Lammers, T., Smart Drug Delivery Systems: Back to the Future Vs. Clinical Reality. *International Journal of Pharmaceutics* **2013,** *454* (1), 527-529.

(37) Zhang, K.; Chen, H.; Guo, X.; Zhang, D.; Zheng, Y.; Zheng, H.; Shi, J., Double-Scattering/Reflection in a Single Nanoparticle for Intensified Ultrasound Imaging. *Scientific Reports* **2015,** *5* (1), 8766.

(38) Wu, H.; Shi, H.; Zhang, H.; Wang, X.; Yang, Y.; Yu, C.; Hao, C.; Du, J.; Hu, H.; Yang, S., Prostate Stem Cell Antigen Antibody-Conjugated Multiwalled Carbon Nanotubes for Targeted Ultrasound Imaging and Drug Delivery. *Biomaterials* **2014,** *35* (20), 5369-5380.

(39) Delogu, L. G.; Vidili, G.; Venturelli, E.; Ménard-Moyon, C.; Zoroddu, M. A.; Pilo, G.; Nicolussi, P.; Ligios, C.; Bedognetti, D.; Sgarrella, F., Functionalized Multiwalled Carbon Nanotubes as Ultrasound Contrast Agents. *Proceedings of the National Academy of Sciences* **2012,** *109* (41), 16612-16617.

(40) Du Toit, L. C.; Govender, T.; Pillay, V.; Choonara, Y. E.; Kodama, T., Investigating the Effect of Polymeric Approaches on Circulation Time and Physical Properties of Nanobubbles. *Pharmaceutical Research* **2011,** *28*, 494-504.

(41) Park, J. H.; Gu, L.; von Maltzahn, G.; Ruoslahti, E.; Bhatia, S. N.; Sailor, M. J., Biodegradable Luminescent Porous Silicon Nanoparticles for in Vivo Applications. *Nature Materials* **2009,** *8* (4), 331-6.

(42) Ehlerding, E. B.; Chen, F.; Cai, W., Biodegradable and Renal Clearable Inorganic Nanoparticles. *Advanced Science* **2016,** *3* (2), 1500223.

(43) Abou Neel, E. A.; Knowles, J. C., Physical and Biocompatibility Studies of Novel Titanium Dioxide Doped Phosphate-Based Glasses for Bone Tissue Engineering Applications. *J Mater Sci Mater Med* **2008,** *19* (1), 377-86.

(44) Bitar, M.; Salih, V.; Mudera, V.; Knowles, J. C.; Lewis, M. P., Soluble Phosphate Glasses: In Vitro Studies Using Human Cells of Hard and Soft Tissue Origin. *Biomaterials* **2004,** *25* (12), 2283-2292.

(45) Gough, J. E.; Christian, P.; Scotchford, C. A.; Jones, I. A., Long-Term Craniofacial Osteoblast Culture on a Sodium Phosphate and a Calcium/Sodium Phosphate Glass. *Journal of Biomedical Materials Research Part A* **2003,** *66A* (2), 233-240.

(46) Ceci-Ginistrelli, E.; Pugliese, D.; Boetti, N. G.; Novajra, G.; Ambrosone, A.; Lousteau, J.; Vitale-Brovarone, C.; Abrate, S.; Milanese, D., Novel Biocompatible and Resorbable Uv-Transparent Phosphate Glass Based Optical Fiber. *Optical Materials Express* **2016,** *6* (6), 2040.

(47) Ceci-Ginistrelli, E.; Pontremoli, C.; Pugliese, D.; Barbero, N.; Boetti, N. G.; Barolo, C.; Visentin, S.; Milanese, D., Drug Release Kinetics from Biodegradable Uv-Transparent Hollow Calcium-Phosphate Glass Fibers. *Materials Letters* **2017,** *191*, 116-118.

(48) Farag, M. M.; El-Rashedi, A. M. I.; Rüssel, C., In Vitro Biocompatibility Evaluation of Canasite-Calcium Phosphate Glass-Ceramics. *Journal of Non-Crystalline Solids* **2018,** *488*, 24-35.

(49) Li, J.; Cai, S.; Xu, G.; Li, X.; Zhang, W.; Zhang, Z., In Vitro Biocompatibility Study of Calcium Phosphate Glass Ceramic Scaffolds with Different Trace Element Doping. *Materials Science and Engineering: C* **2012,** *32* (2), 356-363.

(50) McLaren, J. S.; Macri-Pellizzeri, L.; Hossain, K. M. Z.; Patel, U.; Grant, D. M.; Scammell, B. E.; Ahmed, I.; Sottile, V., Porous Phosphate-Based Glass Microspheres Show Biocompatibility, Tissue Infiltration, and Osteogenic Onset in an Ovine Bone Defect Model. *Acs Applied Materials & Interfaces* **2019,** *11* (17), 15436-15446.

(51) Padilla, S.; Roman, J.; Sanchez-Salcedo, S.; Vallet-Regi, M., Hydroxyapatite/Sio(2)-Cao-P(2)O(5) Glass Materials: In Vitro Bioactivity and Biocompatibility. *Acta Biomater* **2006,** *2* (3), 331-42.

(52) Pickup, D. M.; Guerry, P.; Moss, R. M.; Knowles, J. C.; Smith, M. E.; Newport, R. J., New Sol–Gel Synthesis of a (Cao)0.3(Na2o)0.2(P2o5)0.5 Bioresorbable Glass and Its Structural Characterisation. *Journal of Materials Chemistry* **2007,** *17* (45), 4777.

(53) Knowles, J. C., Phosphate Based Glasses for Biomedical Applications. *Journal of Materials Chemistry* **2003,** *13* (10), 2395.

(54) Santos, E. M.; Radin, S.; Ducheyne, P., Sol-Gel Derived Carrier for the Controlled Release of Proteins. *Biomaterials* **1999,** *20* (18), 1695-700.

(55) Domingues, Z. R.; Cortés, M. E.; Gomes, T. A.; Diniz, H. F.; Freitas, C. S.; Gomes, J. B.; Faria, A. M.; Sinisterra, R. D., Bioactive Glass as a Drug Delivery System of Tetracycline and Tetracycline Associated with Beta-Cyclodextrin. *Biomaterials* **2004,** *25* (2), 327-33.

(56) Ziegler, J.; Mayr-Wohlfart, U.; Kessler, S.; Breitig, D.; Günther, K.-P., Adsorption and Release Properties of Growth Factors from Biodegradable Implants. *Journal of Biomedical Materials Research* **2002,** *59* (3), 422-428.

(57) Govindan, R.; Girija, E. K., Drug Loaded Phosphate Glass/Hydroxyapatite Nanocomposite for Orthopedic Applications. *J Mater Chem B* **2014,** *2* (33), 5468-5477.

(58) Kim, H. W.; Lee, E. J.; Jun, I. K.; Kim, H. E.; Knowles, J. C., Degradation and Drug Release of Phosphate Glass/Polycaprolactone Biological Composites for Hard-Tissue Regeneration. *J Biomed Mater Res B Appl Biomater* **2005,** *75* (1), 34-41.

(59) Coley, W. B., The Treatment of Inoperable Sarcoma by Bacterial Toxins (the Mixed Toxins of the Streptococcus Erysipelas and the Bacillus Prodigiosus). *Proceedings of the Royal Society of Medicine* **1910,** *3* (Surg_Sect), 1-48.

(60) Rosenberg, S. A.; Yannelli, J. R.; Yang, J. C.; Topalian, S. L.; Schwartzentruber, D. J.; Weber, J. S.; Parkinson, D. R.; Seipp, C. A.; Einhorn, J. H.; White, D. E., Treatment of

Patients with Metastatic Melanoma with Autologous Tumor-Infiltrating Lymphocytes and Interleukin 2. *JNCI: Journal of the National Cancer Institute* **1994,** *86* (15), 1159-1166.

(61) van der Bruggen, P.; Traversari, C.; Chomez, P.; Lurquin, C.; De Plaen, E.; Van den Eynde, B.; Knuth, A.; Boon, T., A Gene Encoding an Antigen Recognized by Cytolytic T Lymphocytes on a Human Melanoma. *Science* **1991,** *254* (5038), 1643-1647.

(62) Topalian, S. L.; Weiner, G. J.; Pardoll, D. M., Cancer Immunotherapy Comes of Age. *Journal of Clinical Oncology* **2011,** *29* (36), 4828.

(63) Sharma, P.; Allison, J. P., Immune Checkpoint Targeting in Cancer Therapy: Toward Combination Strategies with Curative Potential. *Cell* **2015,** *161* (2), 205-214.

(64) Mellman, I.; Coukos, G.; Dranoff, G., Cancer Immunotherapy Comes of Age. *Nature* **2011,** *480* (7378), 480-489.

(65) Segal, N. H.; Parsons, D. W.; Peggs, K. S.; Velculescu, V.; Kinzler, K. W.; Vogelstein, B.; Allison, J. P., Epitope Landscape in Breast and Colorectal Cancer. *Cancer Research* **2008,** *68* (3), 889-892.

(66) Shi, H.; Qi, X.; Ma, B.; Cao, Y.; Wang, L.; Sun, L.; Niu, H., The Status, Limitation and Improvement of Adoptive Cellular Immunotherapy in Advanced Urologic Malignancies. *Chinese Journal of Cancer Research* **2015,** *27* (2), 128.

(67) Gilham, D. E.; Anderson, J.; Bridgeman, J. S.; Hawkins, R. E.; Exley, M. A.; Stauss, H.; Maher, J.; Pule, M.; Sewell, A. K.; Bendle, G., Adoptive T-Cell Therapy for Cancer in the United Kingdom: A Review of Activity for the British Society of Gene and Cell Therapy Annual Meeting 2015. *Human Gene Therapy* **2015,** *26* (5), 276-285.

(68) Kazemi, T.; Younesi, V.; Jadidi-Niaragh, F.; Yousefi, M., Immunotherapeutic Approaches for Cancer Therapy: An Updated Review. *Artificial cells, nanomedicine, and biotechnology* **2016,** *44* (3), 769-779.

(69) Yee, C., Adoptive T-Cell Therapy for Cancer: Boutique Therapy or Treatment Modality? *Clinical Cancer Research* **2013,** *19* (17), 4550-4552.

(70) Klebanoff, C. A.; Finkelstein, S. E.; Surman, D. R.; Lichtman, M. K.; Gattinoni, L.; Theoret, M. R.; Grewal, N.; Spiess, P. J.; Antony, P. A.; Palmer, D. C., Il-15 Enhances the in Vivo Antitumor Activity of Tumor-Reactive Cd8+ T Cells. *Proceedings of the National Academy of Sciences* **2004,** *101* (7), 1969-1974.

(71) Rosenberg, S. A.; Yang, J. C.; Sherry, R. M.; Kammula, U. S.; Hughes, M. S.; Phan, G. Q.; Citrin, D. E.; Restifo, N. P.; Robbins, P. F.; Wunderlich, J. R., Durable Complete Responses in Heavily Pretreated Patients with Metastatic Melanoma Using T-Cell Transfer Immunotherapy. *Clinical Cancer Research* **2011,** *17* (13), 4550-4557.

(72) Qian, X.; Wang, X.; Jin, H., Cell Transfer Therapy for Cancer: Past, Present, and Future. *Journal of immunology research* **2014,** *2014*.

(73) Palucka, K.; Banchereau, J., Cancer Immunotherapy Via Dendritic Cells. *Nature Reviews Cancer* **2012,** *12* (4), 265-277.

(74) Hodi, F. S.; O'day, S. J.; McDermott, D. F.; Weber, R. W.; Sosman, J. A.; Haanen, J. B.; Gonzalez, R.; Robert, C.; Schadendorf, D.; Hassel, J. C., Improved Survival with Ipilimumab in Patients with Metastatic Melanoma. *New England Journal of Medicine* **2010,** *363* (8), 711-723.

(75) Phan, G. Q.; Yang, J. C.; Sherry, R. M.; Hwu, P.; Topalian, S. L.; Schwartzentruber, D. J.; Restifo, N. P.; Haworth, L. R.; Seipp, C. A.; Freezer, L. J., Cancer Regression and Autoimmunity Induced by Cytotoxic T Lymphocyte-Associated Antigen 4 Blockade in Patients

with Metastatic Melanoma. *Proceedings of the National Academy of Sciences* **2003,** *100* (14), 8372-8377.

(76) Ribas, A., Releasing the Brakes on Cancer Immunotherapy. *N Engl J Med* **2015,** *373* (16), 1490-1492.

(77) Mahoney, K. M.; Rennert, P. D.; Freeman, G. J., Combination Cancer Immunotherapy and New Immunomodulatory Targets. *Nature reviews Drug discovery* **2015,** *14* (8), 561-584.

(78) Dong, H.; Zhu, G.; Tamada, K.; Chen, L., B7-H1, a Third Member of the B7 Family, Co-Stimulates T-Cell Proliferation and Interleukin-10 Secretion. *Nature Medicine* **1999,** *5* (12), 1365-1369.

(79) Brahmer, J. R.; Tykodi, S. S.; Chow, L. Q.; Hwu, W.-J.; Topalian, S. L.; Hwu, P.; Drake, C. G.; Camacho, L. H.; Kauh, J.; Odunsi, K., Safety and Activity of Anti–Pd-L1 Antibody in Patients with Advanced Cancer. *New England Journal of Medicine* **2012,** *366* (26), 2455-2465.

(80) Sharma, P.; Wagner, K.; Wolchok, J. D.; Allison, J. P., Novel Cancer Immunotherapy Agents with Survival Benefit: Recent Successes and Next Steps. *Nature Reviews Cancer* **2011,** *11* (11), 805-812.

(81) Palucka, K.; Banchereau, J., Dendritic-Cell-Based Therapeutic Cancer Vaccines. *Immunity* **2013,** *39* (1), 38-48.

(82) Chen, Daniel S.; Mellman, I., Oncology Meets Immunology: The Cancer-Immunity Cycle. *Immunity* **2013,** *39* (1), 1-10.

(83) Farkona, S.; Diamandis, E. P.; Blasutig, I. M., Cancer Immunotherapy: The Beginning of the End of Cancer? *BMC Medicine* **2016,** *14* (1), 73.

(84) Drake, C. G.; Jaffee, E.; Pardoll, D. M., Mechanisms of Immune Evasion by Tumors. *Advances in immunology* **2006,** *90*, 51-81.

(85) Fong, L.; Small, E. J., Anti–Cytotoxic T-Lymphocyte Antigen-4 Antibody: The First in an Emerging Class of Immunomodulatory Antibodies for Cancer Treatment. *Journal of Clinical Oncology* **2008,** *26* (32), 5275-5283.

(86) Robert, C.; Thomas, L.; Bondarenko, I.; O'Day, S.; Weber, J.; Garbe, C.; Lebbe, C.; Baurain, J.-F.; Testori, A.; Grob, J.-J., Ipilimumab Plus Dacarbazine for Previously Untreated Metastatic Melanoma. *New England Journal of Medicine* **2011,** *364* (26), 2517-2526.

(87) Freeman, G. J.; Long, A. J.; Iwai, Y.; Bourque, K.; Chernova, T.; Nishimura, H.; Fitz, L. J.; Malenkovich, N.; Okazaki, T.; Byrne, M. C., Engagement of the Pd-1 Immunoinhibitory Receptor by a Novel B7 Family Member Leads to Negative Regulation of Lymphocyte Activation. *The Journal of experimental medicine* **2000,** *192* (7), 1027-1034.

(88) Cha, J.-H.; Chan, L.-C.; Li, C.-W.; Hsu, J. L.; Hung, M.-C., Mechanisms Controlling Pd-L1 Expression in Cancer. *Molecular Cell* **2019,** *76* (3), 359-370.

(89) Yokosuka, T.; Takamatsu, M.; Kobayashi-Imanishi, W.; Hashimoto-Tane, A.; Azuma, M.; Saito, T., Programmed Cell Death 1 Forms Negative Costimulatory Microclusters That Directly Inhibit T Cell Receptor Signaling by Recruiting Phosphatase Shp2. *Journal of Experimental Medicine* **2012,** *209* (6), 1201-1217.

(90) Patsoukis, N.; Bardhan, K.; Chatterjee, P.; Sari, D.; Liu, B.; Bell, L. N.; Karoly, E. D.; Freeman, G. J.; Petkova, V.; Seth, P., Pd-1 Alters T-Cell Metabolic Reprogramming by Inhibiting Glycolysis and Promoting Lipolysis and Fatty Acid Oxidation. *Nature Communications* **2015,** *6* (1), 6692.

(91) Topalian, S. L.; Hodi, F. S.; Brahmer, J. R.; Gettinger, S. N.; Smith, D. C.; McDermott, D. F.; Powderly, J. D.; Carvajal, R. D.; Sosman, J. A.; Atkins, M. B., Safety, Activity, and Immune Correlates of Anti–Pd-1 Antibody in Cancer. *New England Journal of Medicine* **2012,** *366* (26), 2443-2454.

(92) Topalian, S. L.; Sznol, M.; McDermott, D. F.; Kluger, H. M.; Carvajal, R. D.; Sharfman, W. H.; Brahmer, J. R.; Lawrence, D. P.; Atkins, M. B.; Powderly, J. D., Survival, Durable Tumor Remission, and Long-Term Safety in Patients with Advanced Melanoma Receiving Nivolumab. *Journal of Clinical Oncology* **2014,** *32* (10), 1020.

(93) Thommen, D. S.; Schumacher, T. N., T Cell Dysfunction in Cancer. *Cancer Cell* **2018,** *33* (4), 547-562.

(94) Jenkins, R. W.; Barbie, D. A.; Flaherty, K. T., Mechanisms of Resistance to Immune Checkpoint Inhibitors. *British Journal of Cancer* **2018,** *118* (1), 9-16.

(95) Schoenfeld, A. J.; Hellmann, M. D., Acquired Resistance to Immune Checkpoint Inhibitors. *Cancer Cell* **2020,** *37* (4), 443-455.

(96) Lin, A.; Wei, T.; Meng, H.; Luo, P.; Zhang, J., Role of the Dynamic Tumor Microenvironment in Controversies Regarding Immune Checkpoint Inhibitors for the Treatment of Non-Small Cell Lung Cancer (Nsclc) with Egfr Mutations. *Molecular Cancer* **2019,** *18*, 1-18.

(97) Binnewies, M.; Roberts, E. W.; Kersten, K.; Chan, V.; Fearon, D. F.; Merad, M.; Coussens, L. M.; Gabrilovich, D. I.; Ostrand-Rosenberg, S.; Hedrick, C. C., Understanding the Tumor Immune Microenvironment (Time) for Effective Therapy. *Nature Medicine* **2018,** *24* (5), 541-550.

(98) Munn, D. H.; Bronte, V., Immune Suppressive Mechanisms in the Tumor Microenvironment. *Current opinion in immunology* **2016,** *39*, 1-6.

(99) Ghirelli, C.; Hagemann, T., Targeting Immunosuppression for Cancer Therapy. *The Journal of clinical investigation* **2013,** *123* (6), 2355-2357.

(100) Saleh, R.; Elkord, E., Treg-Mediated Acquired Resistance to Immune Checkpoint Inhibitors. *Cancer Letters* **2019,** *457*, 168-179.

(101) Eil, R.; Vodnala, S. K.; Clever, D.; Klebanoff, C. A.; Sukumar, M.; Pan, J. H.; Palmer, D. C.; Gros, A.; Yamamoto, T. N.; Patel, S. J., Ionic Immune Suppression within the Tumour Microenvironment Limits T Cell Effector Function. *Nature* **2016,** *537* (7621), 539-543.

(102) Nakagawa, Y.; Negishi, Y.; Shimizu, M.; Takahashi, M.; Ichikawa, M.; Takahashi, H., Effects of Extracellular Ph and Hypoxia on the Function and Development of Antigen-Specific Cytotoxic T Lymphocytes. *Immunology Letters* **2015,** *167* (2), 72-86.

(103) MacIver, N. J.; Michalek, R. D.; Rathmell, J. C., Metabolic Regulation of T Lymphocytes. *Annual Review of Immunology* **2013,** *31*, 259-283.

(104) Jiang, Y.; Li, Y.; Zhu, B., T-Cell Exhaustion in the Tumor Microenvironment. *Cell Death & Disease* **2015,** *6* (6), e1792-e1792.

(105) Ma, X.; Bi, E.; Lu, Y.; Su, P.; Huang, C.; Liu, L.; Wang, Q.; Yang, M.; Kalady, M. F.; Qian, J., Cholesterol Induces Cd8+ T Cell Exhaustion in the Tumor Microenvironment. *Cell Metabolism* **2019,** *30* (1), 143-156. e5.

(106) Blank, C. U.; Haining, W. N.; Held, W.; Hogan, P. G.; Kallies, A.; Lugli, E.; Lynn, R. C.; Philip, M.; Rao, A.; Restifo, N. P., Defining 'T Cell Exhaustion'. *Nature Reviews Immunology* **2019,** *19* (11), 665-674.

(107) Im, S. J.; Ha, S.-J., Re-Defining T-Cell Exhaustion: Subset, Function, and Regulation. *Immune network* **2020,** *20* (1).

(108) Mpekris, F.; Voutouri, C.; Baish, J. W.; Duda, D. G.; Munn, L. L.; Stylianopoulos, T.; Jain, R. K., Combining Microenvironment Normalization Strategies to Improve Cancer Immunotherapy. *Proceedings of the National Academy of Sciences* **2020,** *117* (7), 3728-3737.

(109) van den Ende, T.; van den Boorn, H. G.; Hoonhout, N. M.; Van Etten-Jamaludin, F. S.; Meijer, S. L.; Derks, S.; de Gruijl, T. D.; Bijlsma, M. F.; van Oijen, M. G.; van Laarhoven, H. W., Priming the Tumor Immune Microenvironment with Chemo (Radio) Therapy: A Systematic Review across Tumor Types. *Biochimica et Biophysica Acta (BBA)-Reviews on Cancer* **2020,** *1874* (1), 188386.

(110) Sanmamed, M. F.; Chen, L., A Paradigm Shift in Cancer Immunotherapy: From Enhancement to Normalization. *Cell* **2018,** *175* (2), 313-326.

(111) Bloy, N.; Garcia, P.; Laumont, C. M.; Pitt, J. M.; Sistigu, A.; Stoll, G.; Yamazaki, T.; Bonneil, E.; Buque, A.; Humeau, J., Immunogenic Stress and Death of Cancer Cells: Contribution of Antigenicity Vs Adjuvanticity to Immunosurveillance. *Immunological Reviews* **2017,** *280* (1), 165-174.

(112) Galluzzi, L.; Buqué, A.; Kepp, O.; Zitvogel, L.; Kroemer, G., Immunogenic Cell Death in Cancer and Infectious Disease. *Nature Reviews Immunology* **2017,** *17* (2), 97-111.

(113) Krysko, D. V.; Garg, A. D.; Kaczmarek, A.; Krysko, O.; Agostinis, P.; Vandenabeele, P., Immunogenic Cell Death and Damps in Cancer Therapy. *Nat Rev Cancer* **2012,** *12* (12), 860-75.

(114) Ahmed, A.; Tait, S. W., Targeting Immunogenic Cell Death in Cancer. *Molecular Oncology* **2020,** *14* (12), 2994-3006.

(115) Yatim, N.; Jusforgues-Saklani, H.; Orozco, S.; Schulz, O.; Barreira da Silva, R.; Reis e Sousa, C.; Green, D. R.; Oberst, A.; Albert, M. L., Ripk1 and Nf-Kb Signaling in Dying Cells Determines Cross-Priming of Cd8+ T Cells. *Science* **2015,** *350* (6258), 328-334.

(116) Wu, D.; Wang, S.; Yu, G.; Chen, X., Cell Death Mediated by the Pyroptosis Pathway with the Aid of Nanotechnology: Prospects for Cancer Therapy. *Angewandte Chemie International Edition* **2021,** *60* (15), 8018-8034.

(117) Li, M.; Kim, J.; Rha, H.; Son, S.; Levine, M. S.; Xu, Y.; Sessler, J. L.; Kim, J. S., Photon-Controlled Pyroptosis Activation (Photopyro): An Emerging Trigger for Antitumor Immune Response. *Journal of the American Chemical Society* **2023,** *145* (11), 6007-6023.

(118) Zhang, Y.; Fang, C.; Zhang, W.; Zhang, K., Emerging Pyroptosis-Engineered Nanobiotechnologies Regulate Cancers and Inflammatory Diseases: A Double-Edged Sword. *Matter* **2022,** *5* (11), 3740-3774.

(119) Bonaventura, P.; Shekarian, T.; Alcazer, V.; Valladeau-Guilemond, J.; Valsesia-Wittmann, S.; Amigorena, S.; Caux, C.; Depil, S., Cold Tumors: A Therapeutic Challenge for Immunotherapy. *Frontiers in Immunology* **2019,** *10*, 168-168.

(120) Tan, Y.; Chen, Q.; Li, X.; Zeng, Z.; Xiong, W.; Li, G.; Li, X.; Yang, J.; Xiang, B.; Yi, M., Pyroptosis: A New Paradigm of Cell Death for Fighting against Cancer. *Journal of Experimental & Clinical Cancer Research* **2021,** *40* (1), 153.

(121) Wu, Y.; Dong, G.; Sheng, C., Targeting Necroptosis in Anticancer Therapy: Mechanisms and Modulators. *Acta Pharmaceutica Sinica B* **2020,** *10* (9), 1601-1618.

(122) Ahmed, A.; Tait, S. W. G., Targeting Immunogenic Cell Death in Cancer. *Molecular Oncology* **2020,** *14* (12), 2994-3006.

(123) Duan, Q.; Zhang, H.; Zheng, J.; Zhang, L., Turning Cold into Hot: Firing up the Tumor Microenvironment. *Trends in Cancer* **2020,** *6* (7), 605-618.

(124) Kroemer, G.; Galluzzi, L.; Kepp, O.; Zitvogel, L., Immunogenic Cell Death in Cancer Therapy. *Annual Review of Immunology* **2013,** *31*, 51-72.

(125) Catanzaro, E.; Feron, O.; Skirtach, A. G.; Krysko, D. V., Immunogenic Cell Death and Role of Nanomaterials Serving as Therapeutic Vaccine for Personalized Cancer Immunotherapy. *Frontiers in Immunology* **2022,** *13*, 925290.

(126) Garg, A. D.; Nowis, D.; Golab, J.; Vandenabeele, P.; Krysko, D. V.; Agostinis, P., Immunogenic Cell Death, Damps and Anticancer Therapeutics: An Emerging Amalgamation. *Biochimica et Biophysica Acta (BBA)-Reviews on Cancer* **2010,** *1805* (1), 53-71.

(127) Obeid, M.; Tesniere, A.; Ghiringhelli, F.; Fimia, G. M.; Apetoh, L.; Perfettini, J.-L.; Castedo, M.; Mignot, G.; Panaretakis, T.; Casares, N., Calreticulin Exposure Dictates the Immunogenicity of Cancer Cell Death. *Nature Medicine* **2007,** *13* (1), 54-61.

(128) Garg, A. D.; Krysko, D. V.; Verfaillie, T.; Kaczmarek, A.; Ferreira, G. B.; Marysael, T.; Rubio, N.; Firczuk, M.; Mathieu, C.; Roebroek, A. J., A Novel Pathway Combining Calreticulin Exposure and Atp Secretion in Immunogenic Cancer Cell Death. *The EMBO journal* **2012,** *31* (5), 1062-1079.

(129) Casares, N.; Pequignot, M. O.; Tesniere, A.; Ghiringhelli, F.; Roux, S.; Chaput, N.; Schmitt, E.; Hamai, A.; Hervas-Stubbs, S.; Obeid, M., Caspase-Dependent Immunogenicity of Doxorubicin-Induced Tumor Cell Death. *The Journal of experimental medicine* **2005,** *202* (12), 1691-1701.

(130) Tan, Y.; Chen, Q.; Li, X.; Zeng, Z.; Xiong, W.; Li, G.; Li, X.; Yang, J.; Xiang, B.; Yi, M., Pyroptosis: A New Paradigm of Cell Death for Fighting against Cancer. *Journal of Experimental & Clinical Cancer Research* **2021,** *40* (1), 1-15.

(131) Zhang, Z.; Zhang, Y.; Xia, S.; Kong, Q.; Li, S.; Liu, X.; Junqueira, C.; Meza-Sosa, K. F.; Mok, T. M. Y.; Ansara, J., Gasdermin E Suppresses Tumour Growth by Activating Anti-Tumour Immunity. *Nature* **2020,** *579* (7799), 415-420.

(132) Wang, Q.; Wang, Y.; Ding, J.; Wang, C.; Zhou, X.; Gao, W.; Huang, H.; Shao, F.; Liu, Z., A Bioorthogonal System Reveals Antitumour Immune Function of Pyroptosis. *Nature* **2020,** *579* (7799), 421-426.

(133) Tang, R.; Xu, J.; Zhang, B.; Liu, J.; Liang, C.; Hua, J.; Meng, Q.; Yu, X.; Shi, S., Ferroptosis, Necroptosis, and Pyroptosis in Anticancer Immunity. *Journal of Hematology & Oncology* **2020,** *13*, 1-18.

(134) Alu, A.; Han, X.; Ma, X.; Wu, M.; Wei, Y.; Wei, X., The Role of Lysosome in Regulated Necrosis. *Acta Pharmaceutica Sinica B* **2020,** *10* (10), 1880-1903.

(135) Aaes, T. L.; Kaczmarek, A.; Delvaeye, T.; De Craene, B.; De Koker, S.; Heyndrickx, L.; Delrue, I.; Taminau, J.; Wiernicki, B.; De Groote, P., Vaccination with Necroptotic Cancer Cells Induces Efficient Anti-Tumor Immunity. *Cell Reports* **2016,** *15* (2), 274-287.

(136) Aaes, T. L.; Verschuere, H.; Kaczmarek, A.; Heyndrickx, L.; Wiernicki, B.; Delrue, I.; De Craene, B.; Taminau, J.; Delvaeye, T.; Bertrand, M. J., Immunodominant Ah1 Antigen-Deficient Necroptotic, but Not Apoptotic, Murine Cancer Cells Induce Antitumor Protection. *The Journal of Immunology* **2020,** *204* (4), 775-787.

(137) Tang, D.; Kang, R.; Berghe, T. V.; Vandenabeele, P.; Kroemer, G., The Molecular Machinery of Regulated Cell Death. *Cell Research* **2019,** *29* (5), 347-364.

(138) Sun, X.; Ou, Z.; Xie, M.; Kang, R.; Fan, Y.; Niu, X.; Wang, H.; Cao, L.; Tang, D., Hspb1 as a Novel Regulator of Ferroptotic Cancer Cell Death. *Oncogene* **2015,** *34* (45), 5617-5625.

(139) Dixon, S. J., Ferroptosis: Bug or Feature? *Immunological Reviews* **2017,** *277* (1), 150-157.

(140) Green, D. R., The Coming Decade of Cell Death Research: Five Riddles. *Cell* **2019,** *177* (5), 1094-1107.

(141) Chu, B.; Kon, N.; Chen, D.; Li, T.; Liu, T.; Jiang, L.; Song, S.; Tavana, O.; Gu, W., Alox12 Is Required for P53-Mediated Tumour Suppression through a Distinct Ferroptosis Pathway. *Nat Cell Biol* **2019,** *21* (5), 579-591.

(142) Demuynck, R.; Efimova, I.; Naessens, F.; Krysko, D. V., Immunogenic Ferroptosis and Where to Find It? *Journal for Immunotherapy of Cancer* **2021,** *9* (12).

(143) Liu, J.; Zhu, S.; Zeng, L.; Li, J.; Klionsky, D. J.; Kroemer, G.; Jiang, J.; Tang, D.; Kang, R., Dcn Released from Ferroptotic Cells Ignites Ager-Dependent Immune Responses. *Autophagy* **2022,** *18* (9), 2036-2049.

(144) Wen, Q.; Liu, J.; Kang, R.; Zhou, B.; Tang, D., The Release and Activity of Hmgb1 in Ferroptosis. *Biochemical and Biophysical Research Communications* **2019,** *510* (2), 278-283.

(145) Yu, Y.; Xie, Y.; Cao, L.; Yang, L.; Yang, M.; Lotze, M. T.; Zeh, H. J.; Kang, R.; Tang, D., The Ferroptosis Inducer Erastin Enhances Sensitivity of Acute Myeloid Leukemia Cells to Chemotherapeutic Agents. *Molecular & cellular oncology* **2015,** *2* (4), e1054549.

(146) Efimova, I.; Catanzaro, E.; Van der Meeren, L.; Turubanova, V. D.; Hammad, H.; Mishchenko, T. A.; Vedunova, M. V.; Fimognari, C.; Bachert, C.; Coppieters, F., Vaccination with Early Ferroptotic Cancer Cells Induces Efficient Antitumor Immunity. *Journal for Immunotherapy of Cancer* **2020,** *8* (2).

(147) Reisetter, A. C.; Stebounova, L. V.; Baltrusaitis, J.; Powers, L.; Gupta, A.; Grassian, V. H.; Monick, M. M., Induction of Inflammasome-Dependent Pyroptosis by Carbon Black Nanoparticles*. *Journal of Biological Chemistry* **2011,** *286* (24), 21844-21852.

(148) Li, J.; Wang, X.; Mei, K.-C.; Chang, C. H.; Jiang, J.; Liu, X.; Liu, Q.; Guiney, L. M.; Hersam, M. C.; Liao, Y.-P.; Meng, H.; Xia, T., Lateral Size of Graphene Oxide Determines Differential Cellular Uptake and Cell Death Pathways in Kupffer Cells, Lsecs, and Hepatocytes. *Nano Today* **2021,** *37*, 101061.

(149) Yin, H.; Fang, L.; Wang, L.; Xia, Y.; Tian, J.; Ma, L.; Zhang, J.; Li, N.; Li, W.; Yao, S.; Zhang, L., Acute Silica Exposure Triggers Pulmonary Inflammation through Macrophage Pyroptosis: An Experimental Simulation. *Frontiers in Immunology* **2022,** *13*, 874459.

(150) Lu, Y.; Xu, S.; Chen, H.; He, M.; Deng, Y.; Cao, Z.; Pi, H.; Chen, C.; Li, M.; Ma, Q.; Gao, P.; Ji, Y.; Zhang, L.; Yu, Z.; Zhou, Z., Cdse/Zns Quantum Dots Induce Hepatocyte Pyroptosis and Liver Inflammation Via Nlrp3 Inflammasome Activation. *Biomaterials* **2016,** *90*, 27-39.

(151) Katifelis, H.; Nikou, M.-P.; Mukha, I.; Vityuk, N.; Lagopati, N.; Piperi, C.; Farooqi, A. A.; Pippa, N.; Efstathopoulos, E. P.; Gazouli, M., Ag/Au Bimetallic Nanoparticles Trigger Different Cell Death Pathways and Affect Damage Associated Molecular Pattern Release in Human Cell Lines. *Cancers* **2022,** *14* (6), 1546.

(152) Bertrand, N.; Wu, J.; Xu, X.; Kamaly, N.; Farokhzad, O. C., Cancer Nanotechnology: The Impact of Passive and Active Targeting in the Era of Modern Cancer Biology. *Advanced Drug Delivery Reviews* **2014,** *66*, 2-25.

(153) Theek, B.; Gremse, F.; Kunjachan, S.; Fokong, S.; Pola, R.; Pechar, M.; Deckers, R.; Storm, G.; Ehling, J.; Kiessling, F., Characterizing Epr-Mediated Passive Drug Targeting Using Contrast-Enhanced Functional Ultrasound Imaging. *Journal of Controlled Release* **2014,** *182*, 83-89.

(154) Xian, C.; Chen, H.; Xiong, F.; Fang, Y.; Huang, H.; Wu, J., Platinum-Based Chemotherapy Via Nanocarriers and Co-Delivery of Multiple Drugs. *Biomaterials Science* **2021,** *9* (18), 6023-6036.

(155) Song, L.; Hao, Y.; Wang, C.; Han, Y.; Zhu, Y.; Feng, L.; Miao, L.; Liu, Z., Liposomal Oxaliplatin Prodrugs Loaded with Metformin Potentiate Immunotherapy for Colorectal Cancer. *Journal of Controlled Release* **2022,** *350*, 922-932.

(156) Lu, J.; Liu, X.; Liao, Y.-P.; Salazar, F.; Sun, B.; Jiang, W.; Chang, C. H.; Jiang, J.; Wang, X.; Wu, A. M., Nano-Enabled Pancreas Cancer Immunotherapy Using Immunogenic Cell Death and Reversing Immunosuppression. *Nature Communications* **2017,** *8* (1), 1811.

(157) Mei, K.-C.; Liao, Y.-P.; Jiang, J.; Chiang, M.; Khazaieli, M.; Liu, X.; Wang, X.; Liu, Q.; Chang, C. H.; Zhang, X., Liposomal Delivery of Mitoxantrone and a Cholesteryl Indoximod Prodrug Provides Effective Chemo-Immunotherapy in Multiple Solid Tumors. *Acs Nano* **2020,** *14* (10), 13343-13366.

(158) Du, X.; Yang, X.; Zhang, Y.; Gao, S.; Liu, S.; Ji, J.; Zhai, G., Transdermal Delivery System Based on Heparin-Modified Graphene Oxide for Deep Transportation, Tumor Microenvironment Regulation, and Immune Activation. *Nano Today* **2022,** *46*, 101565.

(159) Serrano-del Valle, A.; Anel, A.; Naval, J.; Marzo, I., Immunogenic Cell Death and Immunotherapy of Multiple Myeloma. *Frontiers in Cell and Developmental Biology* **2019,** *7*, 50.

(160) Deng, H.; Zhou, Z.; Yang, W.; Lin, L.-s.; Wang, S.; Niu, G.; Song, J.; Chen, X., Endoplasmic Reticulum Targeting to Amplify Immunogenic Cell Death for Cancer Immunotherapy. *Nano Letters* **2020,** *20* (3), 1928-1933.

(161) Li, W.; Yang, J.; Luo, L.; Jiang, M.; Qin, B.; Yin, H.; Zhu, C.; Yuan, X.; Zhang, J.; Luo, Z., Targeting Photodynamic and Photothermal Therapy to the Endoplasmic Reticulum Enhances Immunogenic Cancer Cell Death. *Nature Communications* **2019,** *10* (1), 3349.

(162) Yuan, X.; Qin, B.; Yin, H.; Shi, Y.; Jiang, M.; Luo, L.; Luo, Z.; Zhang, J.; Li, X.; Zhu, C., Virus-Like Nonvirus Cationic Liposome for Efficient Gene Delivery Via Endoplasmic Reticulum Pathway. *ACS Central Science* **2020,** *6* (2), 174-188.

(163) Liu, X.; Liu, Y.; Li, X.; Huang, J.; Guo, X.; Zhang, J.; Luo, Z.; Shi, Y.; Jiang, M.; Qin, B., Er-Targeting Pdt Converts Tumors into in Situ Therapeutic Tumor Vaccines. *Acs Nano* **2022,** *16* (6), 9240-9253.

(164) Jiang, Q.; Zhang, C.; Wang, H.; Peng, T.; Zhang, L.; Wang, Y.; Han, W.; Shi, C., Mitochondria-Targeting Immunogenic Cell Death Inducer Improves the Adoptive T-Cell Therapy against Solid Tumor. *Frontiers in Oncology* **2019,** *9*, 1196.

(165) Zheng, D.; Liu, J.; Xie, L.; Wang, Y.; Ding, Y.; Peng, R.; Cui, M.; Wang, L.; Zhang, Y.; Zhang, C., Enzyme-Instructed and Mitochondria-Targeting Peptide Self-Assembly to Efficiently Induce Immunogenic Cell Death. *Acta Pharmaceutica Sinica B* **2022,** *12* (6), 2740-2750.

(166) Zhang, J.; Zhang, D.; Li, Q.; Jiang, Y.; Song, A.; Li, Z.; Luan, Y., Task-Specific Design of Immune-Augmented Nanoplatform to Enable High-Efficiency Tumor Immunotherapy. *Acs Applied Materials & Interfaces* **2019,** *11* (46), 42904-42916.

(167) Geng, Y.; Xiang, J.; Shao, S.; Tang, J.; Shen, Y., Mitochondria-Targeted Polymer-Celastrol Conjugate with Enhanced Anticancer Efficacy. *Journal of Controlled Release* **2022,** *342*, 122-133.

(168) Chen, H.; Liu, L.; Ma, A.; Yin, T.; Chen, Z.; Liang, R.; Qiu, Y.; Zheng, M.; Cai, L., Noninvasively Immunogenic Sonodynamic Therapy with Manganese Protoporphyrin Liposomes against Triple-Negative Breast Cancer. *Biomaterials* **2021,** *269*, 120639.

(169) Yu, J.; He, X.; Wang, Z.; Wang, Y.; Liu, S.; Li, X.; Huang, Y., Combining Pd-L1 Inhibitors with Immunogenic Cell Death Triggered by Chemo-Photothermal Therapy Via a Thermosensitive Liposome System to Stimulate Tumor-Specific Immunological Response. *Nanoscale* **2021,** *13* (30), 12966-12978.

(170) Zhang, X.; Tang, J.; Li, C.; Lu, Y.; Cheng, L.; Liu, J., A Targeting Black Phosphorus Nanoparticle Based Immune Cells Nano-Regulator for Photodynamic/Photothermal and Photo-Immunotherapy. *Bioactive materials* **2021,** *6* (2), 472-489.

(171) Zhu, Y.; Yang, Z.; Dong, Z.; Gong, Y.; Hao, Y.; Tian, L.; Yang, X.; Liu, Z.; Feng, L., Caco 3-Assisted Preparation of Ph-Responsive Immune-Modulating Nanoparticles for Augmented Chemo-Immunotherapy. *Nano-Micro Letters* **2021,** *13*, 1-18.

(172) Xia, C.; Yin, S.; Xu, S.; Ran, G.; Deng, M.; Mei, L.; Tang, X.; Rao, J.; Li, M.; Zhang, Z.; He, Q., Low Molecular Weight Heparin-Coated and Dendrimer-Based Core-Shell Nanoplatform with Enhanced Immune Activation and Multiple Anti-Metastatic Effects for Melanoma Treatment. *Theranostics* **2019,** *9* (2), 337-354.

(173) Su, Z.; Xiao, Z.; Wang, Y.; Huang, J.; An, Y.; Wang, X.; Shuai, X., Codelivery of Anti-Pd-1 Antibody and Paclitaxel with Matrix Metalloproteinase and Ph Dual-Sensitive Micelles for Enhanced Tumor Chemoimmunotherapy. *Small* **2020,** *16* (7), 1906832.

(174) Du, H.; Zhao, S.; Wang, Y.; Wang, Z.; Chen, B.; Yan, Y.; Yin, Q.; Liu, D.; Wan, F.; Zhang, Q.; Wang, Y., Ph/Cathepsin B Hierarchical-Responsive Nanoconjugates for Enhanced Tumor Penetration and Chemo-Immunotherapy. *Advanced Functional Materials* **2020,** *30* (39), 2003757.

(175) Gao, F.; Zhang, C.; Qiu, W.-X.; Dong, X.; Zheng, D.-W.; Wu, W.; Zhang, X.-Z., Pd-1 Blockade for Improving the Antitumor Efficiency of Polymer–Doxorubicin Nanoprodrug. *Small* **2018,** *14* (37), 1802403.

(176) Xu, W.; Liu, W.; Yang, J.; Lu, J.; Zhang, H.; Ye, D., Stimuli‐Responsive Nanodelivery Systems for Amplifying Immunogenic Cell Death in Cancer Immunotherapy. *Immunological Reviews* **2023**.

(177) Yu, M.; Zeng, W.; Ouyang, Y.; Liang, S.; Yi, Y.; Hao, H.; Yu, J.; Liu, Y.; Nie, Y.; Wang, T., Atp-Exhausted Nanocomplexes for Intratumoral Metabolic Intervention and Photoimmunotherapy. *Biomaterials* **2022,** *284*, 121503.

(178) Jiang, W.; Chen, L.; Guo, X.; Cheng, C.; Luo, Y.; Wang, J.; Wang, J.; Liu, Y.; Cao, Y.; Li, P., Combating Multidrug Resistance and Metastasis of Breast Cancer by Endoplasmic Reticulum Stress and Cell-Nucleus Penetration Enhanced Immunochemotherapy. *Theranostics* **2022,** *12* (6), 2987.

(179) Sun, L.; Shen, F.; Tian, L.; Tao, H.; Xiong, Z.; Xu, J.; Liu, Z., Atp‐Responsive Smart Hydrogel Releasing Immune Adjuvant Synchronized with Repeated Chemotherapy or Radiotherapy to Boost Antitumor Immunity. *Advanced Materials* **2021,** *33* (18), 2007910.

(180) Ameziane-El-Hassani, R.; Schlumberger, M.; Dupuy, C., Nadph Oxidases: New Actors in Thyroid Cancer? *Nature Reviews Endocrinology* **2016,** *12* (8), 485-494.

(181) Gong, Y.; Chen, M.; Tan, Y.; Shen, J.; Jin, Q.; Deng, W.; Sun, J.; Wang, C.; Liu, Z.; Chen, Q., Injectable Reactive Oxygen Species-Responsive Sn38 Prodrug Scaffold with Checkpoint Inhibitors for Combined Chemoimmunotherapy. *Acs Applied Materials & Interfaces* **2020,** *12* (45), 50248-50259.

(182) Jeon, J.; Yoon, B.; Dey, A.; Song, S. H.; Li, Y.; Joo, H.; Park, J. H., Self-Immolative Polymer-Based Immunogenic Cell Death Inducer for Regulation of Redox Homeostasis. *Biomaterials* **2023,** *295*, 122064.

(183) Song, J.; Cheng, M.; Xie, Y.; Li, K.; Zang, X., Efficient Tumor Synergistic Chemoimmunotherapy by Self-Augmented Ros-Responsive Immunomodulatory Polymeric Nanodrug. *Journal of Nanobiotechnology* **2023,** *21* (1), 93.

(184) Jin, F.; Qi, J.; Zhu, M.; Liu, D.; You, Y.; Shu, G.; Du, Y.; Wang, J.; Yu, H.; Sun, M., Nir-Triggered Sequentially Responsive Nanocarriers Amplified Cascade Synergistic Effect of Chemo-Photodynamic Therapy with Inspired Antitumor Immunity. *Acs Applied Materials & Interfaces* **2020,** *12* (29), 32372-32387.

(185) Zhang, Y.; Du, X.; Liu, S.; Yan, H.; Ji, J.; Xi, Y.; Yang, X.; Zhai, G., Nir-Triggerable Ros-Responsive Cluster-Bomb-Like Nanoplatform for Enhanced Tumor Penetration, Phototherapy Efficiency and Antitumor Immunity. *Biomaterials* **2021,** *278*, 121135.

(186) Wu, W.; Chen, M.; Luo, T.; Fan, Y.; Zhang, J.; Zhang, Y.; Zhang, Q.; Sapin-Minet, A.; Gaucher, C.; Xia, X., Ros and Gsh-Responsive S-Nitrosoglutathione Functionalized Polymeric Nanoparticles to Overcome Multidrug Resistance in Cancer. *Acta Biomaterialia* **2020,** *103*, 259-271.

(187) Guo, Y.; Fan, Y.; Wang, Z.; Li, G.; Zhan, M.; Gong, J.; Majoral, J. P.; Shi, X.; Shen, M., Chemotherapy Mediated by Biomimetic Polymeric Nanoparticles Potentiates Enhanced Tumor Immunotherapy Via Amplification of Endoplasmic Reticulum Stress and Mitochondrial Dysfunction. *Advanced Materials* **2022,** *34* (47), 2206861.

(188) Zhang, F.; Chen, F.; Yang, C.; Wang, L.; Hu, H.; Li, X.; Zheng, X.; Wang, Z.; Chang, Z.; Li, T., Coordination and Redox Dual‐Responsive Mesoporous Organosilica Nanoparticles Amplify Immunogenic Cell Death for Cancer Chemoimmunotherapy. *Small* **2021,** *17* (26), 2100006.

(189) Heffeter, P.; Atil, B.; Kryeziu, K.; Groza, D.; Koellensperger, G.; Körner, W.; Jungwirth, U.; Mohr, T.; Keppler, B. K.; Berger, W., The Ruthenium Compound Kp1339 Potentiates the Anticancer Activity of Sorafenib in Vitro and in Vivo. *European Journal of Cancer* **2013,** *49* (15), 3366-3375.

(190) Wernitznig, D.; Kiakos, K.; Del Favero, G.; Harrer, N.; Machat, H.; Osswald, A.; Jakupec, M. A.; Wernitznig, A.; Sommergruber, W.; Keppler, B. K., First-in-Class Ruthenium Anticancer Drug (Kp1339/It-139) Induces an Immunogenic Cell Death Signature in Colorectal Spheroids in Vitro. *Metallomics* **2019,** *11* (6), 1044-1048.

(191) Antuamwine, B. B.; Bosnjakovic, R.; Hofmann‐Vega, F.; Wang, X.; Theodosiou, T.; Iliopoulos, I.; Brandau, S., N1 Versus N2 and Pmn‐Mdsc: A Critical Appraisal of Current Concepts on Tumor‐Associated Neutrophils and New Directions for Human Oncology. *Immunological Reviews* **2023,** *314* (1), 250-279.

(192) Zhao, H.; Teng, D.; Yang, L.; Xu, X.; Chen, J.; Jiang, T.; Feng, A. Y.; Zhang, Y.; Frederick, D. T.; Gu, L., Myeloid-Derived Itaconate Suppresses Cytotoxic Cd8+ T Cells and Promotes Tumour Growth. *Nature Metabolism* **2022,** *4* (12), 1660-1673.

(193) Xia, C.; Li, M.; Ran, G.; Wang, X.; Lu, Z.; Li, T.; Tang, X.; Zhang, Z.; He, Q., Redox-Responsive Nanoassembly Restrained Myeloid-Derived Suppressor Cells Recruitment through Autophagy-Involved Lactate Dehydrogenase a Silencing for Enhanced Cancer Immunochemotherapy. *Journal of Controlled Release* **2021,** *335*, 557-574.

(194) Liu, X.; Li, Y.; Wang, K.; Chen, Y.; Shi, M.; Zhang, X.; Pan, W.; Li, N.; Tang, B., Gsh-Responsive Nanoprodrug to Inhibit Glycolysis and Alleviate Immunosuppression for Cancer Therapy. *Nano Letters* **2021,** *21* (18), 7862-7869.

(195) Huang, Z.; Wang, Y.; Yao, D.; Wu, J.; Hu, Y.; Yuan, A., Nanoscale Coordination Polymers Induce Immunogenic Cell Death by Amplifying Radiation Therapy Mediated Oxidative Stress. *Nature Communications* **2021,** *12* (1), 145.

(196) Zhou, J.-Y.; Wang, W.-J.; Zhang, C.-Y.; Ling, Y.-Y.; Hong, X.-J.; Su, Q.; Li, W.-G.; Mao, Z.-W.; Cheng, B.; Tan, C.-P., Ru (Ii)-Modified Tio2 Nanoparticles for Hypoxia-Adaptive Photo-Immunotherapy of Oral Squamous Cell Carcinoma. *Biomaterials* **2022,** *289*, 121757.

(197) Chen, B.; Yan, Y.; Yang, Y.; Cao, G.; Wang, X.; Wang, Y.; Wan, F.; Yin, Q.; Wang, Z.; Li, Y., A Pyroptosis Nanotuner for Cancer Therapy. *Nature Nanotechnology* **2022,** *17* (7), 788-798.

(198) Li, M.; Kim, J.; Xu, Y.; Kim, J. S., An Acid-Activatable Nanosensitizer Library Realizes Tunable Pyroptosis Activation in Tumors. *Matter* **2023,** *6* (1), 15-18.

(199) Jung, H. S.; Verwilst, P.; Sharma, A.; Shin, J.; Sessler, J. L.; Kim, J. S., Organic Molecule-Based Photothermal Agents: An Expanding Photothermal Therapy Universe. *Chemical Society Reviews* **2018,** *47* (7), 2280-2297.

(200) Zhang, L.; Yang, Q. C.; Wang, S.; Xiao, Y.; Wan, S. C.; Deng, H.; Sun, Z. J., Engineering Multienzyme‐Mimicking Covalent Organic Frameworks as Pyroptosis Inducers for Boosting Antitumor Immunity. *Advanced Materials* **2022,** *34* (13), 2108174.

(201) Zhao, P.; Wang, M.; Chen, M.; Chen, Z.; Peng, X.; Zhou, F.; Song, J.; Qu, J., Programming Cell Pyroptosis with Biomimetic Nanoparticles for Solid Tumor Immunotherapy. *Biomaterials* **2020,** *254*, 120142.

(202) Zhou, J.-J.; Li, X.-H.; He, P.-Y.; Qi, F.-Y.; Ullah, M. W.; Li, S.-J.; Liu, Y.-T.; Bu, L.-L.; Yang, G.; Sun, Z.-J., Implantable Versatile Oxidized Bacterial Cellulose Membrane for Postoperative Hnscc Treatment Via Photothermal-Boosted Immunotherapy. *Nano Research* **2023,** *16* (1), 951-963.

(203) Zhang, Z.; Zhang, X.; Zhao, S.; Feng, W.; Huang, H.; Ding, L.; Chen, Y.; Chen, B., Engineering 2d Silicene-Based Core/Shell Nanomedicine for Gsdme-Induced Synergistic Pyroptosis and Photonic Hyperthermia of Melanoma Carcinoma. *Chemical Engineering Journal* **2023,** *454*, 140175.

(204) Ji, P.; Zhang, S.; Liu, P.; Li, X.; Bao, W.; Cui, X.; Huo, M.; Shi, J., Modulation of Mitochondrial Electron Transport Chain by Pyroptosis Nanoagonists for Photoresponsive Tumor Destruction. *Nano Today* **2022,** *44*, 101511.

(205) Costley, D.; Mc Ewan, C.; Fowley, C.; McHale, A. P.; Atchison, J.; Nomikou, N.; Callan, J. F., Treating Cancer with Sonodynamic Therapy: A Review. *International Journal of Hyperthermia* **2015,** *31* (2), 107-117.

(206) Meng, Q.; Ding, B.; Ma, P. a.; Lin, J., Interrelation between Programmed Cell Death and Immunogenic Cell Death: Take Antitumor Nanodrug as an Example. *Small Methods* **2023,** *7* (5), 2201406.

(207) Rengeng, L.; Qianyu, Z.; Yuehong, L.; Zhongzhong, P.; Libo, L., Sonodynamic Therapy, a Treatment Developing from Photodynamic Therapy. *Photodiagnosis and photodynamic therapy* **2017,** *19*, 159-166.

(208) Yang, Z.; Song, J.; Tang, W.; Fan, W.; Dai, Y.; Shen, Z.; Lin, L.; Cheng, S.; Liu, Y.; Niu, G., Stimuli-Responsive Nanotheranostics for Real-Time Monitoring Drug Release by Photoacoustic Imaging. *Theranostics* **2019,** *9* (2), 526.

(209) McHale, A. P.; Callan, J. F.; Nomikou, N.; Fowley, C.; Callan, B., Sonodynamic Therapy: Concept, Mechanism and Application to Cancer Treatment. *Therapeutic Ultrasound* **2016**, 429-450.

(210) Yin, Y.; Jiang, X.; Sun, L.; Li, H.; Su, C.; Zhang, Y.; Xu, G.; Li, X.; Zhao, C.; Chen, Y., Continuous Inertial Cavitation Evokes Massive Ros for Reinforcing Sonodynamic Therapy and Immunogenic Cell Death against Breast Carcinoma. *Nano Today* **2021,** *36*, 101009.

(211) Chen, J.; Feng, L.; Jin, P.; Shen, J.; Lu, J.; Song, Y.; Wang, G.; Chen, Q.; Huang, D.; Zhang, Y., Cavitation Assisted Endoplasmic Reticulum Targeted Sonodynamic Droplets to Enhanced Anti-Pd-L1 Immunotherapy in Pancreatic Cancer. *Journal of Nanobiotechnology* **2022,** *20* (1), 283.

(212) Wan, G.; Chen, X.; Wang, H.; Hou, S.; Wang, Q.; Cheng, Y.; Chen, Q.; Lv, Y.; Chen, H.; Zhang, Q., Gene Augmented Nuclear-Targeting Sonodynamic Therapy Via Nrf2 Pathway-Based Redox Balance Adjustment Boosts Peptide-Based Anti-Pd-L1 Therapy on Colorectal Cancer. *Journal of Nanobiotechnology* **2021,** *19* (1), 1-26.

(213) Choi, B.; Choi, H.; Yu, B.; Kim, D.-H., Synergistic Local Combination of Radiation and Anti-Programmed Death Ligand 1 Immunotherapy Using Radiation-Responsive Splintery Metallic Nanocarriers. *Acs Nano* **2020,** *14* (10), 13115-13126.

(214) Lu, K.; He, C.; Guo, N.; Chan, C.; Ni, K.; Lan, G.; Tang, H.; Pelizzari, C.; Fu, Y.-X.; Spiotto, M. T.; Weichselbaum, R. R.; Lin, W., Low-Dose X-Ray Radiotherapy–Radiodynamic Therapy Via Nanoscale Metal–Organic Frameworks Enhances Checkpoint Blockade Immunotherapy. *Nature Biomedical Engineering* **2018,** *2* (8), 600-610.

(215) Ting, H.-K.; Page, S. J.; Poologasundarampillai, G.; Chen, S.; Yu, B.; Hanna, J. V.; Jones, J. R., Phosphate Content Affects Structure and Bioactivity of Sol-Gel Silicate Bioactive Glasses. *International Journal of Applied Glass Science* **2017,** *8* (4), 372-382.

(216) Saravanapavan, P.; Jones, J. R.; Pryce, R. S.; Hench, L. L., Bioactivity of Gel–Glass Powders in the Cao-Sio2 System: A Comparison with Ternary (Cao-P2p5-Sio2) and Quaternary Glasses (Sio2-Cao-P2o5-Na2o). *Journal of Biomedical Materials Research Part A* **2003,** *66A* (1), 110-119.

(217) Obata, A.; Jones, J. D. C.; Shinya, A.; Kasuga, T., Sintering and Crystallization of Phosphate Glasses by Co2-Laser Irradiation on Hydroxyapatite Ceramics. *International Journal of Applied Ceramic Technology* **2012,** *9* (3), 541-549.

(218) Novajra, G.; Perdika, P.; Pisano, R.; Baino, F.; Jones, J. R.; Boccaccini, A. R.; Detsch, R.; Vitale-Brovarone, C. In *Tailoring of Bone Scaffold Properties Using Silicate/Phosphate Glass Mixtures*, Key Engineering Materials, Trans Tech Publ: 2015; pp 283-288.

(219) Abou Neel, E. A.; Pickup, D. M.; Valappil, S. P.; Newport, R. J.; Knowles, J. C., Bioactive Functional Materials: A Perspective on Phosphate-Based Glasses. *Journal of Materials Chemistry* **2009,** *19* (6), 690-701.

(220) Pickup, D. M.; Newport, R. J.; Knowles, J. C., Sol-Gel Phosphate-Based Glass for Drug Delivery Applications. *J Biomater Appl* **2012,** *26* (5), 613-22.

(221) Habraken, W. J.; Wolke, J. G.; Jansen, J. A., Ceramic Composites as Matrices and Scaffolds for Drug Delivery in Tissue Engineering. *Adv Drug Deliv Rev* **2007,** *59* (4-5), 234-48.

(222) Kaehr, B.; Townson, J. L.; Kalinich, R. M.; Awad, Y. H.; Swartzentruber, B. S.; Dunphy, D. R.; Brinker, C. J., Cellular Complexity Captured in Durable Silica Biocomposites. *Proceedings of the National Academy of Sciences* **2012,** *109* (43), 17336-17341.

(223) Lou, Y.-R.; Kanninen, L.; Kaehr, B.; Townson, J. L.; Niklander, J.; Harjumäki, R.; Jeffrey Brinker, C.; Yliperttula, M., Silica Bioreplication Preserves Three-Dimensional Spheroid Structures of Human Pluripotent Stem Cells and Hepg2 Cells. *Scientific Reports* **2015,** *5* (1), 13635.

(224) Meyer, K. C.; Labriola, N. R.; Darling, E. M.; Kaehr, B., Shape‐Preserved Transformation of Biological Cells into Synthetic Hydrogel Microparticles. *Advanced Biosystems* **2019,** *3* (4), 1800285.

(225) Gilchrist, T.; Glasby, M. A.; Healy, D. M.; Kelly, G.; Lenihan, D. V.; McDowall, K. L.; Miller, I. A.; Myles, L. M., In Vitro Nerve Repair--in Vivo. The Reconstruction of Peripheral Nerves by Entubulation with Biodegradeable Glass Tubes--a Preliminary Report. *Br J Plast Surg* **1998,** *51* (3), 231-7.

(226) Toumba, K.; Curzon, M., Slow-Release Fluoride. *Caries research* **1993,** *27* (Suppl. 1), 43-46.

(227) Carta, D.; Pickup, D. M.; Knowles, J. C.; Smith, M. E.; Newport, R. J., Sol–Gel Synthesis of the P2o5–Cao–Na2o–Sio2 System as a Novel Bioresorbable Glass. *Journal of Materials Chemistry* **2005,** *15* (21), 2134.

(228) Carta, D.; Knowles, J. C.; Smith, M. E.; Newport, R. J., Synthesis and Structural Characterization of P2o5–Cao–Na2o Sol–Gel Materials. *Journal of Non-Crystalline Solids* **2007,** *353* (11-12), 1141-1149.

(229) Foroutan, F.; Kyffin, B. A.; Abrahams, I.; Knowles, J. C.; Sogne, E.; Falqui, A.; Carta, D., Mesoporous Strontium-Doped Phosphate-Based Sol-Gel Glasses for Biomedical Applications. *Front Chem* **2020,** *8*, 249.

(230) Owens, G. J.; Singh, R. K.; Foroutan, F.; Alqaysi, M.; Han, C.-M.; Mahapatra, C.; Kim, H.-W.; Knowles, J. C., Sol–Gel Based Materials for Biomedical Applications. *Progress in Materials Science* **2016,** *77*, 1-79.

(231) Pickup, D. M.; Valappil, S. P.; Moss, R. M.; Twyman, H. L.; Guerry, P.; Smith, M. E.; Wilson, M.; Knowles, J. C.; Newport, R. J., Preparation, Structural Characterisation and Antibacterial Properties of Ga-Doped Sol–Gel Phosphate-Based Glass. *Journal of Materials Science* **2009,** *44* (7), 1858-1867.

(232) He, T.; Jokerst, J. V., Structured Micro/Nano Materials Synthesized Via Electrospray: A Review. *Biomater Sci* **2020,** *8* (20), 5555-5573.

(233) Kuwahata, Y.; Takehara, H.; Ichiki, T., Comprehensive Study on Electrospray Deposition in the Single Taylor Cone–Jet Mode by Changing the Spatial Electric Potential Using a Ring-Shaped Ternary Electrode. *AIP Advances* **2020,** *10* (4), 045107.

(234) Gross, K.; Andersons, J.; Misevicius, M.; Švirksts, J., Traversing Phase Fields Towards Nanosized Beta Tricalcium Phosphate. *Key Engineering Materials* **2013,** *587*, 97-100.

(235) Dorozhkin, S. V., Amorphous Calcium (Ortho)Phosphates. *Acta Biomaterialia* **2010,** *6* (12), 4457-4475.

(236) Layrolle, P.; Lebugle, A., Characterization and Reactivity of Nanosized Calcium Phosphates Prepared in Anhydrous Ethanol. *Chemistry of Materials* **1994,** *6* (11), 1996-2004.

(237) Baia, L.; Muresan, D.; Baia, M.; Popp, J.; Simon, S., Structural Properties of Silver Nanoclusters–Phosphate Glass Composites. *Vibrational Spectroscopy* **2007,** *43* (2), 313-318.

(238) Ilieva, D.; Jivov, B.; Bogachev, G.; Petkov, C.; Penkov, I.; Dimitriev, Y., Infrared and Raman Spectra of Ga2o3–P2o5 Glasses. *Journal of Non-Crystalline Solids* **2001,** *283* (1), 195-202.

(239) Moustafa, Y. M.; El-Egili, K., Infrared Spectra of Sodium Phosphate Glasses. *Journal of Non-Crystalline Solids* **1998,** *240* (1), 144-153.

(240) Byun, J.-O.; Kim, B.-H.; Hong, K.-S.; Jung, H.-J.; Lee, S.-W.; Izyneev, A. A., Properties and Structure of Ro · Na2o · Al2o3 · P2o5 (R = Mg, Ca, Sr, Ba) Glasses. *Journal of Non-Crystalline Solids* **1995,** *190* (3), 288-295.

(241) Neel, E. A. A.; Knowles, J. C., Biocompatibility and Other Properties of Phosphate-Based Glasses for Medical Applications. **2009**, 10.1533/9781845695477.1.156, 156-182.

(242) Lee, I.-H.; Foroutan, F.; Lakhkar, N. J.; Gong, M.-S.; Knowles, J. C., Sol-Gel Synthesis and Structural Characterization of P2o5–Cao–Na2o Glasses. *Physics and Chemistry of Glasses - European Journal of Glass Science andTechnology Part B* **2013,** *54* (3), 115-120.

(243) Cloupeau, M.; Prunet-Foch, B., Electrostatic Spraying of Liquids: Main Functioning Modes. *Journal of Electrostatics* **1990,** *25* (2), 165-184.

(244) Cloupeau, M.; Prunet-Foch, B., Electrohydrodynamic Spraying Functioning Modes: A Critical Review. *Journal of Aerosol Science* **1994,** *25* (6), 1021-1036.

(245) Zong, H. X.; Xia, X.; Liang, Y. R.; Dai, S. Y.; Alsaedi, A.; Hayat, T.; Kong, F. T.; Pan, J. H., Designing Function-Oriented Artificial Nanomaterials and Membranes Via Electrospinning and Electrospraying Techniques. *Materials Science & Engineering C-Materials for Biological Applications* **2018,** *92*, 1075-1091.

(246) Zhou, J.; Gao, D.; Yao, D.; K. Leist, S.; Fei, Y., Mechanisms and Modeling of Electrohydrodynamic Phenomena. *International Journal of Bioprinting* **2018,** *5* (1), 166.

(247) GaÑÁN-Calvo, A. M., On the General Scaling Theory for Electrospraying. *Journal of Fluid Mechanics* **2004,** *507*, 203-212a.

(248) Cejkova, J.; Stepanek, F., Compartmentalized and Internally Structured Particles for Drug Delivery - a Review. *Current Pharmaceutical Design* **2013,** *19* (35), 6298-6314.

(249) Balmert, S. C.; Little, S. R., Biomimetic Delivery with Micro- and Nanoparticles. *Adv Mater* **2012,** *24* (28), 3757-78.

(250) Champion, J. A.; Mitragotri, S., Role of Target Geometry in Phagocytosis. *Proceedings of the National Academy of Sciences of the United States of America* **2006,** *103* (13), 4930-4934.

(251) Champion, J. A.; Mitragotri, S., Shape Induced Inhibition of Phagocytosis of Polymer Particles. *Pharm Res* **2009,** *26* (1), 244-9.

(252) Muro, S.; Garnacho, C.; Champion, J. A.; Leferovich, J.; Gajewski, C.; Schuchman, E. H.; Mitragotri, S.; Muzykantov, V. R., Control of Endothelial Targeting and Intracellular Delivery of Therapeutic Enzymes by Modulating the Size and Shape of Icam-1-Targeted Carriers. *Molecular therapy : the journal of the American Society of Gene Therapy* **2008,** *16* (8), 1450-1458.

(253) Chen, A. Z.; Yang, Y. M.; Wang, S. B.; Wang, G. Y.; Liu, Y. G.; Sun, Q. Q., Preparation of Methotrexate-Loaded, Large, Highly-Porous Plla Microspheres by a High-Voltage

Electrostatic Antisolvent Process. *Journal of Materials Science-Materials in Medicine* **2013,** *24* (8), 1917-1925.

(254) Misra, A. C.; Bhaskar, S.; Clay, N.; Lahann, J., Multicompartmental Particles for Combined Imaging and Sirna Delivery. *Adv Mater* **2012,** *24* (28), 3850-6.

(255) Zhou, F. L.; Chirazi, A.; Gough, J. E.; Cristinacce, P. L. H.; Parker, G. J. M., Hollow Polycaprolactone Microspheres with/without a Single Surface Hole by Co-Electrospraying. *Langmuir* **2017,** *33* (46), 13262-13271.

(256) Dwivedi, P.; Han, S. Y.; Mangrio, F.; Fan, R.; Dwivedi, M.; Zhu, Z. A.; Huang, F. S.; Wu, Q.; Khatik, R.; Cohn, D. E.; Si, T.; Hu, S. Y.; Sparreboom, A.; Xu, R. X., Engineered Multifunctional Biodegradable Hybrid Microparticles for Paclitaxel Delivery in Cancer Therapy. *Materials Science & Engineering C-Materials for Biological Applications* **2019,** *102*, 113-123.

(257) Zhang, C. C.; Yao, Z. C.; Ding, Q. P.; Choi, J. J.; Ahmad, Z.; Chang, M. W.; Li, J. S., Tri-Needle Coaxial Electrospray Engineering of Magnetic Polymer Yolk-Shell Particles Possessing Dual-Imaging Modality, Multiagent Compartments, and Trigger Release Potential. *Acs Applied Materials & Interfaces* **2017,** *9* (25), 21485-21495.

(258) Doshi, N.; Zahr, A. S.; Bhaskar, S.; Lahann, J.; Mitragotri, S., Red Blood Cell-Mimicking Synthetic Biomaterial Particles. *Proc Natl Acad Sci USA* **2009,** *106* (51), 21495-9.

(259) Li, D.; Marquez, M.; Xia, Y. N., Capturing Electrified Nanodroplets under Rayleigh Instability by Coupling Electrospray with a Sol-Gel Reaction. *Chemical Physics Letters* **2007,** *445* (4-6), 271-275.

(260) Bhaskar, S.; Hitt, J.; Chang, S. W.; Lahann, J., Multicompartmental Microcylinders. *Angew Chem Int Ed Engl* **2009,** *48* (25), 4589-93.

(261) Sarkar, D.; Mondal, B.; Som, A.; Ravindran, S. J.; Jana, S. K.; Manju, C. K.; Pradeep, T., Holey Mos2 Nanosheets with Photocatalytic Metal Rich Edges by Ambient Electrospray Deposition for Solar Water Disinfection. *Global Challenges* **2018,** *2* (12), 1800052.

(262) Jana, A.; Jana, S. K.; Sarkar, D.; Ahuja, T.; Basuri, P.; Mondal, B.; Bose, S.; Ghosh, J.; Pradeep, T., Electrospray Deposition-Induced Ambient Phase Transition in Copper Sulphide Nanostructures. *Journal of Materials Chemistry A* **2019,** *7* (11), 6387-6394.

(263) Suhendi, A.; Nandiyanto, A. B. D.; Munir, M. M.; Ogi, T.; Gradon, L.; Okuyama, K., Self-Assembly of Colloidal Nanoparticles inside Charged Droplets During Spray-Drying in the Fabrication of Nanostructured Particles. *Langmuir* **2013,** *29* (43), 13152-13161.

(264) Liu, B. S.; Nakata, K.; Sakai, M.; Saito, H.; Ochiai, T.; Murakami, T.; Takagi, K.; Fujishima, A., Mesoporous Tio2 Core-Shell Spheres Composed of Nanocrystals with Exposed High-Energy Facets: Facile Synthesis and Formation Mechanism. *Langmuir* **2011,** *27* (13), 8500-8508.

(265) Zhang, Q.; Liu, J.; Wang, X.; Li, M.; Yang, J., Controlling Internal Nanostructures of Porous Microspheres Prepared Via Electrospraying. *Colloid and Polymer Science* **2010,** *288* (14), 1385-1391.

(266) Gao, J.; Li, W.; Wong, J. S.-P.; Hu, M.; Li, R. K. Y., Controllable Morphology and Wettability of Polymer Microspheres Prepared by Nonsolvent Assisted Electrospraying. *Polymer* **2014,** *55* (12), 2913-2920.

(267) Park, C. H.; Chung, N. O.; Lee, J., Monodisperse Red Blood Cell-Like Particles Via Consolidation of Charged Droplets. *J Colloid Interface Sci* **2011,** *361* (2), 423-8.

(268) Ju, X.; Wang, X.; Liu, Z.; Xie, R.; Wang, W.; Chu, L., Red-Blood-Cell-Shaped Chitosan Microparticles Prepared by Electrospraying. *Particuology* **2017,** *30*, 151-157.

(269) Hu, Y.; Wang, J.; Zhang, H.; Jiang, G.; Kan, C., Synthesis and Characterization of Monodispersed P(St-Co-Dmaema) Nanoparticles as Ph-Sensitive Drug Delivery System. *Materials Science and Engineering: C* **2014,** *45*, 1-7.

(270) Gasmi, H.; Danede, F.; Siepmann, J.; Siepmann, F., Does Plga Microparticle Swelling Control Drug Release? New Insight Based on Single Particle Swelling Studies. *Journal of Controlled Release* **2015,** *213*, 120-127.

(271) Bajpai, A. K.; Choubey, J., Design of Gelatin Nanoparticles as Swelling Controlled Delivery System for Chloroquine Phosphate. *Journal of Materials Science-Materials in Medicine* **2006,** *17* (4), 345-358.

(272) Bunker, B. C.; Arnold, G. W.; Wilder, J. A., Phosphate Glass Dissolution in Aqueous Solutions. *Journal of Non-Crystalline Solids* **1984,** *64* (3), 291-316.

(273) Sales, B. C.; Boatner, L. A.; Ramey, J. O., Chromatographic Studies of the Structures of Amorphous Phosphates: A Review. *Journal of Non-Crystalline Solids* **2000,** *263-264*, 155-166.

(274) Weber, J.; Beard, P. C.; Bohndiek, S. E., Contrast Agents for Molecular Photoacoustic Imaging. *Nature Methods* **2016,** *13* (8), 639-650.

(275) Liu, H.; Hu, Y.; Sun, Y.; Wan, C.; Zhang, Z.; Dai, X.; Lin, Z.; He, Q.; Yang, Z.; Huang, P.; Xiong, Y.; Cao, J.; Chen, X.; Chen, Q.; Lovell, J. F.; Xu, Z.; Jin, H.; Yang, K., Co-Delivery of Bee Venom Melittin and a Photosensitizer with an Organic–Inorganic Hybrid Nanocarrier for Photodynamic Therapy and Immunotherapy. *ACS Nano* **2019,** *13* (11), 12638-12652.

(276) Guo, J.; Agola, J. O.; Serda, R.; Franco, S.; Lei, Q.; Wang, L.; Minster, J.; Croissant, J. G.; Butler, K. S.; Zhu, W.; Brinker, C. J., Biomimetic Rebuilding of Multifunctional

Red Blood Cells: Modular Design Using Functional Components. *ACS Nano* **2020,** *14* (7), 7847-7859.

(277) Cao, J.; Zaremba, O. T.; Lei, Q.; Ploetz, E.; Wuttke, S.; Zhu, W., Artificial Bioaugmentation of Biomacromolecules and Living Organisms for Biomedical Applications. *ACS Nano* **2021,** *15* (3), 3900-3926.

(278) Guo, J.; Amini, S.; Lei, Q.; Ping, Y.; Agola, J. O.; Wang, L.; Zhou, L.; Cao, J.; Franco, S.; Noureddine, A.; Miserez, A.; Zhu, W.; Brinker, C. J., Robust and Long-Term Cellular Protein and Enzymatic Activity Preservation in Biomineralized Mammalian Cells. *ACS Nano* **2022,** *16* (2), 2164-2175.

(279) Wang, Y.; Du, W.; Zhang, T.; Zhu, Y.; Ni, Y.; Wang, C.; Sierra Raya, F. M.; Zou, L.; Wang, L.; Liang, G., A Self-Evaluating Photothermal Therapeutic Nanoparticle. *ACS Nano* **2020,** *14* (8), 9585-9593.

(280) Chen, J.; Ma, Y.; Du, W.; Dai, T.; Wang, Y.; Jiang, W.; Wan, Y.; Wang, Y.; Liang, G.; Wang, G., Furin-Instructed Intracellular Gold Nanoparticle Aggregation for Tumor Photothermal Therapy. *Advanced Functional Materials* **2020,** *30* (50), 2001566.

(281) Zhou, J.; Creyer, M. N.; Chen, A.; Yim, W.; Lafleur, R. P. M.; He, T.; Lin, Z.; Xu, M.; Abbasi, P.; Wu, J.; Pascal, T. A.; Caruso, F.; Jokerst, J. V., Stereoselective Growth of Small Molecule Patches on Nanoparticles. *Journal of the American Chemical Society* **2021,** *143* (31), 12138-12144.

(282) Jin, Z.; Mantri, Y.; Retout, M.; Cheng, Y.; Zhou, J.; Jorns, A.; Fajtova, P.; Yim, W.; Moore, C.; Xu, M.; Creyer, M.; Borum, R.; Zhou, J.; Wu, Z.; He, T.; Penny, W.; O'Donoghue, A.; Jokerst, J., A Charge-Switchable Zwitterionic Peptide for Rapid Detection of Sars-Cov-2 Main Protease. *Angewandte Chemie International Edition* **2021,** *e202112995*.

(283) Lee, J. E.; Lee, N.; Kim, T.; Kim, J.; Hyeon, T., Multifunctional Mesoporous Silica Nanocomposite Nanoparticles for Theranostic Applications. *Accounts of Chemical Research* **2011,** *44* (10), 893-902.

(284) Wu, Z.; Zhou, J.; Nkanga, C. I.; Jin, Z.; He, T.; Borum, R. M.; Yim, W.; Zhou, J.; Cheng, Y.; Xu, M.; Steinmetz, N. F.; Jokerst, J. V., One-Step Supramolecular Multifunctional Coating on Plant Virus Nanoparticles for Bioimaging and Therapeutic Applications. *ACS Appl Mater Interfaces* **2022,** *14* (11), 13692-13702.

(285) Du, L.; Nosratabad, N. A.; Jin, Z.; Zhang, C.; Wang, S.; Chen, B.; Mattoussi, H., Luminescent Quantum Dots Stabilized by N-Heterocyclic Carbene Polymer Ligands. *Journal of the American Chemical Society* **2021,** *143* (4), 1873-1884.

(286) Wang, S.; Du, L.; Jin, Z.; Xin, Y.; Mattoussi, H., Enhanced Stabilization and Easy Phase Transfer of $Cspbbr_3$ Perovskite Quantum Dots Promoted by High-Affinity Polyzwitterionic Ligands. *Journal of the American Chemical Society* **2020,** *142* (29), 12669-12680.

(287) Zhan, N.; Palui, G.; Merkl, J.-P.; Mattoussi, H., Bio-Orthogonal Coupling as a Means of Quantifying the Ligand Density on Hydrophilic Quantum Dots. *Journal of the American Chemical Society* **2016,** *138* (9), 3190-3201.

(288) Ding, Z.; Sun, H.; Ge, S.; Cai, Y.; Yuan, Y.; Hai, Z.; Tao, T.; Hu, J.; Hu, B.; Wang, J.; Liang, G., Furin-Controlled Fe_3o_4 Nanoparticle Aggregation and 19f Signal "Turn-on" for Precise Mr Imaging of Tumors. *Advanced Functional Materials* **2019,** *29* (43), 1903860.

(289) Wang, Y.; Li, X.; Chen, P.; Dong, Y.; Liang, G.; Yu, Y., Enzyme-Instructed Self-Aggregation of Fe_3o_4 Nanoparticles for Enhanced Mri T_2 Imaging and Photothermal Therapy of Tumors. *Nanoscale* **2020,** *12* (3), 1886-1893.

(290) Cheng, P.; Pu, K., Molecular Imaging and Disease Theranostics with Renal-Clearable Optical Agents. *Nature Reviews Materials* **2021,** *6* (12), 1095-1113.

(291) Park, J. H.; Gu, L.; von Maltzahn, G.; Ruoslahti, E.; Bhatia, S. N.; Sailor, M. J., Biodegradable Luminescent Porous Silicon Nanoparticles for in Vivo Applications. *Nat Mater* **2009,** *8* (4), 331-6.

(292) Liew, S. S.; Zeng, Z.; Cheng, P.; He, S.; Zhang, C.; Pu, K., Renal-Clearable Molecular Probe for near-Infrared Fluorescence Imaging and Urinalysis of Sars-Cov-2. *Journal of the American Chemical Society* **2021,** *143* (45), 18827-18831.

(293) Huang, J.; Jiang, Y.; Li, J.; He, S.; Huang, J.; Pu, K., A Renal-Clearable Macromolecular Reporter for near-Infrared Fluorescence Imaging of Bladder Cancer. *Angewandte Chemie International Edition* **2020,** *59* (11), 4415-4420.

(294) Nafiujjaman, M.; Chung, S.-J.; Kalashnikova, I.; Hill, M. L.; Homa, S.; George, J.; Contag, C. H.; Kim, T., Biodegradable Hollow Manganese Silicate Nanocomposites to Alleviate Tumor Hypoxia toward Enhanced Photodynamic Therapy. *ACS Applied Bio Materials* **2020,** *3* (11), 7989-7999.

(295) Lyu, Y.; Zeng, J.; Jiang, Y.; Zhen, X.; Wang, T.; Qiu, S.; Lou, X.; Gao, M.; Pu, K., Enhancing Both Biodegradability and Efficacy of Semiconducting Polymer Nanoparticles for Photoacoustic Imaging and Photothermal Therapy. *ACS Nano* **2018,** *12* (2), 1801-1810.

(296) Liang, Y.; Sun, H.; Cao, W.; Thompson, M. P.; Gianneschi, N. C., Degradable Polyphosphoramidate Via Ring-Opening Metathesis Polymerization. *ACS Macro Letters* **2020,** *9* (10), 1417-1422.

(297) Lovell, J. F.; Jin, C. S.; Huynh, E.; MacDonald, T. D.; Cao, W.; Zheng, G., Enzymatic Regioselection for the Synthesis and Biodegradation of Porphysome Nanovesicles. *Angewandte Chemie International Edition* **2012,** *51* (10), 2429-2433.

(298) Sun, H.; Liang, Y.; Thompson, M. P.; Gianneschi, N. C., Degradable Polymers Via Olefin Metathesis Polymerization. *Progress in Polymer Science* **2021,** *120*, 101427.

(299) Sun, H.; Yan, L.; Carter, K. A.; Zhang, J.; Caserto, J. S.; Lovell, J. F.; Wu, Y.; Cheng, C., Zwitterionic Cross-Linked Biodegradable Nanocapsules for Cancer Imaging. *Langmuir* **2019,** *35* (5), 1440-1449.

(300) Sun, H.; Yan, L.; Chang, M. Y. Z.; Carter, K. A.; Zhang, R.; Slyker, L.; Lovell, J. F.; Wu, Y.; Cheng, C., A Multifunctional Biodegradable Brush Polymer-Drug Conjugate for Paclitaxel/Gemcitabine Co-Delivery and Tumor Imaging. *Nanoscale Advances* **2019,** *1* (7), 2761-2771.

(301) Altınogˇlu, E. I.; Russin, T. J.; Kaiser, J. M.; Barth, B. M.; Eklund, P. C.; Kester, M.; Adair, J. H., Near-Infrared Emitting Fluorophore-Doped Calcium Phosphate Nanoparticles for in Vivo Imaging of Human Breast Cancer. *Acs Nano* **2008,** *2* (10), 2075-2084.

(302) Tang, J.; Li, L.; Howard, C. B.; Mahler, S. M.; Huang, L.; Xu, Z. P., Preparation of Optimized Lipid-Coated Calcium Phosphate Nanoparticles for Enhanced in Vitro Gene Delivery to Breast Cancer Cells. *Journal of Materials Chemistry B* **2015,** *3* (33), 6805-6812.

(303) Liu, Z.; Xiao, Y.; Chen, W.; Wang, Y.; Wang, B.; Wang, G.; Xu, X.; Tang, R., Calcium Phosphate Nanoparticles Primarily Induce Cell Necrosis through Lysosomal Rupture: The Origination of Material Cytotoxicity. *Journal of Materials Chemistry B* **2014,** *2* (22), 3480-3489.

(304) Errico, C.; Pierre, J.; Pezet, S.; Desailly, Y.; Lenkei, Z.; Couture, O.; Tanter, M., Ultrafast Ultrasound Localization Microscopy for Deep Super-Resolution Vascular Imaging. *Nature* **2015,** *527* (7579), 499-502.

(305) Demené, C.; Robin, J.; Dizeux, A.; Heiles, B.; Pernot, M.; Tanter, M.; Perren, F., Transcranial Ultrafast Ultrasound Localization Microscopy of Brain Vasculature in Patients. *Nature Biomedical Engineering* **2021,** *5* (3), 219-228.

(306) He, T.; Bradley, D. G.; Zhou, J.; Jorns, A.; Mantri, Y.; Hanna, J. V.; Jokerst, J. V., Hydro-Expandable Calcium Phosphate Micro/Nano-Particles with Controllable Size and Morphology for Mechanical Ablation. *ACS Applied Nano Materials* **2021,** *4* (4), 3877-3886.

(307) He, T.; Jokerst, J. V., Structured Micro/Nano Materials Synthesized Via Electrospray: A Review. *Biomaterials Science* **2020,** *8* (20), 5555-5573.

(308) Sumper, M.; Brunner, E., Learning from Diatoms: Nature's Tools for the Production of Nanostructured Silica. *Advanced Functional Materials* **2006,** *16* (1), 17-26.

(309) Sumper, M.; Kröger, N., Silica Formation in Diatoms: The Function of Long-Chain Polyamines and Silaffins. *Journal of Materials Chemistry* **2004,** *14* (14), 2059-2065.

(310) Lei, Q.; Guo, J.; Kong, F.; Cao, J.; Wang, L.; Zhu, W.; Brinker, C. J., Bioinspired Cell Silicification: From Extracellular to Intracellular. *Journal of the American Chemical Society* **2021,** *143* (17), 6305-6322.

(311) Gottlieb, H. E.; Kotlyar, V.; Nudelman, A., Nmr Chemical Shifts of Common Laboratory Solvents as Trace Impurities. *Journal of Organic Chemistry* **1997,** *62* (21), 7512-7515.

(312) Huang, X.; Zhu, Y.; Zhang, X.; Bao, Z.; Lei, D. Y.; Yu, W.; Dai, J.; Wang, Y., Clam-Inspired Nanoparticle Immobilization Method Using Adhesive Tape as Microchip Substrate. *Sensors and Actuators B: Chemical* **2016,** *222*, 106-111.

(313) Benjaminsen, R. V.; Mattebjerg, M. A.; Henriksen, J. R.; Moghimi, S. M.; Andresen, T. L., The Possible "Proton Sponge" Effect of Polyethylenimine (Pei) Does Not Include Change in Lysosomal Ph. *Molecular Therapy* **2013,** *21* (1), 149-157.

(314) Antonietti, L.; Aymonier, C.; Schlotterbeck, U.; Garamus, V. M.; Maksimova, T.; Richtering, W.; Mecking, S., Core−Shell-Structured Highly Branched Poly(Ethylenimine Amide)S: Synthesis and Structure. *Macromolecules* **2005,** *38* (14), 5914-5920.

(315) Yeh, P.-H.; Sun, J.-S.; Wu, H.-C.; Hwang, L.-H.; Wang, T.-W., Stimuli-Responsive Ha-Pei Nanoparticles Encapsulating Endostatin Plasmid for Stem Cell Gene Therapy. *RSC advances* **2013,** *3* (31), 12922-12932.

(316) Jin, Z.; Du, L.; Zhang, C.; Sugiyama, Y.; Wang, W.; Palui, G.; Wang, S.; Mattoussi, H., Modification of Poly (Maleic Anhydride)-Based Polymers with H2n–R Nucleophiles: Addition or Substitution Reaction? *Bioconjugate Chemistry* **2019,** *30* (3), 871-880.

(317) Catti, M.; Ferraris, G.; Filhol, A., Hydrogen Bonding in the Crystalline State. Cahpo4 (Monetite), P1 or P1? A Novel Neutron Diffraction Study. *Acta Crystallographica Section B Structural Crystallography and Crystal Chemistry* **1977,** *33* (4), 1223--1229.

(318) Curry, N. A.; Jones, D. W., Crystal Structure of Brushite, Calcium Hydrogen Orthophosphate Dihydrate: A Neutron-Diffraction Investigation. *Journal of the Chemical Society A: Inorganic, Physical, Theoretical* **1971**, 10.1039/J19710003725 (0), 3725--3729.

(319) Dickens, B.; Prince, E.; Schroeder, L. W.; Brown, W. E., $Ca(H_2po_4)_2$, a Crystal Structure Containing Unusual Hydrogen Bonding. *Acta Crystallographica Section B Structural Crystallography and Crystal Chemistry* **1973,** *29* (10), 2057--2070.

(320) Liu, S.; Liang, Y.; Ma, X.; Li, H.; Zhang, W.; Tu, D.; Chen, Y., Tunable Photoluminescence and Energy Transfer Efficiency in B-$Ca_3(Po_4)_2$-$Ca_9la(Po_4)_7$:Eu^{2+}, Mn^{2+} Solid

Solution Phosphors Introduced by Emptying Site and Structural Confinement Effect for Solid-State Lighting Application. *Inorganic Chemistry* **2020,** *59* (6), 3596--3605.

(321) Mathew, M.; Brown, W. E.; Schroeder, L. W.; Dickens, B., Crystal Structure of Octacalcium Bis(Hydrogenphosphate) Tetrakis(Phosphate)Pentahydrate, $Ca_8(Hpo_4)_2(Po_4)_4 \cdot 5h_2o$. *Journal of Crystallographic and Spectroscopic Research 1988 18:3* **1988,** *18* (3), 235--250.

(322) Mathew, M.; Schroeder, L. W.; Dickens, B.; Brown, W. E., The Crystal Structure of A-$Ca_3(Po_4)_2$. *Acta Crystallographica Section B* **1977,** *33* (5), 1325--1333.

(323) Schroeder, L. W.; Prince, E.; Dickens, B.; Iucr, Hydrogen Bonding in Ca(H2po4)2.H2o as Determined by Neutron Diffraction. *Acta Crystallographica Section B* **1975,** *31* (1), 9--12.

(324) Tanaka, Y.; Iwasaki, T.; Katayama, K.; Hojo, J.; Yamashita, K., Effect of Ionic Polarization on Crystal Structure of Hydroxyapatite Ceramic with Hydroxide Nonstoichiometry. *Journal of the Japan Society of Powder and Powder Metallurgy* **2010,** *57* (7), 520--528.

(325) Brow, R. K., Review: The Structure of Simple Phosphate Glasses. *Journal of Non-Crystalline Solids* **2000,** *263-264*, 1-28.

(326) Sirsi, S.; Feshitan, J.; Kwan, J.; Homma, S.; Borden, M., Effect of Microbubble Size on Fundamental Mode High Frequency Ultrasound Imaging in Mice. *Ultrasound in medicine & biology* **2010,** *36* (6), 935-948.

(327) Kempen, P. J.; Greasley, S.; Parker, K. A.; Campbell, J. L.; Chang, H. Y.; Jones, J. R.; Sinclair, R.; Gambhir, S. S.; Jokerst, J. V., Theranostic Mesoporous Silica Nanoparticles Biodegrade after Pro-Survival Drug Delivery and Ultrasound/Magnetic Resonance Imaging of Stem Cells. *Theranostics* **2015,** *5* (6), 631-42.

(328) Pastor‐Pérez, L.; Chen, Y.; Shen, Z.; Lahoz, A.; Stiriba, S. E., Unprecedented Blue Intrinsic Photoluminescence from Hyperbranched and Linear Polyethylenimines: Polymer Architectures and Ph‐Effects. *Macromolecular Rapid Communications* **2007,** *28* (13), 1404-1409.

(329) Hunter, A. C., Molecular Hurdles in Polyfectin Design and Mechanistic Background to Polycation Induced Cytotoxicity. *Adv Drug Deliv Rev* **2006,** *58* (14), 1523-31.

(330) Dickens, B.; Prince, E.; Schroeder, L. W.; Brown, W. E., $Ca(H_2po_4)_2$, a Crystal Structure Containing Unusual Hydrogen Bonding. *Acta Crystallographica Section B Structural Crystallography and Crystal Chemistry* **1973,** *29* (10), 2057--2070.

(331) Mathew, M.; Brown, W. E.; Schroeder, L. W.; Dickens, B., Crystal Structure of Octacalcium Bis(Hydrogenphosphate) Tetrakis(Phosphate)Pentahydrate, $Ca_8(Hpo_4)_2(Po_4)_45h_2o$. *Journal of Crystallographic and Spectroscopic Research 1988 18:3* **1988,** *18* (3), 235--250.

(332) Zhang, J.; Huang, D.; Saw, P. E.; Song, E., Turning Cold Tumors Hot: From Molecular Mechanisms to Clinical Applications. *Trends in Immunology* **2022,** *43* (7), 523-545.

(333) Clerc, P.; Jeanjean, P.; Hallali, N.; Gougeon, M.; Pipy, B.; Carrey, J.; Fourmy, D.; Gigoux, V., Targeted Magnetic Intra-Lysosomal Hyperthermia Produces Lysosomal Reactive Oxygen Species and Causes Caspase-1 Dependent Cell Death. *Journal of Controlled Release* **2018,** *270*, 120-134.

(334) Jiang, W.; Yin, L.; Chen, H.; Paschall, A. V.; Zhang, L.; Fu, W.; Zhang, W.; Todd, T.; Yu, K. S.; Zhou, S.; Zhen, Z.; Butler, M.; Yao, L.; Zhang, F.; Shen, Y.; Li, Z.; Yin, A.; Yin, H.; Wang, X.; Avci, F. Y.; Yu, X.; Xie, J., Nacl Nanoparticles as a Cancer Therapeutic. *Advanced Materials* **2019,** *31* (46), 1904058.

(335) Chen, B.; Yan, Y.; Yang, Y.; Cao, G.; Wang, X.; Wang, Y.; Wan, F.; Yin, Q.; Wang, Z.; Li, Y.; Wang, L.; Xu, B.; You, F.; Zhang, Q.; Wang, Y., A Pyroptosis Nanotuner for Cancer Therapy. *Nature Nanotechnology* **2022,** *17* (7), 788-798.

(336) Fan, J.-X.; Deng, R.-H.; Wang, H.; Liu, X.-H.; Wang, X.-N.; Qin, R.; Jin, X.; Lei, T.-R.; Zheng, D.; Zhou, P.-H., Epigenetics-Based Tumor Cells Pyroptosis for Enhancing the Immunological Effect of Chemotherapeutic Nanocarriers. *Nano Letters* **2019,** *19* (11), 8049-8058.

(337) Burgess, D. J., Tissue Penetration of Photodynamic Therapy. *Nature Reviews Cancer* **2012,** *12* (11), 737-737.

(338) Karaz, S.; Senses, E., Liposomes under Shear: Structure, Dynamics, and Drug Delivery Applications. *Advanced NanoBiomed Research* **2023,** *3* (4), 2200101.

(339) Gao, A.; Hu, X.-l.; Saeed, M.; Chen, B.-f.; Li, Y.-p.; Yu, H.-j., Overview of Recent Advances in Liposomal Nanoparticle-Based Cancer Immunotherapy. *Acta Pharmacologica Sinica* **2019,** *40* (9), 1129-1137.

(340) Allemailem, K. S.; Almatroudi, A.; Alrumaihi, F.; Almatroodi, S. A.; Alkurbi, M. O.; Basfar, G. T.; Rahmani, A. H.; Khan, A. A., Novel Approaches of Dysregulating Lysosome Functions in Cancer Cells by Specific Drugs and Its Nanoformulations: A Smart Approach of Modern Therapeutics. *International Journal of Nanomedicine* **2021,** *16*, 5065-5098.

(341) Zhu, S.-y.; Yao, R.-q.; Li, Y.-x.; Zhao, P.-y.; Ren, C.; Du, X.-h.; Yao, Y.-m., Lysosomal Quality Control of Cell Fate: A Novel Therapeutic Target for Human Diseases. *Cell Death & Disease* **2020,** *11* (9), 817.

(342) Piao, S.; Amaravadi, R. K., Targeting the Lysosome in Cancer. *Ann N Y Acad Sci* **2016,** *1371* (1), 45-54.

(343) Li, W.; Yin, S.; Shen, Y.; Li, H.; Yuan, L.; Zhang, X.-B., Molecular Engineering of Ph-Responsive Nir Oxazine Assemblies for Evoking Tumor Ferroptosis Via Triggering Lysosomal Dysfunction. *Journal of the American Chemical Society* **2023,** *145* (6), 3736-3747.

(344) Wojnilowicz, M.; Glab, A.; Bertucci, A.; Caruso, F.; Cavalieri, F., Super-Resolution Imaging of Proton Sponge-Triggered Rupture of Endosomes and Cytosolic Release of Small Interfering Rna. *Acs Nano* **2019,** *13* (1), 187-202.

(345) Benjaminsen, R. V.; Mattebjerg, M. A.; Henriksen, J. R.; Moghimi, S. M.; Andresen, T. L., The Possible "Proton Sponge " Effect of Polyethylenimine (Pei) Does Not Include Change in Lysosomal Ph. *Molecular Therapy* **2013,** *21* (1), 149-157.

(346) He, T.; Bradley, D. G.; Xu, M.; Ko, S.-T.; Qi, B.; Li, Y.; Cheng, Y.; Jin, Z.; Zhou, J.; Sasi, L., Bio-Inspired Degradable Polyethylenimine/Calcium Phosphate Micro-/Nano-Composites for Transient Ultrasound and Photoluminescence Imaging. *Chemistry of Materials* **2022,** *34* (16), 7220-7231.

(347) Alas, M.; Saghaeidehkordi, A.; Kaur, K., Peptide–Drug Conjugates with Different Linkers for Cancer Therapy. *Journal of Medicinal Chemistry* **2021,** *64* (1), 216-232.

(348) Cheng, Y.; Clark, A. E.; Zhou, J.; He, T.; Li, Y.; Borum, R. M.; Creyer, M. N.; Xu, M.; Jin, Z.; Zhou, J.; Yim, W.; Wu, Z.; Fajtová, P.; O'Donoghue, A. J.; Carlin, A. F.; Jokerst, J. V., Protease-Responsive Peptide-Conjugated Mitochondrial-Targeting Aiegens for Selective Imaging and Inhibition of Sars-Cov-2-Infected Cells. *Acs Nano* **2022,** *16* (8), 12305-12317.

(349) Diao, L.; Meibohm, B., Pharmacokinetics and Pharmacokinetic–Pharmacodynamic Correlations of Therapeutic Peptides. *Clinical Pharmacokinetics* **2013,** *52* (10), 855-868.

(350) Roksnoer, L. C.; Heijnen, B. F.; Nakano, D.; Peti-Peterdi, J.; Walsh, S. B.; Garrelds, I. M.; van Gool, J. M.; Zietse, R.; Struijker-Boudier, H. A.; Hoorn, E. J.; Danser, A. H., On the Origin of Urinary Renin: A Translational Approach. *Hypertension* **2016,** *67* (5), 927-33.

(351) Shi, H.; Zhao, N.; Ding, D.; Liang, J.; Tang, B. Z.; Liu, B., Fluorescent Light-up Probe with Aggregation-Induced Emission Characteristics for in Vivo Imaging of Cell Apoptosis. *Organic & Biomolecular Chemistry* **2013,** *11* (42), 7289-7296.

(352) Corbett, J. C. W.; Connah, M. T.; Mattison, K., Advances in the Measurement of Protein Mobility Using Laser Doppler Electrophoresis – the Diffusion Barrier Technique. *Electrophoresis* **2011,** *32* (14), 1787-1794.

(353) Chester, M., Iupac-Iub Joint Commission on Biochemical Nomenclature (Jcbn). Nomenclature of Glycolipids--Recommendations 1997. *European Journal of Biochemistry* **1998,** *257* (2), 293-298.

(354) Schlapschy, M.; Binder, U.; Börger, C.; Theobald, I.; Wachinger, K.; Kisling, S.; Haller, D.; Skerra, A., Pasylation: A Biological Alternative to Pegylation for Extending the Plasma Half-Life of Pharmaceutically Active Proteins. *Protein Engineering, Design and Selection* **2013,** *26* (8), 489-501.

(355) Harper, S. L.; Carriere, J. L.; Miller, J. M.; Hutchison, J. E.; Maddux, B. L. S.; Tanguay, R. L., Systematic Evaluation of Nanomaterial Toxicity: Utility of Standardized Materials and Rapid Assays. *Acs Nano* **2011,** *5* (6), 4688-4697.

(356) Yang, Y.; Zhao, T.; Chen, Q.; Li, Y.; Xiao, Z.; Xiang, Y.; Wang, B.; Qiu, Y.; Tu, S.; Jiang, Y.; Nan, Y.; Huang, Q.; Ai, K., Nanomedicine Strategies for Heating "Cold" Ovarian Cancer (Oc): Next Evolution in Immunotherapy of Oc. *Advanced science (Weinh)* **2022,** *9* (28), e2202797.

(357) Ferrall, L.; Lin, K. Y.; Roden, R. B. S.; Hung, C.-F.; Wu, T.-C., Cervical Cancer Immunotherapy: Facts and Hopes. *Clinical Cancer Research* **2021,** *27* (18), 4953-4973.

(358) Kupcho, K.; Shultz, J.; Hurst, R.; Hartnett, J.; Zhou, W.; Machleidt, T.; Grailer, J.; Worzella, T.; Riss, T.; Lazar, D.; Cali, J. J.; Niles, A., A Real-Time, Bioluminescent Annexin V Assay for the Assessment of Apoptosis. *Apoptosis* **2019,** *24* (1-2), 184-197.

(359) Dunn, K. W.; Kamocka, M. M.; McDonald, J. H., A Practical Guide to Evaluating Colocalization in Biological Microscopy. *American Journal of Physiology-Cell Physiology* **2011,** *300* (4), C723-C742.

(360) Nobre, T. M.; Pavinatto, F. J.; Caseli, L.; Barros-Timmons, A.; Dynarowicz-Łątka, P.; Oliveira, O. N., Interactions of Bioactive Molecules & Nanomaterials with Langmuir Monolayers as Cell Membrane Models. *Thin Solid Films* **2015,** *593*, 158-188.

(361) Elazar, A.; Weinstein, J. J.; Prilusky, J.; Fleishman, S. J., Interplay between Hydrophobicity and the Positive-inside Rule in Determining Membrane-Protein Topology. *Proceedings of the National Academy of Sciences* **2016,** *113* (37), 10340-10345.